SHOCK INDUCED CHEMICAL REACTIONS IN ENERGETIC STRUCTURAL MATERIALS

A Dissertation
Presented to
The Academic Faculty

by

Derek J. Reding

In Partial Fulfillment
of the Requirements for the Degree
Doctor of Philosophy in the
School of Aerospace Engineering

Georgia Institute of Technology
4 December 2008

SHOCK INDUCED CHEMICAL REACTIONS IN ENERGETIC STRUCTURAL MATERIALS

Approved by:

Sathyanaraya V. Hanagud,
Committee Chair
School of Aerospace Engineering
Georgia Institute of Technology

Naresh N. Thadhani
School of Aerospace Engineering
Georgia Institute of Technology

Sathyanaraya V. Hanagud, Adviser
School of Aerospace Engineering
Georgia Institute of Technology

George Kardomateas
School of Aerospace Engineering
Georgia Institute of Technology

David L. McDowell
School of Aerospace Engineering
Georgia Institute of Technology

Massimo Ruzzene
School of Aerospace Engineering
Georgia Institute of Technology

Date Approved: 4 December 2008

To my wife,

Chiung-Hsia Hung,

for her love and support.

ACKNOWLEDGEMENTS

I am most appreciative of my wife, Chiung-Hsia Hung. Without her support and companionship, this thesis could not have been possible. I am deeply thankful to her for everything she did to help motivate me.

I am thankful for my advisor, Prof. Sathya Hanagud, who taught me the value of having curiosity and not to be afraid of challenges. Our conversations often stimulated new ideas for approaching a problem. The same can be said for the support I've received from Prof. David McDowell. His enthusiasm and interest in my research reinforced my confidence in my approach. This enthusiasm is shared by Ryan Austin, with whom I enjoyed many great discussions and collaboration. I thank him very much for sharing his simulation data and for his eagerness to help. Prof. Naresh Thadhani gave me invaluable insight into experimental shock physics and helped me to narrow the scope of my work. I very much thank Prof. Yingjie Liu for his guidance on numerical methods.

The support of my friends, especially Sefano Gonella and Rich Cross, helped me realize my enthusiasm for my work even when we weren't talking about research. In many ways, they helped me realize why I wanted to pursue research so much.

Contents

List of Tables

List of Figures

SUMMARY

Energetic structural materials (ESMs) constitute a new class of materials that provide dual functions of strength and energetic characteristics. ESMs are typically composed of micron-scale or nano-scale intermetallic mixtures or mixtures of metals and metal oxides, polymer binders, and structural reinforcements. Voids are included to produce a composite with favorable chemical reaction characteristics.

In this thesis, a continuum approach is used to simulate gas-gun or explosive loading experiments where a strong shock is induced in the ESM by an impacting plate. Algorithms are developed to obtain equations of state of mixtures. It is usually assumed that the shock loading increases the energy of the ESM and causes the ESM to reach the transition state. It is also assumed that the activation energy needed to reach the transition state is a function of the temperature of the mixture. In this thesis, it is proposed that the activation energy is a function of temperature and the stress state of the mixture. The incorporation of such an activation energy is selected in this thesis. Then, a multi-scale chemical reaction model for a heterogeneous mixture is introduced. This model incorporates reaction initiation, propagation, and extent of completed reaction in spatially heterogeneous distributions of reactants. A new model is proposed for the pore collapse of mixtures. This model is formulated by modifying the Carol, Holt, and Nesterenko spherically symmetric model to include mixtures and compressibility effects.

Uncertainties in the model result from assumptions in formulating the models for continuum relationships and chemical reactions in mixtures that are distributed heterogeneously in space and in numerical integration of the resulting equations. It is

important to quantify these uncertainties. In this thesis, such an uncertainty quantification is investigated by systematically identifying the physical processes that occur during shock compression of ESMs which are then used to construct a hierarchical framework for uncertainty quantification.

Chapter I

INTRODUCTION AND BACKGROUND

1.1 Overview

Energetic structural materials (ESMs) constitute a new class of materials that provide dual functions of strength and energetic characteristics [4, 5, 88, 101, 37]. These materials are typically composed of mixtures of reactive materials, binders, and structural reinforcements. Reactive materials consist of micron-scale or nano-scale inter-metallic particles; mixtures of metals and metal oxides; or oxidizing metals. The role of structural reinforcements, polymer binders, and voids are included to produce a composite. Gas-less reactions and are sometimes called as heat detonations [20]. The failure criteria for ESMs consist of the following two failure branches: (1) one branch consists of strength-based failure. In this branch, the material is expected not fail due to lack of sufficient strength when subjected to static or dynamic loading or when exposed to specified high temperatures; (2) the second branch consists of chemical reaction-based failure. In this branch, chemical reactions are not expected when the structure with ESM is expected to operate under expected static or dynamic loading. Of course, the reaction must initiate and complete when needed.

Major difficulties arise when attempting to understand several processes during intense dynamic loading in ESMs, namely chemical reaction mechanisms, melting, inelastic behavior, and fracture. In particular, atomistic processes in chemical reactions are not well understood [104]. Direct experimental observations with current technology are limited. The physical processes involved are inherently multi-scale [92] that span from quantum mechanical scales to continuum scales in space and fempto second to milliseconds in time.

Current shock induced chemical reaction (SICR) and shock assisted chemical reaction (SACR) models consist of three independent reaction processes, namely *initiation*, *propagation*, and *complete reaction*. In some cases, shock-induced chemical reactions in ESMs are explained [28] by a homogeneous solid-state approach and a heterogeneous solid-liquid approach. In the former approach, a solid-state reaction occurs due to a high density of defects produced in shock compression of high pressures and in a high temperature environment [28]. In the latter approach, one of the reactive mixture components is assumed to be in the liquid state before the reaction initiation proceeds [28, 88].

Another leading process is known as the mechanochemical process that leads to reaction initiation and involves plastic deformation, flow, and mixing of constituents [112]. Thadhani et al. [113] suggested that the initiation of the reaction depends strongly on the relative deformation and the fracture of constituents, or solid state mechanochemical effects. Shock-induced chemical reactions are initiated within the time scales of mechanical (pressure) equilibration; shock-assisted chemical reactions are initiated on the larger time scales of thermal equilibration, after release waves have allowed mechanical relaxation [112]. Gas-gun or explosive loading experiments are a class of experiments that are used to study ESMs and similar reactive powder mixtures under shock conditions [64, 120, 39].

Formulation of models that fully predict all the complex physical processes that occur during shock compression of ESM and reactive material mixtures, without experiments, is an active area of research. Very often we rely on experiments to validate models and in many cases to calibrate unknown model parameters. However, the complex behavior, currently available measurement tools, and the needed measurement time scales of the order of femto seconds and small length scales severely limit the capability of acquiring all the needed experimental data.

Previous shock induced and shock assisted chemical reaction theoretical and computational studies are conducted at either the mesoscale or the macro-scale [14, 15, 33, 34, 5, 29, 37, 88, 101, 4, 5, 29]. The mesoscale is the middle scale and is defined here as the scale that includes a detailed description of metallic or metal oxide powder granules. Macro-scale is concerned with the continuum description of the mixture, therefore individual granules are not explicitly described at this scale. A multi-scale approach that incorporates results from a mesoscale simulation into a macro-scale model does not currently exist. Reasons for this include i) mesoscale simulations for shock induced chemical reactions are relatively new, ii) coupling between chemical and mechanical processes is complex, and iii) currently available chemical reaction models are insufficient for describing chemical reactions in heterogeneous media.

1.2 Shock-Induced Chemical Reactions

Several models and mechanisms are published to describe shock induced chemical reactions. One of the earliest is the ROLLER model by Dremin and Breusov in 1968 [35] in which the sliding interface between two crystals are assumed to produce a small nucleus or roller, which accumulates material in the formation of a new phase. Batsanov in 1986 was one of the first to investigate "superfast induced diffusion under shock loading" [8]. Both the ROLLER and Batsanov models do not include reaction initiation conditions.

In the CONMAH model by Graham [52], physical mechanisms such as, pore collapse, mixing of reactants, shock activation, and heating at sites of intimate reactant contact are considered. The reaction initiation mechanisms include: 1) large degrees of fluid-like plastic flow, 2) turbulent mixing, 3) defect generation, 4) cleansing of existing reacting surfaces, 5) formation of new reactant surfaces, and 6) elevated surface temperatures.

Thermochemical models that are introduced by Boslough in 1990 [20] and others

model the reaction initiation based on a temperature increase due to void collapse. Boslough found that reactions occurred at extremely fast rates as evidenced by temperature increases that could not be explained by the plastic work alone, which he called "heat detonations" or the heat detonation model.

Horie and Kipp present a chemical reaction model for the $Ni+Al$ system (1988 [62]). The heterogeneous model for the heterogeneous distribution of reactants includes particle or grain size and surface area effects. The resulting product formation rate is described by a non-dimensional ordinary differential equation. The spatial heterogeneity is not explicitly simulated.

A model known as the Ballotechnic model is due to Bennett and Horie ([10] in 1994) is an extension of earlier work by Graham et al. [52] and Song et al. [110] Gasless detonation for the $Ni + Al$ system is studied in which heat and volume expansion result from the exothermic chemical reaction. This model assumes a full pore collapse and employs a model known as the snow-plow model [10]. Heat from reaction is included. This model is designed to offer a "closed form prediction of the Hugoniot of the reacted powder" [10]. The model does not include reaction initiation criterion and a finite chemical reaction rate (reaction is instantaneous).

The extended VIR model (1994) is a continuum model by Bennett, Horie, and Hwang [11]. The mixture is separated into two subsystems so that the rate and the extent of reaction are controlled independently in each subsystem. Reaction is only permitted in the subsystem that is downstream of the shock front and a time delay is simulated in the chemical reaction. As with many of the continuum approaches, reaction initiation is based on the heterogeneous solid-liquid approach. Additionally, as with all of the shock induced chemical reaction models [78, 88, 101], thermodynamic quantities are assumed to be in equilibrium.

The BN theory by Baer and Nunziato (1986) models explosive mixtures as phase-separated substances [6]. This theory is formulated for any system of energetic materials including ESMs. The mixture is treated as a fluid in thermodynamic equilibrium. A critical review of this theory is given by Bdzil et al. [9] in 1999. This approach is to study deflagration-to-detonation transition in granular materials. A gas phase is produced due to chemical reactions, thus, it is necessary to modify the model for gas-less reactions of ESM investigated in this thesis.

The model of Namjoshi and Thadhani [87] (2000) predicts reaction synthesis of Ti-Si powder mixture compacts, densified at 5 to 7 GPa. Rapid solid-state diffusion describes the mass mixing. Reaction kinetics are assumed based on Carter's solid-state diffusion [26, 27]. A one dimensional "slab" model is employed for heat conduction. Reactions complete in approximately 10 seconds.

A non-equilibrium thermodynamics continuum model is formulated for a study of ESMs in 2005 by Lu, Narayanan, and Hanagud [78, 88]. A heterogeneous solid-liquid approach for reaction initiation is employed. The core strength to the non-equilibrium thermodynamics framework is the use of extended irreversible thermodynamics and the formulation that yields epressions to calculate heat due to irreversible processes. Also, the rate of entropy production is quantitatively expressed by the non-equilibrium terms [78, 88]. As is needed in all continuum models, it is necessary to determine the parameters by experimental or ab initio methods.

The RAVEN code approach [14, 15, 33, 34, 5, 29, 37] is a mesoscale alternative to the macro-scale models and mechanisms. Material granules with distributed mass are included in a two dimensional space that appears as, flakes, or cylinders of material constituents with binder material such as *Epon*828 and voids [5]. The constituent materials are separated from each other by discrete interfaces or boundaries. Thermomechanical processes including plastic flow, pore collapse, mixing behavior, and heat conduction are simulated with relatively high resolution.

RAVEN is a two dimensional multi-material Eulerian hydrocode developed by Benson [14]. RAVEN uses the monotonic upwind scheme for conservation laws (MUSCL) [73] in an Arbitrary Eulerian-Lagrangian method in which the material interfaces are tracked by Youngs' method [79]. Conserved quantities include mass, momentum, and energy. An example of the RAVEN code approach that is applied to study shock induced chemical reactions is the model (with chemical reactions) by Do and Benson [33]. In this approach, components of the mixture are assumed to be immiscible and to have an infinite transport rate. However, this modeling approach is restricted to applications in which the reaction of the powder mixture is complete. The RAVEN code approach [33, 34] also requires a reaction initiation criterion, namely, the solid-liquid approach. An example microstructure used in the RAVEN code by R. A. Austin [4] is shown in Figure (1).

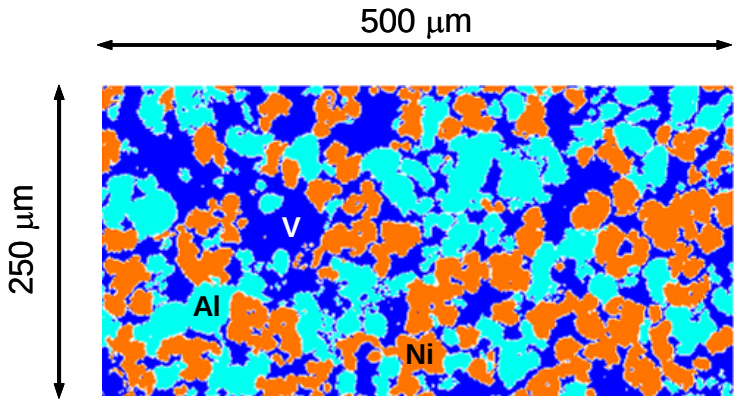

Figure 1: Actual microstructure provided by R. A. Austin. Mixture contains 60% theoretical mass density, particle diameters $d_{Ni} \approx d_{Al} \approx 25\mu m$. Void space, V, is shown in blue.

1.3 Chemical Reaction Models

The three distinct reaction processes, *initiation*, *propagation*, and *complete reaction*, used in the published shock induced chemical reaction models are discussed next. The extent of reaction is defined as the amount of conversion from reactants to products.

1.3.1 Reaction Initiation

Shock initiation of chemical reactions in spatially heterogeneous explosives has centered around the understanding of "hot spot" formation, as introduced by Bowden [22] and Eyring [40]. A hot spot is defined here as a region in which reactants reach a temperature significantly higher than the surrounding material. The amount of reactants and temperature required for a hot spot to be defined is currently unknown. Boyer's [23] (1969) work incorporates hot spots in a reaction rate model for shock initiation of chemical reaction in TNT. More recently, hot spots are used to investigate shock induced chemical reactions for intermetallic mixtures (for example see Austin [4] in 2005).

With the idea of reaction initiation due to hot spots, Lee and Tarver [72] present a phenomenological model which applies to a wide range of explosives and a wide range of shock initiation stimuli. A heterogeneous process is assumed in which the temperatures of the reacted and un-reacted material are not in equilibrium. The hot-spot ignition model is based on experimental observations using $r = 4$ in the rate equation given by,

$$\frac{\partial F}{\partial t} = I(1-F)^x \eta^r + G(1-F)^x F^y p^z. \tag{1.1}$$

In this equation, $\eta = V_o/V_1$, F is the fraction of explosive that has reacted, t is time, V_o is the initial specific volume of the explosive, V_1 is the specific volume of the shocked, unreacted explosive, p is pressure in megabars, and I, x, r, G, y, z are constants.

Equation (1.1) with $r = 4$ is used when the inelastic work required for hot-spot formation, due to void collapse. The so-called p^2 assumption has yielded the best correlation with experimental results. Walker and Wasley propose a similar critical energy criterion for initiation of detonation which is now known as the $P^2\tau = \text{const}$ criterion, where τ is in units of time.

Hot-spot shock ignition and growth-to-detonation, double shock ignition, and

quenching and reignition in solid explosives are in a report by Horie, Hamate, and Greening [61] (2003). Their hot-spot model is a planar, combustion model with a propagating hot and reacting surface that is initially heated by either localized mechanical heating or by other means of external heat supply. Further details are in a review by Bdzil et al. [9].

Recent reaction initiation models, proposed since 2006, are now reviewed [53, 54, 32, 17]. Gur'ev, Gordopolov, and Batsanov [53] propose a mechanism for the chemical transformation and a heterogeneous $Zn-Te$ system. This approach accounts for the increase in specific volume due to the formation of products. Shock wave pressures are strong enough in all cases to initiate chemical reactions since the sample materials are heated to temperatures close to the point in which chemical reactions occur. Solid state reactions are shown to be feasible by evidence of increased shock wave velocity with increased sample pre-heating. In a similar study by Gur'ev, Gordopolov, Batsanov, Merzhanov, and Fortov [54], experiments are performed for the solid state detonation in the zinc-sulfur system. The exothermic solid-state detonation represents a new type of transport phenomena in reactive media.

Dienes, Zuo, an Kershner [32] propose a statistical approach for modeling the dynamic response of brittle materials including explosives. Conventional explosives, PBX-9404, PBX-9502, and PBX-9501 are investigated. Although these explosives are not ESMs, it is useful to examine these models since it is possible to develop similar models to investigate ESMs. Some reaction initiation models are discussed here. Intense heating is hypothesized at crack interfaces during compaction, in which hot spot formation is possible [32]. At low shock velocities, interfacial friction is thought to be a dominant mechanism. Subsequent reaction and possible detonations are considered. The critical temperature for ignition is given by [75],

$$T_c(T_i, \dot{q}) = \frac{E_A}{R} \frac{1}{\ln\left(\rho Q_r Z k T_i / \dot{q}^2\right)} \tag{1.2}$$

where T_i is the initial temperature, $\dot{q}$ is the heating per unit area (flux) due to interfacial friction, E_A is the activation energy, R is the universal gas constant, ρ is the mass density, Q_r is the heat of reaction per unit mass for chemical decomposition, Z is the frequency factor, and k is the thermal conductivity.

The ten hot-spot mechanisms that are pointed out in reference [32] are: 1) Adiabatic compression of cavity gases, 2) Heating of solid adjacent to collapsing cavity, 3) Viscous heating of binder between grains, 4) Friction between impacting surfaces, 5) Localized adiabatic shear, 6) Heating at crack tips, 7) Heating at dislocation pile ups, 8) Spark discharge, 9) Triboluminescent discharge, 10) Decomposition followed by Joule heating of metallic elements. The role that these hot-spot mechanisms have in intermetallic and metal/metal oxide systems is an open area of research.

Reaction initiation mechanisms for sulfur and zinc, bismuth oxide and aluminum, and copper (II) sulfate and sulfur by Gordopolov and Viljoen [49] in 2004 requires an energy release during shock compression. Fracture initiates at the shock front if sufficient energy is dissipated from elastic, chemical, and thermal contributions. Gordopolov and Viljoen suggest that the material "volatilizes" when the dissipated energy reaches the limit of the theoretical strength of the crystalline structure but the storage of energy in excited states may occur prior to this limit.

Bolkhovitinov and Batsanov [17] in 2007 employ the classical Jouguet-Zel'dovich theory, in which the hydrodynamic equations describe the state of the medium in the Jouguet plane, where the chemical reaction is terminated in high explosives. Detonation velocities are shown to closely match experimental results using manganese and zinc chalcogenides.

1.3.2 Reaction Propagation

The modified Arrhenius model by Lu, Narayanan, and Reding [78, 88, 101] is a generalized form of the Arrhenius model used in shock induced chemical reaction studies

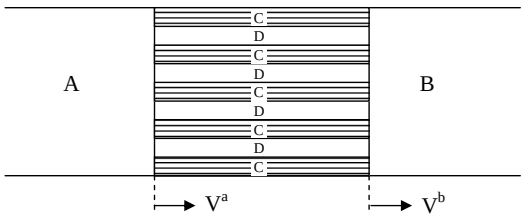

Figure 2: Wagner mechanism

and is given in equation (1.3). The modification accounts for the non-equilibrium reaction rate behind the shock front [78]. However, this modification does not delay the onset of chemical reaction, which depends entirely on the reaction initiation criterion.

$$\begin{aligned} \tau_\Theta \dot{\Theta} + \Theta &= {}^{+}A_o \left({}^{+}\phi_{(l)}\right) \exp\left\{-\frac{{}^{+}\mu_a}{RT}\right\} \prod_{p+} \left[{}^{+}C_p\right]^{{}^{+}v_p} \\ &\quad + {}^{-}A_o \left({}^{-}\phi_{(l)}\right) \exp\left\{-\frac{{}^{-}\mu_a}{RT}\right\} \prod_{p-} \left[{}^{-}C_p\right]^{{}^{-}v_p} \end{aligned} \tag{1.3}$$

where Θ is the chemical reaction rate, τ_Θ is a relaxation time for the chemical reaction rate, R is the universal gas constant ($8.314472 J \cdot K^{-1} \cdot mol^{-1}$), T is the temperature, A_o is the pre-exponential factor, $\phi_{(l)}$ is the mass fraction of the constituents in the liquid phase, μ_a is the activation energy, ${}^{+}()$ refers to the reactant group and ${}^{-}()$ refers to the product group. v_p is the stoichiometric coefficient and C_p (mol/m^3) is the concentration of reactant phase p and is given by,

$$C_p = \frac{\phi_p \bar{\rho}}{M_p} \tag{1.4}$$

and changes in the rate are given by,

$$\dot{C}_p = v_p \Theta. \tag{1.5}$$

1.3.3 Reaction Extent

In most shock induced chemical reaction studies, reaction extent is chosen to be either complete (in cases where complete reactions occur by experimental observation [33]) or partial by estimating the extent of reaction to closely match experimental data [11].

One study that aims to explain partial reactions is due to Batsanov [7], in which a forced diffusion model is used to model solid-phase reactions induced by shock waves. The time needed for a particle of one component to diffuse through a particle of another component is

$$\tau = 2d/\Delta u_{12} \tag{1.6}$$

where d is the particle diameter, u is the particle velocity, and $\Delta u_{12} = u_1 - u_2$. Partial reactions are explained for cases in which Δu_{12} is insufficient for a particle of a certain size to pierce another particle.

1.4 Pore Collapse

Ductile fracture criterion, in porous materials, with shear banding is considered by McClintock, Kaplan, and Berg [81]. McClintock [82] presents a very strong inverse dependence of fracture strain on hydrostatic tension in plastic materials. Dienes, Zuo, an Kershner [32] use this work in modeling explosives.

Oh and Persson [95] propose an empirical equation of state for accurate extrapolation of high-pressure shock Hugoniot states to other thermodynamic states. Porous Hugoniots are extrapolated from corresponding solid Hugoniot data. A similar approach to formulate an equation of state with application to porous mixtures is by Wu and Jing equation [119] in 1996. Geng, Wu, Tan, Cai, and Jing [45, 46, 44] modify this model (2002).

Silvia and Ramesh [30] consider porosity as an internal variable. To investigate dynamic powder consolidation for porous pure iron (up to strain rates exceeding $10^3 s^{-1}$), a finite deformation viscoelastic model is formulated using the theory of composites [30]. These strain rates are not as high as the strain rates that are observed in shock consolidation experiments [85].

Other continuum models to describe pore collapse in energetic granular metallic mixtures are in references [20, 110, 11, 10, 114, 78, 88, 101]. All of these models use

the widely used $P-\alpha$ model by Herrmann [60] to describe pore collapse. A quadratic dependence of porosity on pressure is assumed for all of these studies except for the work in [114]. The $P-\alpha$ model is an equation of state, without temperature effects. The $P-\alpha$ model depends on pressure. A study of dynamic compaction in porous media [18] compares commonly used models, namely $P-\alpha$, $P-\lambda$, and snowplow model.

1.4.1 $P-\alpha$ Model

The $P-\alpha$ model by Herrmann [60] in equation (1.7) is a pore collapse equation of state which is applied in porous aluminum and iron [24, 11]. The quadratic dependence on pressure is given by $n=2$ in equation (1.7). This equation of state assumes that $P=P(\rho)$ only.

$$\alpha = \begin{cases} \alpha_o & ; \quad P < P^e \\ 1+(\alpha_o-1)\left[(P^s-P)/(P^s-P^e)\right]^n & ; \quad P^e \le P \le P^s \\ 1 & ; \quad P^s < P \end{cases} . \tag{1.7}$$

The parameter n describes the order of porosity dependence on the pressure P and is left as a general unknown material parameter. P^e and P^s are the elastic threshold and pore collapse strength respectively. For $P < P^e$, only elastic deformations are assumed to take place and for $P > P^s$ complete closure of the voids is assumed. The porosity is a measure of the void content and is expressed in terms of specific volume v and density ρ by,

$$\alpha = \frac{v}{v_d} = \frac{\rho_d}{\rho} \ge 1 \tag{1.8}$$

where the densities ρ_d and ρ correspond to the dense and porous material at the same temperature and pressure.

The central assumption used in the $P-\alpha$ model is that specific internal energy is the same for the porous material and the fully dense material under identical conditions of pressure and temperature [60]. This assumption implies that the surface

energy of the pores is neglected. The equation of state for the porous material is denoted by,

$$P = f\left(v_d, e\right) = f\left(\frac{v}{\alpha}, e\right). \tag{1.9}$$

1.4.2 $P - \lambda$ Compaction Model

The $P - \lambda$ model, developed by Grady [51, 50] is another model to describe pore collapse. The porous material is split into two separate groups, un-compacted and fully compacted. The mass fraction of compacted mixture is denoted λ and is an irreversible state variable defined by,

$$\lambda = 1 - e^{-(P/Y)^n} \tag{1.10}$$

where Y is the local mixture yield strength, P is the local pressure, and n is the mixture homogeneity.

1.4.3 Spherically Symmetric Model

An alternative to the $P - \alpha$ model is the single pore models with spherical symmetry [24, 36, 91, 25, 92] shown schematically in Figure (3). This model includes viscoplasticity and dynamic effects for a monolithic material with single constituent. These models describe the pressure-density relation in the dynamic process of pore densification due to a shock wave. A critical analysis of the Carroll-Holt model is given by Nesterenko [92] with a detailed discussion of the reasons for the modification of the classical Carroll-Holt model shown schematically in Figure (3(a)). The modified Carroll-Holt model assumes a nondeformable central core [25, 91, 92] as seen in Figure (3(b)). This physically represents the geometry of a granule. The central core prevents the large strains in the hollow sphere model. The pore collapse kinetics are successfully described for shock pressures $1 - 14GPa$ (in copper) based on agreement with experimental shock front thickness [91, 92].

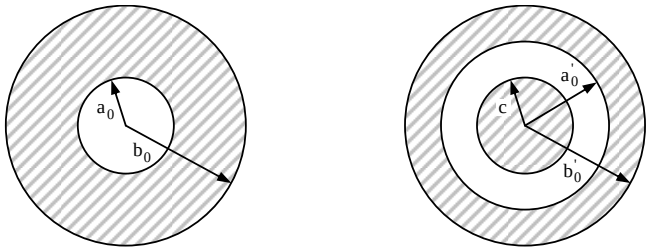

(a) Carroll-Holt model (b) Modified Carroll-Holt model

Figure 3: Spherically symmetric single pore collapse models.

In contrast to the $P - \alpha$ EOS model, the spherically symmetric model gives a history dependent simulation of the pore collapse process. The non-deformable core prevents the outer shell from collapsing to the center. The superscript ($'$) notation in Figure (3(b)) is not included in the following equations for convenience, i.e., $a_o = a_o^{'}$ and $b_o = b_o^{'}$.

It is assumed that plastic flow dominates the pore collapse process. It is also assumed that the outside shell material is incompressible. Pore collapse is not affected by this assumption when α is relatively high [92], or approximately greater than $\alpha = 1.1$. The following geometrical relations describe the radially symmetric motion in the modified hollow sphere model:

$$r^3 - a^3 = r_o^3 - a_o^3, \quad \theta = \theta_o, \quad \varphi = \varphi_o, \tag{1.11}$$

where $r, \theta,$ and φ are spherical polar coordinates, $c \leq r_o \leq b_o$ corresponds to the initial radius of some point with the current coordinate r, and a and a_o are the current and initial inner radii of the model sphere.

The core radius c is determined based on the assumption that the volume of the plastically deformed material (the volume of the outside shell) is equal to the volume of empty space if the initial porosity of the granular material α_o is smaller than the minimal porosity α^* achieved by dense packing of the granules. For cases when $\alpha_o > \alpha^*$, the volume of the outside shell is supposed to be equal to the volume of the

empty space corresponding to the porosity α^*. This porosity is a function of particle morphology. For the random packing of spheres, $\alpha^* = 1.66$ [47].

For granular materials (spherical), the mass in the model spherical cell and the mass in the granular material are equal. The resulting relations between the model parameters and properties of the powder are given in equation (1.12) for the case when $\alpha^* \geq \alpha_o < 2$.

$$b_o = R\sqrt[3]{\alpha_o}, \quad a_o = R, \quad c = R\sqrt[3]{2 - \alpha_o}, \quad \alpha = \left(\frac{a}{a_o}\right)^3 + (\alpha_o - 1)\,, \tag{1.12}$$

where R is the representative particle radius in the granular material. This is generally unknown since the mixture components do not have uniform diameters. R is treated as an unknown material parameter.

Wang, Li, and Yan [116] use the hollow sphere model or Carroll-Holt model to study the mechanisms of energy deposition at the interface between granules in explosively compacted metal powders. A contact between mixture constituents is not assumed to be degraded by physical and chemical processes. Therefore, only a single constituent mixture is demonstrated. Their simulation results [116] show the coupling between strain-rate hardening and thermal softening that results in melting. Melting only occurs in a small region near the inner surface of the shell. Premature melting may have occurred since the spherically symmetrical geometry of the hollow sphere causes a singularity when the inner radius a from Figure (3(a)) approaches zero [92]. Temperature produced due to the plastic work has a logarithmic singularity ($T \sim \ln a$) and viscous dissipation tends to infinity ($T \sim a^{-5/2}$).

Results from Tang, Liu, and Horie [111] demonstrate a need for an improved mesoscale pore collapse model through simulations that show strong localization effects. Benson, Nesterenko, Jonsdottir, and Meyers [15] stress the importance for models to incorporate realistic powder morphology and a non-uniform plastic flow. Their study [15] investigates the transition between quasistatic and dynamic regimes regimes correlates with a defined "microkinetic energy (MKE)" and depends on the

pressure, initial porosity and the mixture strength. MKE is a term introduced by Nesterenko [90, 91, 92] to "describe the qualitative transition from the quasistatic type of particle deformation to the dynamic type of deformation during the shock wave loading of powders".

1.5 Mixture Equation of State

Several methods have been presented [84, 20, 10, 11, 85] to calculate the mixture EOS by using Mie-Grüneisen and Murnaghan EOS models with mass or volume fraction averaged material parameters. Three methods [84, 10, 85] are commonly used in shock studies in which mixtures contain more than one constituent.

1.6 Numerical Approaches

Regardless of any theoretical approach to describe the physical processes in shock induced chemical reactions, the accuracy of the solution usually depends on the numerical implementation. Various approaches are available to solve hyperbolic partial differential equations numerically and to treat material interfaces.

The first methods for solving shock problems numerically were presented in 1950 by Von Neumann and Richtmyer [93] by the use of finite differences of differential operators. These approaches often require the use of an artificial viscosity (case specific) to damp numerical oscillations and a vast majority of implementations are non-conservative [12]. Such approaches are also used in continuum simulations of shock induced chemical reactions [78].

Finite element approaches are used in shock induced chemical reactions such as in the extended VIR model [11] in which artificial viscosity is required. Finite volume approaches such as the Monotone Upstream-centered Schemes for Conservation Laws (MUSCL) algorithm [73] avoid the use of artificial viscosity through the use of slope limiters [73]. This approach is also used in shock induced chemical reactions [88, 101].

A major breakthrough in discontinuity (material interface and shock front discontinuities) front tracking is due to Glimm, Li, and Liu [48] in (2003), with the introduction of conservative front tracking. This method is conservative even at discontinuities and improves accuracy by one order over the conventional algorithms such as ghost fluid method [48].

1.7 Uncertainty Quantification

Uncertainty quantification of numerical simulations is necessary to establish the credibility of a numerical code and is composed of two main activities, verification and validation. A new framework is necessary to conduct validation studies for the purpose of designing energetic structural materials (ESMs) [88, 101, 4, 64].

A systematic hierarchial decomposition with the goal to identify independent experiments is provided in an AIAA Guide [94]. Ultimately the objective is to calibrate parameters and validate the numerical simulation using experimental data, therefore, a validation framework is required. A building-block approach [74] is recommended [94] for assessing the accuracy of the computational results at multiple levels of complexity. The complete system is decomposed into three progressively simpler phases: subsystem cases, benchmark cases, and unit problems.

The state-of-the-art practice for simulation of shock induced chemical reactions involves *model qualification* [94] based on many important physical processes. However, quantitative analysis of these models are difficult since only comparisons between simulation and experiments are performed. Uncertainty quantification requires a verification and validation framework. Although Choi et al. [29] quantify uncertainty in simulations for an non-reacting energetic structural material (shock induced chemical reactions are not considered), errors and uncertainties associated with code verification were not included.

A verification and a validation are possible when all sources of uncertainties are

identified and quantified [94]. The proposed framework quantifies uncertainty at multiple levels in the hierarchy of physical processes in the shock compression of energetic structural materials. This approach maximizes the use of experimental data, other than energetic structural material gas-gun data, for obtaining material constants from calibration.

Uncertainty quantification addresses three fundamental components of computer simulations for physical systems, namely, model qualification, model verification, and model validation [94]. The model qualification requires an understanding of the physical phenomena, thus, the problem is to qualify sets of equations or models for the nature of the physics to be simulated. Errors always exist between a mathematical model and a true physical process because of simplifying assumptions that are made.

Verification is *the process of determining that a model implementation accurately represents the developer's conceptual description of the model and the solution to the model* [94]. Four predominant sources of error are: insufficient spatial discretization convergence, insufficient temporal discretization convergence, lack of iterative convergence, and computer programming [57].

Validation is the *process of determining the degree to which a model is an accurate representation of the real world from the perspective of the intended uses of the model* [94]. The process of verifying the governing equations and validating the set of physical models gives one a historical database that has the potential to improve predictive credibility.

The solution over the entire domain, including the boundaries, is verified for the geometry and loading conditions of interest. Many codes employ shock-capturing schemes such as the MUSCL algorithm that uses flux limiters or built-in functions that limit the flux between cells or nodes. The order of accuracy in fixed cell finite volume lowers by one order near a shock discontinuity compared to the smooth regions. If the observed order-of-accuracy from grid convergence studies lies within the theoretical

order of accuracy in the smooth region and at the discontinuity, then the order-of-accuracy of the limiter is verified [70].

Several methods are available for code verification through grid refinement and some methods are appropriate for non-monotonic convergence that may occur in shock simulations. Relatively simple methods are based on extrapolation or the grid convergence index (GCI)(see method#3 [76]). However, GCI methods can not provide statistical confidence as opposed to response surface methods (RSM) [76]. Further, GCI methods rely on an empirical safety factor, F_s, to provide a confidence interval. Some of the assumptions made in GCI and RSM methods are relaxed in a non-linear Ansatz error model [59]. An Ansatz as defined in [99] is the establishment of the starting equation(s) describing a mathematical or physical problem.

The confidence estimate for a given safety factor is based on the number of grid points used N_g and no consensus has been reached on the value. For example, Roach [103] recommends that with $N_g \geq 3$ an $F_s = 1.25$ provides 95% certainty (5% uncertainty, that would be roughly a 2σ error band if the distribution were Gaussian) error band typical of experimentalists. Note that results are for steady-state fluid flow and heat transfer. Logan and Nitta [76] conclude that $N_g \geq 4$ with $F_s = 1.25$ provides an estimate of 68% certainty (or 1σ) based their database of non-smooth grid convergence studies. A consensus has been reached that it is necessary to explore multiple methods in a systematic verification study and that GCI methods ($N_g \geq 3$) often produce useful information.

Material parameters in the submodels are associated uncertainty in addition to the errors and uncertainty in the model solution. An approach based on principles of physics and Baysian analysis [57] quantifies the uncertainty in the computational model based on inferences with experimental data and on the uncertainty associated with the experimental data itself.

1.8 Shock Compression

1.8.1 Conservation Laws

Conservation of mass and energy and the momentum balance are the governing equations for hydrodynamic simulations involving shock wave propagation. Equations (A.1-A.7) are for the continuum model (macro-scale) in which mixture averages are used. The following equations do not include mass diffusion, i.e., $\mathbf{v}_p = \bar{\mathbf{v}}$ for all constituents p. The conservation equations and momentum balance, explained in more detail in Appendix (A), are given by the following three equations, written in spatial (Eulerian) coordinates:

$$\frac{\partial}{\partial t}\left(\bar{\rho}\right) + \nabla \cdot \left(\bar{\rho}\bar{\mathbf{v}}\right) = 0 \tag{1.13}$$

$$\frac{\partial}{\partial t}\left(\bar{\rho}\bar{\mathbf{v}}\right) + \nabla \cdot \left(\bar{\rho}\bar{\mathbf{v}} \times \bar{\mathbf{v}}\right) = \nabla \cdot \bar{\boldsymbol{\sigma}} + \bar{\rho}\bar{\boldsymbol{f}} + \bar{\boldsymbol{\Psi}}_m \tag{1.14}$$

$$\frac{\partial}{\partial t}\left(\bar{E}\right) + \nabla \cdot \left(\bar{E}\bar{\mathbf{v}}\right) = \nabla \cdot \left(\bar{\boldsymbol{q}}\right) + \bar{\boldsymbol{\sigma}} : \dot{\bar{\boldsymbol{\epsilon}}} + \bar{\Psi}_e \tag{1.15}$$

where t is time. $\bar{\boldsymbol{f}}$ is the specific body force vector. $\bar{\boldsymbol{\sigma}}$ is the stress tensor defined later in Section (D.1). $\dot{\bar{\boldsymbol{\epsilon}}}$ is the mixture strain rate tensor, or rate of deformation tensor. The source terms $\bar{\boldsymbol{\Psi}}_m$ and $\bar{\Psi}_e$ are defined below. $\bar{E}$ is the total energy in the mixture and is defined as

$$\bar{E} = \bar{\rho}^d \left(\bar{e} + \frac{1}{2}\bar{\mathbf{v}} \cdot \bar{\mathbf{v}}\right). \tag{1.16}$$

where $\bar{e}$ is the specific internal energy in the dense mixture since surface energy of the pores is neglected (see Section (1.4.1)) and is defined as

$$\bar{e} = \bar{C}_v \bar{T}. \tag{1.17}$$

$\bar{C}_v$ is the mass fraction averaged specific heat capacity at constant volume in the dense mixture and $\bar{T}$ is the mixture temperature. Equations (1.13-1.15) are supplemented by $n_p - 1$ independent constituent equations given by,

$$\frac{\partial}{\partial t}\left(\phi_p \bar{\rho}\right) + \nabla \cdot \left(\phi_p \bar{\rho}_p \bar{\mathbf{v}}\right) = \Psi_{massp} \tag{1.18}$$

where n_p is the total number of constituents in the mixture. These equations are required to close the solution for $n-1$ independent unknown ϕ_p quantities. Pressure and temperature are not present in equation (1.18) therefore no assumptions concerning these quantities is necessary. The rate of mass production is

$$\Psi_{massp} = \Theta M_p v_p \tag{1.19}$$

where Θ is the reaction rate. M_p is the molar mass and v_p is the stoichiometric coefficient for constituent p. The source terms $\mathbf{\Psi}_m$ and Ψ_e are due to reactions in equation (1.18) and only apply to the continuum-level model. Ψ_m in equation (4.9), representing change in momentum due to reactions, is composed of linear and angular momentum contributions respectively,

$$\bar{\mathbf{\Psi}}_m = \sum_p \Psi_{massp} \left(\mathbf{v}_p + \mathbf{x}_p \times \mathbf{v}_p\right). \tag{1.20}$$

$\mathbf{x}_p$ is the material coordinate unit vector for the p^{th} constituent. The source term Ψ_e in equation (A.8) represents the energy contribution due to reactions and is given by,

$$\bar{\Psi}_e = \sum_p \Psi_{massp} \left(\frac{1}{2}\mathbf{v}_p \cdot \mathbf{v}_p + \mu_{cp}\right), \tag{1.21}$$

where μ_{cp} is the specific chemical potential, for the p^{th} constituent, defined later. The latent heat of melting ΔH_{mp} is accounted for in the numerical solution by limiting the temperature to the melting temperature, T_{mp} for constituent p, until melting is complete. The corresponding difference in the internal energy $\bar{e}$ is used to calculate the amount of melting at each time step.

1.8.2 RAVEN Code

The granular-level physics is captured through the RAVEN code [14]. The thermo-mechanical response of a mixture during shock wave propagation is modeled using the finite element method. It should be noted that the effects of chemical reactions are not included in the current RAVEN code.

A detailed description of the algorithms used in reconstructing the geometry of mixtures for simulation is discussed elsewhere [4]; a brief description is given here to provide a deeper understanding of the underlying model used for the basis of the current models. Much of this description is directly obtained from R. Austin [97]. Details concerning calculated quantities discussed later in this thesis are given in Appendix (B). Statistical volume elements (SVEs) of a particle mixture are subjected to shock waves in the RAVEN code calculations. The SVEs are reconstructed according to certain prescribed mixture attributes (i.e., the mean particle size, the variation in particle size, and the volume fractions of the constituent phases). The mixture is reconstructed in a series of steps. First, a set of particles is generated from a prescribed particle size distribution. Next, particle centroids are located in an SVE of prescribed dimensions using a sequential addition process, where it is possible to place the particles in such a way that spatial correlations within phases are respected. Since RAVEN code calculations are performed on SVEs, it is necessary to simulate multiple instantiations of the same mixture to build up response functions used in later analyses.

A sample mixture for RAVEN code containing $Al + Fe_2O_3 + 20wt.\%EPON828$ is shown in Figure (4) for $U_p = 1km\ s^{-1}$. Boundary conditions are applied to the SVE to replicate nominally one-dimensional shock wave propagation. The shock wave is generated by applying a velocity boundary condition by a driver plate located adjacent to the left surface of the mixture, i.e., the particle velocity U_p. Impact is not simulated since oscillations at the material interface are significant. The velocity boundary condition is quickly ramped up from zero to the peak value in order to avoid ringing in the solution. The periodic boundary conditions ensure displacement continuity and traction cancelation on the top and bottom surfaces. The roller boundary condition imposes zero displacement and zero tangential force at the right surface of the mixture.

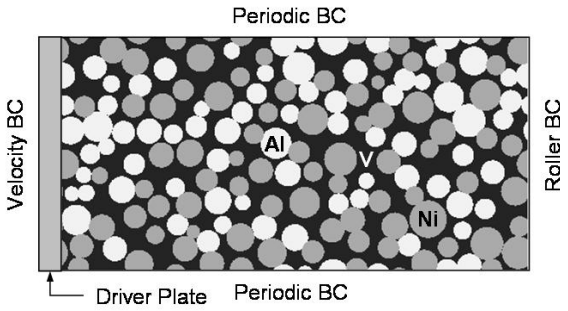

Figure 4: Boundary conditions applied to the SVE.

The initial-boundary value problem is solved using the arbitrary LagrangianEulerian (ALE) method [12]. A two-dimensional multi-material Eulerian code [14] that is specialized for shock micromechanics is used. Here, the governing equations (i.e., the conservation of mass and energy and the momentum balance in equations (A.1-A.8)) are solved using a second-order accurate central differences scheme. The ALE formulation and implementation is discussed in reference [12].

Chapter II

RESEARCH ISSUES AND OBJECTIVES

2.1 Research Issues

The current experimental observations record chemical reactions in reactive material mixtures occur over a time range from hundreds of nanoseconds to microseconds for various reactive material powder mixtures [21, 19, 20, 113, 34]. To simulate these experiments, accurate multi-scale models are needed for predicting shock induced chemical reactions within the rise time of the shock.

In all real systems such as granular metallic powders, reactants are initially separated by a surface or a void. As reaction proceeds, products form between the two reactants has the potential of inhibiting reaction [105]. Material from each side is transported across the product layer to the opposing reactant side and reaction occurs at these surfaces. The mechanisms are currently unknown in most cases. However, mass transport is dependent on several physical factors [105] which include temperature, surface or structural elements, state of stress, diffusion, and fracture. Spatially heterogeneous models [33] have been developed to approximate this behavior. Such models involve two or more reactants with finite interfaces and a finite material spatial description. However, finite mass transport rates across these interfaces have not been proposed in any model used for shock induced chemical reactions. Therefore, a chemical reaction model with finite transport rate in a heterogeneous media is needed.

A transport mechanism is needed to describe the flow of reactants through the product layer. As noted by Do and Benson [33], little is known about the transport mechanism through the product other than that it does not appear to limit the reaction rate for the $Nb - Si$ system. For general systems in which partial reactions

are observed such as in the $2Al + Fe_2O_3$ system studied by Boslough [20], the infinite transport rate assumption is clearly invalid since an infinite transport rate results in complete reactions.

Understanding the mixing mechanism is very important. Diffusion or forced diffusion alone can not explain the mass mixing in real materials during shock compression. Vorticies may form and result in mixing between reactants. Jetting is another phenomena that results in mixing between reactants. However, to form the product compounds, at some level, a diffusion type of process occurs. This is the motivation behind the current study.

Accurate and physically meaningful methods to predict the equation of state (EOS) in porous mixtures are needed. Small differences between various mixture EOS models can result in large differences in simulated shock velocity. During shock compression of ESMs, chemical reaction and pore collapse produce greatly increased temperatures with relatively low pressures. Existing EOS methods [84, 20, 10, 11, 85] use averages of constituent EOS parameters, loosing physically meaningful information such as compressibility of individual constituents and thermal expansion. Accurate and physically meaningful EOS predictions are critical for predicting the influence of chemical reactions on shock velocity.

A major limitation of the spherically symmetric single pore models [24, 91] occurs in the the energy dissipation. Wave reverberations on the scale of the grain size (shock front width) in a two-dimensional model can provide energy dissipation in addition to the dissipation from the plastic flow during pore collapse. Spherically symmetric single pore models can not capture detailed micro-structural behavior due to tremendous geometric simplifications employed to homogenize the true microstructure. However, these models allow one to gain valuable insight since temperature and plastic work are localized and the mechanics is on the length scale of the actual pores. An important requirement for the existing spherically symmetric models is to incorporate mixture

rules and compressibility effects.

Existing models [20, 11, 78, 88, 101] do not incorporate granular models or RAVEN code results. Chemical reaction implementation is complex [33] even with infinite transport rate. Therefore, a motivation in this thesis is a need for a multi-scale approach to incorporate RAVEN code results into continuum level energetic structural material (ESM) shock compression simulations.

Since the physical processes involved in the shock compression of ESMs are coupled, Hugoniot experiments are relied upon solely to obtain multiple material constants in existing models [35, 8, 52, 20, 110, 11, 10, 34, 78, 88, 101]. These models have greatly improved our understanding of experimental results involving post-shock examination and real-time measurements. However, the unknown material parameters in these models are difficult to obtain. Not all unknown material parameters independently affect the measured quantities in the experiment. For example, changes in a parameter in the chemical reaction rate model may have the same effect on the simulated shock velocity as changes in a pore collapse model parameter. Therefore, the goal is to calibrate unknown material parameters in each sub-model to experiments in which only the corresponding physical effects are present. For example, the pore collapse model is calibrated to Hugoniot experiments in which no chemical reactions occur. In the case of shock compression of ESMs, the amount of chemical reaction and the time at which chemical reactions occur are often unknown.

Previous models used to describe shock induced chemical reactions have shortcomings. The extended VIR model has the shortcoming that there is no physically based reason for selecting the amount of reactants in the subsystems. The extent of reaction is left as a model parameter to be calibrated with experiments, thus, predictive capability is diminished significantly. In the non-equilibrium thermodyanmic model, the most significant shortcoming is the need to calibrate several material constants. In the models by Do and Benson [33] and Bennett and Horie [11], predictive

capability is lacking for cases when partial reactions occur.

2.2 Objectives

The objectives are summarized as follows:

- Formulate procedures to obtain the unknown equation of state parameters of a mixture with chemical reactions during the passing of a shock wave or shock induced chemical reactions.

- Construct models that can be used to calculate shock induced chemical reactions in heterogeneous media consisting of reactive materials with binder and reinforcement. Then, illustrate the procedure with 1-D strain approximation for special cases. The model includes finite mass transport rate, the activation energy to be a function of both temperature and stress parameters, and mesoscale reaction.

- Develop techniques to quantify the uncertainty in shock simulation computer codes and formulate techniques for verification and validation.

The multi-scale model presented is useful for the design of novel materials formed through shock synthesis. In addition, this model provides higher fidelity physical representation of shock induced chemical reactions than previous models. This model is useful for incorporation into the RAVEN code.

2.3 Thesis Outline

A procedure to accurately calculate the equation of state of a mixture during the passage of a shock wave, shock induced chemical reactions is discussed in Chapter (3) and includes the proposed spherically symmetric pore collapse model for a mixture and compressibility effects. A more detailed description of the homogeneous chemical reaction model is given along with the granular level reaction (GLR) model, modeled

as heterogeneous media, and mesoscale reaction (MSR) model in Chapter (4). The gas-gun simulation is explained in Chapter (5) and the sources for uncertainty are given in Chapter (6).

A significant contribution of this thesis is the formulation of chemical reactions and thermomechanical processes which are represented in separate sets of models are integrated. The models have a strong link of deriving information from the RAVEN code and incorporating the chemical reaction model. However, chemical and thermomechanical models are run separately due to the difference in spatial and temporal scales. Both models are used in the continuum gas-gun simulation where temperature is transferred between the reaction and thermomechanical models.

The proposed granular level reaction (GLR), mesoscale reaction (MSR), and pore collapse models are part of a multi-scale modeling approach to investigate shock induced chemical reactions in Chapter (4). Figure (5) shows the framework in which the RAVEN code (a discrete particle simulation) results are incorporated into chemical reaction and pore collapse equation of state models. The $Ni + Al$ system is chosen for the study involving the complete model integration spanning mesoscale and macroscale models. The advantage for this system is the experimental evidence, from pressure gauges and post-shock recovery, suggesting the presence of shock induced chemical reactions.

The proposed multi-scale model framework is demonstrated using two separate case studies, namely the $Fe_2O_3 + Al$ system and the $Al + Ni$ system. The thermite system ($Fe_2O_3 + Al$) is used to elucidate the granular level reaction models and mixture equation of state methods. The $Al + Ni$ system is used to demonstrate the heterogeneous granular level reaction and mesoscale reaction models and the spherically symmetric pore collapse model, which are then used in the gas-gun simulation. The main contribution for the $Fe_2O_3 + Al$ system is to demonstrate the advantages

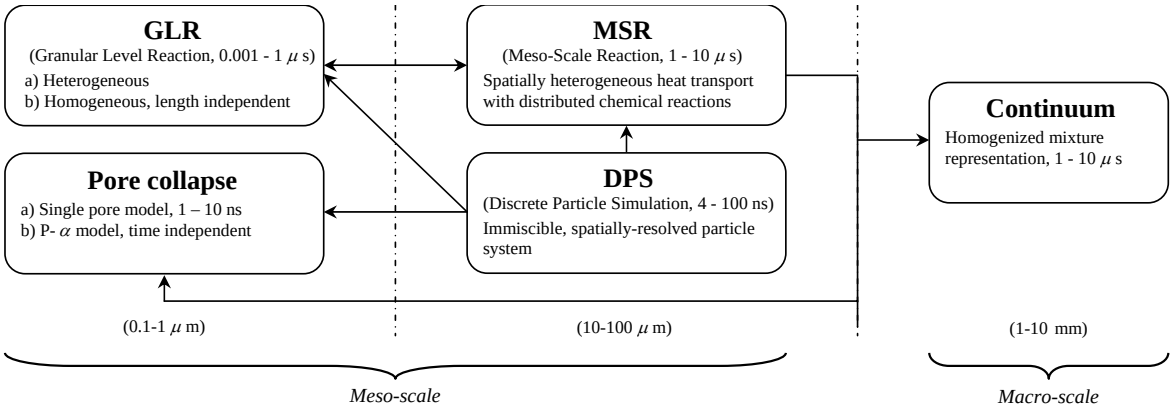

Figure 5: Multi-scale model schematic with models in boxes and arrows to indicate information flow. Time and length scales are typical for gas-gun experiment simulations in which micron-scale or nano-scale inter-metallic granules are considered. Note: the homogeneous GLR model does not have spatial dependency; the $P - \alpha$ pore collapse model does not have either time or spatial dependency.

of the proposed equation of state algorithms, show results for the granular level reaction model, and show fully integrated chemical reaction results. Unfortunately, no experimental data exist for the latter case. Fortunately, experimental data does exist for the $Al + Ni$ system. For the $Al + Ni$ system, the qualities of the spherically symmetric pore collapse model are demonstrated along with granular level reaction and mesoscale reaction models. These demonstrate that reactions can occur within a nanosecond, which is much faster than standard diffusion. The completely integrated multi-scale model is demonstrated for the $Al + Ni$ system through comparison with gas-gun experiments in which reaction is evidenced.

Chapter III

CONSTITUTIVE RELATIONSHIPS

The constitutive relationships for reactive material mixtures are discussed in this chapter. The formulation of mixture equation of state methods is a new contribution and is an improvement over the three previously discussed methods#1-3 [10, 84, 85]. The second new contribution given is the modification of a spherically symmetric pore collapse model to include a mixture of reactive materials and compressibility effects. Published pore collapse models do not consider mixtures [92].

3.1 Equation of State for Mixtures

3.1.1 Mixture Rules Used by Bennett and Horie [10](Method#1)

The mixture averaged isentropic parameter and pressure derivative are obtained respectively by,

$$\bar{\beta}_{S_o} = \frac{1}{\bar{\rho}_o}\left[\sum_p \frac{\phi_p}{\rho_{op}\beta_{S_op}}\right]^{-1} \tag{3.1a}$$

$$\bar{\beta}'_{S_o} = \bar{\rho}_o\bar{\beta}^2_{S_o}\left[\sum_p \frac{\phi_p\left(1+\beta'_{S_op}\right)}{\rho_{op}\beta^2_{S_op}}\right] - 1 \tag{3.1b}$$

The reference temperature T_o is usually taken as room temperature, $\approx 298K$. ρ_o is the reference density. $\bar{\rho}$ is defined in a later chapter. Γ is the Grüneisen parameter. ϕ_p is the mass fraction for constituent or phase p. This method assumes that

$$\beta_{T_o} \cong \beta_{S_o} = \rho_o C_o^2 \tag{3.2a}$$

$$\beta'_T \cong \beta'_S = 4S_1 - 1 \tag{3.2b}$$

where S_1 is the slope of the $U_s - U_p$ curve. The following relationship is assumed,

$$\rho\Gamma = \rho_o\Gamma_o. \tag{3.3}$$

The quantities $\bar{C}_v$ and $\bar{\Gamma}$ are are grouped together and approximated by the mixture rule [11].

$$\bar{C}_v\bar{\Gamma} = \bar{\beta}_T \sum_p \frac{\phi_p C_{vp}\Gamma_p}{\beta_{Tp}}. \tag{3.4}$$

The Murnaghan equation of state (EOS) [86] for a mixture is given by

$$\bar{P} = \frac{\bar{\beta}_{T_o}}{\bar{\beta}'_{T_o}}\left[\left(\frac{\bar{\rho}}{\bar{\rho}_o}\right)^{\bar{\beta}'_{T_o}} - 1\right] + \bar{C}_v\bar{\Gamma}_M\bar{\rho}_o\left(\bar{T} - \bar{T}_o\right) \tag{3.5}$$

where $\beta_{T_o} = -V(\partial P/\partial V)|_{T_o}$ is the isothermal bulk modulus at the reference temperature, $\beta'_{T_o} = (\partial\beta/\partial P)|_{T_o}$ is the pressure derivative of the isothermal bulk modulus at the reference temperature, C_v is the specific heat capacity under constant volume, ρ_o is the reference density, and Γ_M is a material parameter similar to the Grüneisen parameter Γ. Equation (D.17) is easily inverted, i.e., solved for ρ.

3.1.2 Mixture Rule Based on Mass Fraction Averages at $0K$ Isotherms [84] (Method#2)

Two methods are discussed by Meyers [85]. This method is due to McQueen et al. [84]. In the following equation, all quantities are mixture averaged and the overbar is omitted for clarity. The pressure is calculated by solving the differential equation,

$$\left(\frac{dP}{dv}\right)_{T_o} + \frac{\Gamma_o}{v_o}P_{T_o} = \frac{\Gamma_o}{2v_o}\left[P_H + \left(\frac{v_o}{\Gamma_o} + v - v_o\right)\left(\frac{C_o^2 + 2S_1\left[v_o - S_1\left(v_o - v\right)\right]}{\left[v_o - S_1\left(v_o - v\right)\right]^4}\right)\right] \tag{3.6}$$

where the subscript o denotes the reference state and P_{T_o} is the pressure at the reference state temperature T_o. v is the specific volume. All terms on the right hand side of equation (3.6) are known since,

$$P_H = \frac{C_o^2\left(v_o - v\right)}{\left[v_o - S_1\left(v_o - v\right)\right]^2}. \tag{3.7}$$

This method uses mass fraction averages for quantities in equation (3.6). For example, the heat capacity is $\bar{C}_v = \sum_p \phi_p C_{vp}$. A mass fraction average is used to calculate the Grüneisen ratio as

$$\left(\frac{\bar{v}_o}{\bar{\Gamma}_o}\right) = \sum_p \phi_p \left(\frac{v_{op}}{\Gamma_{op}}\right). \tag{3.8}$$

3.1.3 Mixture Rule Based on Mass Fraction Averages [85](Method#3)

This method has been used in the study of shock induced chemical reactions [88]. In the example given by Meyers [85], the Mie-Grüneisen EOS parameters C_o and S_1 and the mixture reference density $\bar{\rho}_o$ are given by,

$$\bar{C}_o = \sum_p \phi_p C_{op} \;\; ; \;\; \bar{S}_1 = \sum_p \phi_p S_{1p} \;\; ; \;\; \bar{\rho}_o = \sum_p \phi_p \rho_{op} \tag{3.9}$$

The Mie-Gr*ü*neisen EOS is written in terms of the specific energy e or temperature T and specific volume v as,

$$\bar{P}(e,v) = \frac{\bar{C}_o^2\left(\bar{v}_o - \bar{v}\right)}{\left[\bar{v}_o - \bar{S}_1\left(\bar{v}_o - \bar{v}\right)\right]^2} + \frac{\bar{\Gamma}}{\bar{v}}\left[\bar{e} - \frac{1}{2}\left(\frac{\bar{C}_o\left(\bar{v}_o - \bar{v}\right)}{\bar{v}_o - \bar{S}_1\left(\bar{v}_o - \bar{v}\right)}\right)^2\right] \tag{3.10}$$

where C_o is the acoustic wave speed, S_1 is the slope of the linear $U_s - U_p$ curve,U_p is the particle velocity, and Γ is the Gr*ü*neisen parameter.

3.1.4 Porous Mixture Equation of State (This Thesis)

The objective is to calculate the equation of state of the mixture. A representative volume element ΔV contains 1 to p number of mixture constituents and void. As the representative volume element tends to zero, the result is point x_i in space and mixture mechanics are formulated for a point in a space. The numerical solution of a dynamic response problem including shock-induced chemical reactions depends on discretization and finite volume elements.

The mixture theories are developed by Truesdel, Toupin and other mechanicians. In Truesdel's mixture theory, the motion of each constituent is defined [98] as

$$x = X^i(\mathbf{X}^i, t), \quad i = 1...p. \tag{3.11}$$

The velocity of each constituent is given by,

$$v^i = \frac{\partial X^i}{\partial t}. \tag{3.12}$$

The mass density of the mixture is defined as

$$\bar{\rho} = \sum_{i=1}^{p} \rho^i. \tag{3.13}$$

The average velocity is

$$\bar{v} = \frac{1}{\bar{\rho}} \sum_{i=1}^{p} \rho^i v^i. \tag{3.14}$$

The diffusion velocity of the i^{th} component is

$$v_d^i = v^i - v. \tag{3.15}$$

The stress and hence the pressure is defined in the following way. A symbol s is used to denote a surface in the body that intersects x. The normal to the surface is n_s. The partial traction and the partial stress tensor σ^i are defined by

$$t^i = \left[\sigma^i\right]^T n_s \tag{3.16}$$

and the total stress is

$$t = \sum_{i=1}^{p} t^i; \quad \sigma = \sum_{i=1}^{p} \sigma^i. \tag{3.17}$$

The consequences of equation (3.13) are discussed. For clarity, the following relationship is given as

$$\begin{aligned} \lim_{\Delta v \to 0} \bar{\rho} \Delta v &= \rho^1 \Delta v + \rho^2 \Delta v + ... + \rho^p \Delta v \\ &= \Delta m^1 + \Delta m^2 + ... + \Delta m^p \end{aligned}. \tag{3.18}$$

Thus, it is seen that

$$\lim_{\Delta v \to 0} \rho^i = \frac{\Delta m_i}{\Delta v}. \tag{3.19}$$

Thus, if an element Δv contains only Aluminum (Al) and Nickel (Ni) and each occupies 50% of Δv, then

$$\rho^{Al} = \lim_{\Delta v \to 0} \frac{2.7 \Delta v/2}{\Delta v} = \lim_{\Delta v \to 0} \frac{\Delta m^1}{\Delta v} = 2.7/2 = 1.35 \ g/cc. \tag{3.20}$$

Similarly, $\rho^{Ni} = 5.9/2 = 2.95 \ g/cc$. To characterize the equation of state of the constituents Al or Ni, the Mie-Grüniesen equation of state is used that depends on

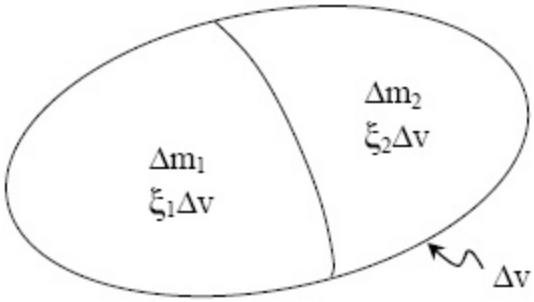

Figure 6: Two constituent mixture.

the initial density of 2.7 and not 1.35. Thus, the following modifications are sometimes considered.

For example, for a mixture with two constituents (Figure (6)),

$$\begin{aligned} \xi_1 \Delta v + \xi_2 \Delta v &= \Delta v \\ \xi_1 + \xi_2 &= 1 \end{aligned} \tag{3.21}$$

The quantity ξ is known as the volume fraction and

$$\sum_{i=1}^{p} \xi_p = 1. \tag{3.22}$$

Now ρ_l^i is defined as

$$\rho_l^i = \lim_{\Delta v \to 0} \frac{\Delta m_i}{\xi_i \Delta v} \tag{3.23}$$

and the relationship between ρ_l^i and ρ^i of Truesdell are

$$\xi_i \rho_l^i = \rho^i \text{ (Truesdell)} \tag{3.24}$$

$$\sum_{i=1}^{p} \xi_i \rho_l^i = \bar{\rho} \text{ (Truesdell)} \tag{3.25}$$

where ρ_l^i represents the true density of the component and yields correct $P - \rho \cdot T$ relationship with EOS like the Mie-Gr*ü*niesen EOS.

With these modifications, the void is now introduced to derive EOS similar to those of Herrmann [60]. To illustrate the procedure, a mixture with two constituents and void is considered in Figure (7).

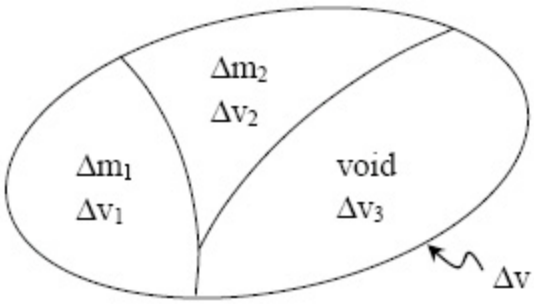

Figure 7: Two constituent mixture with void.

A quantity α is defined as

$$\alpha \frac{\Delta v}{\Delta v_1 + \Delta v_2} = \frac{\Delta v}{\xi_1 \Delta v + \xi_2 \Delta v} = \frac{1}{\xi_1 + \xi_2} \tag{3.26}$$

or

$$\alpha(\xi_1 + \xi_2) = 1. \tag{3.27}$$

In general,

$$\alpha \left(\sum_{i=1}^{p} \xi_i^p \right) = 1 \tag{3.28}$$

if ρ_l^d is used to denote the dense solid, i.e.,

$$\rho_l^d = \frac{\Delta m_1 + \Delta m_2}{\Delta v_1 + \Delta v_2}. \tag{3.29}$$

Similarly,

$$\rho_l^{porous} = \frac{\Delta m_1 + \Delta m_2}{\Delta v}. \tag{3.30}$$

Then,

$$\frac{\rho_l^d}{\rho_l^{porous}} = \frac{\Delta v}{\Delta v_1 + \Delta v_2} = \frac{v}{v_d} = \alpha = \frac{1}{\xi_1 + \xi_2}. \tag{3.31}$$

3.1.4.1 Equation of State for a Mixture

To illustrate the procedure, consider a mixture with four constituents (A, B, C, D) and void. If at any instant $\rho_l^A, \rho_l^B, \rho_l^C$ and ρ_l^D are the densities where temperature T is known. The individual pressures P_A, P_B, P_C and P_D can be determined. In the

mixture theory, T is assumed to be the same throughout Δv at this stage.

$$\begin{aligned} P_A &= f_A(\rho_A, T_A) \\ P_B &= f_B(\rho_B, T_B) \\ P_C &= f_C(\rho_C, T_C) \\ P_D &= f_D(\rho_D, T_D) \\ P_{air} &= f_{air}(\rho_{air}, T_{air}) \end{aligned} \tag{3.32}$$

To simplify the initial discussion, $P_{void} = P_{air} = f_{air}(\rho_l^{air}, T)$. Later, it is assumed that voids do not carry any of the pressure. Then equation (3.17) is used to obtain the mixture pressure with modification to account for voids.

$$P = \sum P^i \quad or \quad P = \alpha \sum P^i. \tag{3.33}$$

Thus, the general iteration procedure to obtain the EOS of a mixture is uniform as follows.

At the end of the n^{th} iteration, it is assumed that $\bar{P}, \bar{T}, \bar{\phi}, \phi^p, \xi^p, \alpha_L$, and α_U, are known. α_L and α_U are defined as the lower and upper bounds, respectively. The iteration starts with

$\alpha^* = 1/2(\alpha_U + \alpha_L)$

$\xi_p^{n+1} = \frac{\xi_p^n}{\alpha^* \sum \xi_p}$

$\phi^p \Delta m = \Delta m^p$ .. mass fractions

$\rho_l^p = \Delta m^p / \xi^p \Delta v$ (Δv = Cell volume)

$p^p = f^p(\rho_l^p, T)$

Obtain $P = \alpha \sum P^p$

Check for tolerances and repeat iteration with new values of α_L and α_U until tolerance limits are obtained.

Now the procedure is illustrated for specific cases, namely the homobaric and uniform strain methods.

The uniform strain assumption states that the strain is equal for all constituents as shown in Figure (8-b), thus, constituent volume fractions remain constant. The uniform strain assumption may be viewed as an idealization of an infinitely thin slice of the mixture material, or as $\Delta x \rightarrow 0$ in Figure (8-b). This assumption states that pressure equilibrium has not been reached. In this case, it is assumed from equation (D.2) that the surface area of each constituent is proportional to its volume fraction. Therefore the pressure for the porous mixture $\bar{P}$ is approximated by equations (D.2)-(D.6).

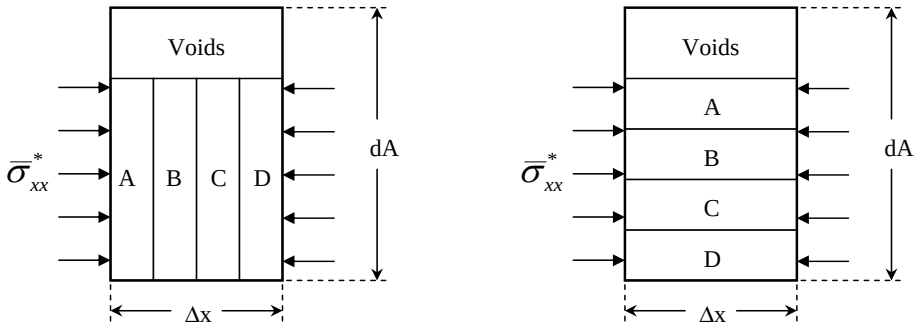

(a) Homobaric. (b) Uniform strain.

Figure 8: Porous mixture theories.

All of the three previous methods discussed in this thesis use a mixture average for equation of state model parameters. This simplifies the computation of the general problem stated above by reducing the number of equation of state equations from 5 to 1. The model by Bennett and Horie [10](Method#1) assumes that the equation of state material parameters are averaged, which reduces the number of equation of state equations to 1 and the number of heat conduction equations reduces to 1. Therefore, the equation of state for the model by Bennett and Horie is a single equation with a single unknown. Similarly, the method provided by Meyers [85](Method#2) uses mass fraction averages for quantities in equation (3.6). In addition, the mixture rule based on mass fractions [85] (Method#3) uses a mass fraction average for equation

of state model parameters.

To demonstrate the proposed porous mixture EOS methods, the $P-\alpha$ model by Herrmann [60] is first modified to incorporate the mixture. The pressure for the porous mixture $\bar{P}$ in equations (3.36-a-b) includes contributions from constituents p by using the porous volume fractions, i.e.,

$$\alpha \sum_{p} \xi_p = 1. \tag{3.34}$$

Components in the mixture are assumed to be in thermal equilibrium. f_p is the pressure EOS for each solid or liquid mixture constituent p. The porous mixture average density $\bar{\rho}$ with porosity α has the corresponding initial values $\bar{\rho}_o$ and α_o at $t = 0$, so that the dense mixture has the average density $\bar{\rho}_o^d = \bar{\rho}\alpha_o$.

The new algorithms for the mixture equation of state are derived as follows. The equation of state is assumed to take the form,

$$P_p = f_p\left(v_{dp}, e_p\right) = f_p\left(\frac{v_p}{\alpha}, e_p\right) \tag{3.35}$$

where v_d is the dense specific volume. The next step is to sum the constituents p in equation (3.35) and use the definition from equation (3.34). First, the special cases of homobaric and uniform strain are discussed.

For the homobaric case, any two components denoted by p and r have $P_p = P_r$ for $p \neq r$, therefore,

$$\bar{P}_{ho} = \alpha \sum_{p} f_p\left(\frac{\rho_{op}}{\rho_p}, \bar{T}\right) \xi_p \tag{3.36}$$

For the uniform strain case, $\frac{\rho_p}{\rho_{op}} = \frac{\bar{\rho}^d}{\bar{\rho}_o^d}$ for all p

$$\bar{P}_{us} = \alpha \sum_{p} f_p\left(\frac{\bar{\rho}_o^d}{\bar{\rho}^d}, \bar{T}\right) \xi_p. \tag{3.37}$$

It is important to note that there are no mixture averages for the equation of state parameters. For example, β_{S_o}, β'_{S_o}, Γ.

Difference between homobaric method and three alternative methods:

The difference between the homobaric method and Method#1 is that the homobaric method does not average the equation of state parameters. This means that the condition $P_p = P_r$ for $p \neq r$ is satisfied exactly in the homobaric method. Method#1 can not accomplish this because only one equation is solved. The homobaric method employs any acceptable form of the equation of state. For example, Grüneisen and Murnaghan equation of state. However, Method#1 can not employ Grüneisen equation of state. The difference between the homobaric method and Method#2 is that the homobaric method does not average the equation of state parameters. Method#2 employs a single equation of state for the mixture compared to the use of p number of constituent equation of state equations in the homobaric method. The difference between the homobaric method and Method#3 is that the homobaric method does not average the equation of state parameters. Method#3 employs a single equation of state for the mixture compared to the use of p number of constituent equation of state equations in the homobaric method.

The difference between the uniform strain method and Method#1 is that the uniform strain method does not average the equation of state parameters. The proposed uniform strain method employs any acceptable form of the equation of state. For example, Grüneisen and Murnaghan equation of state. The difference between the uniform strain method and Method#2 is that the uniform strain method does not average the equation of state parameters. Method#2 employs a single equation of state for the mixture compared to the use of p number of constituent equation of state equations in the uniform strain method. The difference between the uniform strain method and Method#3 is that the uniform strain method does not average the equation of state parameters. Method#3 employs a single equation of state for the mixture compared to the use of p number of constituent equation of state equations in the uniform strain method.

Equations (3.36) and (3.37) are implicit and are solved using the bisection method

iteratively as seen in the algorithms given in Figure (9). The bisection method is chosen over potentially faster methods for robustness. Matlab scripts for both the homobaric and uniform strain algorithms are given in Appendix (F.3).

An algorithm is proposed for the solution of the homobaric assumption. This algorithm shows the methodology on how to apply the theory presented above in equation (3.36). The assumptions include maintaining all mixture components at the same temperature and pressure. The algorithm solves for the pressure and individual constituent densities for a specified mixture density. The homobaric algorithm in Figure (9-a) shown below uses the new mass fractions that remain constant during the iterations. Constituent volume fractions are re-calculated until the mixture density converges. The aim is to calculate the mixture pressure for a specified mixture density. The homobaric algorithm steps are written as follows.

Given: The mixture density $\bar{\rho}$ is obtained at each time step in a hydrocode simulation and it is calculated from the conservation equations. Similarly, the mixture temperature $\bar{T}$ is specified from the conservation of energy. The mass fractions ϕ_p and volume fractions ξ_p are given by the conservation of mass and the chemical reaction equation. Thus we know $\bar{P}, \bar{T}, \phi_p, \xi_p$.

Assumptions: All constituents are assumed to have the same pressure P_p and temperature $\bar{T}$.

To find: The goal is to obtain the mixture pressure $\bar{P}$.

Homobaric algorithm:

1. The mixture pressure $\bar{P}$ is calculated using the upper and lower bounds. The upper bound $\bar{P}_U$ is equal to twice the maximum pressure expected. This is an estimate and needs modification if and estimated pressure is unknown. The lower bound $\bar{P}_L$ is equal to zero.This is consistent with the bisection method given in Appendix (D.5). Therefore, $\bar{P} = 1/2(\bar{P}_U + \bar{P}_L)$.

2. Obtain the constituent densities ρ_p from the corresponding equation of state

using the mixture average pressure and temperature, i.e., $\rho_p = f_p^{-1}\left(\bar{P}, \bar{T}\right)$.

3. Calculate the constituent volume fractions ξ_p and normalize using the mixture porosity that is calculated from $\bar{P}$ in step 1, i.e., $\xi_p^{i+1} = \frac{\xi_p^{i+1}}{\alpha^{i+1}(\bar{P})\sum_p \xi_p^{i+1}}$, where i is the iteration (see Figure (9(a))).

4. Re-calculate the mixture density $\bar{\rho}^*$ based on ρ_p in step 2, i.e., $\bar{\rho}^* = \sum_p \xi_p^{i+1}\rho_p^{i+1}$.

5. Check $\bar{\rho}^*$ against the specified mixture density $\bar{\rho}$. If the error is less than the tolerance, then the iterations are stopped.

6. Decide if $\bar{P}$ becomes the new upper or lower bound according to the bisection method.

7. Repeat steps 1-6 until iterations have converged in step 5.

If the initial guesses for P_L and P_U bound the solution, then the bisection method employed will converge to a local minima [63]. A discussion of the conditions under which the bisection method converges are discussed in detail in Appendix (D.5).

The uniform strain algorithm in Figure (9-b) uses the initial volume fractions. When chemical reactions change the mass fractions, the reference density $\bar{\rho}_o^d$ is calculated using $\rho_p = \rho_{op}$. From the definition of the uniform strain assumption, shown above, the ratio of the volume fractions between constituents remains constant. Therefore, volume fractions are proportionally scaled according to equation (3.34). Again, the aim is to calculate the mixture pressure for a specified mixture density. The uniform strain algorithm steps are written as follows.

Given: The mixture density $\bar{\rho}$ is obtained at each time step in a hydrocode simulation and it is calculated from the conservation equations. Similarly, the mixture temperature $\bar{T}$ is specified from the conservation of energy. The volume fractions ξ_p are given by the conservation of mass and change due to the chemical reaction equation. Volume fractions are initially specified. Thus we know $\bar{\rho}, \bar{T}$ and ξ_p.

Assumptions: All constituents are assumed to have the same change in ρ_p/ρ_{op} and temperature T_p, i.e., $\frac{\rho_p}{\rho_{op}} = \frac{\bar{\rho}^d}{\bar{\rho}^d_o}$ for all p. Generally, the strain varies. The uniform strain algorithm is a special case of the general approach given above. Iterations are only required when the porosity is $\alpha_o > 1$.

To find: The goal is to obtain the mixture pressure $\bar{P}$.

Uniform strain algorithm:

1. The mixture porosity α^* is calculated using the upper an lower bounds. The upper bound α_U is the initial porosity α_o and the lower bound α_L is 1. This is consistent with the bisection method given in Appendix (D.5). Therefore, $\alpha^* = 1/2(\alpha_U + \alpha_L)$.

2. Calculate the constituent volume fractions ξ_p and normalize using α^* in $\xi_p^{i+1} = \frac{\xi_p^{i+1}}{\alpha^{i+1}\sum_p \xi_p^{i+1}}$.

3. Calculate the mixture pressure $\bar{P}$ using the mixture density $\bar{\rho}$, temperature $\bar{T}$, α^*, and constituent volume fractions ξ_p, i.e., $\bar{P}_{us} = \alpha^* \sum_p f_p \left(\frac{\bar{\rho}^d_o}{\bar{\rho}^d}, \bar{T}\right) \xi_p$.

4. Check α^* against the mixture porosity $\alpha(\bar{P})$. If the error is less than the tolerance, then the iterations are stopped. The porosity is calculated using,

$$\alpha(\bar{P}) = \begin{cases} \alpha_o & ; \quad \bar{P} < P^e \\ 1 + (\alpha_o - 1)\left[\left(P^s - \bar{P}\right)/\left(P^s - P^e\right)\right]^n & ; \quad P^e \leq \bar{P} \leq P^s \\ 1 & ; \quad P^s < \bar{P} \end{cases} . \tag{3.38}$$

5. Decide if α^* becomes the new upper or lower bound according to bisection method.

6. Repeat steps 1-5 until iterations have converged in step 4.

In practice, tight tolerances ($Tol = 0.01\%$ error) are used for the proposed algorithms. Although this tolerance is computationally expensive with approximately

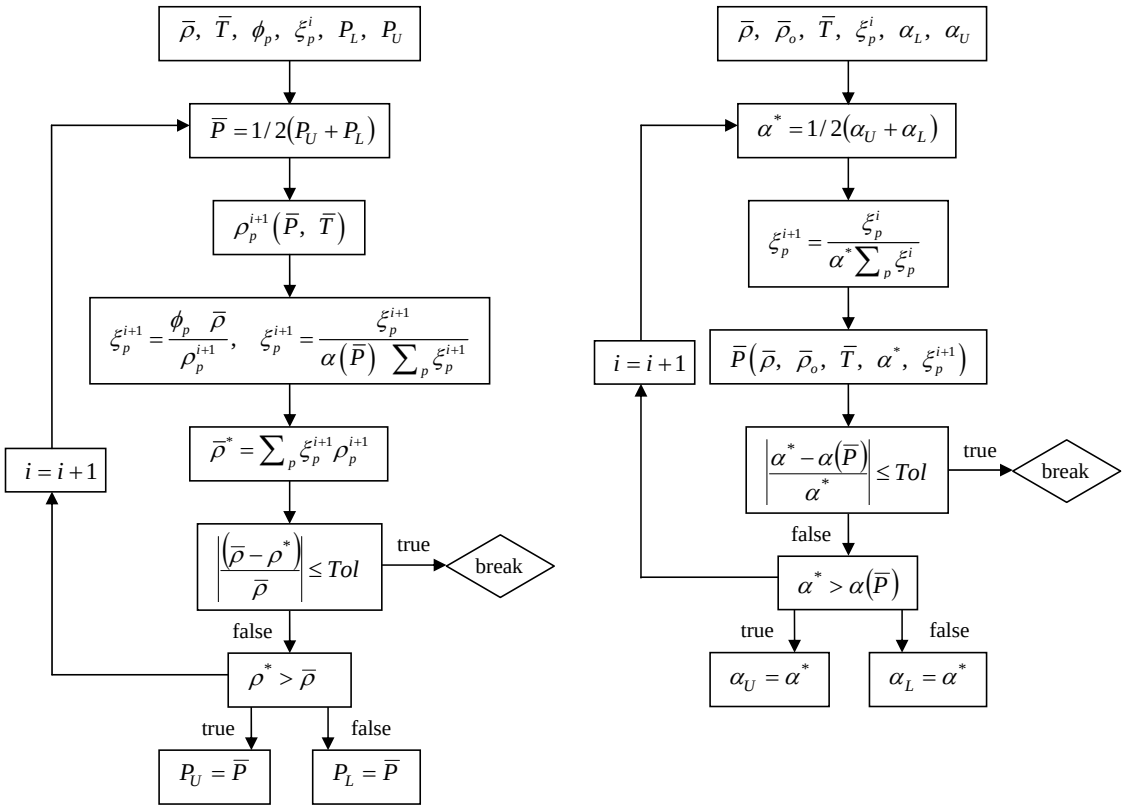

(a) Homobaric Mixture

(b) Uniform Strain

Figure 9: Mixture EOS Algorithms

$10 - 20$ iterations, high accuracy results are obtained. Please see Appendix (D.5) for details concerning the monotonicity of the equation of state and the bisection method.

The mixture parameter C_m is defined as the fraction of the pressure from homobaric mixture assumption, $\bar{P}_{ho}$. This mixture rule is stated as,

$$P_{mix} = \bar{P}_{ho} \cdot C_m + \bar{P}_{us} \cdot (1 - C_m) \ \ , \ \ 0 \le C_m \le 1. \tag{3.39}$$

Pressure equilibration in simulated mixtures occurs well within the rise time of a shock wave [4] therefore it is expected that $C_m \to 1$ approximates real mixtures.

Table 1: Input parameters used in the stoichiometric $Al+Fe_2O_3 \rightarrow Al_2O3+2Fe$ reaction.

Parameter	Al	Fe_2O_3	Al_2O_3	Fe	$Epon828$	$Units$
M	26.98	159.69	101.96	55.85	–	$g \cdot mol^{-1}$
ν	2	1	1	2	–	–
ϕ_o	0.2526	0.7474	0	0	0	–
ξ_o[a]	0.3976	0.6024	0	0	0	–
ϕ_o (20 wt.% Epon828)	0.2021	0.5979	0	0	0.20	–
ξ_o[a](20 wt.% Epon828)	0.2109	0.3195	0	0	0.4696	–

[a] Calculated by using solid densities in Table (15).

Table 2: Reactant material parameters.

Parameter	$Al-1100$ [66]	Fe_2O_3[a]	$Epon828$[a]	$Units$
Shear modulus, G	26.0	104	1.4	GPa
Yield strength, $\sigma_{y,o}$	105	800	60	MPa
Melting temperature, T_m	926	1780	533	K
Latent heat of melting, ΔH_m	390	600	–	$kJ \cdot kg^{-1}$

[a] Estimated from [4, 5].

3.2 Thermite System Case Study

3.2.1 Mixture Equation of State Results

The shock compression of the $2Al + Fe_2O_3$ is considered in stoichiometric ratios with up to 20 wt.% Epon828 and distention ratio as high as $\alpha = 1.666$. Initial mass fractions and corresponding volume fractions of the dense mixture ξ_o are given in Table (1).

Constituent Grüneisen and Murnaghan EOS parameters are given in Table (15) in Appendix (D). Equations for both EOS models are given in Appendix (D.2). The Grüneisen and Murnaghan EOS models need to produce similar pressures to make fair comparisons between mixture models. The Murnaghan EOS constituent parameters for Al and Fe_2O_3 are adjusted in Table (15) in Appendix (D) to approximate the $T = 298K$ isotherm pressure calculated using the Grüneisen model.

3.2.2 Pressure-density model characterization

3.2.2.1 Fully Dense Mixture Equation of State Characterization

Methods#1-3 are compared using the constituent Grüneisen EOS parameters with the exception of Method#1 which requires Murnaghan EOS parameters. For the Homobaric method, the pressure difference between using Grüneisen and adjusted Murnaghan EOS constituent parameters is less than 1% for the pressure range (<30GPa) considered in this thesis (see Figure (10)). The new EOS methods are compared to Methods#1-3 for the fully dense stoichiometric mixture of $2Al + Fe_2O_3$ with and without 20 wt.% Epon828 in Figure (10(a)) with the exception of Method#2 in Figure (10(b)) (see explanation below).

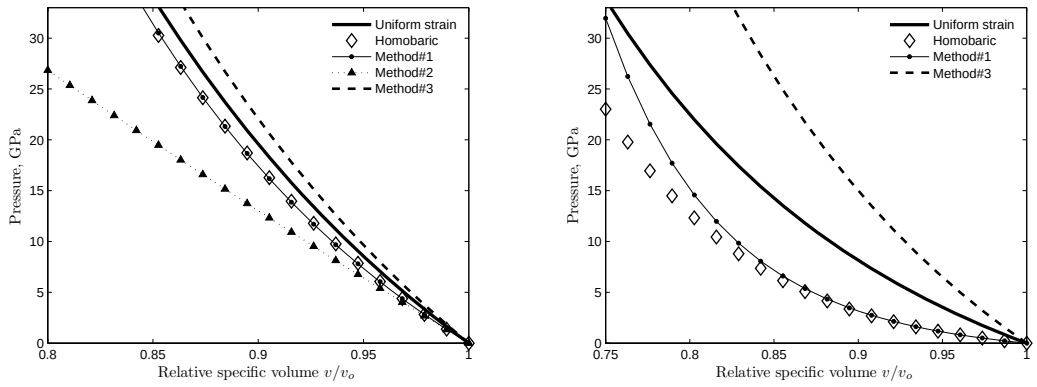

(a) No Epon828.

(b) 20 wt.% Epon828.

Figure 10: $T = 298K$ isotherm predicted by three mixture EOS methods compared to the homobaric and uniform strain methods for the fully dense stoichiometric mixture of $2Al + Fe_2O_3$ with and without 20 wt.% Epon828.

Homobaric and uniform strain methods:

The uniform strain method calculates higher pressures compared to the homobaric method in Figure (10). The uniform strain method provides higher pressures for the same relative volume change since the stiffest material dominates the load carrying capability of the mixture. This effect is exaggerated with the addition of Epon828

since this constituent has a low bulk modulus and high volume fraction compared to the other constituents.

Method#1:

For both mixtures (with and without Epon828) in Figure (10), Method#1 closely approximates the homobaric method up to $P = 10GPa$. This agreement is not surprising since the bulk modulus and its pressure derivative are volume fraction averaged at the $T = 298K$ isotherm.

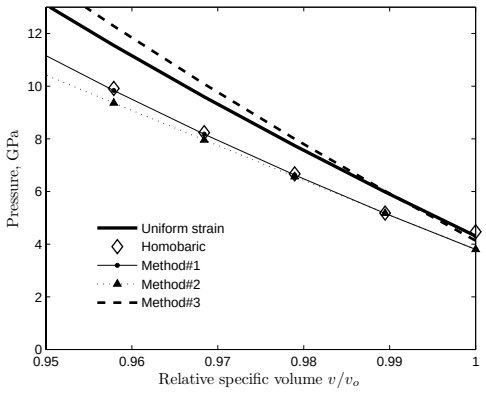

Figure 11: $T = 1000K$ isotherm predicted by two mixture EOS methods compared to the homobaric and uniform strain methods for the fully dense stoichiometric mixture of $2Al + Fe_2O_3$.

Method#1 deviates from the homobaric method at higher temperature isotherms, for high temperature and low pressure conditions as shown in Figure (11). This illustrates a fundamental aspect of the homobaric method in which the constant volume thermal contribution to the pressure has non-physical effects. Here, the homobaric assumption is invalid since the thermal pressure contribution in one of the constituents will be too high. It is necessary to use the general method outlined above. Therefore, constituent pressures can not be equilibrated without imposing either negative pressures or negative volume fractions, both of which are non-physical. Therefore, $P_p \geq 0$ and $\xi_p \geq 0$ are imposed for all constituents. The homobaric method approximates the uniform strain method as $v \rightarrow v_o$ since the constituent pressures are not equal at the lower pressures in Figure (11). Method#1 does not have have the pressure and temperature limitations that are displayed for the homobaric method. However, Method#1 is non-physical since there can not be any physical pressure equilibration between the constituents.

This is because the EOS parameters are averaged.

Method#2:

Results of this method are shown in Figure (10(a)). Lower pressures are predicted compared to the homobaric method, thus, results from Method#2 are not bounded by the homobaric and uniform strain methods. This method is an acceptable approximation for some alloys and compounds [85]. For the mixture in this study, Figure (10(a)) shows that Method#2 does not reasonably approximate the case in which mechanical equilibrium is assumed for $P > 5GPa$. Data could not be obtained from the MIXTURE program [121] for the 20 wt.% Epon828 case due to its relatively low acoustic wave speed C_o.

Method#3:

Mass averaging all of the Mie-Grüneisen EOS parameters leads to an overestimation of the mixture average density $\bar{\rho}$ for the stoichiometric $2Al + Fe_2O_3$ mixture. The effects of this overestimation are indicated by elevated pressures that exceed the uniform strain method as seen in Figure (10). Method#3 results are relatively close to the uniform strain results when when all mixture quantities are close to the same density (see Figure (10(a))). However, when the 20 wt.% Epon828 is added, the pressure increases significantly due to the overestimation of $\bar{\rho}$.

3.2.3 Porous Mixture Equation of State Characterization

The homobaric and uniform strain methods are applied to porous stoichiometric mixture of $2Al + Fe_2O_3$ with and without 20 wt.% Epon828 in Figure (12) using equations (3.36). Here, it is assumed that $P^e = 250MPa$, and $P^s = 3GPa$ based on experimental data for a mixture containing spherical $Ni + Al$ granules [39] with the porosity $\alpha_o = 1.66$. As shown in Figure (11), the homobaric and uniform strain methods show considerable differences when 20 wt.% Epon828 is included in the non-porous mixture. However, these pressure differences are much smaller for the porous

mixture ($\alpha \geq 1$) since the mixture density $\bar{\rho}^d$ does not change significantly during pore collapse. This is not the case after the pores have collapsed. The effect of the pore collapse is an increase in temperature. Therefore a small change in density will result.

Homobaric and uniform strain results are shown in Figures (12(c)) to (12(d)) for distension ratio pressure dependencies in the range $n = [1, 4]$. Higher values of n physically correspond to porous materials with lower strength. Parameter n may be adjusted to reflect the strength in porous mixtures with various morphologies such as flake and spherical powders [39].

Figure (13) shows that for a single constituent material, the homobaric and uniform strain algorithms give the same results. For this case, Epon828 is chosen for the material, which is compressed much more than the 20wt.% Epon828 case shown for the same pressures.

3.2.4 Mixture Equation of State Summary

The case study results in Figures (10) and (11) show that Method#2 does not approximate the homobaric method nearly as well as Method#1 does. Therefore, Method#1 should be used instead of Method#2 when mechanical equilibration is assumed in the mixture. However, Method#1 does not approximate the homobaric assumption at high pressures when the bulk moduli of constituents are considerably different. For example, agreement between Method#1 and the homobaric model was observed for the $20wt.\%Epon828$ case up to pressures near $10GPa$. Method#3 should be used with extreme caution as a crude approximation for materials with constituents that have similar densities.

The main disadvantage of the proposed methods is the increased number of iterations required. The extended VIR model [11] requires an estimated 4-8 iterations per time step compared to the 10-20 iterations required in the proposed methods. Further

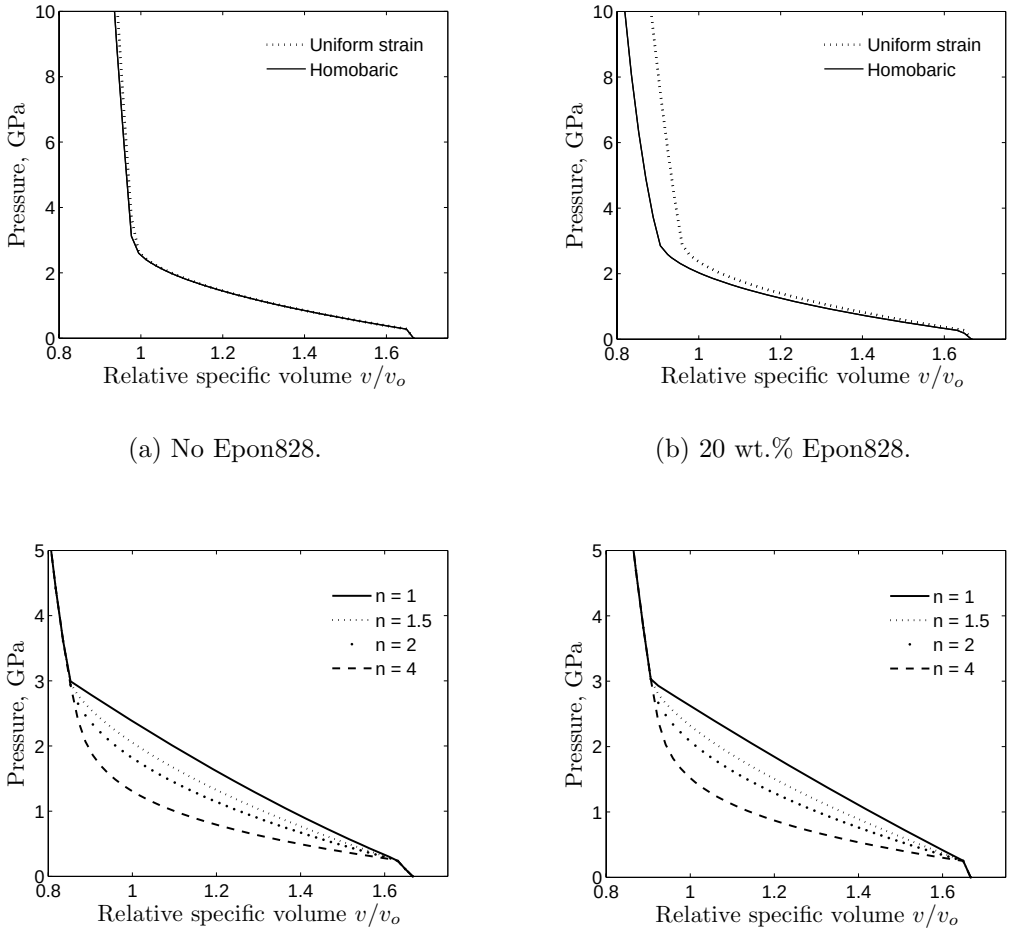

(a) No Epon828.

(b) 20 wt.% Epon828.

(c) Homobaric.

(d) Uniform strain.

Figure 12: Simulation results with $P^e = 250MPa$, and $P^s = 3GPa$ for the $T = 298K$ isotherm. The mixture is stoichiometric $2Al+Fe_2O_3$ + Epon828 and $\alpha_o = 1.66$. (a)-(b) Compare effect of adding Epon828 with $n = 2$. (c)-(d) Homobaric and uniform strain methods with various orders n of α dependence on pressure with 20 wt.% Epon828.

computations are required to compute the approximate derivatives in equation (F.3).

The proposed algorithms are subject to limitations resulting from approximations made in constituent EOS models. For example, the homobaric assumption is observed to be invalid for low pressure and high temperature conditions. This limitation is not present if the constituent EOS model does not have a constant volume thermal pressure contribution (the last term in the right hand side of the pressure equation

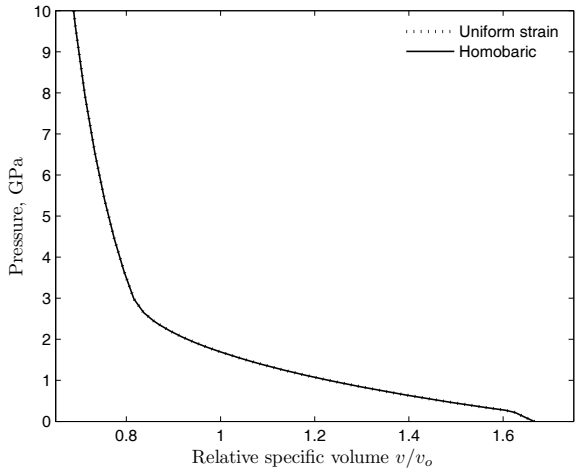

Figure 13: Simulation results with $P^e = 250MPa$, and $P^s = 3GPa$ for the $T = 298K$ isotherm. The material is Epon828 and $\alpha_o = 1.66$. The lines are overlapping.

of state).

3.3 Spherically Symmetric Mixture Model

The spherically symmetric pore collapse mode by Caroll, Holt and Nesterenko [24, 25, 92] does not consider a mixture. This section gives the derivation for the modified spherically symmetric pore collapse models for a mixture. Material parameters are introduced that are calibrated with RAVEN code results.

When $\alpha_o > \alpha^*$, the spherical granules are assumed to repack [92] during the pore collapse when $\alpha^* \leq \alpha < \alpha_o$. Since the mass of the model cell (core plus shell) is equal to the mass of the granule and the density of the model is equal to the initial density of the powder (incompressibility is assumed),

$$b_o = R\sqrt[3]{\alpha_o}, \quad a_o = R\sqrt[3]{\alpha_o - \alpha^* + 1}, \quad c = R\sqrt[3]{2 - \alpha^*}, \tag{3.40}$$

R is the representative granule radius in the granular material. At the moment when the porosity is equal to α^*, the outer and inner radii of the shell become $b^* = R\sqrt[3]{\alpha^*}$, and $a^* = R$. Further densification resulting in porosity smaller than α^* must include viscoplastic dissipation.

The motion is spherically symmetric (1D) as given by the following geometrical relations that describe the radially symmetric motion in the modified hollow sphere model [91]. In the hollow sphere model $c = 0$. As discussed by Carrol, Kim, and Nesterenko,

$$r^3 - a^3 = r_o^3 - a_o^3, \quad \theta = \theta_o, \quad \varphi = \varphi_o, \tag{3.41}$$

where $r, \theta,$ and φ are spherical polar coordinates, $c \leq r_o \leq b_o$ corresponds to the initial radius of some point with the current coordinate r, and a and a_o are the current and initial inner radii of the model sphere. The motion is completely determined by the inner radius $a(t)$. The velocity is obtained by differentiating equation (1.11) with respect to time to give [25, 91],

$$\dot{r} = \frac{a^2\dot{a}}{r^2} = \frac{a^2\dot{a}}{\left(r_o^3 - a_o^3 + a^3\right)^{2/3}}. \tag{3.42}$$

and the acceleration can be written in terms of a potential ζ [25],

$$\ddot{r} = \frac{\partial \zeta}{\partial r}, \quad \zeta = \frac{a^2\ddot{a} + 2a\dot{a}^2}{r} - \frac{a^4\dot{a}^2}{2r^4}. \tag{3.43}$$

The values of $\alpha, r,$ and b are written in terms of the pore radius a by

$$\begin{aligned} &\alpha = 1 + (\alpha_o - 1)a^3/a_o^3, \quad r^3 = \left(r_o^3 - a_o^3 + a^3\right), \\ &b = a^3 + a_o^3/\left(\alpha_o - 1\right). \end{aligned} \tag{3.44}$$

The equation of motion for spherical geometry is

$$\frac{\partial \bar{\sigma}_{rr}}{\partial r} + \frac{2}{r}\tilde{\bar{\sigma}} = \bar{\rho}_s \ddot{r}. \tag{3.45}$$

where the mixture density is

$$\bar{\rho}(s) = \sum_{i=1}^{p} \xi_i \rho_i^l \tag{3.46}$$

and $\tilde{\bar{\sigma}} = \bar{\sigma}_{rr} - \bar{\sigma}_{\theta\theta}$ is the shear stress in the mixture. The energy balance equation (with no radiative or conductive heat supply) is written as [91]

$$\bar{\rho}_s \dot{e} = -\frac{2\tilde{\bar{\sigma}}\dot{r}}{r}. \tag{3.47}$$

where e is the specific internal energy. Expressing equation (3.47) as a function of temperature T,

$$\bar{\rho}_s \dot{T} = -\frac{1}{\bar{C}_v} \frac{2\tilde{\bar{\sigma}}\dot{r}}{r}. \tag{3.48}$$

where, $\bar{C}_v$ for p number of constituents, is the heat capacity at constant volume for the mixture.

$$\bar{\sigma}_{rr} = \begin{cases} 0 & at \quad r = a \\ -P(t) & at \quad r = b \end{cases}. \tag{3.49}$$

Since the incompressibility is assumed in equation (3.41), $\bar{\rho}_s = const.$ This means that the density does not change in the pore collapse model only. Density changes in the macro-scale continuum simulation because the only output from the pore collapse model is the porosity, α. The incompressibility assumption is relaxed later.

From the assumptions in equation (3.41), the initial (α_o) and current (α) porosities of the real material are connected with the model geometry by the relations

$$\alpha_o = \frac{b_o^3}{b_o^3 - a_o^3} = \frac{\bar{\rho}_s}{\bar{\rho}_{po}} \quad ; \quad \alpha = \frac{b^3}{b^3 - a^3} = \frac{\bar{\rho}_s}{\bar{\rho}_p} \tag{3.50}$$

where b is the current outer radius.

The expression for $\bar{\sigma}$, for a mixture, is different from approach that is discussed and used by Carrol, Kim, and Nesterenko. From the mixture theory that is discussed in section (3.1.4),

$$\bar{\sigma}_{ij} = \sum_{i=1}^{p} \sigma^i. \tag{3.51}$$

In this equation, it is assumed that there are p number of constituents in the mixture. Then, the quantity $\bar{\sigma}$ is

$$\bar{\sigma} = \bar{\sigma}_{rr} - \bar{\sigma}_{\theta\theta} = \sum_{i=1}^{p} \bar{\sigma}^i = \sum_{i=1}^{p} (\bar{\sigma}^i_{rr} - \bar{\sigma}^i_{\theta\theta}). \tag{3.52}$$

To introduce the temperature effect, a viscoplastic behavior is assumed for $\bar{\sigma}$, with temperature dependent yield strength Y_i and viscosity η_i. These are similar to those discussed by Durmin and Sulkov for a "single constituent" material. Then, for the

species i,

$$\sigma^i = Y_i(T) - 6\eta_i(T)\frac{\dot{r}}{r}. \tag{3.53}$$

The variation of the yield strength with the temperature depends on the selected specific material. In general, yield strength decreases with temperature and becomes equal to zero at the melting temperature T_i^m. After melting, the material behaves like a viscous liquid with the coefficient of viscosity η_m. Then, the following approximation is assumed for Y^i.

$$\begin{aligned} Y^i &= Y_i^o \left[\sum_{n=1}^{N} a_{yn}^i \left(1 - \tfrac{T}{T_m^i}\right)^n\right], \quad && T < T_m^i \\ &= 0, \quad T > T_m^i && i = 1, 2, ...p \end{aligned} \tag{3.54}$$

Similarly

$$\eta^i = \eta_m^i \exp\left(\sum_{n=1}^{N} B_i^n \left(\frac{1}{T} - \frac{1}{T_m^i}\right)^n\right)_{i=1,2,...p}, \quad T < T_m^i. \tag{3.55}$$

with these equations, the spherically symmetric compaction problem is formulated in the following way.

A non-dimensional interaction coefficient $0 \leq \mu_{Isp} \leq 1$ between constituents s and p is introduced to account for friction between any two constituents in the mixture. The modified constituent yield strength becomes

$$Y_i^o = \frac{1}{1 - \xi_p} \sum_{s \neq p} \mu_{Isp} Y_p^o \tag{3.56}$$

This equation is based on the mixture theory described earlier in this chapter.

Assuming the incompressible behavior, the governing equations are as follows,

$$\begin{aligned} P(t) &= 2\int_a^b \left[\sum_{i=1}^{p} Y_o^i \left\{a_{yn}^i \left(1 - \tfrac{T}{T_m^i}\right)^n\right\} - \right. \\ &\quad \left. \sum_{i=1}^{p} 6\eta_m^i \exp\left(\sum_{n=1}^{N} B_i^n \left(\tfrac{1}{T} - \tfrac{1}{T_m^i}\right)^n\right)\right] \tfrac{\dot{r}}{r}\tfrac{dr}{r} - \\ &\quad \bar{P}_s \left[(a\ddot{a} + 2\dot{a}^2)(1 - a/b) - 1/2\dot{a}^2(1 - a^4/b^4)\right]; \quad T < T_m \end{aligned} \tag{3.57}$$

$$\begin{aligned} \bar{\rho}(s) &= \textstyle\sum_{i=1}^{p} \xi_i \rho^i \\ b &= \left[a^3 + \tfrac{a^3}{\alpha_o - 1}\right]^{1/3} \end{aligned} \tag{3.58}$$

$$r = \left(r_o^3 - a_o^3 + a^3\right)^{1/3}. \tag{3.59}$$

$$\begin{aligned} \bar{\rho}_s \bar{c} \dot{T} \; &= -\left[2\sigma_{i=1}^{p} Y_o^i \left\{a_{yn}^i (1 - T/T_m^i)^n\right\}\right] \frac{\dot{r}}{r} + \\ &\left[12 \sum_{i=1}^{p} \eta_m^i \exp\left(\sum_{n=1}^{N} B_i^n \left(\frac{1}{T} - \frac{1}{T_m^i}\right)^n\right)\right] \left(\frac{\dot{r}}{r}\right)^2; \quad T < T_m \end{aligned} \tag{3.60}$$

It is noted that $\bar{\rho}_s$ and $\bar{c}$ do not change because of incompressibility. Initial conditions are

$$\begin{aligned} a(0) &= a_o \\ \dot{a}(0) &= 0 \\ T(r_o, T) &= T_o \end{aligned} \tag{3.61}$$

In these equations, $P(t)$ is given as the boundary conditions. Equations (3.57) to (3.60)) are used to solve for $a(t)$, $b(t)$, $\gamma(t)$, and $T(t)$. Then the equation (3.48) is used to find $\dot{e}(t)$. Similarly, kinetic energy of the hollow sphere is obtained. Calculations are continued until the inner radius approaches T_m.

Some observations of the approximate model are as follows. The rate of compaction increases with inertial effects. Also, discussed by Carroll et. al. for a full compaction at a finite $P(t)$, the rate of compaction is expected to decrease to zero. If not inertial term has the potential to become unbounded. This is also discussed by Carroll et al. for a single constituent. These effects result from the fact that there is no dissipation. These can be controlled by formulating the problem such that the work done by applied $P(t)$ is finite. Then it is necessary to consider compressibility such that a reflection of the finite shock wave results from the inner boundary at $r = a(t)$. When $T \geq T_m^i$, the material is a viscous liquid and thus is not considered in this analysis.

The average density represents the uniformly blended mixture density. However, the mixture surrounding the pore is not uniformly blended. Here, the assumption of mechanical equilibrium between mixture constituents during pore collapse is relaxed

by introducing a scaling factor C_I to obtain the modified mixture density as

$$\bar{\rho}_s^* = \rho_{min} + C_I \left(\bar{\rho}_s - \rho_{min} \right); \quad 0 \leq C_I \leq 1 \tag{3.62}$$

where $\rho_{min} = \min_{i=1}^{p}(\rho_i)$ is the minimum density of all of the mixture constituents.

3.3.1 Compressibility Considerations

The problem considered consists of a hollow sphere of initial internal radius a_o and external radius b_o, in a single constituent material and not a mixture. The sphere is subjected to an external pressure $P(t)$ on the outer radius $b = b(t)$ To introduce compressibility into the Carol, Kim, and Nesterenko model, the compressibility is approximated by an idealized locking approximation. This approximation results in a finite shock velocity until the effects of the external pressure reach the internal radius. A schematic of the pressure-density plot is given in Figure (14). ρ_l is shown in Figure (15).

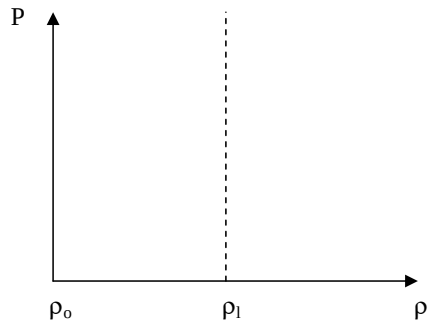

Figure 14: Pressure-density schematic for compressible material with idealized locking.

The viscoplastic stress-strain relationship is still assumed to be valid between the strain deviator and deformation. It is possible to replace the ideal locking behavior by an elastic-locking behavior used by Hanagud and Ross [56] in deriving the compressible cavity expansion theory for deep penetration of solids by impacting projectiles.

The approximate value of the locking density is obtained from a knowledge of the external pressure $P(t)$ at $r = b(t)$ and the equation of state of the material. In

the ideal-locking approximation, once the pressure is applied the material reaches the density ρ_l but the shock wave speed is finite. A schematic of the cross section of the pore is shown in Figure (15). Eulerian coordinates are used in this analysis.

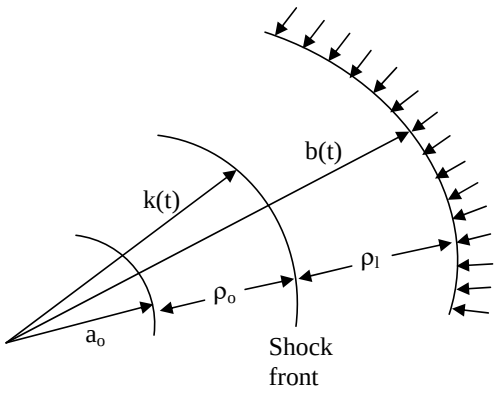

Figure 15: Schematic of the pore cross section with a traveling shock front in Eulerian coordinates.

In the region $k(t) < r < b(t)$, the density is constant at $\rho = \rho_l$. Then

$$\frac{\partial v}{\partial r} + \frac{2v}{r} = 0 \tag{3.63}$$

where $v(t)$ is the particle velocity. Then

$$v(t) = \frac{f(t)}{r^2}. \tag{3.64}$$

$f(t)$ is an unknown function that should be determined. $(\sigma_r - \sigma_\theta) = \sigma'$ has a viscoplastic relationship with both $y(T)$ and $\eta(T)$ depending on the temperature, as described before. Then σ_r is determined from the spherical symmetric equation of motion that is valid in the region $k(t) < r < b(t)$, i.e.,

$$\frac{\partial \sigma_r}{\partial r} + \frac{\sigma_r - \sigma_\theta}{r} = \rho \frac{D\theta}{\partial t}. \tag{3.65}$$

$$\frac{Dv}{Dt} = \frac{\partial v}{\partial t} + v\frac{\partial v}{\partial r}. \tag{3.66}$$

$$\sigma_\theta - \sigma_r = Y(1 - T/T_m) - \eta(T)(\dot{\epsilon}_\theta - \dot{\epsilon}_r); \quad T < T_m. \tag{3.67}$$

In large deformation,

$$\epsilon_r = \ln(r) - \ln(r_o). \tag{3.68}$$

Because of locking approximation,

$$-(\epsilon_r + 2\epsilon_\theta) = \epsilon_l \quad \text{(constant)}. \tag{3.69}$$

$$\dot{\epsilon}_\theta - \dot{\epsilon}_r = \frac{v}{r} - \frac{\partial \theta}{\partial r}. \tag{3.70}$$

From equation (3.68),

$$\dot{\epsilon}_\theta - \dot{\epsilon}_r = \frac{3f}{r^3}. \tag{3.71}$$

Then,

$$\frac{\partial \sigma_r}{\partial r} = \frac{2Y(T)}{r} - \frac{2}{r}\eta \cdot \frac{3f}{r^3} + \rho_l \left(\frac{\dot{f}}{r^2} - \frac{2f^2}{r^5} \right). \tag{3.72}$$

The coefficient 6 in the second term on the right hand side of equation (3.72) agrees with Dunin and Surkov (as stated by Caroll, Kim, and Nesterenko). Then

$$\sigma_r = 2Y \ln(r) - \rho_l \frac{\dot{f}}{r} + \frac{1}{2}\rho_l \frac{f^2}{r^4} + \eta_m \int_k^r \frac{18f}{r^3} dr' \exp\left(B \left[\frac{1}{T} - \frac{1}{T_m} \right] \right) + g(t). \tag{3.73}$$

At $r = b$, $\sigma_r = -P(t)$, where

$$-P(t) = 2Y \ln(b) - \rho_l \frac{\dot{f}}{b} + 1/2\rho_l \frac{f^2}{b^5} + \eta \int_k^b \frac{6f}{r'^3} dr' \exp\left(B \left[\frac{1}{T} - \frac{1}{T_m} \right] \right) + g(t). \tag{3.74}$$

This equation is used to obtain $g(t)$. There are two discontinuity conditions at the shock front. The conservation of mass yields,

$$\rho_l(\dot{k} - [\sigma]_{r=k}) = \rho_o \dot{k}, \tag{3.75}$$

or

$$\rho_l \left\{ \dot{k} - \rho_l \frac{f}{k^2} \right\} = \rho_o \dot{k}. \tag{3.76}$$

This yields an expressions $f(t)$ as a function of k and $\dot{k}$ as

$$f = k^2 \dot{k}(1 - \rho_o/\rho_l) = \hat{\alpha} k^2 \dot{k} \tag{3.77}$$

where

$$\hat{\alpha} = 1 - \rho_o/\rho_l. \tag{3.78}$$

The only remaining unknown is a differential equation for $\dot{k}$. This is obtained by the impulse momentum relationship,

$$\sigma_r]_{r=k} = -\rho_p \left[(\dot{k} - v)v\right]_{r=k}. \tag{3.79}$$

σ_r at $r = k$ is known from equation (3.73) after $g(p)$ is substituted from equation (3.72) with known $g(t)$ i.e.,

$$\begin{aligned} \sigma_r = \quad & -P(t) + 2Y_o\left(\tfrac{1}{T} - \tfrac{1}{T_m}\right)\ln\left(\tfrac{r}{b}\right) + 6\eta\int_b^r \tfrac{f}{r'^3}dr' \exp\left(B\left[\tfrac{1}{T} - \tfrac{1}{T_m}\right]\right) \\ & +\rho_l\dot{f}\left(\tfrac{1}{b} - \tfrac{1}{r}\right) - \tfrac{1}{2}\rho_l f^2\left(\tfrac{1}{b^4} - \tfrac{1}{r^4}\right) \end{aligned}. \tag{3.80}$$

The two shock jump conditions are based on conservation of mass. First, the conservation of mass condition across shock wave is used to express $f(t)$ in terms of k as shown in equations (3.77) and (3.78). Then the impulse-momentum relationships across the shock is used to find a integro-differential equation for $k(t)$ as shown by,

$$\begin{aligned} & -P(t) + 2Y\ln\left(\tfrac{k}{a}\right) + 6\eta\int_b^k \tfrac{f}{r'^3}dr' \exp\left(B\left[\tfrac{1}{T} - \tfrac{1}{T_m}\right]\right) \\ & +\rho_l\dot{f}\left(\tfrac{1}{b} - \tfrac{1}{k}\right) - \tfrac{1}{2}\rho_l f^2\left(\tfrac{1}{b^4} - \tfrac{1}{k^4}\right) \\ & = \rho_l\left(\dot{k} - \rho_l\tfrac{f}{k^2}\right)\tfrac{f}{k^2} \end{aligned}. \tag{3.81}$$

with $f = \hat{\alpha}k^2\dot{k}$. The value of $b(t)$ is related to $k(t)$ by,

$$(b^3 - k^3)\rho_l = (b_o^3 - k^3)\rho_o. \tag{3.82}$$

The energy equation becomes,

$$\begin{aligned} \rho_l c\dot{T} \quad & = (\sigma_\theta - \sigma_r)(\dot{\epsilon}_\theta - \dot{\epsilon}_r) \\ & = \left[Y\left(1 - \tfrac{T}{T_m}\right) - \eta\exp\left(B\left[\tfrac{1}{T} - \tfrac{1}{T_m}\right]\right)\right]\tfrac{9f^2}{r^6} \end{aligned}. \tag{3.83}$$

Equation (3.81) and (3.82) are used to find $b(t)$ and $k(t)$ with given $P(t)$. Then $T(t)$ is obtained from equation (3.83). These equations are valid until k reaches a_o.

3.3.2 Ni+Al System Results

The new incompressible spherically symmetric pore collapse model is demonstrated for the $Ni + Al$ mixture with volume fractions $\xi_{Ni} = 0.5$ and $\xi_{Al} = 0.5$ and initial porosity $\alpha_o = 1.639$. R is estimated from mixture morphology as the average representative granule radius shown previously in Figure (1).

For the pore collapse model, the duration of the shock front $\hat{\tau}$ is the time required for the pore to close $\alpha = 1$ as shown in Figures (18-16). Computation of r, in equations (3.42) and (3.48), is performed with 4^{th} order Runge-Kutta and a time step of $0.5ns$. Figures (18-16) show the sensitivity to changes in the material parameters with respect to the pore closure, temperature, stress, and strain rate. These plots are useful in determining how the unknown parameters, C_I, μ_f, can be calibrated using RAVEN code results. Since the results from the hollow sphere are at the time of pore collapse, the strain rate is extraordinarily high due to the asymptotic behavior of the material flow into the center of the sphere. The strain rate is lower in the modified Carroll Holt model. However, the strain rates are still over predicted.

3.4 Incorporation of the Incompressible Spherically Symmetric Pore Collapse Model

The spherically symmetric pore collapse model is integrated into the framework in Figure (5) by incorporating information from both the RAVEN code and macro-scale continuum models. The summary of equations for the mixture modified pore collapse

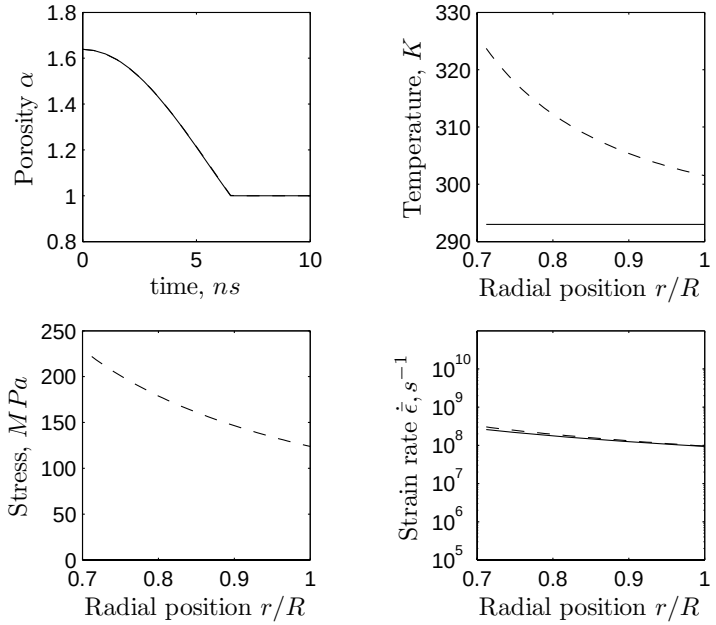

Figure 16: Pore collapse with $P = 3GPa$, $R = 25\mu m$, and $C_I = 1$ with $\mu_f = 0$ in the solid line and $\mu_f = 1$ in the dashed line. The lines nearly overlap in the upper left plot. Temperature, stress, and strain rate are given at the point of pore closure.

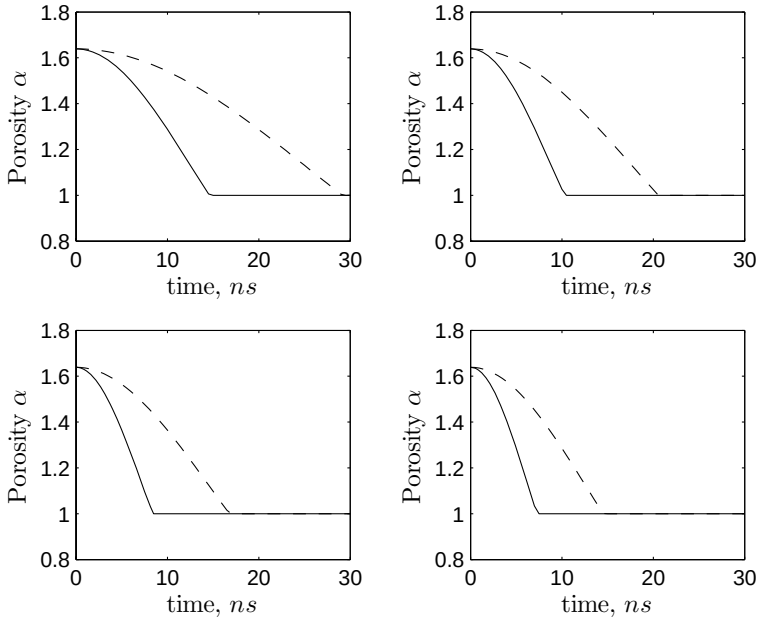

Figure 17: Pore collapse with $P = 3GPa$ (upper left), $P = 6GPa$ (upper right), $P = 9GPa$ (lower left), $P = 12GPa$ (lower right), $C_I = 1$, and $\mu_f = 1$ with $R = 25\mu m$ in the solid line and $R = 50\mu m$ in the dashed line.

model is given by,

$$\dot{r} = \frac{a^2\dot{a}}{r^2} = \frac{a^2\dot{a}}{\left(r_o^3 - a_o^3 + a^3\right)^{2/3}} \tag{3.84a}$$

$$\ddot{r} = \frac{\partial\zeta}{\partial r}, \quad \zeta = \frac{a^2\ddot{a} + 2a\dot{a}^2}{r} - \frac{a^4\dot{a}^2}{2r^4} \tag{3.84b}$$

$$\frac{\partial\bar{\sigma}_{rr}}{\partial r} + \frac{2}{r}\bar{\tilde{\sigma}} = \bar{\rho}_s\ddot{r} \tag{3.84c}$$

$$\bar{\rho}_s\dot{T} = -\frac{1}{\bar{C}_v}\frac{2\bar{\tilde{\sigma}}\dot{r}}{r} \tag{3.84d}$$

$$\bar{\rho}_s^* = \rho_{min} + C_I\left(\bar{\rho}_s - \rho_{min}\right); \quad 0 \leq C_I \leq 1 \tag{3.84e}$$

$$\dot{\bar{\gamma}} = \sum_p \dot{\gamma}_p = 2\frac{\dot{r}}{r} \tag{3.84f}$$

$$\bar{\tilde{\sigma}} = \bar{Y}(\dot{\gamma}, \bar{T}) \tag{3.84g}$$

$$Y^i = Y_i^o\left[\sum_{n=1}^{N} a_{yn}^i\left(1 - \frac{T}{T_m^i}\right)^n\right], \quad T < T_m^i \tag{3.84h}$$

$$Y^i = 0, \quad T > T_m^i \tag{3.84i}$$

$$\eta^i = \eta_m^i \exp\left(\sum_{n=1}^{N} B_i^n\left(\frac{1}{T} - \frac{1}{T_m^i}\right)^n\right)_{i=1,2,\ldots p}, \quad T < T_m^i \tag{3.84j}$$

$$Y_i^o = \frac{1}{1-\xi_p}\sum_{s\neq p}\mu_{Isp}Y_p^o \tag{3.85a}$$

$$\begin{aligned} P(t) \;&= 2\int_a^b \left[\sum_{i=1}^p Y_o^i\left\{a_{yn}^i\left(1-\tfrac{T}{T_m^i}\right)^n\right\} - \right. \\ &\left.\sum_{i=1}^p 6\eta_m^i \exp\left(\sum_{n=1}^N B_i^n\left(\tfrac{1}{T}-\tfrac{1}{T_m^i}\right)^n\right)\right]\tfrac{\dot r}{r}\tfrac{dr}{r} - \\ &\bar P_s\left[(a\ddot a+2\dot a^2)(1-a/b)-1/2\dot a^2(1-a^4/b^4)\right]; \quad T<T_m \end{aligned} \tag{3.85b}$$

$$\tau^* = \tau_0^*\left(\hat\rho\right)\left[1-\left\{\frac{kT}{\Delta G_0}\ln\left(\frac{v_0\left(\hat\rho\right)}{\dot{\bar\gamma}^p}\right)\right\}^{1/q}\right]^{1/p} \tag{3.85c}$$

$$\frac{\partial\hat\rho}{\partial\dot{\bar\gamma}^p} = M_{II}\left(\dot{\bar\gamma}^p\right) - k_a\left(\dot{\bar\gamma}^p,T\right)\left[\hat\rho-\hat\rho_0\right] \tag{3.85d}$$

$$\dot\epsilon = \dot\epsilon_0\exp\left[\frac{\Delta G\left(\sigma_t/\hat\sigma_t\right)}{kT}\right] \tag{3.85e}$$

$$\sigma = \sigma_a + \left[\left(s_I\left(\dot\epsilon,T\right)\hat\sigma_I\right)^n + \left(s_\epsilon\left(\dot\epsilon,T\right)\hat\sigma_\epsilon\right)^n\right]^{1/n} \tag{3.85f}$$

$$s_i = \left(1-\left[\frac{kT}{g_{oi}\mu(T)b^3}\ln\frac{\dot\epsilon_{0i}}{\dot\epsilon}\right]^{1/q_i}\right)^{1/p_i} \tag{3.85g}$$

$$\frac{d}{d\epsilon}\hat\sigma_\epsilon = \theta_0\left(\dot\epsilon\right)\left(1-\frac{\tanh\left[\frac{2\hat\sigma_\epsilon}{\hat\sigma_{\epsilon s}}\right]}{\tanh(2)}\right) \tag{3.85h}$$

where $\dot{\bar\gamma}^p$ is the effective plastic shear strain rate (see Appendix (D.3)), $\tau_0^*\left(\hat\rho\right) = \Delta G_0\sqrt{\hat\rho}/(ba)$ is the thermally activated part of the threshold stress (i.e. the stress barrier associated with short range obstacles at 0 K with activation distance a), $v_0\left(\hat\rho\right) = f\hat\rho v_D b^2$ is the attempt frequency factor at $0K$, k is Boltzmann's constant, ΔG_0 is the activation energy at $0K$, and p and q are constants that describe the shape of the energy barrier. Here, f is the fraction of mobile dislocations, v_D is the Debye frequency, $M_{II}\left(\dot{\bar\gamma}^p\right)$ is the rate-dependent dislocation multiplication term, $\hat\rho_0$ is the initial dislocation density, and $k_a\left(\dot{\bar\gamma}^p,T\right)$ is the dislocation annihilation factor, $\hat\sigma_t$ is the mechanical threshold stress, ΔG is the free energy, $\dot\epsilon_0$ is a constant, s_i is the thermally activated component of the stress, Burgers vector is $b = 2.517\mathring{A}$ and g_{oi} is the normalized total activation free energy that characterizes obstacle i and $\dot\epsilon_{0i} = 10^7 s^{-1}$. $g_{oI} = 0.103$ corresponding to $\hat\sigma = 11MPa$ and $g_{o\epsilon} = 1$ (typical for

long-range dislocation/dislocation interactions which are less thermally activated) [43]. The material parameters p_i and q_i have physical interpretations [71] similar to those used in the Klepaczko model. Here, $p_\epsilon = p_I = 2/3$ and $q_\epsilon = q_I = 1$ which correspond to box-like obstacles. $\hat{\sigma}_{\epsilon_s}$ is the steady state value of $\hat{\sigma}_\epsilon$ and θ_0 is the Stage II hardening rate. These parameters are fit to strain-rate data [43] and given by $\theta_0 = 5.04 + 0.103 \ln(\dot{\epsilon})\ GPa$ and $\hat{\sigma}_{\epsilon_s} = 870.8 + 12.8 \ln(\dot{\epsilon})\ MPa$. Further details and description is given in Appendix (D.2).

3.5 Continuum 1D strain model interface

In this thesis, the macro-scale continuum model is solved by numerically integrating the conservation equations (A.1-A.8) in space and time to provide the mixture density. The mixture is compressible in the continuum model and incompressibility is assumed in the pore collapse model. Momentum is spherically symmetric, thus, it does not influence the continuum 1-D strain model. Temperature localized within the pore collapse model is not coupled to the continuum 1-D strain model since the temperature generated by the work done by the pore collapse is already accounted for.

The mixture density in the 1-D strain model is used in the pore collapse model to calculate the pressure. The pressure is iterated until the required density is reached. Iterations are performed by choosing lower and upper pressure bounds, i.e., P_L, P_U respectively as shown previously in the algorithms in Figure (9). All history dependent parameters $\boldsymbol{w}$ such as the inner pore radius $a(t)$, velocity $\dot{a}(t)$, and constituent strength parameters are advected according to equation (3.86).

$$\frac{\partial}{\partial t}(\boldsymbol{w}) + \nabla \cdot (\boldsymbol{w}\bar{\mathbf{v}}) = 0. \tag{3.86}$$

Results from the spherically symmetric pore collapse as implemented in the 1D strain are shown in Figures (18) and (19).

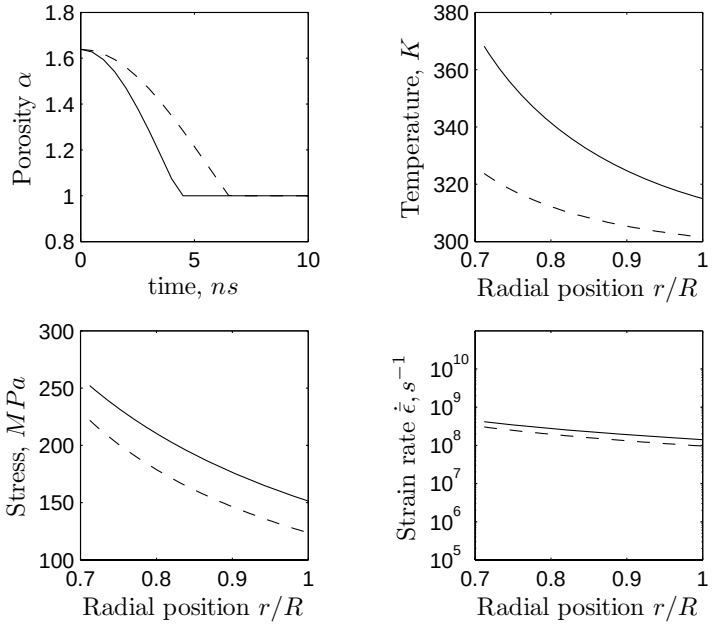

Figure 18: Pore collapse with $P = 3GPa$, $R = 25\mu m$, and $\mu_f = 1$ with $C_I = 0$ in the solid line and $C_I = 1$ in the dashed line. Temperature, stress, and strain rate are given at the point of pore closure.

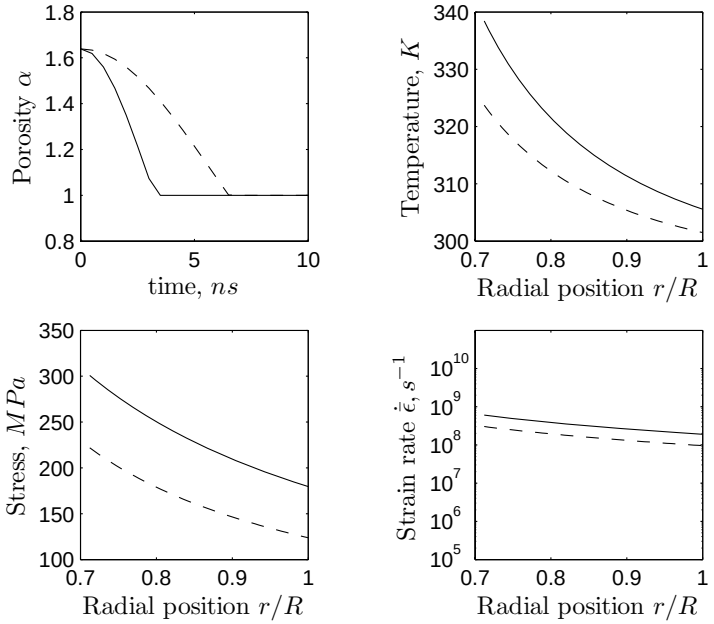

Figure 19: Pore collapse with $P = 3GPa$, $C_I = 1$, and $\mu_f = 1$ with $R = 25\mu m$ in the solid line and $R = 50\mu m$ in the dashed line. Temperature, stress, and strain rate are given at the point of pore closure.

3.6 RAVEN code model interface

RAVEN code results for E_d, τ are used to obtain the unknown pore collapse model parameters, R, C_I, and μ_{Isp}. The pressure applied to the surface of the pore collapse model P_m is approximated by the linear time dependence [92] which is written as

$$P_m(t) = \begin{cases} P_1 + (P^* - P_1)t/\tau & (0 \leq t \leq \tau), \\ P^* & (t > \tau). \end{cases} \tag{3.87}$$

It is assumed that $P^* = P_{st}$ is the final shock pressure downstream in the RAVEN code and τ is the duration of the shock front in the RAVEN code. Both quantities are obtained from Figure (44). P_1 is the pressure at which point higher pressures result in plastic flow. Pressure in the elastic range ($0 \leq P < P_1$) is neglected here because the elastic densification is negligible in comparison with the densification due to plastic pore collapse during strong shocks. For strong shocks, it is assumed that $P_1 = 0$ since the shock front thickness is approximately equal to the largest granule size in the mixture [92].

The assumption in equation (D.2) approximates mechanical equilibrium. Therefore, the mixture strength in equation (3.54) implies consistency with the mixture theory employed in the RAVEN code [5], in which a single-iteration pressure-equilibration mixture theory is employed. It is noted that full mechanical equilibrium is not imposed in the RAVEN code because a shock wave would traverse a mesh element multiple times before the pressure equilibrates. Integration is based on calibrating three model parameters.

The two criterion are $f = [E_d, \tau]$ and three model parameters $[R, C_I, \mu_{Ips}]$ to optimize the fit between the pore collapse results $\hat{f}_i(k)$ and the RAVEN code results $f_i(k)$, where k denotes the two experiment conditions $[u, \mathfrak{M}]$ which represent the steady state particle velocity imposed in the RAVEN code (see equation (B.5)) and mixture morphology respectively. The corresponding RAVEN code stationary pressure P_{st} is input into the pore collapse model boundary condition in equation

(3.87). This is a partially constrained multi-criterion optimization problem. The linear weighting method takes the form

$$\begin{aligned} &\textit{minimize} \quad \sum_{i=1}^{2} w_i \sqrt{\frac{1}{N_{runs}} \sum_{k=1}^{N_{runs}} \left(\frac{f_{ik} - \hat{f}_{ik}(R, C_I, \mu_{Ips})}{f_{ik}} \right)^2} \\ &\textit{such that} \quad \sum_{i=1}^{2} w_i = 1 \\ &\qquad\qquad R \geq 0 \\ &\qquad\qquad 0 \leq C_I \leq 1 \\ &\qquad\qquad 0 \leq \mu_{Ips} \leq 1 \end{aligned} \tag{3.88}$$

where w_i is the weighting factor assigned to the two criterion. The least squares approach includes normalization to obtain the optimal solution based on the true percent error between RAVEN code and gas-gun simulation results.

The pore collapse model results $\hat{f}(k)$ contain continuous solutions for parameters $[R, C_I, \mu_{Ips}]$ in each experiment k. A response surface is constructed in the three parameter coordinates for each set experimental conditions.

3.7 Summary

The mixture model proposed for use in a spherically symmetric pore collapse equation of state allows for calibration based on morphology and surface conditions. Inertial effects, representative granule size, and granular surface sliding effects. Simulated pore collapse under-predicts the pore collapse time $\hat{\tau}$ that is observed from RAVEN code results. This is primarily due to non-uniform pressure at the shock front in the RAVEN code. Additionally, two dimensional effects in the RAVEN code may not be well represented by the spherical geometry.

The proposed model incorporates mechanical threshold stress model and Klepaczko constituent strength models. These models have not been included in a spherically symmetric pore collapse model to date. A strong reason for this is the difficulty of implementation. A further complication is encountered when incorporating the mixture pore collapse model into the gas-gun simulation. The iterative approach taken

in this study provides a robust method for future researchers to employ.

Chapter IV

CHEMICAL REACTION

This chapter contains the formulation of a new chemical reaction model and techniques to bridge a granular level chemical reaction model into a macro-scale continuum level model. The mesoscale is defined in this thesis as the length and time scales appropriate for describing the interactions between individual granules in a granular mixture. This model consists of the conservation equations, the reaction model, reaction initiation, boundary conditions, and initial conditions.

4.1 Chemical Reaction Model

The complete chemical reaction model consists of two distinct levels of modeling, namely granular level and mesoscale. The RAVEN code provides information that is used by both the granular level and mesoscale models. A detailed discussion of assumptions model characteristics for the mesoscale model are given later. This section only describes the granular level model. The goal is to find a formulation of a chemical reaction model that can be used to study chemical reactions in a heterogeneous media of granular mixture of reactants.

Input: Mixture temperature $\bar{T}$, contact length between reactants CL, amount of reactants A_{cs} (area with unit depth), contact site locations with nearest neighbor distributions denoted by NN_{cs}, hot spot locations NN_{hs}, hot spot temperature T, and pressure P, for the location between two granules of reactants, is obtained from the RAVEN code. This information is not taken from the macro-scale continuum model since the RAVEN code has 2D spatial resolution of microstructures.

Desired output: The output is the mass fractions given by the rate equation

(discussed later),

$$\dot{\phi}_p = \frac{\dot{s}(t)}{L_B} \frac{\nu_p M_p}{\sum_p \nu_p M_p} \tag{4.1}$$

where the p constituents are summed over the reactants or the products, $\dot{\phi}_p$ is rate of change of the mass fraction for the p^{th} constituent, L_B is the length of the two granules, M_p is the molar mass, ν_p is the stoichiometric coefficient, and $\dot{s}(t)$ is the velocity of the reaction surface in the granular level reaction model. $\dot{\phi}_p$ is used as an input in the mesoscale model.

Assumptions: Chemical reactions are not assumed to increase additional mixing of the constituents. Heat transport employs a volume fraction mixture average of the conductivity between contact sites. Mass transport is assumed to be 1D. Nearest neighbor distributed quantities are assumed to be independent. Temperature at the contact site is 1D and heat is transported to the surrounding mixture over the entire contact site domain , $T = T(x)$. The state of stress at a contact site is assumed to be hydrostatic. Chemical reactions are assumed to be reversible and homogeneous at the surface to keep the formulation general for reactions in heterogeneous media, in which reactions occur at the surface. In this case, the reverse reaction is important. The steps are summarized as follows:

1. Reaction initiation is by the solid-liquid approach. The melting of one of the constituents produces reaction initiation.

2. The reaction rate at the surface is determined by both the mass transport to the surface and the chemical reaction rate at the surface. The Arrhenius equation is given by,

$$\Theta = k C_A^{\nu_A} C_B^{\nu_B} \tag{4.2}$$

$$k = A_o \exp\left(\frac{-\Delta\mu_a(T, \boldsymbol{\sigma})}{RT}\right) \tag{4.3}$$

where Θ is the reaction rate, k is the reaction coefficient, C is the concentration, ν is the stoichiometric coefficient, A_o is the pre-exponential factor or Arrhenius

constant, T is temperature, $\boldsymbol{\sigma}$ is the Cauchy stress tensor, μ is Gibbs free energy, R is the universal gas constant. If the stressed state is considered with only hydrostatic pressure P, the chemical potential becomes

$$\mu_i(\boldsymbol{\sigma}, T) \cong \mu_i(P^o, T) + PV_i \tag{4.4}$$

where $P^o = 1atm$ is the ambient pressure. Therefore, the change in free energy due to pressure is

$$\Delta\mu_\sigma = \sum_i P_i V_i \tag{4.5}$$

where the summation must include all mixture constituents with corresponding pressure P_i.

3. Mass transport is given by,

$$\frac{\partial C_A}{\partial t} = D_A(T, \boldsymbol{\sigma})\nabla^2 C_A + \nabla \mathbf{v}_A C_A. \tag{4.6}$$

where, C_A is the concentration for reactant A, $\mathbf{v}$ is the translation velocity, $D_A(T, \boldsymbol{\sigma})$ is a constant described in detail later. The temperature and state of stress are initially given by the RAVEN code results.

4. Reaction produces heat at the rate given by,

$$\Psi_S(x = s(t)) = \frac{\partial s}{\partial t} \cdot \left[{}^{-}\Delta\mu^o(P^o, \bar{T}) - {}^{+}\Delta\mu^o(P^o, \bar{T}) \right] \tag{4.7}$$

where μ^o is Gibbs free energy at the energy of formation, s is the surface location, T is temperature, P is pressure, $^+$ designates forward reaction, and $^-$ designates reverse reaction.

5. The rate of change of the mass fraction is given by equation (4.1). This is directly input into the mesoscale reaction model discussed in a later section.

4.2 RAVEN Code

RAVEN [14] is a finite element code developed at the University of California, San Diego.

4.2.1 Differential equations

The differential equations used in the Raven code are given by the conservation of mass, momentum balance, and conservation of energy in Eulerian coordinates, i.e.,

$$\frac{\partial \rho}{\partial t} + \nabla \cdot (\rho \mathbf{v}) = 0 \tag{4.8}$$

$$\frac{\partial \rho \mathbf{v}}{\partial t} + \nabla \cdot (\rho \mathbf{v} \times \mathbf{v}) = \nabla \cdot \boldsymbol{\sigma} + \rho \boldsymbol{f} \tag{4.9}$$

$$\frac{\partial \rho e}{\partial t} + \nabla \cdot (\rho e \mathbf{v}) = \boldsymbol{\sigma} : \dot{\boldsymbol{\epsilon}} \tag{4.10}$$

where, ρ is the density, t is time, $\mathbf{v}$ is velocity vector, $\boldsymbol{\sigma}$ is the stress tensor, f is the body force, e is the specific internal energy, and $\dot{\boldsymbol{\epsilon}}$ is the strain rate. Since mixture averages are not employed, ρ is the density for a constituent at a specific spatial location.

4.2.2 Assumptions

Model geometry is constructed by generating synthetic distributions of granules that conform to stereological measures of actual microstructures [4]. The resulting mixtures appear similar to those shown in in Figure (20). The assumed boundary conditions, roller boundary on the left and right, velocity on top, and transmitting boundary on bottom, are shown for the mixture in the figure on the left hand side in Figure (20) [13].

4.2.3 Finite Difference Equations

A Lagrangian calculation embeds a computational mesh in the material domain and solves for the position of the mesh at discrete points in time as shown in Figure (21). Since the mesh is embedded in the material, the motion of the material is inferred from the motion of the mesh [12].

RAVEN is an explicit code since the solution is advanced from time t^n to t^{n+1} without any iterations, and the difference between them is $t^{n+1/2}$ [12]. Stability

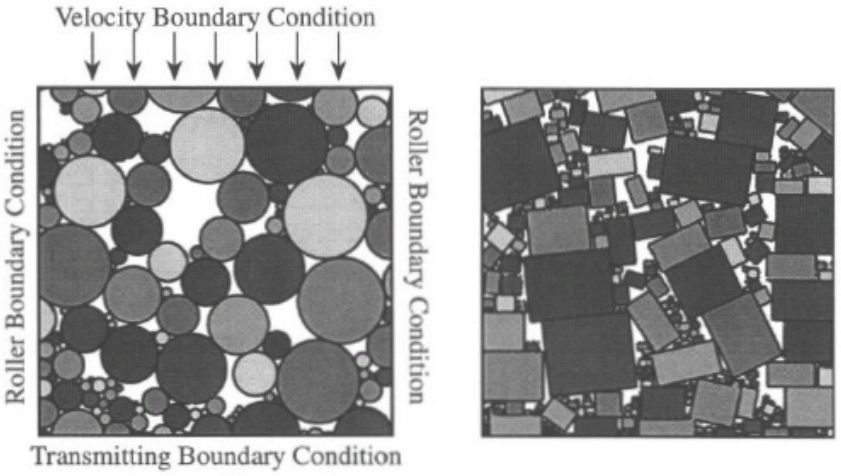

Figure 20: The initial configurations of cylindrical (19% porosity) and rectangular prismatic (16% porosity) Cu particle distributions simulated by Benson (illustrations taken from [13]).

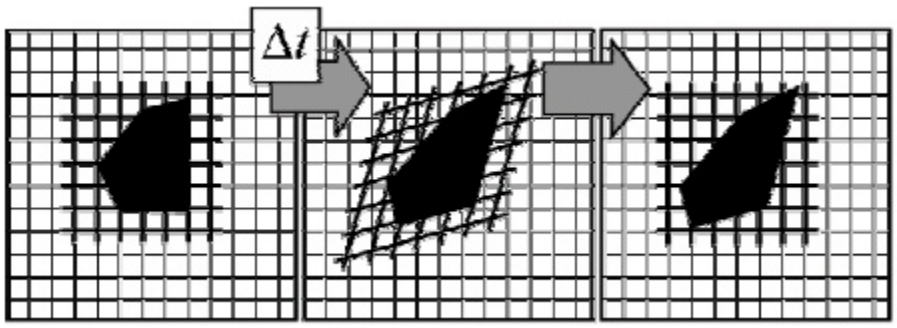

Figure 21: Operator splitting is achieved by a Lagrangian step followed by an Eulerian step(illustration taken from [12]).

conditions are discussed in [12]. The following equations are summarized from [12, 4]. The central difference method is used. The second order accurate integration is given for the general function f by,

$$f^{n+1} = f^n + f^{n+1/2}_{,t}\Delta t^{n+1/2} + O((\Delta t^{n+1/2})^3). \tag{4.11}$$

The position x is updated based on the velocity, i.e.,

$$x_i^{n+1} = x_i^n + \dot{x}_i^{n+1/2}\Delta t. \tag{4.12}$$

Applying equation (4.11) again gives the integration rule for the velocity.

$$u_i^{n+1} = u_i^n + \dot{u}_i^{n+1/2}\Delta t. \tag{4.13}$$

4.2.4 Method of Solution

Operator splitting is employed. The governing equations may be expressed in the generalized transport form

$$\frac{\partial}{\partial t}\phi + \dot{\boldsymbol{u}} \cdot \nabla\phi = \Phi \tag{4.14}$$

where the quantity ϕ represents a generalized solution variable and Φ is a source term. Operator splitting is a method of decoupling the material transport from the governing equations. The generalized transport equation is decomposed into the following terms

$$\frac{\partial}{\partial t}\phi = \Phi \tag{4.15}$$

$$\frac{\partial}{\partial t}\phi + \boldsymbol{u} \cdot \phi = 0. \tag{4.16}$$

Thus, the governing differential equations are replaced by sets of equations that can be solved sequentially. This solution technique involves two steps: a Lagrangian step, defined by Eq. (4.15), and an Eulerian step, defined by Eq. (4.16). The Lagrangian step, which is performed first, advances the solution in time. The Eulerian step, which is performed afterwards, accounts for material transport. Eulerian formulations are used to simulate the dynamic responses of spatially-resolved particle

systems subjected to shock loading, where the stress-strain response of each phase is modeled using distinctive constitutive relations.

4.2.4.1 Lagrangian Step

The Lagrangian calculations performed here adhere broadly to the framework used in many traditional Lagrangian formulations. There is, however, a complicating factor: the allowance of more than one material in a single element. The calculations are adapted to handle this behavior through the introduction of a mixture theory similar to the theory presented later in this thesis. Details are given in [12]. The flow of calculations performed in a Lagrangian step is summarized as follows:

1. The forces at the nodes are calculated from the stress state an applied forces at t^n.

2. Nodal accelerations are calculated from the nodal forces at t^n.

3. The acceleration is integrated to obtain the velocity at $t^{n+1/2}$.

4. The velocity is integrated to obtain the displacement at t^{n+1}.

5. The density is calculated from the deformation gradient at t^{n+1}.

6. The total strain rate at $t^{n+1/2}$ is calculated from the velocity gradient.

7. The total strain rate is partitioned among the materials in a mixed element according to a mixture theory.

8. The deviatoric stress in each material is updated using an objective stress rate, where the stress increment from the constitutive model is added at the midpoint of the time step.

9. The mean deviatoric stress tensor in an element is calculated according to a mixture theory.

10. The updated artificial shock viscosity and hourglass viscosity are calculated from the time-centered velocity.

11. The internal energy is updated based on the work done during the time step.

12. The pressure is calculated from the equation of state (EOS) based on the internal energy and density at t^{n+1}.

13. The updated total stress tensor is calculated now that all components are known at t^{n+1}.

14. A new time step Δt^{n+1} is calculated based on the Courant stability criterion.

4.2.4.2 Eulerian Step

The remapping of the solution described by the Lagrangian mesh to the Eulerian mesh involves the following procedures:

1. The volume transported between elements is calculated.

2. The mean values of the solution variables associated with the transported volume are calculated and advected.

3. The material interfaces within a mixed element are reconstructed.

4. The computational meshes are reconciled and the calculation proceeds to the next Lagrangian step.

4.3 Chemical Reaction Model

The general form for the chemical reactions $k = 1...N_r$ is written from [67] as

$$\sum_{i=1}^{{}^{+}N_{sk}} {}^{+}\nu_{ik}\left[C_i\right] \rightleftharpoons \sum_{i=1}^{{}^{-}N_{sk}} {}^{-}\nu_{ik}\left[C_i\right] \tag{4.17}$$

for ${}^{+/-}N_s$ reactant and product species, respectively. In the equations, ${}^{+}()$ denotes the reactant group and ${}^{-}()$ denotes the product group or forward and backward

processes, respectively. ν_{ik} is the stoichiometric coefficient. C_i (mol/m^3) is the molar concentration species i. For the specific case of $2Al + Fe_2O_3$, the reaction rate for reaction k is given by [88],

$$\tau_{\Theta k}\dot{\Theta}_k + \Theta_k = {}^{+}k_k \prod_{i=1}^{{}^{+}N_{sk}} [C_i]^{{}^{+}\nu_{ik}} - {}^{-}k_k \prod_{i=1}^{{}^{-}N_{sk}} [C_i]^{{}^{-}\nu_{ik}} . \tag{4.18}$$

The modified Arrhenius rate coefficients are given by [105] as,

$$\begin{aligned} {}^{+}k_k &= {}^{+}A_k \; T^{{}^{+}\beta_k} \; P^{{}^{+}\eta_k} \; {}^{+}f_k(1-\varphi) \exp\left\{-\tfrac{\Delta^{+}\mu_{ak}}{RT}\right\}, \\ {}^{-}k_k &= {}^{-}A_k \; T^{{}^{-}\beta_k} \; P^{{}^{-}\eta_k} \; {}^{-}f_k(1-\varphi) \exp\left\{-\tfrac{\Delta^{-}\mu_{ak}}{RT}\right\} \end{aligned} . \tag{4.19}$$

φ is the global degree of conversion of the reactant.

The total differential of the internal energy dU in equation (4.20) considers the energy in a stressed solid where dS is the differential entropy production [105].

$$dU = TdS + V\bar{\boldsymbol{\sigma}} : d\bar{\boldsymbol{\epsilon}} + \sum \mu_i dn_i \tag{4.20}$$

where V is the partial molar volume and dn_i is the number of moles of component i. Here, $\boldsymbol{\epsilon}$ and $\boldsymbol{\sigma}$ are symmetric tensors [105]. We may relate the chemical potential in equation (4.20) to the Gibbs free energy μ and Helmholtz free energy H, i.e,

$$\mu_i(\boldsymbol{\sigma}, T) = \left(\frac{\partial \mu}{\partial n_i}\right)_{n_j, \boldsymbol{\sigma}, T} = \left(\frac{\partial H}{\partial n_i}\right)_{n_j, \boldsymbol{\sigma}, T} - V\sigma_{jk} \cdot d\epsilon_{jk}. \tag{4.21}$$

If we consider the stressed state with only hydrostatic pressure P, the chemical potential becomes

$$\mu_i(\boldsymbol{\sigma}, T) \cong \mu_i(P^o, T) + P_i V_i \tag{4.22}$$

where $P^o = 1atm$ is the ambient pressure. Therefore, the change in free energy due to pressure is

$$\Delta\mu_\sigma = \sum_i P_i V_i \tag{4.23}$$

where the summation must include all mixture constituents with corresponding pressure P_i. Figure (22) shows an ideal case for $\Delta\mu_\sigma$ when both the reactants and the products are at $P = 0$ and the transition state is at $P < 0$.

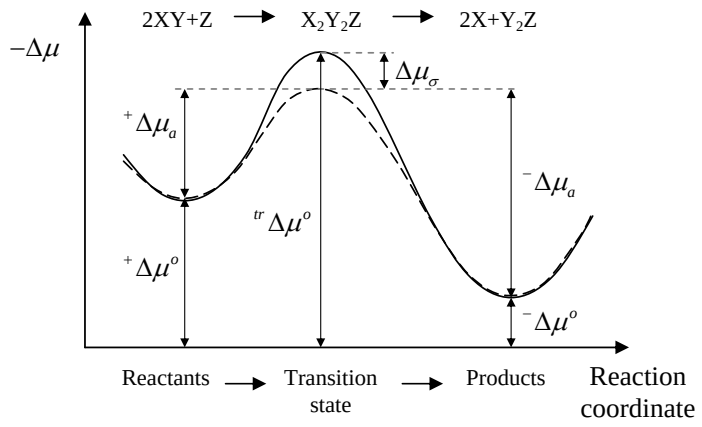

Figure 22: Idealized schematic of the reaction path.

The partial molar volume of constituent i is

$$V_i = \frac{M_i}{\rho_i} v_i. \tag{4.24}$$

In equation (4.24), M_i is the molar mass with units g/mol. For the constituents in the mixture, the molar masses are $M_{Al} = 26.98$, $M_{Fe_2O_3} = 159.69$, $M_{AlO} = 42.98$, and $M_{Fe_2O} = 127.69$.

The zero stress (or ambient pressure $P^o = 1atm$) chemical potential or thermal contribution is defined in equation (4.25).

$$\begin{aligned} \mu_p(P^o, T) = \quad & \Delta\mu_p(P^o, T) = \Delta H^f_{o_p}(P^o, T^o) + \textstyle\int_{T'=T_o}^{T} c_{vp}(P^o, T')dT' \\ & -T \cdot \left[\Delta S_p(P^o, T^o) - \textstyle\int_{T'=T_o}^{T} \frac{c_{vp}(P^o, T')}{T'} dT'\right] \end{aligned} \tag{4.25}$$

where $T^o = 298K$ is the reference temperature and c_{vp} is the heat capacity for constant volume for constituent p. The stoichiometric mixture change in free energy for $P = P^o$ is given by

$$^{+/-}\Delta\mu^o(P^o, T) = \sum_p \mu_p(P^o, T) \cdot v_p \tag{4.26}$$

and is shown for both reactants and products respectively in Figure (22).

4.4 Chemical Reaction in Heterogeneous Media: Granular Level Model

The system is initially composed of two reactants, at a single contact site. Each granule is represented by a continuum in 1D spatial coordinates based on the size of the reactant granules at the contact site. The model explicitly describes the reaction at the interface between the reactants. Heat and material transport through the product layer are included. A consideration of the pressure and temperature are shown to initiate reaction.

The homogeneous media GLR model is defined in this thesis by considering all constituents in a contact site to exist at a single continuum point in space. Fundamental chemical reaction descriptions are given in Appendix (C). Reaction kinetics assume the form in equation (4.18). The transition state is described in Appendix (C.1). A review of the functional forms in equation (4.19) are given by Smith and Chaudhri [109], in which ${}^{+}f(1-\varphi) = 1$ for 1D phase boundary growth. f is a function with a form that corresponds to a process to limit chemical reaction and the extent of completion, which is used in equation (4.19). This is the form assumed in this study since reactions are assumed to be faster than is permitted by the standard concentration based diffusion reaction, i.e., ${}^{+}f(1-\varphi) = 1/\alpha$ for 1D diffusion controlled growth. We assume that ${}^{-}f(1-\varphi) = 0$ since we assume that the reaction is irreversible.

Austin [4, 5, 29] used the RAVEN code, a 2-D plane strain multi-material Eulerian hydrocode developed by Benson [14]. These simulations were conducted on Al+Fe_2O_3 + 20 wt.% epoxy and volume % void content at imposed velocities in the RAVEN code as high as approximately $1km/s$. The density and distribution of *contact sites* (locations where reactants are in contact) as a function of time were obtained. A contact site is shown in Figure (23), where Fe_2O_3 and Al granules are surrounded by an epoxy matrix.

Results from the RAVEN code provide the physical basis for determining the initial

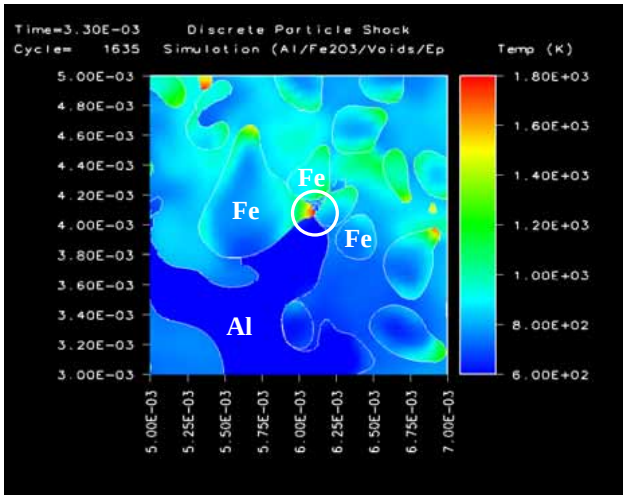

Figure 23: RAVEN code simulation of $Fe_2O_3 - Al$.

conditions to be used in the case study. Physical processes such as the collisions of the constituents, pore collapse, jetting, and plastic flow are represented explicitly in reference [33]. Therefore, the deformed mixture, after the passage of the shock, represents a state of the mixture prior to shock induced chemical reactions (see Figure (23)). Reactants clearly must be transported through the product layer that forms after reaction.

4.4.1 Surface Reaction Mechanism

The majority of real reactions are complex and take place via the transition state [65]. Heterogeneous chemical reactions involve two or more phases (solid and gas, solid and liquid, two immiscible liquids) in which one or more reactants undergo chemical change at an interface [2]. Heterogeneous catalysis such as the reaction $N_2 + 3H_2 \rightarrow 2NH_3$ in the Haber-Bosch process involve molecular processes at the gas-solid interface. The fundamental mechanism in this reaction has only recently been understood through experimentation and modeling by the 2007 Nobel Laureate Gerhard Ertl for "his studies of chemical processes on solid surfaces".

For example, consider the single-step reaction in Figure (22) with the reaction $2XY + Z \rightleftharpoons X_2Y_2Z \rightarrow 2X + Y_2Z$. The subscript $k = 1$ is left out of the following

equations for convenience. The overall surface reaction is viewed as two separate physical processes, namely formation of the activated complex X_2Y_2Z at the transition state and subsequent formation of the final product $2X + Y_2Z$.

The first process $2XY + Z \rightleftharpoons X_2Y_2Z$ is endothermic. Formation of X_2Y_2Z at the surface depends on the product concentration at the surface, free energy $\Delta\mu$ at the surface, and the mobility of reactants from the materials to the surface.

The second process $X_2Y_2Z \rightarrow 2X + Y_2Z$ is exothermic and usually assumed to be irreversible or ${}^{-}k = 0$ since its activation energy is much higher, i.e., $\Delta^{-}\mu_a \gg \Delta^{+}\mu_a$ (see Figure (22)). However, supply of reactants to the reaction surface is limited by finite mass-transport rate in the proposed model. Additionally, reaction is inhibited due to formation of products $2X + Y_2Z$ at the surface since the product concentration is much higher at the surface than in the entire mixture. Therefore, the reverse rate ${}^{-}k$ is included in this study. The separation of the reactants due to the formation of the products is a physical process that occurs [105].

These two processes limit the reaction propagation. The 1D transport assumption permits these processes. A 3D model may elucidate alternative processes including mixing. This proposed reaction model only permits significant reaction propagation if surface temperature and state of stress are sufficiently high.

4.4.1.1 Surface Flux

We idealize the separation of reactants by an equiaccessible planar surface in which the reaction is supplied by diffusion transport of reactants. The surface reaction rate is Θ, with the two constituents (A, B) becomes [105]

$$\Theta = kC_A^{\nu_A} C_B^{\nu_B} \tag{4.27}$$

$$k = A_o \exp\left(\frac{-\Delta\mu_a(T, \boldsymbol{\sigma})}{RT}\right) \tag{4.28}$$

where subscripts are used to denote mixture constituents for clarity. The subscript a denotes activation (see Figure (22)). R is the universal gas constant, T is the temperature, C is the concentration, and A_o is the frequency factor or a model parameter that is usually fit to experimental results. Here, the activation energy per mole of reactants $\mu_a(T, \boldsymbol{\sigma})$ is a function of temperature and the state of stress. If the stressed state is considered with only hydrostatic pressure P, the chemical potential becomes

$$\mu_i(\boldsymbol{\sigma}, T) \cong \mu_i(P^o, T) + PV_i \tag{4.29}$$

where $P^o = 1atm$ is the ambient pressure. Therefore, the change in free energy due to pressure is

$$\Delta\mu_\sigma = \sum_i P_i V_i \tag{4.30}$$

where the summation must include all mixture constituents with corresponding pressure P_i.

The reaction rate must be equal to the rate at which the reactants reach the surface by diffusion or turbulent diffusion [65] and by the reaction rate at the surface. The reaction rate must be equal to the rate at which reactants reach the surface and are consumed at the surface because reaction can not occur unless both reactants are in contact. We define the i^{th} constituent mass-transport coefficient as $\beta_i = D_i(T, \boldsymbol{\sigma})/\delta$, which controls the transport of the reactants from the material away from the interface to the reaction interface. $D_i(T, \boldsymbol{\sigma})$ is the diffusivity constant. The term δ refers to the distance between a location in the reactant, $s(t) - \delta$, and the surface of the reaction, $s(t)$. This can be expressed in 1D coordinates as in Figure (24) or in higher dimensions if $s(t) - \delta$ represents lies on a line that is normal to the surface reaction at $s(t)$ and passes through the point x_{jI}. This distance is required to separate the two reactants. The concentration of each constituent at the surface is denoted C_i'.

The mass flux [65] is given as,

$$J_i = \beta_i \left(C_i - C_i'\right) = \Theta\left(C_A', C_B'\right)/\nu_i. \tag{4.31}$$

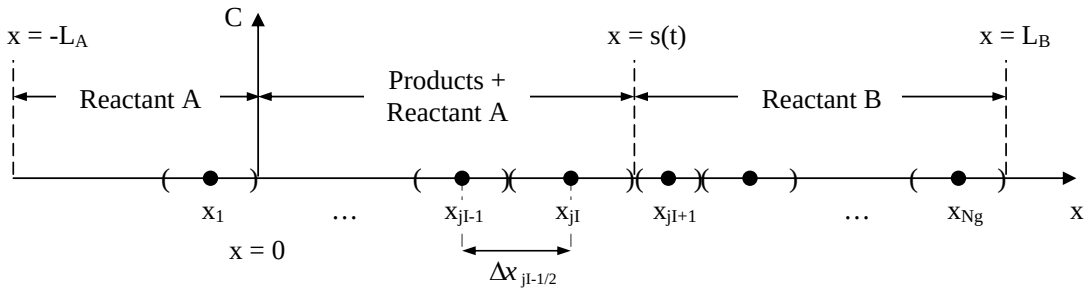

Figure 24: 1D grid for the heterogeneous granular level reaction simulation with moving reaction front at $x = s(t)$ and local non-uniform grid at x_{jI}, x_{jI+1} with s(t=0)=0. The origin is fixed in space with respect to the reactants.

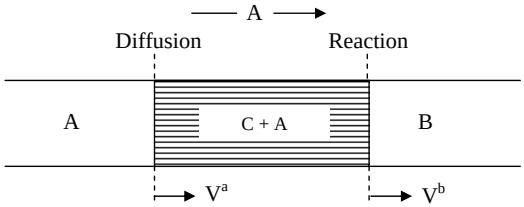

Figure 25: Rate controlling mechanism.

The reaction surface location, with velocity V^a in Figure (25) at a given time, is denoted as $s(t)$ for convenience and is given by the flux in equation (4.32). ν_i is the stoichiometric coefficient for the i^{th} constituent. Diffusion mass-transport is defined on the 1D spatial coordinate $0 <= x < s(t)$ by the stationary diffusion equation, similar to the heat equation (4.44), and is given by

$$J_A = \left(D_A \frac{\partial C_A}{\partial x} \right)_{x=s(t)} = \frac{\Theta}{\nu_A} = C'_A \frac{\partial s}{\partial t}. \tag{4.32}$$

Let $A = XY$ and $B = Z$ from the example reaction with the rate determining transport mechanism in Figure (25). The surface concentrations C'_A and C'_B are obtained from equations (4.18) and (4.31) with $\tau_\Theta = 0$ and Θ_1 is the mass-transport determining reaction rate to the surface. Since reactant A is transported through the products, $C'_B = C_B$. Therefore, the concentration at the surface for reactant A, with $\nu_A = 2$ for the class of reactions studied in this thesis, is given by

$$C'_A = \frac{-\beta_A + \sqrt{\beta_A^2 + 4^+k_1 C_B^{\nu_B} (\beta_A C_A + {}^-k_1 C_C'^{\nu_C})}}{2^+k_1 C_B^{\nu_B}} \tag{4.33}$$

where $C = X_2Y_2Z$ is the intermediate product. The translation term $\mathbf{v}_A C'_A = 0$ since reactant A does not penetrate the surface $s(t)$. Equation (4.33) represents the concentration of reactant A in the product layer of the reaction. This equation is easily obtained using equations (4.27), (4.31), and (4.32).

4.4.2 Mass Transport

Mass transport is referred to as *forced* interdiffusion [31] since the transport rate depends on stress and translation velocity v. We assume that diffusivity for reactant A, $D_A(T, \boldsymbol{\sigma})$, is a constant and the diffusion equation takes the form,

$$\frac{\partial C_A}{\partial t} = D_A(T, \boldsymbol{\sigma})\nabla^2 C_A + \nabla \mathbf{v}_A C_A. \tag{4.34}$$

The diffusion equation is generally 3D. In this thesis the diffusion equation is 1D, therefore, the operator is given by $\nabla = \partial/\partial x$. The rate of change in the translation velocity vector $\mathbf{v}_A$ is obtained from the momentum balance given by,

$$\frac{\partial}{\partial t}\left(\rho_A \mathbf{v}_A\right) + \nabla \cdot \left(\rho_A \mathbf{v}_A \times \mathbf{v}_A\right) = \nabla \cdot \boldsymbol{\sigma} \tag{4.35}$$

where $\mathbf{v}_A$ is the only unknown because ρ_A is assumed to be constant in the GLR and mesoscale reaction models.

In 1D, equation (4.36) becomes,

$$\frac{\partial}{\partial t}\left(\rho_A \mathbf{v}_A\right) + \frac{\partial}{\partial x} \cdot \left(\rho_A \mathbf{v}_A \times \mathbf{v}_A\right) = \nabla \frac{\partial \boldsymbol{\sigma}}{\partial x} \tag{4.36}$$

Generally, there are three main energy contributions in a shock induced chemical reaction, namely shock compaction, pore collapse, and plastic work. All of these are accounted explicitly by Do and Benson [34]. However, their reaction model has infinite transport rate. In this thesis, the stress contribution is considered to affect the transition state in the mass transport model. This is demonstrated for the case in which the pressure is considered.

The diffusion constant in equation (4.34) depends on temperature and on the stress state via the activation energy and is given by,

$$\Delta\mu_D(\boldsymbol{\sigma}) = \Delta\mu_{Do} + \Delta\mu_\sigma \tag{4.37}$$

with $\Delta\mu_\sigma$ from equation (4.23). $\Delta\mu_{Do}$ is a material parameter obtained from experiments. Both $\Delta\mu_{Do}$ and $\Delta\mu_\sigma$ are constants.

$$D(T, \boldsymbol{\sigma}) = D_o \exp\left(\frac{-\Delta\mu_D(\boldsymbol{\sigma})}{RT}\right). \tag{4.38}$$

The spatial coordinate x is defined with the origin $x = 0$ located at the diffusion interface in Figure (25). The characteristic length of the reactant B granule is L_B. The reactant lengths are assumed to be proportional to the volume fraction, i.e., $L_A/L_B = \xi_A/\xi_B$.

The concentration of reactant A at $x = 0$ is C_A^o given by equation (4.39) with ${}^A\xi = {}^A\phi = 1$, which remains constant with respect to time until reactant A is depleted at time t^*.

$$C_i = \frac{\phi_i \bar{\rho}}{M_i}. \tag{4.39}$$

The boundary conditions for equation (4.34) are written as

$$\left.\begin{array}{ll} C_A = C_A^o & \text{for } t < t^* \\ \frac{\partial C_A}{\partial x} = 0 & \text{for } t \geq t^* \end{array}\right\} \quad \text{at } x = 0$$
$$C_A = C_A' \qquad\qquad \text{at } x = s(t) \tag{4.40}$$

and are applied as shown in Figure (24).

4.4.2.1 Discrete Form

The 1D discrete form of equation (4.34) on a uniform Eulerian grid Δx with time step n, omitting the subscript A on the concentration, is

$$C_j^{n+1} = C_j^n + \frac{\Delta t^n \cdot D_{Al}^n(T_j, P_j)}{\Delta x^2}\left[C_{j+1}^n - 2C_j^n + C_{j-1}^n\right]. \tag{4.41}$$

The uniform grid size is $\Delta x = 1/(N_g - 1)$ and N_g is the number of grid points. Initially, the $s(t = 0) = 0$ and moves at the velocity defined by equation (4.32). At the reaction surface $s(t)$ shown in Figure (24), we have a non-uniform grid with the flux from equation (4.31). The concentration of reactant A is given by

$$C_{jI}^{n+1} = C_{jI}^{n} + \frac{2\Delta t^n}{\Delta x + \Delta x_{jI}} \left(-\frac{\Theta}{v_{Al}} - D_{Al}^{n}(T_j, P_j) \left[\frac{C_{jI}^{n} - C_{jI-1}^{n}}{\Delta x_{jI-1/2}} \right] \right) \tag{4.42}$$

since the cell centered at $x(jI)$ has a moving cell edge $s(t)$ and $\Delta x' \geq \Delta x/2$. At time $t = 0$, the node $jI = 1$.

The stability condition for the diffusion transport is obtained from [63] and stated as

$$\Delta t^{n+1} \leq \min \left[\frac{1}{2} \frac{\left(\frac{\Delta x}{2}\right)^2}{\max_j \left(D_{Al}^{n}(T_j, P_j)^n\right)}, \frac{\Delta x}{2} \frac{1}{\frac{\partial s^n}{\partial t}} \right]. \tag{4.43}$$

$s(t)$ in Figure (24) moves from left to right. When the new location s^{n+1} from equation (4.32) is such that $\Delta x_{jI+1}^{n+1} \leq \Delta x/2$, the cells are reconstructed such that mass is conserved and $jI = jI + 1$. The time step used in this study is given by multiplying Δt from equation (4.43) by $CFL = 0.8$ $(0 < CFL \leq 1)$, which is the Courant Friedrichs and Lowey condition.

4.4.3 Post Reaction Granular Level Reaction Heat Transport and Melting

The stationary form of Fourier's law is used for the local continua with mixture temperature $\bar{T}$. This permits the temperature calculation of the reacting region without material flow. The heat flux in the mixture is given by,

$$\bar{\boldsymbol{q}} = -\bar{k}_q \nabla \bar{T} \tag{4.44}$$

where $\bar{k}_q$ is the mixture heat conduction coefficient. $\bar{k}_q$ and the mixture density are volume fraction averaged.

The heat conduction equation is given by,

$$\frac{\partial \left(\rho c_v T\right)}{\partial t} = \nabla \cdot \left(\bar{k}_q \nabla T\right). \tag{4.45}$$

If the mass fraction averaged heat capacity is $\bar{c}_p$ and the density $\bar{\rho}$ in equation are assumed to be constant with respect to time (incompressible) and $\bar{k}_q$ is spatially independent, then equation (4.45) simplifies to give us,

$$\frac{\partial \bar{T}}{\partial t} = \bar{\kappa}(T)\nabla^2 \bar{T} \tag{4.46}$$

where $\bar{\kappa}$ is the thermal diffusivity with units $m^2 \cdot s^{-1}$ and is given by,

$$\bar{\kappa}(T) = \frac{\bar{k}_q}{\bar{\rho}\bar{c}_p(T)}. \tag{4.47}$$

Heat is transported in the model in the region containing the reactant products and the reactant B, i.e., $0 \leq x \leq L_B$ in Figure (24), and heat is generated at the reaction interface. The source term $\Psi_{MS}(x)$ given below bridges the granular level reaction and the mesoscale models. The mesoscale reaction model is discussed later. The heat conduction equation is given by,

$$\frac{\partial \left(\bar{\rho}\bar{c}_v \bar{T}\right)}{\partial t} = \nabla \cdot \left(\bar{k}_q \nabla \bar{T}\right) + \Psi_S(x = s(t)) + \Psi_{MS}(x). \tag{4.48}$$

The material parameters and temperature are spatially dependent and are averaged based on the composition at the spatial coordinate x. $\bar{k}_q(x)$ is the volume fraction (ξ) average heat conduction coefficient and $\bar{\rho}(x)$ is the average density. The mixture heat capacity $\bar{c}_v(x)$ and temperature $\bar{T}(x)$ are averaged on a mass fraction (ϕ) basis.

From equations (4.26) and (4.32), the source term Ψ_S due to the heat supplied or produced by the exothermic reaction at the interface is given by,

$$\Psi_S(x = s(t)) = \frac{\partial s}{\partial t} \cdot \left[{}^{-}\Delta\mu^o(P^o, \bar{T}) - {}^{+}\Delta\mu^o(P^o, \bar{T}) \right]. \tag{4.49}$$

Heat transfer between the GLR and mesoscale models is necessary since the GLR model is embedded within the mesoscale model. This means that at each time step in the mesoscale simulation, the GLR model is run at each contact site or location in which reactants are in contact. Heat is transferred based on the ensemble average energy in the GLR, which given by,

$$\hat{e} = \int_0^{L_B} \bar{T}\bar{\rho}\bar{c}_v dx. \tag{4.50}$$

Implementation in a mesoscale model that relates the $\dot{\hat{e}}$ to $\Psi_{MS}(x)$ is provided later. According to this model description, diffusion occurs within the GLR model regardless of the heat transfer between the GLR and mesoscale reaction models.

The latent heat of melting (fusion) ΔH_{mi} requires energy at the rate given by,

$$\frac{\partial \hat{e}}{\partial t} = \dot{\phi}_i \mid_{s \to l} \Delta H_{mip}, \tag{4.51}$$

such that the temperature $T = T_{mi}$ remains constant while the solid phase mass fraction $\phi_i \mid_s > 0$ for reactant i.

For the mixture reaction model [88], constituents are assumed to be in thermal equilibrium and the solid-liquid approach is employed unless otherwise specified. The heat source term for the binary mixture with reactants $i = 1, 2$ is written in the form,

$$\Psi_S = \sum_{k=1}^{N_r} \sum_{i=1}^{2} \dot{\phi}_{ik} \cdot \left[{}^{-}\Delta\mu_k^o(P^o, \bar{T}) - {}^{+}\Delta\mu_k^o(P^o, \bar{T}) \right] \tag{4.52}$$

where ${}^{+/-}\Delta\mu^o(P^o, \bar{T})$ are given in equation (4.26).

4.4.4 Boundary Conditions and Initial Conditions

For equation (4.48), the boundaries at $x = 0, L_B$ are adiabatic, i.e., the heat flux $q = 0$. This is necessary since there is no information for temperatures beyond the boundaries. This permits the heat to be transferred from the entire 1D domain instead of only the boundaries. For complete reactions in the case where $\dot{\hat{e}} = 0$, the temperature in the region $0 \leq x \leq L_B$ will be approximately equal to the adiabatic temperature calculated in the homogeneous GLR model.

Initial conditions:

Temperature is initially distributed according to mixture temperature T_b and hot spot temperature T_{hs} at the reactant interface by,

$$T(x, t=0) = \begin{cases} T_b + \frac{(T_{hs} - T_b)}{\Delta x_{hs}^2} \left(x - \Delta x_{hs}\right)^2 & ; \quad 0 \leq x \leq \Delta x_{hs} \\ T_b & ; \quad \Delta x_{hs} < x \leq L_B \end{cases} \tag{4.53}$$

where a parabolic distribution is assumed. Note that T_b and T_{hs} are only used to initialize the temperature. T_{hs} is estimated from the RAVEN code results. Δx_{hs} is the size of the hot spot shown in Figure (26-a). Δx_{hs} depends on the temperature distribution obtained from the mesoscale simulation. A hot spot is defined as a region in which reactants are at a significantly higher temperature than the neighboring material. The definition for the temperature difference and size of the hot spot are a current topic of research and are discussed further later in this thesis. The point at which $t = 0$ is based on the assumed stationary condition in the mesoscale simulation. For example, at time Δt_{st} downstream of the shock front, the formation of contact sites may reach a near-stationary condition when mixing has nearly stopped.

4.4.5 Numerical Solution

The solution to equation (4.46) is similar to the 1D discrete mass transport equations but with a smaller time step $\tilde{n} < n$ in equation (4.54). $\tilde{n}$ is obtained from the stability conditions since it represents the number of time steps.

$$T_j^{\tilde{n}+1} = T_j^{\tilde{n}} + \frac{\Delta t^{\tilde{n}} \cdot \bar{\kappa}_j^{\tilde{n}}(T_j^n)}{\Delta x^2} \left[T_{j+1}^{\tilde{n}} - 2T_j^{\tilde{n}} + T_{j-1}^{\tilde{n}}\right] + \Psi_{S,j}^n + \Psi_{MS,j}^n. \tag{4.54}$$

To satisfy the constraints used to derive equation (4.46), $\bar{k}_q$ is spatially independent and calculated for all constituents p at the j node, i.e.,

$$\bar{k}_q^n = \sum_{j=2}^{N_g} \sum_p \xi_{p,j}^n k_{qp,j}^n. \tag{4.55}$$

The average heat capacity $\bar{c}_{p,j}$ at each node j only changes at n time steps to conserve energy. T_j is re-calculated to conserve energy by applying equation (1.17).

$\Psi_{S,j}^n$ is added to the interface nodes at $x = x_{jI}, x_{jI+1}$ proportionally to the respective cell sizes at time t^n, i.e.,

$$\Psi_{S,j}^n = \frac{\Delta x_j^n}{2\Delta x} \frac{\Delta e_{rxn}^n}{\bar{c}_{v,j}^n \bar{\rho}_j^n} \tag{4.56}$$

where Δe_{rxn} is the heat supplied by the GLR model and is given by,

$$\Delta e^n_{rxn} = \frac{s^{n+1} - s^n}{\Delta x} \frac{\bar{\rho}_o}{\sum_{p=1}^{2} M_p \nu_p} \left[{}^{-}\Delta\mu^o(P^o, T) - {}^{+}\Delta\mu^o(P^o, T) \right]. \tag{4.57}$$

The change in the average temperature in the GLR model $\Delta\hat{T}$ is due to heat transport calculated in the mesoscale model and heat generation due to the heat of reaction in the GLR model. This heat is distributed proportionally to each node based on the local heat conduction at t^n, i.e.,

$$\Psi^n_{MS,j} = \frac{\left(\bar{T}^n + \Delta\hat{T}^n - T^n_j\right) \sum_{i=2}^{N_g} \bar{c}^n_{v,i} \bar{\rho}^n_i \Delta x^n_j}{\bar{c}^n_{p,j} \bar{\rho}^n_j \Delta x^n_j} \tag{4.58}$$

since $\bar{k}_q$ is spatially independent. $\bar{T}$ is the ensemble average temperature in the contact site given by,

$$\bar{T}^n = \frac{\sum_{i=2}^{N_g} T^n_j \bar{c}^n_{p,j} \bar{\rho}^n_j \Delta x^n_j}{\sum_{i=2}^{N_g} \bar{c}^n_{v,j} \bar{\rho}^n_j \Delta x^n_j}. \tag{4.59}$$

The adiabatic boundary conditions are applied at the ghost cells $x = x_1, x_{N_g+1}$ and are given by $T^{n+1}_1 = T^{n+1}_2$ and $T^{n+1}_{N_g+1} = T^{n+1}_{N_g}$. For complete reactions in the adiabatic case (i.e., $\Psi_{q_k} = 0$), the temperature in the region $0 \leq x \leq L_B$ will be approximately equal to the adiabatic temperature calculated in the homogeneous GLR model. Note that reactants are always in stoichiometric quantities in all comparisons.

The stability condition is given by,

$$\Delta t^{\tilde{n}+1} \leq \frac{1}{2} CFL \cdot \frac{\left(\frac{\Delta x}{2}\right)^2}{\max_j \left(\bar{\kappa}^n_j\right)}. \tag{4.60}$$

4.4.6 Contact Site Description

A contact site from statistical volume element (SVE) or 2D domain in the RAVEN code [4] is converted to the current model representation as shown in Figure (26). The model is 1D and the temperature is transferred from the node x_i.

Figure (26(a)) is the contact site in a 2D mesoscale reaction model domain with the finite difference grid. The grid size is chosen to be approximately half the size of the

contact site in the reaction model. Smaller grids are employed in the RAVEN code. A statistical volume element in the RAVEN code is the two dimensional representation of the mixture. Granules in the mixture are located based on the nearest neighbor distribution obtained from experiments [4]. The mesoscale model grid spacing is one to ten times smaller than the diameter of the granules, which can range from hundreds of nanometers to microns in the current study. Therefore, the mass m_k for the k^{th} contact site is much larger than the mass of material m_{ij} contained within a cell area $A_{ij} = \Delta x^2$ with unit depth on the uniform mesoscale reaction model grid. The contact sites are idealized to have cylindrical geometry centered at a node x_i, y_j contained within the cell outlined in the dashed lines.

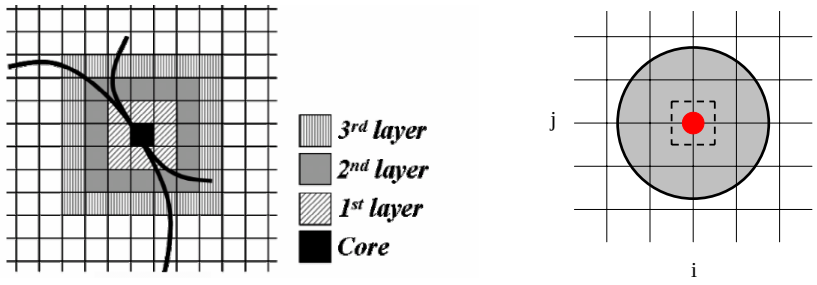

(a) Contact site from SVE

(b) Schematic of idealized contact site

Figure 26: Contact site from SVE is converted to a homogeneous representation.

Displacement reactions are assumed in the product formation zone according to the Wagner mechanism [115] (shown in Figure (2)) for two reasons. Displacement reactions are reactions in which reactants remain separate from the products (unmixed). First, the rate determining diffusion process involves the transport of a single reactant through one of the product constituents (solid or liquid phase), for example reactant A is transported through product C. This occurs when the diffusion activation energy for reactant A in product C is much lower than for any other reactant through the products. The reactant and product may be in liquid or solid state. Second, the Wagner mechanism has been observed [122] for a reaction similar to the thermite

reaction, namely $Fe + Cu_2O \rightarrow FeO + Cu$, in which diffusion of the Fe^{2+} cations were found to determine the rate of the reaction. Generally, the Wagner mechanism is an assumed model to predict the rate-determining mass transport mechanism. The mass is assumed to separate as shown schematically in Figure (2).

The Wagner mechanism [115] is a displacement mechanism used for reaction modeling. This model describes the mixture of two or more constituents separating in the parallel direction of the material flow.

Transport of reactant A through the product layer as depicted in Figure (25) determines the amount of reactants at the reaction surface. Therefore, reactions do not occur at the $A - C$ interface. The product layer assumption holds for both solid and liquid phases. However, in this thesis, liquid products are assumed since the adiabatic temperature from the heat of reaction exceeds the melting temperature of the reactants. The velocity of the diffusion and reaction surfaces are denoted V^a and V^b, respectively.

Summary of the reaction model:

1. The reaction model consists of a granular reaction model and a mesoscale reaction model.

2. The granular reaction model simulates chemical reactions between a solid and liquid. Temperature and pressure are included in the activation energy with affects both the mass transport and the chemical reaction at a surface.

3. The mesoscale reaction model is based on the RAVEN code statistical distributions for contact site location, amount of reactants, temperature, pressure, and contact length between reactants. This model uses the granular level reaction and simulates the heat transport between contact sites.

4.4.7 Granular Level Reaction

For the $2Al + Fe_2O_3$ thermite reaction, we consider the following transition state [88] with the one-step reaction mechanism:

$$\begin{aligned} &2Al + Fe_2O_3 \rightarrow AlO + 2Fe_2O + Al \ - \ Heat \\ &AlO + 2Fe_2O + Al \rightarrow 1/3Al_2O_3 + 1/2FeAl_2O_4 + 1/3Al + 3/2Fe \ + \ Heat \end{aligned} . \tag{4.61}$$

The products Al_2O_3, $FeAl_2O_4$, Al, and Fe are assumed to form between the reactants and displace according to the Wagner mechanism. Fan et al. [41] suggest that diffusion of Al in $FeAl_2O_4$ with an activation energy ΔG_{D_o} of $162kJ/mol$ [55] is the rate controlling mechanism (see equation (4.38)). Therefore we assume that the rate determining mass transport process is the Al through the $FeAl_2O_4$. From Figure (25), we have $A = Al$, $B = Fe_2O_3$, and $C = FeAl_2O_4$ for the thermite reaction. The hydrostatic case is considered, i.e., $D(T, P)$, with homobaric pressure P defined for $0 \leq x \leq L_B$.

Experimentally measured shock temperatures are reported in the range of $2700K - 3400K$ for the porous thermite system $2Al + Fe_2O_3$ by Boslough [20]. The powder contains Al and Fe_2O_3 with mean granule sizes of $\leq 1\mu m$ and $\leq 0.3\mu m$, respectively. Therefore, the Fe_2O_3 length $L_B = 150nm$ is estimated by the radius of the mean granule diameter. The approximately stoichiometric mixture is hot pressed to contain $\sim 50\%$ voids and fired from a gas-gun at velocities of $1.1183km/s$ and $1.293km/s$ into a LiF window. Time resolved temperatures are obtained from pyrometry measurements. Thermal equilibration in the fine grained powder is estimated to occur within $\sim 100ns$, which is suggested by Boslough to be the upper bound to the time that reactions take place.

Transition state:

The transition state ($AlO + 2Fe_2O + Al$) is identified based on energy considerations discussed above [88]. The various transition states considered with corresponding free

Table 3: Reaction energies (P^o, T) for the thermite reaction (4.61) per one mole of reactants, i.e., $2/3Al + 1/3Fe_2O_3$.

Energy;[ab] (kJ/mol)	A_0 (kJ/mol)	A_1 $(kJ/mol \cdot K)$	A_2 $(kJ/mol \cdot K^2)$
${}^{+}\Delta\mu^o$	$-2.617E2$	$-6.868E-2$	$-28.11E-6$
${}^{tr}\Delta\mu^o$	$-1.461E2$	$-1.317E-1$	$-29.37E-6$
${}^{-}\Delta\mu^o$	$-5.054E2$	$-3.708E-2$	$-1.933E-5$
${}^{+}\Delta\mu_a$	$1.156E2$	$-6.306E-2$	$-1.264E-6$

[a] 2^{nd} order least squares fit to Gibbs free energy [1] with residual $R^2 \geq 0.9992$

[b] $P^o = 1atm$ is the reference pressure and $\leq T \leq 3000K$.

energies are given by Narayanan [88]. The products formed in equation (4.61) are taken from the experimental observations by Fan et al. [41]. Their study shows formation of Al_2O_3 and $FeAl_2O_4$ from X-ray diffraction (XRD) of the reacted thermite mixture. Analysis of the differential scanning calorimetry (DSC) data resulted in an activation energy of $145kJ/mol$ for the thermite reaction $8Al + 3Fe_2O_3$ (at ambient pressure). This compares well with the transition state energy barrier and heat of formation as a function of temperature obtained from [1]. A second order polynomial least squares fit in the form $\Delta\mu(T) = A_0 + A_1T + A_2T^2$ was obtained and the coefficients are given in Table (3). For the contribution from equation (4.23), the pressure P is assumed to be constant for all reactants, transition state, and products. This assumption is based on the observations for the reactants by Austin [4], in which pressure nearly equilibrates within a few granules downstream of the shock front. Once reaction begins, pressures are not equilibrated, however, mechanical equilibrium is assumed to occur much faster than mass transport.

Reaction kinetics:

For lack of experimental evidence, the parameters in equation (4.18) follow the traditional Arrhenius form. Therefore, $\beta = \eta = 0$, $f(1-\alpha) = 1$, and $\tau_\Theta = 0$ for

the heterogeneous GLR model calculations. Pressure and temperature dependencies are only included through the assumed transition state. The remaining unknown parameters are ${}^{+}A$ and ${}^{-}A$.

Material parameters:

The diffusion activation energy of $162kJ/mol$ reported by Fan et al. [41] could not be found in the cited reference [55]. However, Fe diffusion into $FeAl_2O_4$ was found to have an activation energy of $273kJ/mol$ [55]. In this study, the energy is conservatively assumed to be $273kJ/mol$ with corresponding diffusion constant $D_o = 3.15 \times 10^{-4} m^2/s$ calibrated at $T = 1470K$. To obtain increased accuracy, additional experimental data is required to calculate the constant $D_o(T)$ and the diffusion activation energy $\Delta\mu_{D_o}$ for $800K < T < 3000K$. The constituent heat capacity $c_{vp}(T)$ values [1] for the temperature range $T = [300, 3000]K$ are least squares fit to piecewise fourth order polynomials with residuals $R^2 \geq 0.98$. The chemical reaction relaxation times $\tau_\Theta = 0, 10, 100ns$ are studied here based on the concept that chemical reactions are delayed by approximately $100ns$ [78]. Remaining material properties are given in Table (7). Constituent densities, thermal conductivity, melting temperatures are taken from [11, 4] unless otherwise specified. Properties are assumed to be the same for both solid and liquid phases except for the density of melted Al, which is assumed to be $2380kg\ m^{-3}$. The density for $FeAl_2O_4$ is obtained from [117]. The density for AlO is estimated to be equal to the density of Al_2O_3 and the density $5700kg\ m^{-3}$ is estimated for Fe_2O [106].

Initial and boundary conditions:

The initial temperature distribution and pressure is obtained from Raven code results, reported by Austin [5], for the mixture containing $Al + Fe_2O_3$ + 20 wt.% epoxy and 2% voids. The granule diameters are $0.30\mu m$ for Al and $0.10\mu m$ for Fe_2O_3. For an imposed granule velocity $V_p = 1km\ sec^{-1}$, the stationary pressure is $P \cong 10GPa$ and the average hot spot temperature is $T_{hs} \cong 1400K$. Although the pressure is twice

Table 4: Material properties for the reactants in the $2Al + Fe_2O_3$ system in stoichiometric quantities given by equation (4.61). Properties are assumed to be the same for both solid and liquid phases.

Property	Units	Al	Fe_2O_3	Al_2O_3	$FeAl_2O_4$
Molar mass, M	$g\ mol^{-1}$	26.98	159.7	102.0	173.8
Initial volume fractions, ξ_o	–	0.428	0.572	0	0
Density, ρ	$kg\ m^{-3}$	2700	5274	5274	2960
Thermal conductivity, k_q	$W\ m^{-1}K^{-1}$	210	5	35	4[a]
Melting temperature, T_m	K	926	1780	–	–
Latent heat of melting, ΔH_m	$kJ\ kg^{-1}$	390	600[b]	–	–

[a] Estimated from [108].
[b] Estimated from survey of oxides [106].

that of Boslough's experiments, the mixture temperature $T_b \cong 800K$ is approximately $200K$ lower than is calculated for the 50% porous mixture [20] since the work done by void collapse in the 2% mixture is much smaller. Therefore, the contact site temperatures $T_b = 800K$ and $T_{hs} = 1400K$ are employed to estimate the initial conditions between contact sites in Boslough's experiments.

The pressure in the granular mixture [5] equilibrates within approximately $5ns$ to $10ns$, therefore, the pressure gradients are neglected in this case study. Reactions at the surface occur on the order of fempto seconds, thus, pressure gradients affect the reaction kinetics. This is neglected in the current study since these affects are assumed to be small compared to the concentration gradient. At time $t > 0$ downstream of the shock front, the initial pressure P_o is assumed to be stationary until relaxation begins at time $t = t_P$. For demonstration purposes, pressure decreases to $P = 0$ during the relaxation time τ_P is given by,

$$P(t) = P_o \left[1 - (t - t_P)^2 / \tau_P^2\right], \quad t_P < t \leq t_P + \tau_P. \tag{4.62}$$

The adiabatic condition is assumed. For all models, heat is not dissipated to the surroundings. This assumption permits an equal comparison between these two models.

4.5 Thermite System Case Study

4.5.1 Granular Level Reaction Analysis

The *Al* concentration along the x-coordinate in the product layer (see Figure (25)) is shown for various times during a reaction in Figure (27). Reaction nearly stops after time $t = t_P$ since the mass-transport strongly depends on the pressure contribution (see Figure (28)). Although the temperature exceeds $2000K$, the thermal contribution alone is not sufficient to propagate the reaction. Values for the pressure relaxation in equation (4.62), $t_P = 804ns$ and $\tau_P = 100ns$, have been selected to approximate temperatures observed in Boslough's experiments [20]. The pressure relaxes to zero within $340ns$ in this case study, however, even much smaller decreases in pressure will yield similar partial reactions as are demonstrated in this study. This pressure relaxation is estimated such that the resulting reaction is consistent with experimental observations [20].

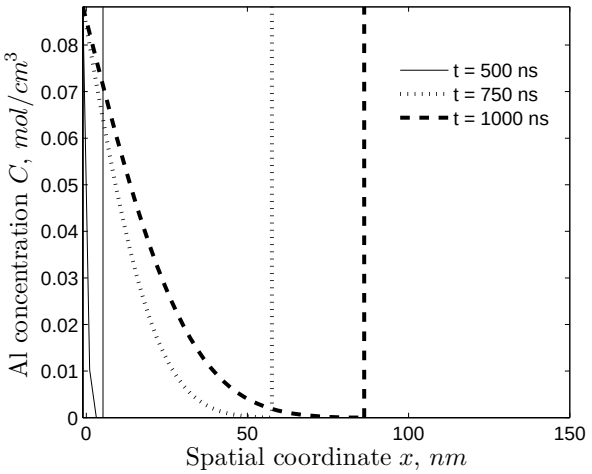

Figure 27: 1D *Al* transport through the product layer in the heterogeneous GLR model. Vertical lines represent $x = s(t)$ at times t in *nanoseconds (ns)*, for the case: $L_B = 150nm$, ${}^{+}A_{)} = {}^{-}A_0 = 1000$, $T_b = 800K$, $T_{hs} = 1400K$, $P_o = 3.9GPa$, $t_P = 240ns$, and $\tau_P = 100ns$.

Time history for the mixture average temperature T corresponding to the ensemble in equation (4.50) is shown in Figure (28). Two values for the forward reaction

rate are given to demonstrate the rate dependence for Boslough's experiments #2274 ($P_o = 4.4GPa$) and #2279 ($P_o = 3.9GPa$) [20]. For the case in which $A_0 = 1000$ and $P_o = 4.4GPa$, complete reaction occurs and the mixture temperature is $T = 3276K$. This is lower than the estimated $4000K$ [20] since the heat of melting is included in the present study. The reaction extent is 72% when $A_0 = 1000$, $P_o = 3.9GPa$, and the pressure relaxation time $t_P = 804ns$ is estimated such that the temperature approximates the experimentally measured temperature of $2550K$.

When $A_0 = 1000$ and $P_o = 3.9GPa$, only .4% reaction occurs with a temperature of $920K$, much less than the experimentally estimated value of $2700K$; the reaction extent is 72% (calculated from the simulation). The pressure contribution determines the extent of reaction and the pre-exponential factor ${}^{+}A_o$ determines initial reaction rate.

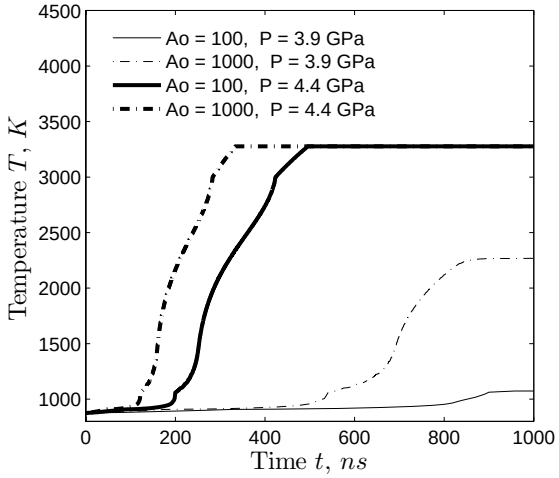

Figure 28: Heterogeneous GLR model, $L_B = 150nm$, ${}^{-}A_0 = 0$, $T_b = 800K$, $T_{hs} = 1400K$, $t_P = 240ns$, and $\tau_P = 100ns$.

The reaction rate in the equilibrium homogeneous model is exponentially dependent on the mixture temperature T (see equation (4.19)). The use of $\tau_\Theta \simeq 100ns$ delays the onset of the reaction. However, τ_Θ and ${}^{+}A_0$ are not independent parameters as shown in Figure (29) for the cases ${}^{+}A_0 = 10, \tau_\Theta = 0$ and ${}^{+}A_0 = 100, \tau_\Theta = 100ns$. Regardless of the values for ${}^{+}A_0$ and τ_Θ, reactions always proceed to completion if

heat is not dissipated from the mixture.

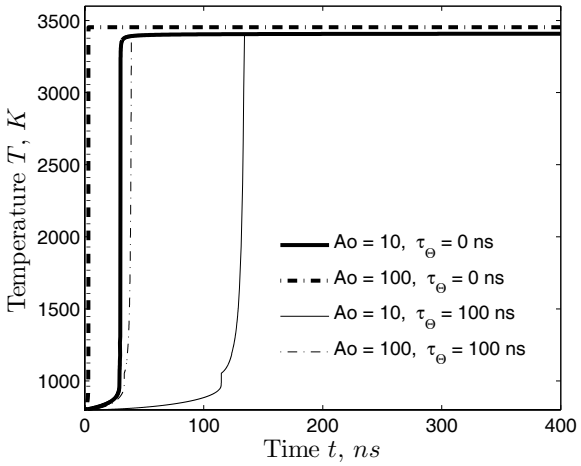

Figure 29: Homogeneous GLR model, $P = 0$, ${}^{-}A_0 = 0$, $T(t = 0) = T_b = 800K$.

The heterogeneous and homogeneous GLR models are compared in Figure (35). Both models, presented in this thesis, use the pressure dependent activation energy from equations (4.22-4.23) for the reaction in equation (4.61). The reaction rate decreases for increases in pressure since $\Delta\mu_\sigma > 0$ for $P > 0$ in the thermite reaction in equation (4.61). Figure (35) shows that the homogeneous reaction rate increases only after pressure nearly relaxes to zero. For the heterogeneous GLR model, $\sum_i V_i < 0$ for the diffusion process $Al \rightarrow FeAl_2O_4$, thus mass transport of Al to the reaction surface increases. Therefore, the overall reaction rate in the heterogeneous reaction increases as the pressure increases.

In the heterogeneous GLR model, an increase in ${}^{-}A_0$ significantly reduces the rate of reaction as demonstrated in Figure (35). As mentioned earlier, the reverse reaction in the homogeneous GLR model (see equations (4.18)-(4.19)) has very little effect as shown in Figure (35) when ${}^{-}A_0$ is within a few orders of magnitude of ${}^{+}A_0 = 0$.

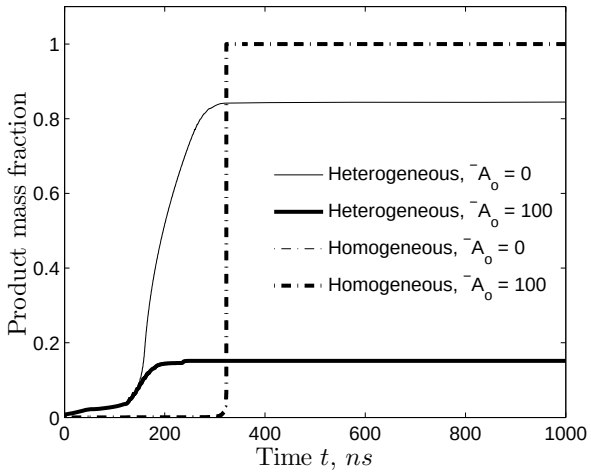

Figure 30: Product formation from heterogeneous media and homogeneous media GLR models, $L_B = 150nm$, $^{+}A_0 = 1000$, $T(t = 0) = T_b = 800K$, $T_{hs} = 1400K$, $P_o = 4.4GPa$, $t_P = 240ns$, $\tau_P = 100ns$, and $\tau_\Theta = 0$. For the homogeneous reaction, the curves for $^{-}A_0 = 0$ and $^{-}A_0 = 100$ are overlapping.

4.6 $Ni + Al$ System Case Study

4.6.1 Granular Level Reaction Model

Estimated contact site and hot spot distributions, hot spot temperatures, contact length, area, and pressure are summarized for the case study in Table (5). These parameters are obtained from the RAVEN code.

Table 5: Distribution parameters at $t = 4ns$ for $Ni + Al$ with granule velocity $U_p = 1km\ s^{-1}$

Distribution (units)	Type	μ	σ
Contact site $NN1$ location (μm), NN_{cs}	N	1.1	.25
Hot spot $NN1$ location (μm), NN_{hs}	N	2.0	1.0
Hot spot temperature (K), T	Log-N	1400	200
Contact length (μm), CL	Log-N	0.1	.05
Contact site area (μm^2), A	Log-N	0.1	.05
Contact site pressure (GPa), P	Log-N	2.81	1.0

Transition state:

The transition state ($Ni_{(s)} + 3Al_{(l)}$) at zero pressure is identified based on energy considerations discussed in [88]. The various transition states considered with corresponding free energies are given by Narayanan [88]. The transition state energy

barrier and heat of formation as a function of temperature are obtained from [1]. A second order polynomial least squares fit in the form $\Delta\mu(T) = A_0 + A_1 T + A_2 T^2$ was obtained and the coefficients are given in Table (6). The quantity ${}^{+}\Delta\mu^o$ is from equation (4.23) and represents the heat of formation. The pressure P is assumed to be constant for all reactants, transition state, and products.

Table 6: Reaction energies $\Delta\mu(P^o, T) = A_0 + A_1 T + A_2 T^2$ for the reaction containing $Ni + 3Al$ per one mole of reactants, i.e., $3/4Al + 1/4Ni$.

Energy[ab] (kJ/mol)	A_0 (kJ/mol)	A_1 $(kJ/mol \cdot K)$	A_2 $(kJ/mol \cdot K^2)$
${}^{+}\Delta\mu^o$	$-7.690E-3$	$-5.209E1$	$1.426E4$
${}^{tr}\Delta\mu^o$	$-7.639E-3$	$-6.026E1$	$2.194E4$
${}^{-}\Delta\mu^o$	$-6.927E-3$	$-4.934E1$	$-2.456E4$
${}^{+}\Delta\mu_a$	$5.116E-5$	$-8.167E0$	$7.672E3$
${}^{-}\Delta\mu_a$	$-7.119E-4$	$-1.092E1$	$4.650E4$

[a] 2^{nd} order least squares fit to Gibbs free energy [1] with residual $R^2 \geq 0.9992$.
[b] $P^o = 1atm$ is the reference pressure and $\leq T \leq 3000K$.

Reaction kinetics:

Parameters $\beta = \eta = 0$, $f(1-\alpha) = 1$, and $\tau_\Theta = 0$ are for the heterogeneous media GLR model calculations. Pressure and temperature dependencies are only included through the transition state. The remaining unknown parameters are ${}^{+}A_0$, ${}^{-}A_0$.

In the surface reaction, we assume that δ is small compared to the reactant granule diameters $0.1 - 1\mu m$. The value $\delta = 1nm$ is selected in this study since transport to the surface is dominated by the transport of reactant A in the mixture containing the products.

Material parameters:

The interdiffusion material parameters are obtained from available experimental results [58]. The diffusion parameter is estimated as $D_0 = 2.26 \times 10^{-6} m^2 s^{-1}$ from [58]. The activation energy is estimated as $\Delta\mu_{Do} = 273kJ/mol$ from the results of a similar system studied by Fan et al. [41]. This is considered to be a high estimate [100]. The

remaining parameters and material composition are summarized in Table (7).

Table 7: Material parameters for the constituents in the $Ni+Al+20wt.\%EPON828$ system with the reaction containing $Ni + 3Al$.

Property	$Al_{(s)}$	$Ni_{(s)}$	$Al_{(l)}$	$Al_3Ni_{(l)}$	Epon828	Units
Molar mass, M	26.98	58.59	26.98	139.6	–	$kg/kmol$
Stoich. coeff., ν	-3	-1	–	1	–	–
Initial vol. frac., ξ_o	0.46	0.10	0	0	0.44	–
Density, ρ	2700	8909	2380	3368	1200	kg/m^3
Conductivity, k_q	222	90.7	222	189	0.2	$W/m \cdot K$
Melting temp., T_m	926	1728	–	–	533	K

Initial and boundary conditions:

The granule diameters are approximately $25\mu m$ for both Al and Ni granules. For an imposed granule velocity $V_p = 1km\ sec{-}1$, the stationary pressure is $P \cong 5GPa$ and the average hot spot temperature is $T_{hs} \cong 1400K$ (estimated from RAVEN simulations as described in Appendix (B)). Although the pressure is twice that of Boslough's experiments, the mixture temperature $T_b \cong 800K$ is approximately $200K$ lower than the value that is calculated for the 50% void mixture [20] since the work done by void collapse in the 2% void mixture is much smaller than in the 50% void mixture. Therefore, the contact site temperatures $T_b = 800K$ and $T_{hs} = 1400K$ are employed to estimate the initial conditions between contact sites in Boslough's experiments.

The pressure in the granular mixture equilibrates within approximately $\hat{\tau} \approx 5 - 10ns$, where $\hat{\tau}$ is the time required for pressure to equilibrate. Reactions on the order of microseconds are considered. Therefore, the pressure gradients are neglected in the case study. At time $t > 0$ downstream of the shock front, the initial pressure P_o is assumed to be stationary until relaxation begins at time $t = t_P$. The stationary assumption is based on observations in RAVEN code simulations [4]. Pressures are expected not to be in equilibrium during chemical reactions. As mentioned previously, these pressure gradients are assumed to be small compared to the effect

of the concentration gradient with forced diffusion. For demonstration purposes, the pressure decreases to $P = 0$ during the relaxation time τ_P and is given by equation (4.62).

The adiabatic condition is assumed for both the heterogeneous media-based GLR model, heat is not dissipated to the surroundings. This assumption permits a comparison between these two models. The numerical solution for both the heterogeneous and homogeneous media-based GLR models is obtained from the finite difference method summarized as,

$$\begin{aligned} C_j^{n+1} &= C_j^n + \tfrac{\Delta t^n \cdot D_{Al}^n(T_j,P_j)}{\Delta x^2}\left[C_{j+1}^n - 2C_j^n + C_{j-1}^n\right] \\ C_{jI}^{n+1} &= C_{jI}^n + \tfrac{2\Delta t^n}{\Delta x + \Delta x_{jI}}\left(-\tfrac{\Theta}{v_{Al}} - D_{Al}^n(T_j,P_j)\left[\tfrac{C_{jI}^n - C_{jI-1}^n}{\Delta x_{jI-1/2}}\right]\right) \\ \Delta t^{n+1} &\leq \min\left[\tfrac{1}{2}\tfrac{\left(\frac{\Delta x}{2}\right)^2}{\max_j\left(D_{Al}^n(T_j,P_j)^n\right)}, \tfrac{\Delta x}{2}\tfrac{1}{\frac{\partial s^n}{\partial t}}\right]. \end{aligned} \tag{4.63}$$

4.6.2 Granular Level Reaction Analysis

We compare the heterogeneous media-based GLR model to the homogeneous media-based GLR model in equation (4.18) in Figures (31(a)-31(b)). All reactants are in stoichiometric quantities. For the heterogeneous media-based model, initial temperature is given by equation (4.53) with $T_{hs} = 1400K, T_b = 800K$. The homogeneous media-based model is assumed to initially have the temperature $T_b = 800K$. The heterogeneous and homogeneous media-based models are given adiabatic boundary conditions (no heat losses to the environment). Both models have the pressure dependent activation energy from equations (4.22)-(4.23) for the the reaction in equation (4.61).

Homogeneous media-based GLR model:

This model is defined by equations (4.18) and (4.19). The assumption is that a mixture containing the reactants is described by a single rate equation. Therefore, there is no explicit spatial representation. This model has been applied to shock

induced chemical reactions by [11, 33, 34, 78, 88]. This model is described here as a homogeneous model since a homogeneous mixture representation is employed. Homogeneous is defined as "of uniform structure or composition throughout" [3].

The reaction rate in the equilibrium ($\tau_\Theta = 0$) homogeneous media-based model is exponentially dependent on the mixture temperature $\bar{T}$. The relaxation time, $\tau_\Theta \simeq 100ns$, delays the onset of the reaction. Figure (31(a)) shows this trend for different frequency factors. As A_o increases, the reaction rate increases. However, changes in the frequency factor have a much more significant effect for this reaction.

Heterogeneous media-based GLR model:

Reaction rate depends strongly on temperature $\hat{T}$ and pressure P in the GLR model as shown in Figures (31(b)). As in the homogeneous media-based model, the surface reaction in the GLR model decreases due to increases in pressure. However, $\sum_i V_i < 0$ for the diffusion process $Al \rightarrow Al_3Ni_{(l)}$, thus diffusion increases the concentration of Al reactant at the surface which increases the reaction rate. This is a calculated value, no assumptions are made. When the reaction is limited by diffusion, the reaction rate is relatively insensitive to changes in the frequency factor A_o.

Granule size effects are demonstrated in Figure (31(b)). The diameter of the Ni granule is $D = 0.3, 0.5\mu m$, with a stoichiometric quantity of Al in both cases. Figure (31(b)) shows that the reaction rate of the adiabatic granule system increases with smaller granule size. The reaction process is initially independent of the granule size, thus, the heat from reaction is also initially independent of the granule size. As the granule size decreases, the temperature $\hat{T}$ increases faster since mass is transported over a shorter distance to complete the reaction. In contrast, the homogeneous model is insensitive to granule size.

A sensitivity study for the additional stress term μ_σ in equation (4.23) is shown in Figure (32). As pressure increases, initiation occurs. Reaction propagation is faster with further increases in pressure.

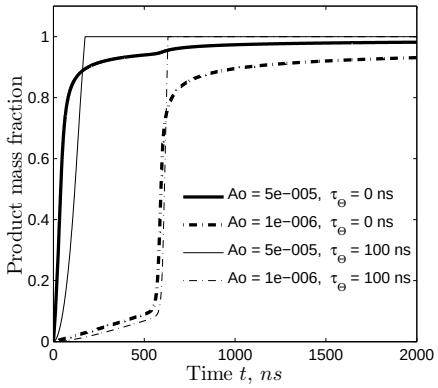

(a) Homogeneous GLR model, $P = 3GPa$.

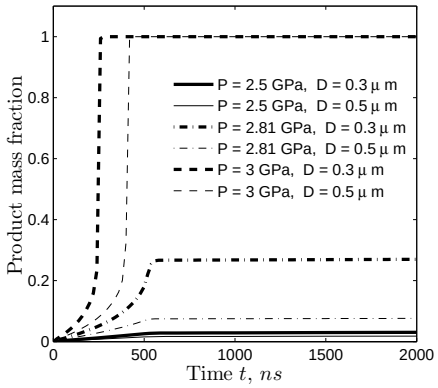

(b) Heterogeneous GLR model.

Figure 31: Comparison of chemical reaction models under adiabatic conditions.

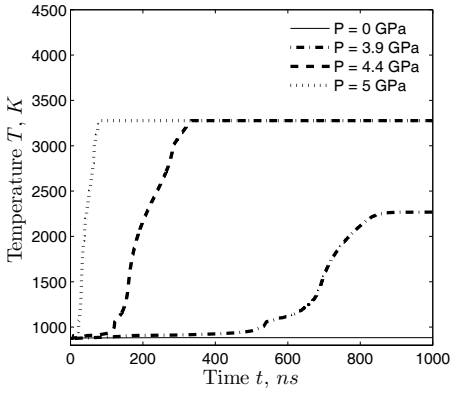

Figure 32: Heterogeneous GLR model shown with various pressures under adiabatic conditions.

4.7 Mesoscale Reaction

Granular Level Chemical Reactions:

The granular level reaction model physically represents the material transport on the granule length scale. Initial temperature, pressure, and amount of constituents at the contact sites from RAVEN code results are incorporated into the granular level model. Since the temperature in the granular level reaction is linked to the mesoscale simulation, the reaction rate depends on heat released by neighboring contact site reactions during shock induced chemical reactions.

Heterogeneous and homogenous granular level reaction models contain different mechanisms to describe reaction kinetics in the mixture. The Wagner model is an ideal mechanism employed in this study to describe the assumed displacement reactions with a rate-determining step. However, the true mechanisms in ultra-fast reactions in metal powders have not yet been determined through experiments. Alternative displacement reaction mechanisms may be incorporated with corresponding spatially dependent diffusion coefficient and activation energy.

Mesoscale Reactions:

A mesoscale chemical reaction model is used to bridge the heterogeneous media GLR model to the continuum model. Initial conditions for the granular level reaction are specified by RAVEN code statistical distributions at each reactant contact site. The mesoscale reaction model contains many of these contact sites and provides the non-equilibrium temperature distribution that is initialized based on RAVEN code statistical distributions. Reaction evolution may proceed in many ways depending on 1) the distribution of contact sites (related to granule sizes and binder content) and 2) the temperature and state of stress at the contact sites (related to particle velocty/shock velocity, plastic flow, pore collapse, and morphology). The resulting macro-scale continuum reaction is given by the averages taken from the mesoscale reaction model and accounts for reaction initiation, propagation, and extent with

only three unknown material parameters, ${}^{+}A_o, {}^{-}A_o, \tau_p$ (forward and reverse Arrhenius constant and relaxation time).

Chapter V

1-D CHEMICAL REACTIONS: NUMERICAL SIMULATIONS

The gas-gun experiment is simulated by incorporating the constitutive and chemical reaction sub-models into a numerical solution of the conservation equations (see Figure (5)). The original contribution here is the algorithm for solving the gas-gun simulation and the mixture 2D model with results for a Taylor test simulation.

The MATLAB codes developed for the following 1D and 2D simulations are given in Appendix (G) and (H), respectively.

5.1 Summary of Equations

For the 1D strain model with heterogeneous media-based chemical reactions, the following equations, p+43 equations and p+43 unknowns, are used:

$$\frac{\partial}{\partial t}\left(\bar{\rho}\right)+\nabla\left(\bar{\rho}\bar{\mathbf{v}}\right)=0 \tag{5.1a}$$

$$\frac{\partial}{\partial t}\left(\phi_p\bar{\rho}_p\right)+\nabla\left(\phi_p\bar{\rho}\bar{\mathbf{v}}\right)=\Psi_{massp} \tag{5.1b}$$

$$\Psi_{massp}=\Theta M_p\nu_p \tag{5.1c}$$

$$\bar{\Psi}_{k,LM}=\sum_p\Psi_{massp}\bar{\mathrm{v}}_k\ \ ;\ \ \bar{\Psi}_{k,AM}=\sum_p\Psi_{massp}\mathbf{e}_{ijk}x_j\bar{\mathrm{v}}_k \tag{5.1d}$$

$$\frac{\partial}{\partial t}\left(\bar{\rho}\bar{\mathrm{v}}_k\right)+\frac{\partial}{\partial x_k}\left(\bar{\rho}{\bar{\mathrm{v}}_k}^2\right)-\frac{\partial}{\partial x_k}\left(\bar{\sigma}_{kj}\right)=\bar{\rho}\bar{f}_k+\bar{\Psi}_{k,LM} \tag{5.1e}$$

$$\frac{\partial}{\partial t}\left(\bar{\rho}\mathbf{e}_{ijk}x_j\bar{\mathrm{v}}_k\right)+\frac{\partial}{\partial x_k}\left(\bar{\rho}\mathbf{e}_{ijk}x_j\bar{\mathrm{v}}_k^2\right)-\frac{\partial}{\partial x_k}\left(\mathbf{e}_{imn}x_m\bar{\sigma}_{nk}\right)=\bar{\rho}\mathbf{e}_{ijk}x_j\bar{f}_k+\bar{\Psi}_{k,AM} \tag{5.1f}$$

$$\tau_{\Theta k}\dot{\Theta}_k+\Theta_k={}^{+}k_k\prod_{i=1}^{{}^{+}N_{sk}}\left[C_i\right]^{{}^{+}\nu_{ik}}-{}^{-}k_k\prod_{i=1}^{{}^{-}N_{sk}}\left[C_i\right]^{{}^{-}\nu_{ik}} \tag{5.1g}$$

$${}^{+}k_k={}^{+}A_k\ T^{{}^{+}\beta_k}\ P^{{}^{+}\eta_k}\ {}^{+}f_k(1-\varphi)\exp\left\{-\frac{\Delta^{+}\mu_{ak}}{RT}\right\} \tag{5.1h}$$

$$\Theta=kC_A^{\nu_A}C_B^{\nu_B} \tag{5.1i}$$

$$k=A_o\exp\left(\frac{-\Delta\mu_a(T,\boldsymbol{\sigma})}{RT}\right) \tag{5.1j}$$

$$J_A=\left(D_A\frac{\partial C_A}{\partial x}\right)_{x=s(t)}=\frac{\Theta}{\nu_A}=C'_A\frac{\partial s}{\partial t} \tag{5.1k}$$

$$C'_A=\frac{-\beta_A+\sqrt{\beta_A^2+4{}^{+}k_1C_B^{\nu_B}(\beta_AC_A+{}^{-}k_1C_C^{\prime\nu_C})}}{2{}^{+}k_1C_B^{\nu_B}} \tag{5.1l}$$

$$\frac{\partial C_A}{\partial t}=D_A(T,\boldsymbol{\sigma})\nabla^2C_A+\nabla\mathbf{v}_AC_A \tag{5.1m}$$

$$\Delta\mu_D(\boldsymbol{\sigma})=\Delta\mu_{Do}+\Delta\mu_\sigma \tag{5.1n}$$

$$D(T,\boldsymbol{\sigma})=D_o\exp\left(\frac{-\Delta\mu_D(\boldsymbol{\sigma})}{RT}\right) \tag{5.1o}$$

$$\Psi_S=\sum_{k=1}^{N_r}\sum_{i=1}^{2}\dot{\phi}_{ik}\cdot\left[{}^{-}\Delta\mu_k^o(P^o,\bar{T})-{}^{+}\Delta\mu_k^o(P^o,\bar{T})\right] \tag{5.1p}$$

$$\bar{\vec{q}}=-\bar{k}_q\nabla\bar{T}+\bar{C}_v\bar{\rho}\bar{\vec{\mathrm{v}}}\bar{T} \tag{5.1q}$$

$$\frac{\partial\left(\rho c_pT\right)}{\partial t}-\nabla\cdot\left(\bar{k}_q\nabla T\right)=S_q \tag{5.1r}$$

$$P=\frac{\beta_{T_o}}{\beta'_{T_o}}\left[\left(\frac{\rho}{\rho_o}\right)^{\beta'_{T_o}}-1\right]+C_v\Gamma_M\rho_o\left(T-T_o\right) \tag{5.1s}$$

$$\tau_u = \alpha_i \mu(T) b \sqrt{\hat{\rho}} \tag{5.2a}$$

$$\mu(T) = \mu_o \left[1 - \frac{T}{T_m} \exp\left\{ \theta_* \left(1 - \frac{T_m}{T} \right) \right\} \right] \tag{5.2b}$$

$$\tau^* = \tau_0^* \left(\hat{\rho} \right) \left[1 - \left\{ \frac{kT}{\Delta G_0} \ln \left(\frac{v_0 \left(\hat{\rho} \right)}{\dot{\bar{\gamma}}^p} \right) \right\}^{1/q} \right]^{1/p} \tag{5.2c}$$

$$\frac{\partial \hat{\rho}}{\partial \dot{\bar{\gamma}}^p} = M_{II} \left(\dot{\bar{\gamma}}^p \right) - k_a \left(\dot{\bar{\gamma}}^p, T \right) \left[\hat{\rho} - \hat{\rho}_0 \right] \tag{5.2d}$$

$$k_a \left(\dot{\bar{\gamma}}^p, T \right) = k_o \left(\frac{\dot{\bar{\gamma}}^p}{\dot{\gamma}_0} \right)^{-2 m_0 T} \tag{5.2e}$$

$$\dot{\epsilon} = \dot{\epsilon}_0 \exp \left[\frac{\Delta G \left(\sigma_t / \hat{\sigma}_t \right)}{kT} \right] \tag{5.2f}$$

$$\sigma = \sigma_a + \left[\left(s_I \left(\dot{\epsilon}, T \right) \hat{\sigma}_I \right)^n + \left(s_\epsilon \left(\dot{\epsilon}, T \right) \hat{\sigma}_\epsilon \right)^n \right]^{1/n} \tag{5.2g}$$

$$s_i = \left(1 - \left[\frac{kT}{g_{oi} \mu(T) b^3} \ln \frac{\dot{\epsilon}_{0i}}{\dot{\epsilon}} \right]^{1/q_i} \right)^{1/p_i} \tag{5.2h}$$

$$\frac{d}{d\epsilon} \hat{\sigma}_\epsilon = \theta_0 \left(\dot{\epsilon} \right) \left(1 - \frac{\tanh \left[\frac{2 \hat{\sigma}_\epsilon}{\hat{\sigma}_{\epsilon_s}} \right]}{\tanh(2)} \right) \tag{5.2i}$$

$$\mu(T) = 84.52 - \frac{8.839}{\exp \frac{258}{T} - 1} \quad \{GPa\} \tag{5.2j}$$

$$\dot{r} = \frac{a^2 \dot{a}}{r^2} = \frac{a^2 \dot{a}}{\left(r_o^3 - a_o^3 + a^3 \right)^{2/3}} \tag{5.2k}$$

$$\ddot{r} = \frac{\partial \zeta}{\partial r}, \quad \zeta = \frac{a^2 \ddot{a} + 2 a \dot{a}^2}{r} - \frac{a^4 \dot{a}^2}{2 r^4} \tag{5.2l}$$

$$\frac{\partial \bar{\sigma}_{rr}}{\partial r} + \frac{2}{r} \tilde{\bar{\sigma}} = \bar{\rho}_s \ddot{r} \tag{5.2m}$$

$$\bar{\rho}_s \dot{e} = - \frac{2 \tilde{\bar{\sigma}} \dot{r}}{r} \tag{5.2n}$$

$$\bar{\rho}_s^* = \rho_{min} + C_I \left(\bar{\rho}_s - \rho_{min} \right); \quad 0 \leq C_I \leq 1 \tag{5.2o}$$

$$\dot{\bar{\gamma}} = \sum_p \dot{\gamma}_p \xi_p = 2 \frac{\dot{r}}{r} \tag{5.2p}$$

$$\tilde{\bar{\sigma}} = \bar{Y} (\dot{\gamma}, \bar{T}) \tag{5.2q}$$

$$\bar{Y} = \sum_p \xi_p Y_p^* \tag{5.2r}$$

$$Y_p^* = \frac{1}{1 - \xi_p} \sum_{s \neq p} \mu_{Isp} Y_p \xi_s \tag{5.2s}$$

Equations (5.1-m,n,o,r) and equations (5.2-o,r,s) include new contributions from all other models. The symbols are summarized as follows: ρ is the density, the overbar represents a mixture, t is time, v is velocity, ϕ is the mass fraction, Ψ_{mass} is the mass source term, the subscript p is the phase or constituent, Θ is the reaction rate, M is the molar mass, ν is the stoichiometric coefficient, $\Psi_{k,LM}$ is the linear momentum source term, $\Psi_{k,AM}$ is the angular momentum source term, $\mathbf{e}$ is the alternating tensor, x_i is the spatial location in the x-coordinate, σ is the Cauchy stress tensor, f is the body force or function form of reaction dependence on porosity, τ is the relaxation time, C is the concentration, k is the reaction coefficient, A is the pre-exponential factor or Arrhenius constant, T is temperature, P is pressure, μ is Gibbs free energy, R is the universal gas constant, J is the mass flux, D is the diffusion constant, β is the mass transport coefficient, q is the heat flux, k_q is the heat conduction coefficient, c_p is the heat capacity at constant volume, S_q is the source term for heat generation, $\beta_{T_o} = -V(\partial P/\partial V)|_{T_o}$ is the isothermal bulk modulus at the reference temperature, $\beta'_{T_o} = (\partial\beta/\partial P)|_{T_o}$ is the pressure derivative of the isothermal bulk modulus at the reference temperature, C_v is the specific heat capacity under constant volume, ρ_o is the reference density, Γ_M is a material parameter similar to the Grüneisen parameter Γ, τ_u is the internal (athermal) stress, α_i is the dislocation/obstacle interaction coefficient, μT is the temperature-dependent shear modulus, b is the Burgers vector, $\hat{\rho}$ is the dislocation density, where T_m is the melting temperature, θ_* is a material constant, $\dot{\bar{\gamma}}^p$ is the effective plastic shear strain rate, $\tau_0^*(\hat{\rho}) = \Delta G_0\sqrt{\hat{\rho}}/(ba)$ is the thermally activated part of the threshold stress, $v_0(\hat{\rho}) = f\hat{\rho}v_D b^2$ is the attempt frequency factor at $0K$, k is Boltzmann's constant, ΔG_0 is the activation energy at $0K$, p and q are constants that describe the shape of the energy barrier, $M_{II}(\dot{\bar{\gamma}}^p)$ is the rate-dependent dislocation multiplication term, $\hat{\rho}_0$ is the initial dislocation density, $k_a(\dot{\bar{\gamma}}^p, T)$ is the dislocation annihilation factor, k_o is the anihilation factor at $0K$, m_0 is the strain-hardening rate-sensetivity constant, $\dot{\gamma}_0 = v_0(\hat{\rho})$ is the threshold strain rate, $\hat{\sigma}_t$ is the

mechanical threshold stress, ΔG is the free energy, $\dot{\epsilon}_0$ is a constant, k is Boltzmann's constant, r is the radial coordinate in the spherically symmetric pore collapse model, a is the initial inner radius of the pore, C_I is a material parameter, ρ_{min} is the density of the least dense constituent in the mixture, Y is the yield strength, ξ is the volume fraction, and μ_{Isp} are the friction coefficients between constituents s and p.

5.2 Computational Algorithm

An overview of the implementation is given to clarify the meaning of the theory that has been presented. Solving the systems of equations and supporting material models is performed such that the order of accuracy is consistent. Typically, the equation of state is calculated once per time step where two or more Runge-Kutta steps have been taken to solve the conservation equations [12]. This reduces the computation time significantly. Since the influence of the reaction and phase transitions on the shock velocity are unknown, these quantities are calculated each time the conservation equations are solved as follows:

1. Calculate mixture averaged reaction rate from equation (A.3), Ψ_{massp}^{n+1}. This is done by using the heterogeneous media-based chemical reaction model described in the previous chapter. Results from the RAVEN code are needed for inputs to initialize the mesoscale reaction model. This is used to calculate the new mass fractions, ϕ_p^{n+1}, using equations (A.2). Update the concentrations χ_p using equation (C.2). The inputs are the initial mass fractions, and all of the parameters required from the RAVEN code (described in the previous chapter).

2. Conservation of mass, momentum, and energy are solved to give $\bar{\rho}^{n+1}$, $\bar{\vec{v}}^{n+1}$, $\bar{E}^{n+1}$, where n is denotes the time step.The finite volume equations are given

by,

$$\begin{aligned}
\bar{\rho}^{n}_{j+1/2} &= \tfrac{1}{2}\left[\bar{m}^{nL}_{j+1/2} + \bar{m}^{nR}_{j+1/2}\right] - \tfrac{\alpha^n}{2}\left(\bar{\rho}^{nR}_{j+1/2} - \bar{\rho}^{nL}_{j+1/2}\right) \\
\bar{m}^{n}_{j+1/2} &= \tfrac{1}{2}\left[\bar{m}^{nL}_{j+1/2}\bar{v}^{nL}_{j+1/2} - \bar{\sigma}^{nL}_{j+1/2} + \bar{m}^{nR}_{j+1/2}\bar{v}^{nR}_{j+1/2} - \bar{\sigma}^{nR}_{j+1/2}\right] \\
&\quad -\tfrac{\alpha^n}{2}\left(\bar{m}^{nR}_{j+1/2} - \bar{m}^{nL}_{j+1/2}\right) \\
\bar{E}^{n}_{j+1/2} &= \tfrac{1}{2}\left[\bar{E}^{nL}_{j+1/2}\bar{v}^{nL}_{j+1/2} + \bar{q}^{nL}_{j+1/2} - \bar{\sigma}^{nL}_{j+1/2}\bar{v}^{nL}_{j+1/2} + \bar{E}^{nR}_{j+1/2}\bar{v}^{nR}_{j+1/2}\right. \\
&\quad \left. +\bar{q}^{nR}_{j+1/2} - \bar{\sigma}^{nR}_{j+1/2}\bar{v}^{nR}_{j+1/2}\right] - \tfrac{\alpha^n}{2}\left(\bar{E}^{nR}_{j+1/2} - \bar{E}^{nL}_{j+1/2}\right)
\end{aligned} \tag{5.3}$$

where $m = \rho v$.

3. Use the porous mixture equation of state relationships with $\bar{\rho}^{n+1}$ and $\bar{E}^{n+1}$ to approximately solve Reimann problem at the material interface and the hydrostatic stress at all points in the material. The Reimann problem is given simply by the form,

$$U_t + A(U)_x = 0. \tag{5.4}$$

where the subscripts denote differentiation. This correlates to the conservation of mass and energy and the momentum balance.

4. Return to the *previous* time step deviators, $\sigma^{'n}_{ij}$, the yield surface. Plastic work from this was accounted for when solving the conservation of energy in step 2. With 1D strain, equivalent stress is given by,

$$\sigma_{eq} = \sqrt{\frac{3}{2}\left(\left(\bar{\sigma}'_{xx}\right)^2 + 2\left(\bar{\sigma}'_{yy}\right)^2\right)} \tag{5.5}$$

5. Calculate the the stress from the decomposition given by,

$$\bar{\boldsymbol{\sigma}}' = \bar{P}\boldsymbol{I} - \bar{\boldsymbol{\sigma}}. \tag{5.6}$$

6. Update the deviatoric stress from step 5 using the pressure from step 3.

7. Calculate the new mass fractions ϕ_p from the melting and chemical reaction model.

8. Update the volume fractions for each species and phase, ξ_{op}. Calculate new mixture averaged quantities, heat capacity $\bar{C}_v$, and heat conduction coefficient $\bar{k}_q$.

9. Repeat steps 1-8 in accordance with the Runge-Kutta time stepping scheme.

These calculations are initiated by specifying initial position and velocity for all materials within the computational domain. The equation of state in step 3 is updated from the new mass fractions calculated in the previous time step (step 1) and using the new density and internal energy from step 2. The reaction equations are calculated from the updated pressure and temperature in steps 3 and 2, respectively. The deviatoric stress is not returned to the yield surface until after it has been used in the conservation of energy (see step 4), thus, allowing the plastic work from the deviators to be accounted for.

5.3 Simulated Gas-Gun Experiment for the Thermite System

Gas gun experiments are simulated for the $2Al + Fe_2O_3$ + 50 wt.% Epon828 + $\alpha_o = 1.01$ material up to pressures of $\sim 23GPa$ [64]. Here, a copper driver plate with thickness of $2mm$ is simulated impacting the sample material of $2mm$. The material interface is given by the dashed vertical line close to $x = 2mm$ in Figure (33(a)). The four plots include the pressure, particle velocity, temperature, and density along the x-axis of the simulated copper (on the left) and the sample material (on the right). Included in Figure (33(a)) are the points used to calculate the pressure and particle velocity used for comparison with experimental data in Figure (34).

The time history of the shock front location is used to calculate the simulated shock velocity and is shown in Figure (33(b)). The location is calculated from interpolating the particle velocity at a constant pressure that is approximately 50% of the shock pressure. Simulation results are shown with $CFL = 0.4$ and 400 nodes along the

x-axis.

Figure (34) shows that the homobaric and uniform strain methods bound the experimental data up to approximately $Up = 0.8km/s$ or $P = 6GPa$. The pressure from the homobaric assumption is within the error bars of all but one experimental point ($Up = 607 \pm 0.004km/s$ for pressures $P \leq 10GPa$. For comparison, spatially resolved particle simulations resulted in $Us = 2.54 + 1.44Up$ which is within 7% error in low pressure regimes and within 15% error in higher pressure regimes [5].

The shock wave that propagates through the copper plate attached to the sample material will interact with the interface between the copper and sample material. The particle velocity in the copper plate attached to the sample is half of the velocity of the impacting copper plate. However, the interactions are complex and a simulation of this impact requires an additional plate. This modification of the simulation is not required to plot the Hugoniot curve for the material. The simulation shows the correct Us-Up and P-Up data, which is valid to compare with the experimental data. The simulation data is not expected to overlap with the experiments.

The 1D gas-gun simulations incorporate mixture strength in the stress tensor, which is not included in most of the previous continuum shock induced chemical reaction models considered in this study [20, 10, 11, 88]. Simulation results show reasonable agreement with experimental data. The homobaric and uniform strain methods bound the experimental data up to approximately $5GPa$ in Figure (33). The homobaric method approximates the experimental data much better than the uniform strain method. These results suggest that mechanical equilibrium is reached within the rise time of the shock.

5.4 $Ni + Al$ System Simulated Gas-Gun Experiment

Results from the mesoscale reaction model and the spherically symmetric mixture pore collapse model are included in 1D gas-gun simulation and shown in Figure (37).

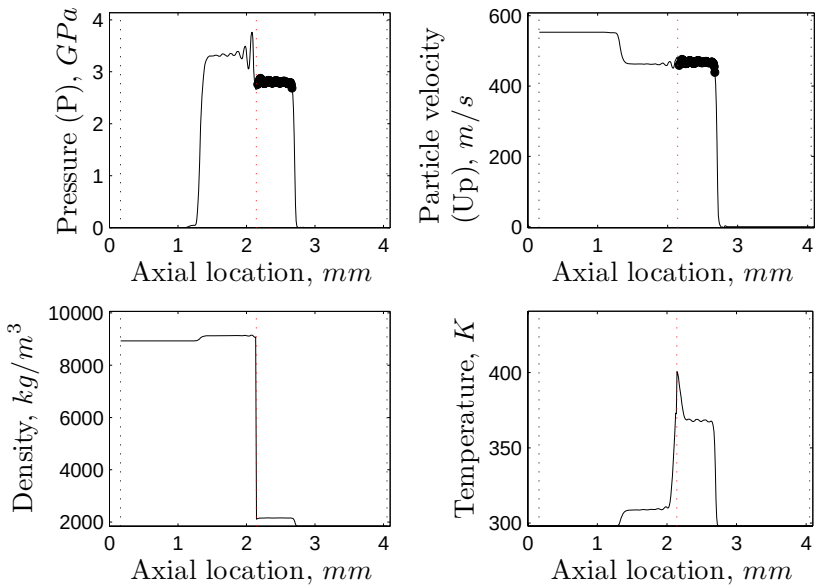

(a) Simulation results at time $t = 200 nanoseconds$.

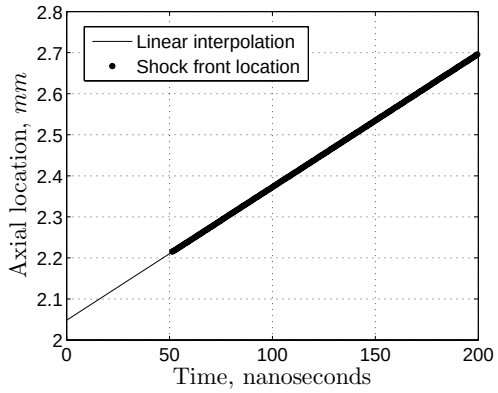

(b) Shock front time history.

Figure 33: Simulation results with the copper flyer impact velocity $V_s = 553 m/s$ for the stoichiometric mixture $2Al + Fe_2O_3$ + 50 wt.% Epon828 + $\alpha_o = 1.01$ with $n = 2$ and uniform strain method. The data points used to interpolate P and Up are shown in the top two plots and appear as bold lines since $n_x = 400$ nodes were used.

This is the fully integrated multi-scale model simulation. Simulation uncertainty is estimated at a maximum of 3% with 95% confidence based on convergence studies [99]. However, iterative errors are up to 11% due to oscillations in the pressure as a function

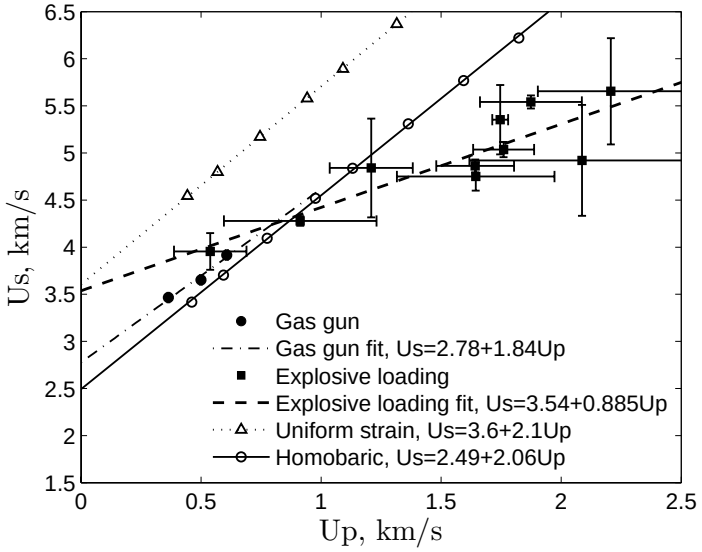

(a) Shock velocity-particle velocity.

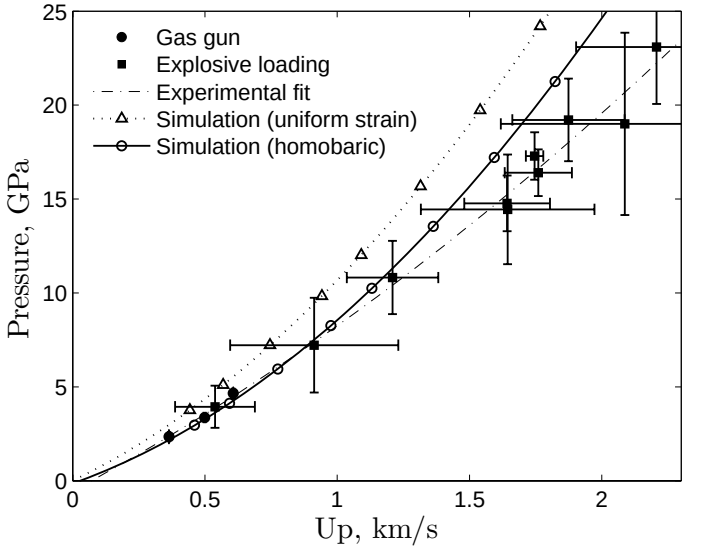

(b) Pressure-particle velocity.

Figure 34: Simulation results compared to experimental data for the stoichiometric mixture $2Al + Fe_2O_3$ + 50 wt.% Epon828 + $\alpha_o = 1.01$ with $n = 2$.

of the axial coordinate. These oscillations are a result of combining the advection of pore geometry with the irreversibility requirement. Therefore, only a qualitative

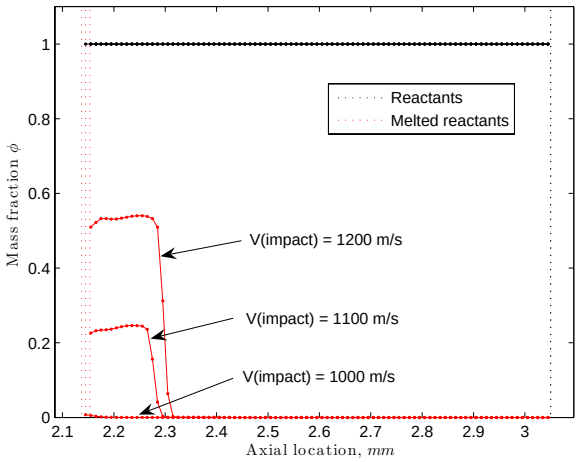

Figure 35: Melting behavior for various shock velocities in the stoichiometric mixture $2Al + Fe_2O_3 + \alpha_o = 1.66$ with $n = 2$.

comparison can be made.

To simplify computation, a fourth order polynomial is fit to the mesoscale reaction mass fraction time history. This approach assumes that heat transfer within the gas-gun simulation does not influence the reaction kinetics, which is reasonable for high velocity impact. Therefore, over-estimation of the reaction kinetics is expected.

Simulations are conducted only for the $Ni + Al$ system with 45% theoretical mass density (low density) cases with Cu impact velocities given by the experimental values [39]. $1:1$ initial volume ratios are used. Shot #0540 is shown with and without reaction for comparison. Reasonable agreement is observed between simulation and experiment for non-reaction cases. Careful adjustments are made to the pore radius in the pore collapse equation of state. Additionally, a careful selection of spatial step and CFL is performed to reach the reported values. Due to instability in the pore collapse equation of state, the following results in Table (8) are only valid for qualitative assessment. However, the results do represent the fully integrated multi-scale model. Note that the pressure calculation has deviations of up to 10% due to the oscillations near the material interface.

For the simulated reaction cases, ${}^{+}A_0 = 1 \times 10^3$, ${}^{-}A_0 = 0$, and the mesoscale reaction parameters from Table (5) are employed. Reaction proceeds to 23.5% according to the mesoscale reaction model, resulting in an increase in shock velocity that nearly matches the experimental increase for the case in which reaction is evidenced [39].

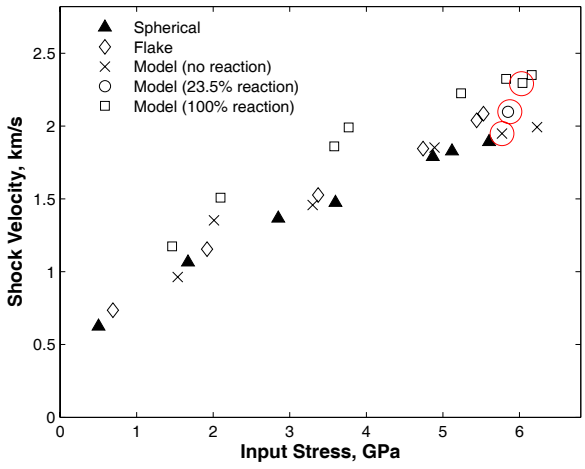

Figure 36: Gas-gun results from experiments [39] and simulation. MSR reaction kinetics are included one experiment. 100% reaction is shown for all spherical powder cases. The red circles represent propagated pressure data for the same pressure loading condition. Error bars are omitted for clarity. Maximum experimental error ranges of 0.05 (y-axis) and 0.2 (x-axis) are based on measurement uncertainty. Simulation errors are up to approximately 14%.

For the 60% theoretical mass density cases without reaction, a pressure pulse is applied to the $Ni + Al$ surface with quadratic dependence on time (see equation (4.53)). The reason for employing the pressure boundary is to demonstrate increased accuracy in the equation of state iterations. This shows that reducing oscillations in at the interface increases the accuracy in the solution given in Table (9). The overall trend in Figure (37) is matched by the simulations. An increase in shock velocity is seen in the simulation due to the stiffness in the spherically symmetric pore collapse equation of state. A further increase in shock velocity occurs due to 100% reaction. Note that shot #0520 is missing due to the inability to track a shock wave in the simulation according to the methods developed earlier.

Table 8: Gas-gun simulation results for the $Ni + Al$ 45% TMD powder mixture with impact velocity from experiments [38].

Shot Number	U_{impact} (km/s)	P (GPa)	U_s (km/s)
0532	1.004	3.30	1.458
0539	0.669	2.01	1.353
0540	0.951	5.77	1.949
0540[b]	0.951	5.15	2.098
0606	0.912	4.89	1.853
0607	0.430	1.54	0.963
0612	1.012	6.23	1.993

[a] Based on maximum iterative errors in the equation of state calculation.
[b] 23.5% reaction occurs according to the mesoscale reaction kinetics.

Table 9: Gas-gun simulation results for the $Ni + Al$ 60% TMD powder mixture with impact velocity from experiments [38].

Shot Number	P (GPa)	U_s (km/s)	U_p (km/s)	% Error[a]
0407	1.55	1.001	0.376	2
0412	3.59	1.461	0.606	4.3
0414	5.48	1.875	0.788	5.7
0428	2.93	1.253	0.539	2
0504	2.16	1.165	0.475	2
0506	2.85	1.350	0.582	4.1
0513	4.09	1.698	0.668	4.7
0514	5.31	1.838	0.773	5.5

[a] Based on maximum iterative errors in the equation of state calculation.

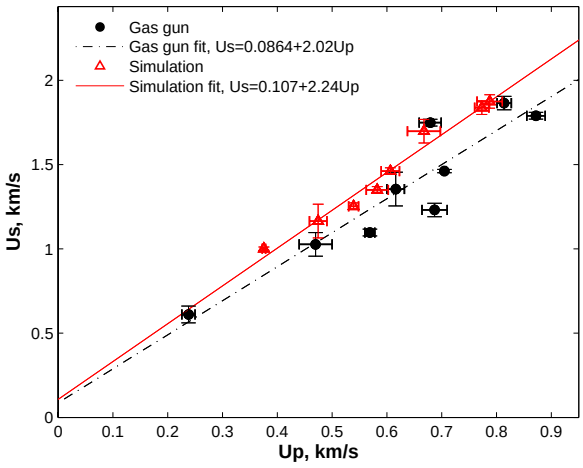

Figure 37: Gas-gun results from experiments [39] and simulation. No reaction occurs in any case. Error bars on simulation results are the addition of iterative and convergence errors.

The mass fraction time history at at the material interface between the impactor and the sample material ($Ni + Al$) is plotted in Figure (38).

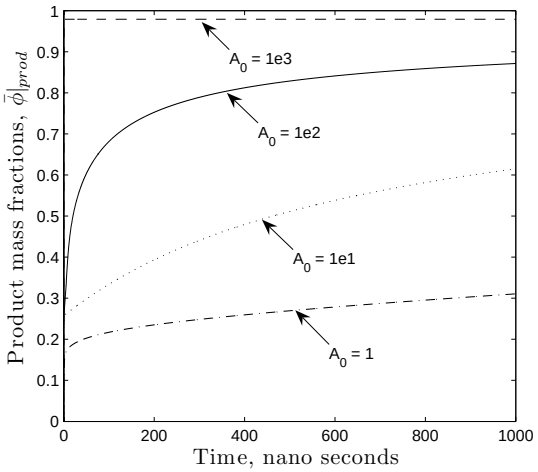

Figure 38: Mesoscale reaction model ensemble mass fractions for various forward frequency factors.

5.5 2D Simulation

The following finite difference approach for the energetic mixture in Lagrangian coordinates is based on the equations used by the HEMP computer program to solve

problems in elasticity and plasticity in plane geometry or cylindrical geometry including rotation about the axis of cylindrical symmetry [118].

The 2D simulations are useful for understanding the conditions in which 2D effects in the gas-gun experiment are significant. For example, reflected waves from the surface on the outer circumference of the sample material can influence the axial shock front velocity.

The fundamental equations of motion in x, y coordinates with cylindrical symmetry and rotation about the x axis are given in Lagrangean coordinates for the mixture by,

$$\frac{d\dot{x}}{dt} = \frac{1}{\bar{\rho}}\left[\frac{\partial\bar{\Sigma}_{xx}}{\partial x} + \frac{\partial\bar{T}_{xy}}{\partial y} + \frac{\bar{T}_{xy}}{y}\right], \tag{5.7}$$

$$\frac{d\dot{y}}{dt} = \frac{1}{\bar{\rho}}\left[\frac{\partial\bar{T}_{xy}}{\partial x} + \frac{\partial\bar{\Sigma}_{xy}}{\partial y} + \frac{\bar{\Sigma}_{yy} - \bar{\Sigma}_{\theta\theta}}{y}\right] + \omega^2 y, \tag{5.8}$$

$$\frac{1}{y}\frac{d(\Omega)}{dt} = \frac{1}{\bar{\rho}}\left[\frac{\partial\bar{T}_{\theta x}}{\partial x} + \frac{\partial\bar{T}_{y\theta}}{\partial y} + 2\frac{\bar{T}_{y\theta}}{y}\right], \tag{5.9}$$

where $\Omega = y^2\omega$ and ω is the angular rotation also given by $\dot{\theta}$. θ is the polar coordinate in cylindrical coordinates that is orthogonal to the x-axis. The state of stress is is denoted by $s^n_{xx}, s^n_{yy}, T^n_{xy}$ and mixture averages are calculated from equation (D.4). $\bar{\rho}$ is calculated from equation (3.58).

The conservation of mass for the mass element M is given simply by,

$$\frac{dM}{dt} = 0. \tag{5.10}$$

This simply means that no mass leaves or enters the element.

The first law of thermodynamics gives us the rate of change for the internal energy per original volume $\bar{E}$ as,

$$\dot{\bar{E}} = -(\bar{P}+\bar{q})\dot{\bar{V}} + \bar{V}\left(\bar{s}_{xx}\dot{\bar{\epsilon}}_{xx} + \bar{s}_{yy}\dot{\bar{\epsilon}}_{yy} + \bar{s}_{\theta\theta}\dot{\bar{\epsilon}}_{\theta\theta} + \bar{T}_{xy}\dot{\bar{\epsilon}}_{xy} + \bar{T}_{y\theta}\dot{\bar{\epsilon}}_{y\theta} + \bar{T}_{\theta x}\dot{\bar{\epsilon}}_{\theta x}\right) + \Psi_S, \tag{5.11}$$

where $\bar{V} = \bar{\rho}_0/\bar{\rho}$ is the mixture relative volume, $\bar{\rho}_0$ is the reference mixture density. Ψ_S is given by equation (4.52).

Velocity strains are given by,

$$\begin{aligned}
&\dot{\bar{\epsilon}}_{xx} = \frac{\partial \dot{x}}{\partial x}, \quad \dot{\bar{\epsilon}}_{yy} = \frac{\partial \dot{y}}{\partial y}, \quad \dot{\bar{\epsilon}}_{\theta\theta} = \frac{\dot{y}}{y}, \\
&\dot{\bar{\epsilon}}_{xy} = \frac{\partial \dot{y}}{\partial y} + \frac{\partial \dot{x}}{\partial x}, \quad \dot{\bar{\epsilon}}_{y\theta} = y\frac{\partial \omega}{\partial y} = \left[\frac{\partial (y\omega)}{\partial y} - \omega\right], \quad \dot{\bar{\epsilon}}_{\theta x} = \frac{\partial (y\omega)}{\partial x}.
\end{aligned} \tag{5.12}$$

The stress deviator tensor is given by,

$$\begin{aligned}
&\dot{\bar{s}}_{xx} = 2\bar{\mu}\left(\dot{\bar{\epsilon}}_{xx} - \tfrac{1}{3}\frac{\dot{\bar{V}}}{\bar{V}}\right), \quad \dot{\bar{s}}_{yy} = 2\bar{\mu}\left(\dot{\bar{\epsilon}}_{yy} - \tfrac{1}{3}\frac{\dot{\bar{V}}}{\bar{V}}\right), \quad \dot{\bar{s}}_{\theta\theta} = 2\bar{\mu}\left(\dot{\bar{\epsilon}}_{\theta\theta} - \tfrac{1}{3}\frac{\dot{\bar{V}}}{\bar{V}}\right), \\
&\dot{\bar{T}}_{xy} = \bar{\mu}\dot{\bar{\epsilon}}_{xy}, \quad \dot{\bar{T}}_{y\theta} = \bar{\mu}\dot{\bar{\epsilon}}_{y\theta}, \quad \dot{\bar{T}}_{\theta x} = \bar{\mu}\dot{\bar{\epsilon}}_{\theta x},
\end{aligned} \tag{5.13}$$

where $\bar{\mu}$ is the volume fraction averaged shear modulus.

The mixture pressure $\bar{P}$ is calculated from the Murnaghan equation of state equation of state given in equation (D.17). Equation of state parameters are averaged using the approach by Bennett, Horie, and Hwang [11] in equations (3.1)-(3.4).

The total stresses are a result of equation (D.6) and are given by,

$$\begin{aligned}
\bar{\Sigma}_{xx} &= -\left(\bar{P} + \bar{q}\right) + \bar{s}_{xx}, \\
\bar{\Sigma}_{yy} &= -\left(\bar{P} + \bar{q}\right) + \bar{s}_{yy}, \\
\bar{\Sigma}_{\theta\theta} &= -\left(\bar{P} + \bar{q}\right) + \bar{s}_{\theta\theta}.
\end{aligned} \tag{5.14}$$

Numerical oscillations in the mixture are damped through the use of the artificial viscosity $\bar{q}$ given by,

$$\bar{q} = C_0^2 \rho L^2 \left(\frac{ds}{dt}\right)^2 + C_L \bar{\rho} L \bar{a} \left|\frac{ds}{dt}\right| \tag{5.15}$$

The mixture average is implied in the constants C_0 and C_L. L is a measure of the grid size, $\bar{a}$ is the local sound speed, and $\bar{\rho}$ is the local density. Von Mises yield criterion is employed. For the 1D plain strain problem, the yield stress is given earlier by equation (D.11). The yield criterion for ideal plasticity is written as,

$$\sqrt{2\bar{J}} - \sqrt{\frac{2}{3}}\bar{Y} \leq 0, \tag{5.16}$$

where $\bar{Y}$ is the plastic flow stress and $2\bar{J}$ is the second invariant of the deviatoric stress tensor.

5.5.1 Simulated Bar Impact Experiment

To demonstrate the 2D radially symmetric code, an Al rod of length $L = 0.5m$ with velocity $V = 1000m/s$ in the x-direction is shown with Lagrangian grid points in Figure (39). The axial velocity is given in Figure (40). The material crushes up and expands radially at the fixed boundary condition at $x = 0.5m$. Soon after this time ($8.5\mu s$), "hour glass" modes skew the mesh. To correct this, an artificial viscosity can be used [118].

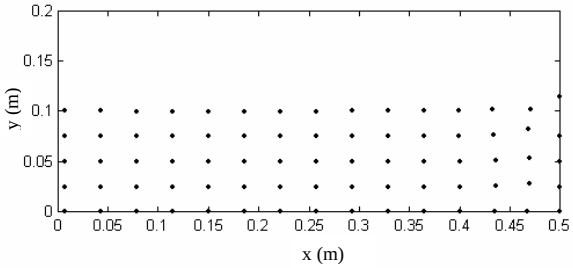

Figure 39: Cylinder along the x-axis shown with grid points at $t = 8.5\mu s$.

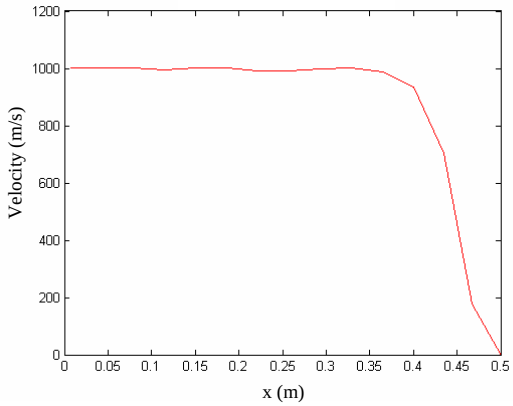

Figure 40: Axial velocity of cylinder at $t = 8.5\mu s$.

Chapter VI

UNCERTAINTY QUANTIFICATION

Sources of uncertainty in computer simulations of gas-gun experiments with ESMs are investigated. This includes a proposed framework needed for model calibration and validation. Uncertainty due to numerical discretization in the 1D code is quantified. Since an exact solution can not be obtained, a solution extrapolation is employed with associated uncertainty based on the grid convergence index (GCI) method [102].

6.1 Validation Approach

The complete system involving the intense dynamic loading of ESMs is decomposed into three progressively simpler phases: subsystem cases, benchmark cases, and unit problems as shown in Figure (41). The conceptual ESMs model includes mixture equation of state, plastic flow and void collapse, reaction initiation criterion and extent of reaction, and heat conduction. The unit problems with a mixture* refer to cases involving solid and porous mixtures with various morphologies.

In Figure (41), the arrows in bold are chosen to be the primary source of validation given the current availability of experiments to choose from *and* given the current theoretical models that are available. For example, Figure (41) illustrates the sole reliance on gas-gun experiments to validate the ESM model. It is seen that at least two of the unit problems are only described at this time by the gas-gun experiment. Clearly, chemical reactions are the weakest link as no experiments exist that can be used to isolate the chemical reaction initiation and kinetics in the present study. Fortunately heat transfer does not play as important of a role in the shock environment, therefore, many simplifications along this chain are often justified.

The goal is to obtain a purely deterministic model to avoid the need for estimating

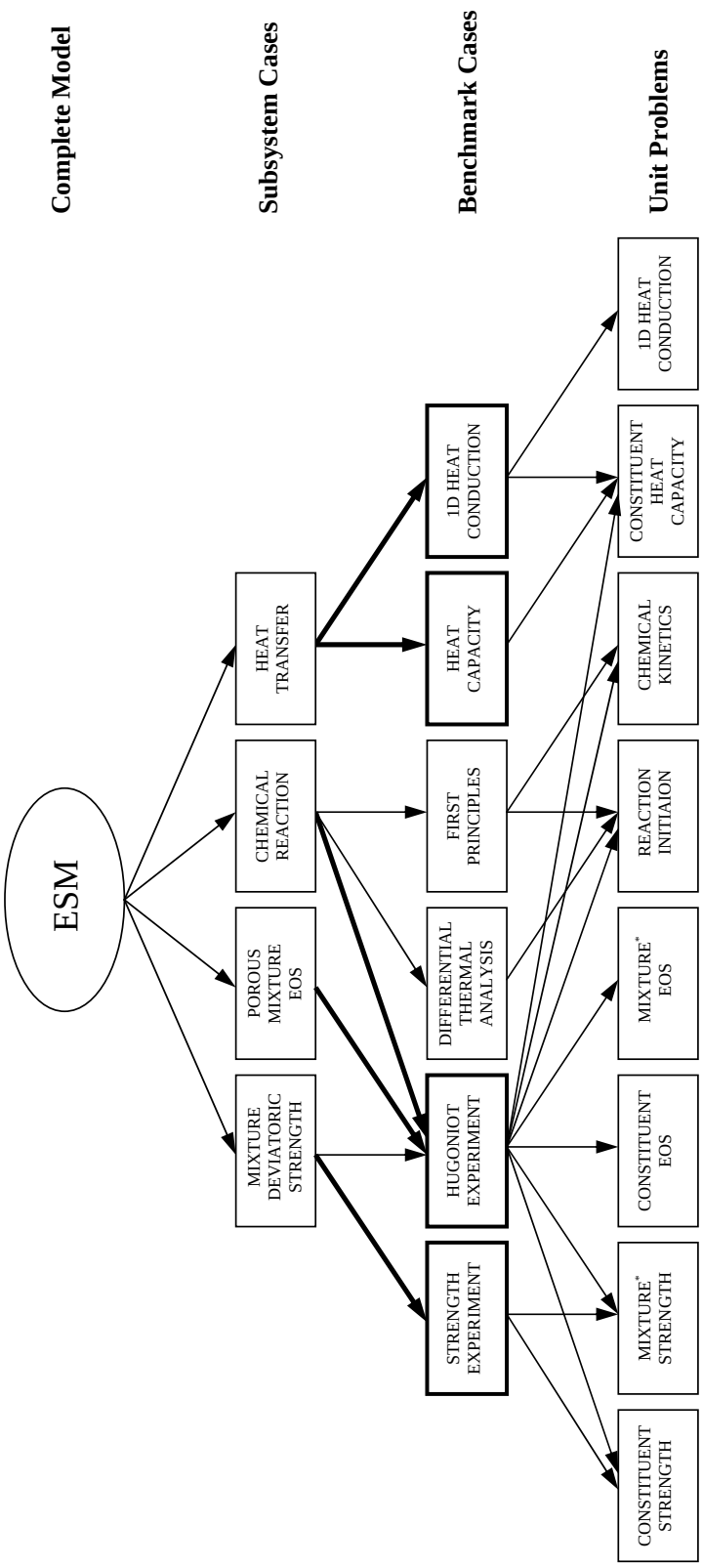

Figure 41: Validation phases

empirical material constants. At present this is not the case. The form of material parameters that are desired in the benchmark cases depends entirely on the form of the theoretical model that is used to represent the physical processes. For the continuum modeling approach used in this thesis, the use of unknown material constants that are listed in Table 10 are required. In this thesis, the activation energy E_a is included to generalize the framework for current continuum shock induced chemical reaction and shock assisted chemical reaction models. E_a is usually the activation energy.

Material parameters in Table 10 and Figure (42) are generalized and grouped according to the type of the model that uses these parameterss for simplicity of notation. $\boldsymbol{\alpha}_p$ represents a set of material parameters in an EOS relationship for a solid material constituent that depends on density ρ and specific internal energy e. For example Murnaghan and Mie-Grüneisen models may be used. $\boldsymbol{\alpha}_\sigma$ represents the set of material parameters in a constitutive model such as Johnson-Cook and Drucker-Prager models. Note that an overbar denotes a mixture averaged quantity.

6.1.1 Hierarchy of Experiments

As shown in table 10, the material parameters are obtained from various experiments. To understand the submodels contained in a simulation code, it is necessary to use a hierarchy of experiments [57]. Essentially one works backwards from the case studies to the benchmark cases in Figure (41). Figure (42) shows conceptual process for combining information from several experiments involving various levels of integration.

Heat capacity and heat conduction are shown for completion in Figure (42) to illustrate the four experiments highlighted in Figure (41), although strictly speaking, the uncertainties in the heat capacity experiments propagate to the gas-gun simulations. However, uncertainties in heat capacity $\bar{C}_v$ and heat conduction coefficient $\bar{k}$ are usually ignored and appropriate mixture rules are applied. Therefore, in the

Table 10: Possible experiments to obtain material constants are denoted by "X" and check marks denote experiments that are not necessary but would be of benefit. Hugoniot refers to either gas-gun or shock loading experiments.

Experiment	E_a	A	ϕ_c	n	C_m	$\boldsymbol{\alpha}_p$	$\bar{\boldsymbol{\alpha}}_\sigma$	$\boldsymbol{\alpha}_\sigma$	$\bar{C}_p$	C_p	$\bar{k}_q$	k_{qi}
ESM Hugoniot	X	X	X	X	X							
Constituent Hugoniot						X						
Constituent Porous Hugoniot				✓*								
Differential Thermal Analysis †	✓											
ESM Taylor Test §							✓*					
Constituent Taylor Test §								X				
ESM Heat Capacity									✓*			
Constituent Heat Capacity										X		
ESM 1D Heat Cond.											✓*	
Constituent 1D Heat Cond.												X

* Material constants that can be approximated by mixture rules with constituent material constants.

† Experiment does not currently exist under conditions appropriate for this study. A theoretical approach involving first principles may be considered.

§ Alternative high strain rate strength experiments may be used.

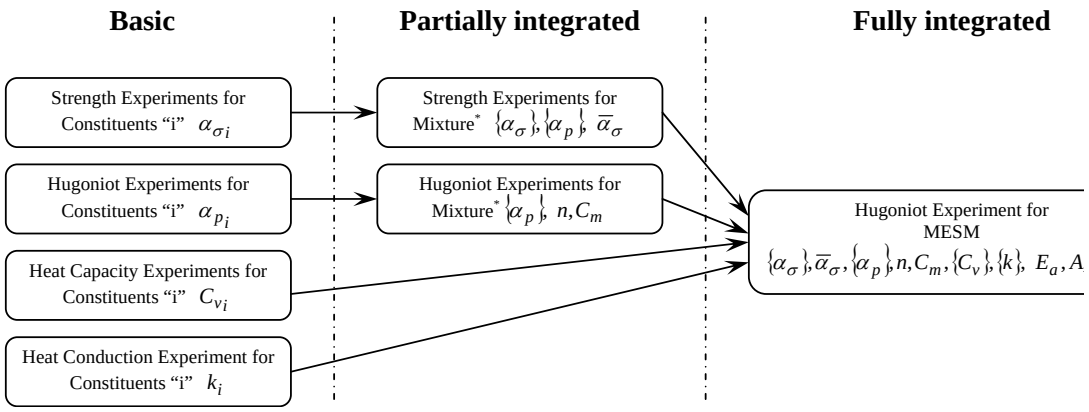

Figure 42: Example of an experimental hierarchy required for tracking uncertainty from experiments in which four benchmark cases from Figure (41) are considered. The brackets $\{\cdot\}$ denote the group of constituent parameters and the overbar denotes the mixture properties.

fully integrated model, there are only three unknown material parameters that need to be inferred from ESM gas-gun experiments, E_a, A, ϕ_c. These are the activation energy, Arrhenius constant, and extent of reaction, respectively. If a *partially integrated* experiment is not available, the parameter(s) are simply left as an unknown in the *fully integrated* experiment. For example, if a gas-gun experiment of a porous component is either deemed an invalid approximation of the ESM material or is simply not available, then the parameters n and C_M become additional unknowns in the ESM gas-gun experiment.

The Bayesian approach to the analysis is perfectly suited for conducting inference about models [57]. Bayes' theorem gives the probability for a parameter vector $\boldsymbol{a}$ for a given set of data $\boldsymbol{d}$ and information I

$$p(\boldsymbol{a}|\boldsymbol{d}, I) \propto p(\boldsymbol{d}|\boldsymbol{a})p(a|I) \; . \tag{6.1}$$

6.2 Calibration

Calibration is the step where inferences are made about the material parameters with corresponding uncertainties that are introduced in the physics based models, namely the chemical reaction, plasticity, and pore collapse models. One way to view this is to

recognize the parameters as degrees of freedom that have corresponding uncertainty distributions which are also degrees of freedom. The parameters that give the best agreement between the experimental evidence and the theoretical model are needed. This is usually quantified by using the minimum chi-squared method[16]. The goal is to minimize χ^2 in equation (6.2), which is the measure of the goodness of fit.

$$\chi^2 \equiv \sum_i \frac{[d_i - y_i(\boldsymbol{a})]^2}{\sigma_i} \tag{6.2}$$

where, d_i is the i^{th} experimentally measured data point with standard deviation σ_i, y_i is the numerical solution, and $\boldsymbol{a}$ is the parameter vector.

In this application, it is necessary to use the computational model itself to calibrate some of the material parameters. Since the interest is in calibrating the *theoretical* model and not the *computational* model, a correction is applied to the numerical result. If the estimated numerical error from the computational model is approximately constant over the range of values for the material constants, then the verification result for a single case is applied to correct the computational solutions approximately. Otherwise, either the verification procedure is applied for each combination of material parameters (brute force method needed during each iteration in the optimization routine) or construct a surrogate model using a reduced number of points that cover the required range of material constants (response surface method). Since the simulation results are computationally expensive, the response surface method is chosen.

6.3 Verification Assessment

Verification involves quantifying the error associated with solving the governing equations regardless of the values of the material coefficients. Therefore this task is performed first. The most important part of verification is to perform spatial and temporal step size refinement studies.

The first step is to identify the metric or quantity of interest for observing convergence. In the interest of length and simplicity, a single metric is chosen, namely

the shock velocity U_s, which is a convenient quantity for comparison with gas-gun experiments.

6.3.1 Models of Convergence Error

The exact solution is denoted the symbol F^* and the discrete solutions in the simplified notation are denoted by the symbol $F_{x,t} = F(\Delta x, \Delta t)$. The general error metric in equation (6.3) is defined by using the norm of the difference between the continuous and numerical solutions.

$$e_{x,t} = \| F^* - F_{x,t} \| \tag{6.3}$$

For the 1D shock wave speed, the error is the absolute value of the difference, i.e., $e_{x,t} = |F^* - F_{x,t}|$.

The Richardson Extrapolation Estimation (REE) technique assumes that the solution is in the asymptotic convergence regime, neglects higher order terms, and the discretized solutions are given by equation (6.4-a),

$$F_{x,t} = F^* + \alpha^* h_i^{p^*} \tag{6.4a}$$

$$F_{x,t} = \tilde{F} + \tilde{\alpha} h_i^{\tilde{p}} \tag{6.4b}$$

where α^* is a fitting constant, p^* is the convergence rate or order-of-convergence, and h_i is either the spatial or the temporal step size, $1/N_{cells}$. Equation (6.4a) is rarely if ever observed in practice. $\tilde{F}$ in equation (6.4b) refers to a solution that approximates F^* by extrapolation such as the REE technique or by response surface method (RSM) for a given set of fitting parameters $\{\tilde{\lambda}_o, \tilde{\alpha}, \tilde{p}\}$. The term on the right hand side of equation (6.4b) is the space-only or time-only error Ansatz [59] and takes the general form,

$$\tilde{e}_{x,t} = \tilde{\lambda}_o + \tilde{\alpha} h_i^{\tilde{p}} + h.o.t. \,. \tag{6.5}$$

with three fitting parameters, $\{\tilde{\lambda}_o, \tilde{\alpha}, \tilde{p}\}$.

If an exact solution is known, then p^* is evaluated exactly using a minimum of $N_g = 2$ grid solutions. In many cases such as ours the exact solution is unknown.

Additionally, the asymptotic region under which equations (6.4) are a reasonable approximation is unknown. An estimated order-of-convergence is calculated with three grid points $N_g = 3$, constant refinement ratio r_h, constant α and constant convergence rate p, as in Roache [102], as:

$$\tilde{p}_r = \log\left[(F_1 - F_3)\,/\,(F_1 - F_2)\right]\,/\,\log\left[r_h\right]\ . \tag{6.6}$$

where F_1, F_2, and F_3 are the fine, medium, and coarse grid solutions respectively. $N_g = 3$ is superior to $N_g = 2$ and marginally worse than $N_g = 4$. If the grid convergence is monotonic with constant convergence rate, then $\tilde{p}_r = p^*$ and the extrapolated solution $\tilde{F}$ is

$$\tilde{F} = F^* = F_1 + (F_1 + F_2)\,/\left(r_h^{\tilde{p}} - 1\right) \tag{6.7}$$

However, $\tilde{F} = F^*$ is clearly not the case in this thesis as is seen later. Further, $\tilde{p}$ and $\tilde{\alpha}$ are rarely constants. One basic approach to study realistic convergence is to assume an empirical safety factor F_s to provide the GCI or the uncertainty expressed as [102]:

$$GCI = F_s \left|\frac{F_1 - F_2}{F_1}\right| / \left(r_h^{\tilde{p}_r} - 1\right) \tag{6.8}$$

As mentioned earlier, no consensus has been reached as to the uncertainty that is represented by a given value of F_s with a given N_g. Therefore, this method is used as a first approximation only. Throughout this chapter, a conservative safety factor $F_s = 3$ with $N_g = 3$ is assumed [102] to estimate the uncertainty 68% of the time (or 1σ) since Gaussian a distribution is assumed.

Until this point, three main assumptions are made. The error Ansatz in equation (6.5) assumes that, 1) numerical solution convergence is monotonic, 2) space-time coupling effects are neglected, and 3) higher order (above single order) terms are negligible. A non-linear Ansatz model due to Hemez et al. [59] relaxes these three assumptions and takes the following form in equation (6.9).

$$\hat{e}_{x,t} = \lambda_o + \alpha(\Delta x)^p + \beta(\Delta t)^q + \delta(\Delta x)^r(\Delta t)^s + h.o.t. \tag{6.9}$$

where λ_o is the intercept or bias error, α, β, δ are regression coefficients, p is the convergence rate in space, q is the convergence rate in time, and r, s are space-time coupling orders of convergence.

6.3.2 Optimization Procedure Used to Fit the Error Ansatz Models

The coefficients in equation (6.5) are solved analytically as in equation (6.6). This is not the case with obtaining the coefficients in equation (6.9). Therefore, a numerical optimization solver is used to best-fit the coefficients $\{\lambda_o, \alpha, \beta, \delta, p, q, r, s\}$ in equation (6.9). The best fit is based on the set of numerical solutions $F_{x,t}$ from N_{Runs} simulations or computer runs with different grid refinements. The objective function to be minimized is chosen to be the mean squared error (MSE) and is given by,

$$MSE = \sqrt{\frac{1}{N_{Runs}} \sum_{k=1..N_{Runs}} \left[\tilde{e}_{x,t}(k) - \hat{e}_{x,t}(k)\right]^2} \tag{6.10}$$

The minimization of equation (6.10) is similar to the approach by Hemez et al. [59] with a slight difference, namely, F^* is replaced by $\tilde{F}$ from equation (6.7) in the error definition in equation (6.3). Here and from now on, this estimated error is defined as:

$$\tilde{e}_{x,t} = \tilde{F} - F_{x,t} \ . \tag{6.11}$$

In this thesis, better convergence is obtained by not taking the absolute value in equation (6.11).

The mean squared error in equation (6.10) is minimized using $MATLAB^{TM}$ with the function *fminsearch.m*. This function implements the Nelder-Mead simplex method [89], a multidimensional unconstrained nonlinear optimizer. The default termination tolerances (10^{-4}) on the function value and the output quantity are used. Typically, $200 - 2000$ iterations are required for convergence in this study. Iterations are performed until the initial guess and the output coefficients are within the tolerance (10^{-4}).

6.3.3 Grid Convergence Study

The use of both the space-only model and the space-time model is demonstrated through a case study. Here, the goal is to minimize the uncertainty or convergence index (GCI) by systematically investigating several subsets the space-time grid refinement space. The following four steps are followed in the analysis of the numerical solution:

1. Extrapolate a solution for the shock velocity $\tilde{F}$ (from equation (6.7) assuming $\tilde{p} = \tilde{p}_r$ with associated grid convergence index (GCI) from equation (6.8).

2. Apply the 3-parameter space-only fit using equation (6.5) and optimization procedure in Section (6.3.2).

3. Fit the 8-parameter space-time model in equation (6.9) using the extrapolated solution from step (1) and the initial guess for parameters $\{\tilde{\lambda}_o, \tilde{\alpha}, \tilde{p}\}$ from step (2).

4. Select the best subset based on minimum convergence index (GCI) from step#1 and the minimum MSE from step#3. p is obtained from the non-linear ansatz fit to recalculate the extrapolated solution using equation (6.7).

The systematic analysis is conducted in steps#1-3 to i) identify a possible asymptotic region within the full set of simulation data and ii) verify the order-of-convergence obtained in step#1. In step#1, the goal is to seek the three point spatial data set that provides the lowest GCI since the GCI indicates the degree of asymptotic convergence. Then, use step#2 mainly as a way to improve the initial guess for the 8 parameter fit in step#3 and also serves as a check on the general trends observed. Step#2 provides an exact solution which is useful to check against the order-of-convergence in step#1 and step#3. Step#3 exploits the property of the non-linear equation since the data used in the fit may not necessarily fall within the asymptotic

regime, however, the goodness of fit or MSE must be relatively small to accurately represent the simulation data.

These steps are demonstrated and explained below for the simulation of a gas gun experiment, in which the impactor velocity is 922 m/s. The sample material is fully dense, i.e., $\alpha_o = 1.0$, and the mixture is in stoichiometric quantities for the reaction $3Al + Ni \rightarrow NiAl_3$. Here, the material parameters are assumed to be: $C_m = 0.5$, $n = 2$, $A_o = \phi_c = 0$. C_m is the proportion of homobaric to uniform strain pressure, n is the order of the $P - \alpha$ model, A_o is the frequency factor or Arhenius parameter, and ϕ_c is extent of reaction and ranges from 0 to 1. Currently, no analytical solution exists for the shock velocity in this simulation.

Step #1:

The full set of of grid refinements for this case study includes three spatial grids using $N_{cells} = \{1800, 1350, 800, 600, 450, 400, 300, 200, 150\}$, and time step refinement with $CFL = \{0.1, 0.2, 0.3, 0.4, 0.5, 0.6, 0.7, 0.8, 0.9\}$. Although not always practical, the low CFL values are used for completeness. There are four sets of data with constant spatial refinement ratio $\{F_{2f},\ F_{2c},\ F_{3f},\ F_{3c}\}$ with respective grid sets $N_{cells} = \{[800, 400, 200],[600, 300, 150],[1800, 600, 200],[1350, 450, 150]\}$. Three point spatial refinements are chosen to reduce the number of simulations required during the calibration and validation steps.

The space-only model is to fit to each of the four spatial grid sets in N_{cells} at each CFL value to obtain the order-of-convergence and extrapolated solutions $\tilde{F}$ and $\tilde{F}'$. For each grid set, the minimum GCI among all of the CFL values is calculated and listed in Table (12) with its corresponding extrapolated solution $\tilde{F}$.

The four grid sets have the lowest GCI when $CFL < 0.5$ and GCI values when $CFL \geq 0.5$ are found to be significantly higher in some cases (see Figure (43(b))). Therefore, screened data $(\cdot)'$ for a 3-point spatial grid set is defined as a subset of the

Table 11: Results for the three point extrapolations in step#1. The $CFL, \tilde{F}, CGI, \tilde{p}$ correspond to the values obtained from the three point spatial refinement at the CFL value that results in the lowest GCI in the subset $F_{x,t}$. CGI_{max} is the highest GCI among all of the CFL values in the subset.

$F_{x,t}$	r_h	CFL	$\tilde{p}_r$	$\tilde{F}$ (m/s)	CGI %	CGI_{max}%
F_{2f}	2	0.2	2.81	5937.93	0.13	0.25
F_{2c}	2	0.7	2.51	5940.59	0.53	0.53
F_{3f}[a]	3	0.4	3.59	5940.33	0.02	0.05
F_{3c}	3	0.5	2.53	5939.74	0.03	0.10

[a] Best extrapolation based on minimum GCI.

spatial grid containing CFL values up to the CFL value with the lowest corresponding CGI. For example, if the GCI is lowest when $CFL = 0.4$ for the spatial grid set {[800, 400, 200]}, then the corresponding subset ({[800, 400, 200]})′ contains $CFL =$ {0.1, 0.2, 0.3, 0.4}. Each subset contains at least the three lowest CFL values.

The extrapolated values and associated uncertainties (GCI) are used in the propagation of uncertainty. Then, use the extrapolated solution $\tilde{F}$ corresponding to CFL value that yields the lowest GCI with corresponding $\tilde{p}$. However, the most conservative GCI over the grid subset denoted CGI_{max} (CGI'_{max} for screened subsets) are used and given in Table (11).

Step #2:

In all cases, the 3 parameter (space-only) fit converges within less than 200 iterations. The spatial order-of-convergence is given in Table (12). The only exception to the procedure in step#1 is for F'_{all}, in which $0.1 \leq CFL \leq 0.5$ and $300 \leq N_{cells} \leq 1800$ are included. This is used for comparing to results from the systematic study in step#4.

The maximum difference between the error equation and the estimated error in equation (6.11) over the grid set (or subset) is defined as

$$\Delta\tilde{e} = \underset{x,t}{max} \left|\tilde{e} - \hat{e}\right| \ . \tag{6.12}$$

The MSE and the $\Delta\tilde{e}$ are used to make comparisons between the four grid sets and their corresponding subsets.

Table 12: Fit the 3 parameter error ansatz in step#2.

$F_{x,t}$	$\tilde{\lambda}_o$ [c]	$\tilde{\alpha}$	$\tilde{p}$	MSE [c]	$\Delta\tilde{e}$ [c]
F_{all}	5.06	-2.8×10^6	1.97	8.80	32.84
F_{2f} [b]	0.88	-3.2×10^7	2.42	5.62	14.90
F_{2c}	8.11	-1.8×10^6	1.87	13.31	34.86
F_{3f} [a]	1.36	-1.0×10^8	2.64	5.59	14.90
F_{3c}	1.83	-9.9×10^6	2.22	13.17	34.86
$\tilde{\lambda}'_o$ [c]	$\tilde{\alpha}'$	$\tilde{p}'$	MSE' [c]	$\Delta\tilde{e}'$ [c]	
F_{all}	2.62	-7.1×10^8	2.96	1.37	3.39
F_{2f} [b]	1.76	-2.8×10^7	2.41	1.55	3.33
F_{2c}	9.75	-1.3×10^6	1.81	11.74	33.05
F_{3f} [a]	1.55	-7.5×10^8	3.04	2.40	5.82
F_{3c}	1.46	-1.7×10^7	2.36	4.43	13.75

[a] Contains the best subset based on minimum GCI.
[b] Contains the best subset based on minimum MSE.
[c] Units are m/s.

Step #3:

Now the space-time model is fit to each grid set to obtain the unknown equation parameters. The best fit parameters and order-of-convergence are given in Table (13).

The numerical solution over the full grid set $F_{x,t} = F_{full}$ is shown in Figure (43(a)). The space-time fit from equation (6.9) and the estimated error from equation (6.11) are shown for two CFL values in Figure (43(b)). Figure (43) shows that $F_{x,t}$ depends much more on the spatial refinements compared to the temporal refinements. The

8 parameter ansatz approximates $F_{x,t}$ relatively well considering the non-monotonic behavior in $F_{x,t}$.

Step #4:

The subset F'_{3f} contains the lowest mean squared error (MSE) and the lowest grid convergence index (GCI), therefore, this is selected as the best subset in this example problem. $p' = 2.98$ is substituted from the 8 parameter ansatz into equation (6.7) with the spatial values corresponding to $CFL = 0.4$ to yield $\tilde{F} = 5940.29 m/s$ and $GCI = 0.02\%$, which are nearly identical to the values calculated in Table (11). The numerical solution is expressed within one standard deviation of the mean as $\tilde{F} = 5940.29 \pm 1.18 m/s$.

The selection of the subset F'_{3f} a not surprising result since F'_{3f} includes the most refined spatial data out of all of the subsets considered in this study. Now it is necessary to understand this result by exploring the limits of the asymptotic regime. However, not enough information is available to define the exact range of the asymptotic region. However, the selection of F'_{3f} is elucidated by examining the results from steps#1-3.

Before analyzing the convergence, the concern is to examine if the spatial order-of-convergence in this grid set which is approximately $p = 2.98$ from the 8 parameter fit to F'_{3f}. The value $p = 2.98$ is higher than expected since $1 \leq p \leq 2$ from the MUSCL algorithm and $p \leq 1$ from the ghost fluid method applied at the material interface which is zero order accurate. This value is lower than the extrapolated value $p = 3.59$ from step#1 given in Table (11) and approximately the same as the 3 parameter fit $p = 3.04$. Most of the data in Tables (11) - (13) suggests that $p \cong 2 - 2.5$. The 8 parameter fit to F_{full} is $p = 1.5$ which is lower than all of the other values due to non-monotonic convergence over the entire span considered in this data set. The 8 parameter fit to the screened set F'_{full} is $p = 2.96$, where non-monotonic convergence

seen in the range $0.6 \leq CFL \leq 0.9$ and $150 \leq N_{cells} \leq 200$ has been removed. This value is nearly identical to the value $p = 2.98$ from the 8 parameter fit to F'_{3f}, therefore, indicating that F'_{3f} represents the behavior of the data better than the other subsets.

Temporal convergence:

The systematic identification of the subsets $F'_{x,t}$ significantly reduces the mean squared error (MSE) in Table (13). The screened subsets $F'_{x,t}$ except F'_{2c} contain $CFL \leq 0.5$ which indicates that asymptotic convergence is more likely to occur when $CFL \leq 0.5$. GCI values when $CFL = 0.1$ for all four grid subsets are found to be relatively close to the minimum value, thus, a limit as temporal refinements become infinitely fine is not observed in this study. In practical applications, $CFL \leq 0.1$ is prohibitively expensive and does not always yield improved results.

Spatial convergence:

From Table (11), it is seen that the grid convergence index (GCI) for the coarse subsets is approximately twice that of the fine subsets, thus, the coarse subsets may not be within the asymptotic regime. The mean squared error (MSE) in the fine subsets tended to improve much more than in the coarse subsets. This observation provides further evidence that the two coarsest spatial grid sizes are not within the asymptotic regime. As in the temporal convergence, there is no indication from this data as to the limit in the asymptotic region when the spatial refinements become infinitely fine.

6.3.4 Summary

A framework given in this chapter outlines the procedure to identify and quantify the sources of uncertainty in computational simulations of ESMs. In addition to being a

necessary part of the validation process, the current systematic investigation of the design problem from a hierarchial sequence of physical processes demonstrates how one can reduce the number of unknown material parameters in the *fully integrated* experiment. It is possible to eliminate all but three unknown parameters in the continuum model, which must be obtained by calibration with ESM gas-gun experiments, namely, $\{E_a, A, \phi_c\}$ where ϕ_c is only used in this chapter for simplification. These parameters physically represent reaction initiation, kinetics, and extent of reaction, which are the least understood processes in shock induced chemical reactions.

The verification procedure is demonstrated by using gas-gun simulation results in which Cu impacts a non-porous stoichiometric $Ni_3 + Al$ mixture. The procedure systematically identifies the best space-time grid refinement subset with the lowest grid convergence index (GCI) and best linear and non-linear equation fits, i.e., the lowest mean squared error (MSE) values. This criteria identified the subset F_{3f} which closely matches the observed order-of-convergence from the linear and non-linear equation fits to the set F'_{all} in which coarse grid refinements are screened out.

By identifying the subset F_{3f}, the i) number of simulations required to obtain the extrapolated value is reduced, and ii) extrapolated value with the lowest uncertainty or grid convergence index (GCI) is determined. In all of the cases observed, the 8 parameter non-linear equation fit resulted in a lower mean squared error (MSE) (by 5 times in many cases) compared to the space only 3 parameter linear equation fit. Therefore, the non-linear equation better approximates the actual numerical error.

The validation framework presented in this thesis is appropriate for the state of the art models used to study ESMs.

Table 13: Fit the 8 parameter error ansatz in step#3.

$F_{x,t}$	λ_o [c]	α	β	δ	p	q	r	s	MSE [c]	$\Delta\tilde{e}$ [c]
F_{all}	3.6	-1.6×10^{6}	-7.6×10^{-20}	8.7×10^{5}	1.50	-19.92	1.42	-0.04	4.99	19.17
F_{2f}	3.8	-4.9×10^{8}	-1.4×10^{4}	1.4×10^{4}	2.96	0.98	0.00	0.98	3.25	9.71
F_{2c}	8.7	-1.1×10^{7}	-3.6×10^{2}	1.5×10^{2}	2.28	1.50	-0.14	1.58	6.99	15.25
F_{3f} [a,b]	0.9	-1.3×10^{7}	4.6×10^{3}	-5×10^{29}	2.32	69.8	12.2	0.47	3.19	8.67
F_{3c}	1.4	-1.8×10^{7}	0.0	-7.3×10^{5}	2.41	-75.29	1.82	1.01	5.58	17.02

$F'_{x,t}$	λ'_o [c]	α'	β'	δ'	p'	q'	r'	s'	MSE' [c]	$\Delta\tilde{e}'$ [c]
F'_{all}	4.2	-7.1×10^{8}	-1.1×10^{1}	-4.0×10^{2}	2.96	1.73	7.20	0.07	0.82	1.89
F'_{2f}	1.1	-5.8×10^{7}	-2.3×10^{5}	2.3×10^{5}	2.56	3.55	0.00	3.56	0.46	0.93
F'_{2c}	9.4	-8.3×10^{5}	2.3×10^{9}	-6.6×10^{6}	1.76	56.8	2.13	2.61	2.55	7.00
F'_{3f} [a,b]	1.9	-5.1×10^{8}	-6.1×10^{2}	-1.2×10^{11}	2.98	6.77	4.13	1.32	0.43	1.04
F'_{3c}	1.8	-1.4×10^{7}	-8.2×10^{9}	-8.6×10^{8}	2.33	32.1	3.15	2.68	1.14	2.65

[a] Contains the best subset based on minimum GCI.

[b] Contains the best subset based on minimum MSE.

[c] Units are m/s.

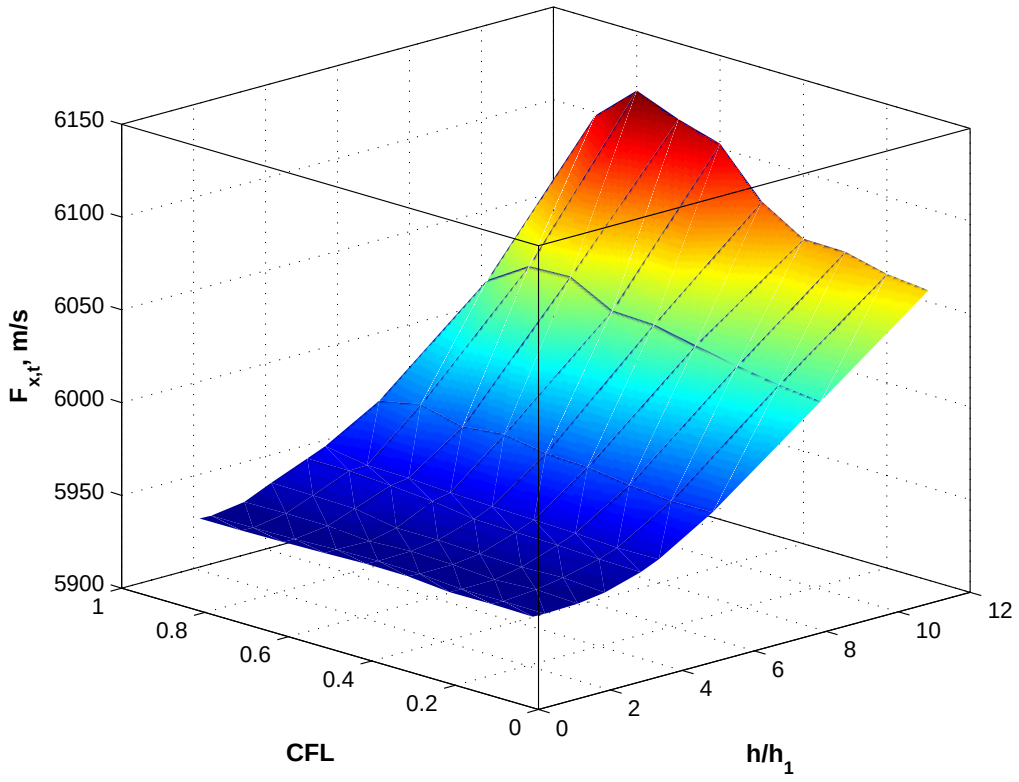

(a) Numerical solution.

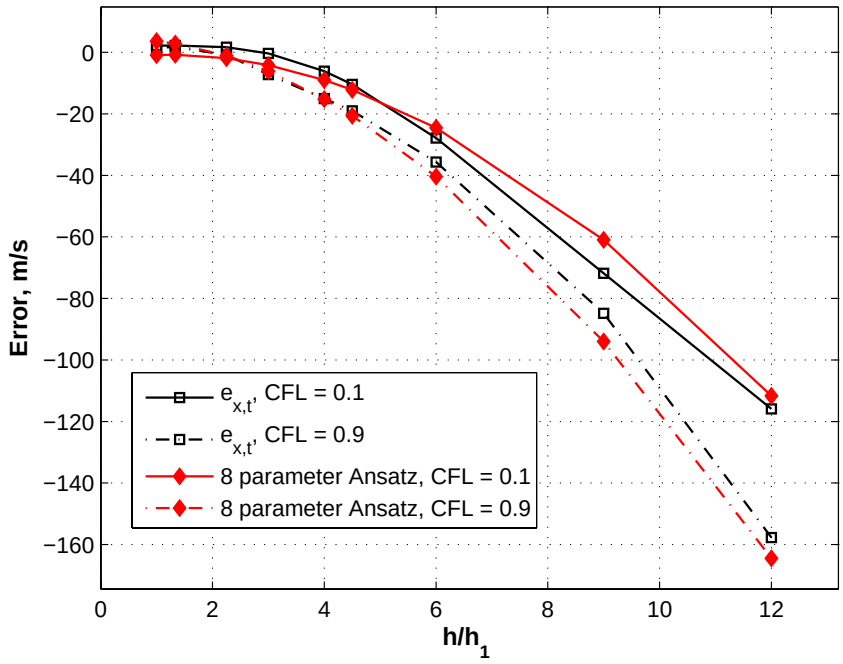

(b) 8 parameter Ansatz fit with $\tilde{F} = 5940.33\ m/s$.

Figure 43: Shock wave speed with entire range of grid refinement.

Chapter VII

CONCLUSIONS

This thesis accomplishes the primary goal of developing a fully physics based mechanochemical continuum level description of shock induced chemical reactions. The multi-scale approach developed in this thesis is focused on integrating granular level and mesoscale material behavior into a macro-scale continuum model. All of the proposed models are physically based on the mesoscale RAVEN code results. Mechanical and chemical processes are implicitly coupled. The proposed mesoscale reaction model is the first attempt to bridge mesoscale model results into a chemical reaction model.

Temperatures within the heterogeneous granular level reaction are conducted over the granule length scale. In contrast, the homogeneous model can not spatially describe the temperature.

Incorporation of the pressure in the activation energy shows qualitative improvement compared to the homogeneous granular level reaction model. The case study shows that the reaction propagation is controlled by the diffusion process for critical pressure and temperature conditions that are consistent with experimental results for a pure thermite mixture. Therefore, the mass-transport process undermines the solid-liquid reaction initiation criteria. Reactions that initiate do not necessarily propagate in the granular level reaction; propagation is limited by the mass transport of reactants through the product layer. Reverse reactions are significant in the granular level reaction, which is a result of the reduced reactant concentration at the reaction surface. These characteristics are not captured by the homogeneous granular level reaction model.

Important conclusions for the mesoscale reaction model:

- Merzhanov criteria are not needed for identification of reaction sites. Only the temperature and stress is needed at contact sites for reaction initiation according to the granular level reaction models. Merzhanov criterion is not needed if if another criterion, such as the implicit criterion in this thesis, is used. But it is one objective approach.

- The mesoscale reaction model implicitly simulates mass transport due to plastic flow that forms reaction contact sites via contact site distributions obtained from RAVEN code.

- Reasonable agrement is observed between the gas-gun simulation and the experiments with the mesoscale reaction model incorporated.

Mixture Equation of State:

The proposed porous mixture equation of state methods introduced in this thesis are robust and represent homobaric and uniform strain assumptions. These methods are useful in ESM studies and offer the following advantages over existing porous mixture equation of state methods:

- Constituent equation of state models are not required to have the same form and are not required to be easily inverted.

- Any form of pore collapse model may be employed. This permits the use of history dependent models such as the Carroll-Holt model.

- The mixture equation of state is physically represented since material parameters are not averaged.

- A weighted combination (C_m) of the two proposed methods may be used in continuum scale codes such as finite element or finite volume codes.

Spherically Symmetric Pore Collapse Equation of State:

The modified spherically symmetric pore collapse equation of state incorporates mixture rules and compressibility effects, both of which have not been introduced in previous models. Pore collapse is slower than expected although incorporation into the gas-gun simulation results in close correlation with the Hugoniot from experimental data.

Uncertainty Quantification:

From the gas-gun simulations, it is found that:

1. The verification method given in this thesis is well motivated since the determination of analytical solutions is difficult even for the simple case of a pure Al target.

2. Although the solution convergence trend may be very different in two cases (with and without porosity), the systematic verification approach identifies the same best grid set based on lowest GCI, i.e., F_{3f}.

3. Once the code is verified for one microstructure, no further convergence studies are required.

Case Studies:

Both case studies are used to demonstrate the capability of the proposed models. For the $Fe_2O_3 + Al$ system, simulated reactions agree with experimental results in which partial reactions occur. Equation of state algorithms were shown to have good agreement with ESM experimental results for pressures $P \leq 10GPa$. The entire multiscale model approach is combined in the $Ni + Al$ system. Although a pressure adjustment was required to calibrate the spherically symmetric pore collapse model, due in part to shock front pressure non-uniformity, comparison between the simulation and the experimental gas-gun results shows relatively close agreement. The estimated extent of reaction from the mesoscale reaction model is 23% which shows an increase

in shock velocity that closely matches the increase observed in experiments. The 100% reaction cases bound the 23% case and have shock velocities higher than the non reacting cases.

Summary of Contributions:

Table (14) summarizes the main contributions and lists the authors whose work has been improved upon in this thesis. Although this author list is not exhaustive, these are the leaders in their respective modeling approaches.

Future Work:

- Perform molecular dynamics simulations to calculate the equation of state for the $Ni + Al$ system at high temperatures and pressures.
- Use the multiscale approach as a means to develop non-equilibrium thermodynamics models and calibrate the unknown relaxation times.
- Employ conservative front tracking in the gas-gun simulation code. This will reduce the overheating at the material interface and increase the order of convergence. The followup verification study can be compared to the study given in this thesis.

Table 14: Shock induced chemical reaction studies. Each study is compared against the main contributions in this thesis.

	Multiscale rxn model	Heterogeneous chemical rxn	Mixture EOS	Sphere symm. pore collapse	Verification & Validation
Graham (1987)		X			
Horie and Kipp (1988)		X			
Boslough (1990)			X		
Bennett and Horie (1994)			X		
Bennett, Horie, Hwang (1994)			X		
Namjoshi and Thadhani (2000)	X	X			
Lu, Narayanan, Hanagud (2005)			X		
Choi et al. (2005)[a]			X		X
Austin et al. (2006)[a]			X		
Eakins et al. (2007)[a]		X	X		
Reding and Hanagud (2008)	X	X	X	X	X

[a] Not a shock induced chemical reaction study, however, these studies are important in understanding the thermomechanical processes involved.

Appendix A

CONSERVATION EQUATIONS

Conservation of mass and energy and the momentum balance are the governing equations for hydrodynamic simulations involving the passage of shock waves. The conservation equations and momentum balance are respectively given by the following three equations, written in spatial coordinates.

A.0.5 Conservation of Mass

$$\frac{\partial}{\partial t}\left(\bar{\rho}\right) + \nabla\left(\bar{\rho}\bar{\mathbf{v}}\right) = 0 \tag{A.1}$$

which is supplemented by *n-1* independent constituent PDE's,

$$\frac{\partial}{\partial t}\left(\phi\bar{\rho}_p\right) + \nabla\left(\phi_p\bar{\rho}\bar{\mathbf{v}}\right) = \Psi_{massp}. \tag{A.2}$$

The rate of mass production is

$$\Psi_{massp} = \Theta M_p \nu_p \tag{A.3}$$

where Θ is the phase transformation rate, M_p is the molar mass, and ν_p is the stoichiometric coefficient for constituent p. The rate of phase transitions including chemical reaction and melting are calculated in Chapter (4).

A.0.6 Conservation of Momentum

The rate of mass production Ψ_{massp} from equation (A.3) results in a change in momentum. Assuming the mixture is homokinetic, the linear and angular momentum source terms are given respectively by,

$$\bar{\Psi}_{k,LM} = \sum_p \Psi_{massp}\bar{\mathrm{v}}_k \;\; ; \;\; \bar{\Psi}_{k,AM} = \sum_p \Psi_{massp}\mathbf{e}_{ijk}x_j\bar{\mathrm{v}}_k \tag{A.4}$$

where $\mathbf{e}_{ijk}$ is the second order alternating tensor. The conservation of linear momentum is

$$\frac{\partial}{\partial t}\left(\bar{\rho}\bar{\mathrm{v}}_k\right) + \frac{\partial}{\partial x_k}\left(\bar{\rho}\bar{\mathrm{v}}_k{}^2\right) - \frac{\partial}{\partial x_k}\left(\bar{\sigma}_{kj}\right) = \bar{\rho}\bar{f}_k + \bar{\Psi}_{k,LM} \tag{A.5}$$

where summation on j is implied and $\bar{\boldsymbol{f}}$ is the body force. The conservation of angular momentum is

$$\frac{\partial}{\partial t}\left(\bar{\rho}\mathbf{e}_{ijk}x_j\bar{\mathrm{v}}_k\right) + \frac{\partial}{\partial x_k}\left(\bar{\rho}\mathbf{e}_{ijk}x_j\bar{\mathrm{v}}_k^2\right) - \frac{\partial}{\partial x_k}\left(\mathbf{e}_{imn}x_m\bar{\sigma}_{nk}\right) = \bar{\rho}\mathbf{e}_{ijk}x_j\bar{f}_k + \bar{\Psi}_{k,AM} \tag{A.6}$$

for $k = 1, 2, 3$.

A.0.7 Conservation of Energy

The rate of mass production Ψ_{massp} results in energy due to change in kinetic energy and heat release (respectively) in equation(A.7) that result from phase transformations.

$$\bar{\Psi}_{KE} = \sum_p \Psi_{massp}\frac{1}{2}\sum_k \bar{\mathrm{v}}_k^2 \;\; ; \;\; \bar{\Psi}_S = \sum_p \Psi_{massp}\mu_p \tag{A.7}$$

where μ is the specific chemical potential. $\bar{\Psi}_S$ accounts for both heat of fusion when melting phase transitions occur and heat of reaction when products are formed due to chemical reaction.

The conservation of energy is given by,

$$\frac{\partial}{\partial t}\left(\bar{E}\right) + \nabla\cdot\left(\bar{E}\bar{\mathbf{v}}\right) + \nabla\cdot\bar{\boldsymbol{q}} - \sum_k\sum_i \frac{\partial}{\partial x_i}\left(\bar{\sigma}_{ik}\bar{\mathrm{v}}_k\right) = \sum_k \bar{\rho}f_k\bar{\mathrm{v}}_k + \bar{\Psi}_{KE} + \bar{\Psi}_S \tag{A.8}$$

where E is the total energy defined as

$$\bar{E} = \bar{\rho}\left(\bar{e} + \frac{1}{2}\sum_k \bar{\mathrm{v}}_k^2\right) \tag{A.9}$$

and e is the specific internal energy. The body force $\boldsymbol{f}$ is assumed to be negligible compared to the shock pressure and will not be included from this point on.

Appendix B

RAVEN CODE

B.1 Discrete Granular Simulation Quantities

The RAVEN code is employed as part of the multi-scale framework in Figure (5). A shock is assumed to cause reactants to contact each other, and temperatures and pressures increase throughout the region behind the shock. The location of the contact sites, amount of surface area of contact between the reactants, temperature, and pressure are obtained from the dynamic response of clusters of reactants. This information is used to formulate reaction initialization in the proposed models. Information from the mesoscale reaction is directly input into the macroscale continuum model. This is described in detail in the Section on the mesoscale reaction model.

B.1.1 Contact Site Distribution

Statistical distributions from the dynamic response of discrete clusters are used to locate the contact sites with corresponding temperature, contact length, reactant quantities, and pressure. The method employed to obtain these distributions is described below. In the following definitions, contact site and hot spot quantities have the subscripts cs and hs respectively. A two-point spatial correlation, i.e., the nearest-neighbour distribution $NN1$ obtained from the RAVEN code results, is employed to quantify the spatial positioning of the contact sites. The mean $\mu_{NN1_{cs}}$ and standard deviation $\sigma_{NN1_{cs}}$ denote the $NN1$ distribution in equation (E.2) for the distance between contact sites. The contact site density ρ_{cs} $\{sites/\mu m^2\}$ is the number of contact sites n_{cs} per area downstream of the shock.

B.1.2 Contact Site Temperature

The temperature at the interface between reactants at a contact site is classified into the following two groups: 1) contact sites classified as *hot spots* in which plastic flow has generated high heat at the interface, and 2) all remaining contact sites with interface temperature close to the average bulk material temperature T_b, the temperature is $T_b < T < T_{th}$, where T_{th} is the threshold temperature.

The hot spot density ρ_{hs} is the number of hot spots n_{hs} per area downstream of the shock. Let $\mu_{T_{hs}}$ and $\sigma_{T_{hs}}$ be the mean and standard deviation lognormal temperature distribution for hot spots.

$$T_k = \begin{cases} \text{Log-N}(\mu_{T_{hs}}, \sigma_{T_{hs}}) & \text{for} k = 1...n_{hs} \\ T_b & \text{for } k = n_{hs}+1...n_{cs} \end{cases} . \tag{B.1}$$

The final piece of temperature data required from the RAVEN code is a measure of the mean bulk temperature of the mixture. The mean bulk temperature is calculated as the mass average of the temperature field in all volumes of the mixture below the aforementioned threshold temperature, T_{th}.

B.1.3 Steady Mechanical State

It is assumed that a "steady" mechanical state is reached some distance behind the shock front in the absence of chemical reactions. Here, the stress state is nearly hydrostatic and the mass mixing has reached a terminal state. Under such conditions, the surface area of contact between reactants per unit shocked volume will approach a constant value, as shown in Figure (44). The time at which this occurs (demarcated as τ in the figure) is of importance to our analysis. Here A_c is the contacting surface area of reactants in the mixture and V_s is the shocked volume.

Distributions of the contact surface area and the contact surface temperature in the statistical volume element (SVE) are calculated at $t = \tau$. It is also possible to calculate joint-probability distributions of the contact surface area and temperature

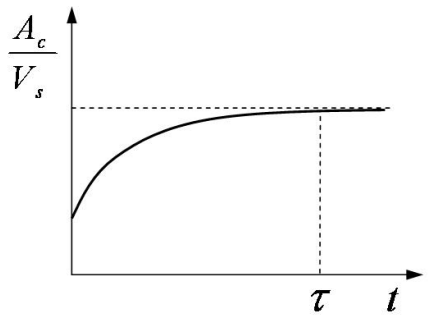

Figure 44: Contact surface area evolution.

for a higher-order description of the shocked mixture. Since the distribution of "hot" reactant surfaces is of importance to our analysis, the nearest-neighbor distribution is computed for contact surface above a prescribed threshold temperature at $t = \tau$. Since the threshold temperature is somewhat arbitrary, it may be taken as the minimum melting temperature of all reactants at zero pressure.

B.1.4 Amount of Reactants at a Contact Site

Reactants in stoichiometric quantities at the contact sites occupy a volume in the mixture that is approximated by the area with unit depth, i.e., A_k at the k^{th} contact site. The following definitions are for the binary reaction with the entire mixture contains reactants in stoichiometric quantities. A_k is calculated based on the contact site configuration that is reached at Δt_{st}.

In reality, the reactant interface geometry is complex and multiple contact sites may be located on the surface of a single granule. Although the geometry does not change significantly after the stationary condition is reached ($t = \Delta t_{st}$), mixing occurs due to chemical reaction. Material is added and removed from contact sites and new contact sites may be formed. Therefore, the amount of reactants at a contact site is difficult if not impossible to estimate accurately.

We assume that A_k remains independent of the chemical reaction process. A_k is estimated based on the sum of the initial mean areas $\mu_{A,p} = \frac{1}{4}\pi\mu_{DI,p}^2$ for reactants

p. This represents the mean area of the contact sites. The mean maximum amount of reactants at a contact site is $\mu_A|_{max} = \mu_{A,1} + \mu_{A,2}$, which corresponds to a single contact between two reactants in stoichiometric quantities. The mean area μ_A with a lognormal distribution is defined for the binary reactive mixture as

$$\mu_A = \begin{cases} \mu_A|_{max}, & if \quad \mu_A|_{max} \leq \mu_A|_{lim} \\ \mu_A|_{lim}, & otherwise \end{cases} \tag{B.2}$$

where $\mu_A|_{lim}$ is the mean limit amount of reactants at a contact site such that all of the reactants are contained within contact sites, i.e.,

$$\mu_A|_{lim} = \frac{\alpha_o \cdot A_{RAVEN} \cdot (1 - A_f(epoxy))}{n_{cs}} \tag{B.3}$$

where α_o is the initial mixture porosity, $A_f(epoxy)$ is the epoxy area fraction, and A_{RAVEN} is the total area in the SVE.

The mean area has a lognormal standard deviation given by,

$$\sigma_A = \frac{1}{2} \sum_{p=1}^{2} (\frac{1}{4} \pi \sigma_{DI,p}^2) \tag{B.4}$$

since the reactants p in the mixture are in stoichiometric quantities.

The contact length CL is estimated based on the geometry of the compacted mixture. Two morphologies are of interest in this thesis, namely spherical and flake. For spherical, $CL \approx r\sqrt{\pi}$, where r is the radius of the median sized undeformed grain in the mixture. For flake, CL is estimated as the longest dimension of the median sized undeformed flake in the mixture.

B.2 Boundary Conditions

A shock wave generated by a velocity boundary condition imposed at the particle velocity U_p at one end of the powder in Figure (4). To minimize the numerical oscillations caused by an abrupt change in the velocity profile, the velocity of the piston generating the shock is ramped with the quadratic function

$$u(t) = u \min\left(1, (t/t_{blend})^2\right), \tag{B.5}$$

where u is the steady state particle velocity and t_{blend} is equal to the first output step time.

The left and right boundaries are symmetric planes, with normal and tangential unit vectors $\mathbf{n}$ and $\mathbf{t}$, respectively, which impose the following conditions,

$$\mathbf{u} \cdot \mathbf{n} = 0, \quad \boldsymbol{\sigma} \cdot \mathbf{t} = 0 \tag{B.6}$$

on the particle velocity $\mathbf{u}$ and Cauchy stress $\boldsymbol{\sigma}$. A transmitting boundary condition, developed by McGlaun [83], permits the wave to pass through the powder without reflection.

B.3 Numerical Results

To evaluate the results of the computer calculations, the mean values of the parameters were defined by

$$\Phi_m(y) = \frac{1}{l} \int_0^l \Phi(x, y) dx, \tag{B.7}$$

where $\Phi(x, y)$ is a solution variable, x is parallel to the shock front, and y is the distance from the wall at which the velocity boundary condition is imposed.

The parameters calculated in every element include the total kinetic energy

$$E_{Tkin} = \sum_{i=1}^{NMAT} \frac{1}{2} \rho_i u_i u_i V_{f,i}, \tag{B.8}$$

the internal energy

$$E_{int} = \sum_{i=1}^{NMAT} \left[E_{c,i} + \int_0^t \sigma_i^{'} : \dot{\epsilon}_{p,i} dt \right] V_{f,i}, \tag{B.9}$$

the pressure and the density

$$P = \sum_{i=1}^{NMAT} P_i \left(\rho_i, E_i \right) V_{f,i}, \quad \rho = \sum_{i=1}^{NMAT} \rho_i V_{f,i}, \tag{B.10}$$

Here $NMAT$ is the number of materials in the element at the current time, ρ_i and $V_{f,i}$ and $V_{c,i}$ are, correspondingly, the current density, the volume fraction, and the current

volume of the ith material. The two latter parameters are connected as follows:

$$V_{f,i} = \frac{V_{c,i}}{\sum_{j=1}^{NMAT} V_{c,j}}, \quad \sum_{j=1}^{NMAT} V_{f,j} = 1, \tag{B.11}$$

Note that $V_{c,i}$ is not the specific volume of the ith material. Additionally, two mesoscopic parameters are the microkinetic energy

$$\begin{aligned} &E_{mkin} = E_{Tkin} - E_{Mkin}, \quad E_{Mkin} = \tfrac{1}{2}\rho u_m u_m, \\ &u_m(y) = \tfrac{1}{l}\int_0^l u_y(x,y)dy, \end{aligned} \tag{B.12}$$

and the spin

$$\omega = \frac{1}{l}\left(\frac{\partial u_2}{\partial x_1} - \frac{\partial u_1}{\partial x_2}\right), \tag{B.13}$$

where E_{Mkin} is the macrokinetic energy.

Note that for the calculation of the microkinetic energy, the mean value of the velocity u_m in its definition is used. These parameters are not measurable in the experiments but they are very important to the overall material behavior.

B.4 Quantities for Pore Collapse Model Calibration

During pore collapse, the most important quantities needed to calibrate the pore collapse model are the total energy dissipated E_d and the duration of the shock front τ. Pore collapse model parameters are calibrated to maximize agreement between RAVEN code and pore collapse model results for E_d and τ. The duration of the shock front, τ, is measured from RAVEN code simulation and is on the order of 3 particle diameters [92] for lower pressures (near the pore crush strength). τ decreases as the shock pressure increases. For example [92], the shock front thickness is approximately equal to 1 particle diameter for 13 GPa.

The pressure boundary condition for the pore collapse model is calculated from the RAVEN code results. Spatial distributions of pressure calculated in the finite element simulations are highly non-uniform due to the heterogeneity of powder microstructures. Therefore, averaging techniques must be used to convert the heterogeneous

pressure distributions to measures that can be used to calibrate the pore collapse model. In a method similar to that used by Benson and Conley [21], a slice of the microstructure has been taken at the horizontal centreline of the SVE. The values of pressure for the nodes that fall on the horizontal centreline are recorded. This construction yields a 1D distribution of pressure along the axial direction (y) of the microstructure, which shall be known as the centreline pressure P_c (averaging has not been performed here). If one imagines taking a horizontal slice of the microstructure at every nodal position in the transverse direction (x) and averaging the values, transversely averaged 1D profiles of pressure are obtained along the axial direction of the SVE as

$$\bar{P}_j = \frac{1}{N_x} \sum_{k=1}^{N_x} P_{j,k}. \tag{B.14}$$

Here, $\bar{P}_j$ is the transversely averaged pressure on the centreline at node j, N_z is the number of nodes in the transverse direction and $P_{j,k}$ is the pressure value at the node (j, k). The 1D transversely averaged pressure profiles are averaged along the axial position of the SVE (behind the shock front) to obtain the stationary pressure P_{st}, which may be compared with the propagated stress in experiments.

The pressure boundary condition for the pore collapse model is calculated from the RAVEN code results by using the final pressure or stationary pressure P_{st} downstream of the shock wave in the RAVEN code given by,

$$P_{st} = \frac{\rho_f u^2}{\left(\frac{\rho_f}{\rho_o} - 1\right)}. \tag{B.15}$$

Appendix C

CHEMICAL KINETICS

The general form for the chemical reactions $k = 1...N_r$ is written from [67] as

$$\sum_{i=1}^{{}^{+}N_{sk}} {}^{+}\nu_{ik}\left[C_i\right] \rightleftharpoons \sum_{i=1}^{{}^{-}N_{sk}} {}^{-}\nu_{ik}\left[C_i\right] \tag{C.1}$$

for ${}^{+/-}N_s$ reactant and product species, respectively. In the equations, ${}^{+}()$ denotes the reactant group and ${}^{-}()$ denotes the product group or forward and backward processes, respectively. ν_{ik} is the stoichiometric coefficient. C_i (mol/m^3) is the molar concentration species i defined as

$$C_i = \frac{\phi_i \bar{\rho}}{M_i} \tag{C.2}$$

and changes in the rate given by,

$$\dot{C}_i = \sum_{k=1}^{N_r} \nu_{ik}\Theta_k. \tag{C.3}$$

The volume fraction is (ξ) and the average density is $\bar{\rho} = \sum_i \xi_i \rho_i$ for all constituents i in the mixture. ϕ_i is the mass fraction and M_i is the molar mass for constituent i. Θ_k is the chemical reaction rate for reaction k. In the current study, only singe step reactions are considered, therefore, $k = 1$ is used.

The Arrhenius equation, introduced in equation (1.3), is rewritten in a generalized form in equations (C.4-C.5). This equation comes from [88, 78]. The reaction rate for reaction k is given by,

$$\tau_{\Theta k}\dot{\Theta}_k + \Theta_k = {}^{+}k_k \prod_{i=1}^{{}^{+}N_{sk}} \left[C_i\right]^{{}^{+}\nu_{ik}} - {}^{-}k_k \prod_{i=1}^{{}^{-}N_{sk}} \left[C_i\right]^{{}^{-}\nu_{ik}}. \tag{C.4}$$

The equilibrium form is obtained by letting $\tau_\Theta = 0$ and is known as the parabolic rate law used in many chemical reaction systems [96]. This is similar to the approach

taken in CHEMKIN [67] and by Do and Benson [33]. The modified Arrhenius rate coefficients are given by [105] as,

$$\begin{aligned} {}^{+}k_k &= {}^{+}A_k \; T^{+\beta_k} \; P^{+\eta_k} \; {}^{+}f_k(1-\varphi) \exp\left\{-\frac{\Delta^{+}\mu_{ak}}{RT}\right\}, \\ {}^{-}k_k &= {}^{-}A_k \; T^{-\beta_k} \; P^{-\eta_k} \; {}^{-}f_k(1-\varphi) \exp\left\{-\frac{\Delta^{-}\mu_{ak}}{RT}\right\} \end{aligned} \quad . \tag{C.5}$$

φ is the global degree of conversion of the reactant and is defined by the conversion of the reactants, i. e., $\varphi = 1-(\phi_1+\phi_2)$ for binary reactions or reactions in which two reactants are considered. R is the universal gas constant ($8.314472 J \cdot K^{-1} \cdot mol^{-1}$). T is the reacting temperature or temperature at the location where the reactants are in contact. P is the pressure. A is the pre-exponential or frequency factor. μ_a is the activation energy. The traditional Arrhenius form has β and η equal to zero and $f(1-\varphi) = 1$. In the modified form [105], β and η can be different from zero and are usually determined empirically.

C.1 Transition State

The main contribution developed in this section is the addition of the stress in the calculation of the transition state energy. This has not been attempted in any previous study on shock induced chemical reactions.

Both reaction and diffusion rates depend on the change in the free enthalpy $\Delta\mu_a$ with the assumed Arrhenius kinetic rate parameter given by,

$$k = k_o \exp\left(\frac{-\Delta\mu_a}{RT}\right). \tag{C.6}$$

$\Delta\mu_a$ is the energy required to reach the transition state. k_o is related to the frequency of the particle in its potential well. This refers to the reactant and product states. The exponential term represents the probability (from Boltzmann statistics) that an attempt will succeed in reaching the transition state and depends on $\Delta\mu_a$ and T.

The transition state is assumed in this thesis to be the intermediate reaction step between the reactant mixture and the product state. For example, the transition

state is X_2Y_2Z in the reaction $2XY + Z \rightarrow X_2Y_2Z \rightarrow 2X + Y_2Z$, where $v_1 = -2$, $v_2 = -1$, $v_3 = 2$, and $v_4 = 1$ are the stoichiometric coefficients corresponding to the quantities, XY, Z, X, Y_2Z (see Figure(45)). The opposite signs for reactants and products is for the purpose of the mass balance,

$$\sum_p M_p v_p = 0 \tag{C.7}$$

where v_p is the stochiometric coefficient for constituent p.

The total differential of the internal energy dU in equation (C.8) considers the energy in a stressed solid where dS is the differential entropy production [105].

$$dU = TdS + V\bar{\boldsymbol{\sigma}} : d\bar{\boldsymbol{\epsilon}} + \sum \mu_i dn_i \tag{C.8}$$

where V is the partial molar volume and dn_i is the number of moles of component i. Here, $\boldsymbol{\epsilon}$ and $\boldsymbol{\sigma}$ are symmetric tensors [105]. The chemical potential in equation (C.8) is related to the Gibbs free energy μ and Helmholtz free energy H, i.e,

$$\mu_i(\boldsymbol{\sigma}, T) = \left(\frac{\partial \mu}{\partial n_i}\right)_{n_j, \boldsymbol{\sigma}, T} = \left(\frac{\partial H}{\partial n_i}\right)_{n_j, \boldsymbol{\sigma}, T} - V\sigma_{jk} \cdot d\epsilon_{jk}. \tag{C.9}$$

We neglect the first term on the RHS of equation (C.9) since it is usually small compared to the second term [105], which is the reversible work done at a given stress by the volume expansion $Vd\boldsymbol{\epsilon}$ if dn_i is added to the system under stress [105].

If the stressed state is considered with only hydrostatic pressure P, the chemical potential becomes

$$\mu_i(\boldsymbol{\sigma}, T) \cong \mu_i(P^o, T) + PV_i \tag{C.10}$$

where $P^o = 1atm$ is the ambient pressure. Therefore, the change in free energy due to pressure is

$$\Delta\mu_\sigma = \sum_i P_i V_i \tag{C.11}$$

where the summation must include all mixture constituents with corresponding pressure P_i. Figure (45) shows an ideal case for $\Delta\mu_\sigma$ when both the reactants and the

products are at $P = 0$ and the transition state is at $P < 0$. Generally this is not the case, therefore, it is assumed in all computations shown in this thesis that the pressure is constant for all reactants, transition state, and products. Under this constant pressure assumption, when $P > 0$ as is the case for shock compression, $\Delta\mu_\sigma < 0$ as shown in Figure (45) is obtained only when $\sum_i V_i < 0$ which corresponds to a transition state molar volume less than the reactant molar volume. This means that reactions may proceed at an increased rate due to an increase in pressure.

The partial molar volume of constituent i is

$$V_i = \frac{M_i}{\rho_i} v_i. \tag{C.12}$$

The zero stress (or ambient pressure $P^o = 1atm$) chemical potential or thermal contribution is defined in equation (C.13).

$$\begin{aligned} \mu_p(P^o, T) = \quad & \Delta\mu_p(P^o, T) = \Delta H^f_{o_p}(P^o, T^o) + \int_{T'=T_o}^{T} c_{p_p}(P^o, T')dT' \\ & -T \cdot \left[\Delta S_p(P^o, T^o) - \int_{T'=T_o}^{T} \frac{c_{p_p}(P^o, T')}{T'} dT'\right] \end{aligned} \tag{C.13}$$

where $T^o = 298K$ is the reference temperature and c_{p_p} is the heat capacity for constant pressure for constituent p. The stoichiometric mixture change in free energy for $P = P^o$ is given by

$$^{+/-}\Delta\mu^o(P^o, T) = \sum_p \mu_p(P^o, T) \cdot v_p \tag{C.14}$$

and is shown for both reactants and products respectively in Figure (45).

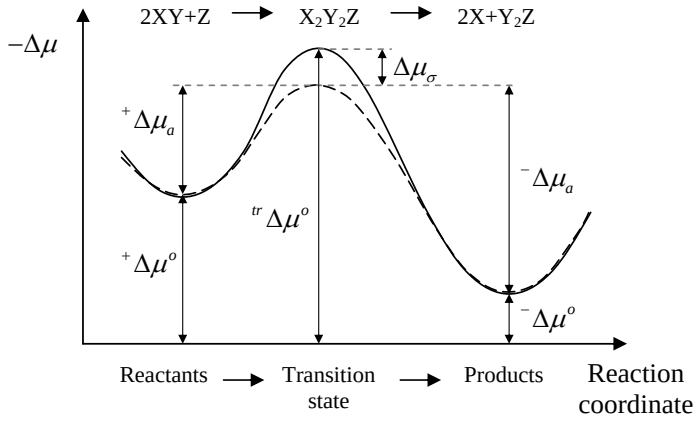

Figure 45: Idealized schematic of the reaction path.

Appendix D

CONSTITUENT MATERIAL MODELS AND PROPERTIES

D.1 Mixture Strength

In the macro-scale, each constituent in a mixture is separated by interfaces with other constituents or voids. Physical discreteness is transformed to a mathematical continuum. A continuum is defined in a Euclidean space with each point in the space is identical as a particle and is continuously distributed throughout the volume and during a deformation points in the neighborhood of a point will remain in the corresponding neighborhood in the deformed domain after deformation.

We follow the partial traction and partial stress description by Trusdell, Rajagopal, and Tao [98] in which $\mathcal{S}$ is a surface in the body. $\mathbf{n}_{\mathcal{S}}$ is the normal vector to $\mathcal{S}$ at the point $\mathbf{x}$ contained within the body. The notation presented here is altered from the form given by Rajagopal and Tao [98] by defining the traction vector $\boldsymbol{t}_p$ and the Cauchy stress tensor $\boldsymbol{\sigma}_p$ associated with each constituent p in the mixture, where

$$\boldsymbol{t}_p = (\boldsymbol{\sigma}_p)^T \mathbf{n}_{\mathcal{S}}. \tag{D.1}$$

Since this thesis is focused on small particle mixtures such as micron-scale or nano-scale inter-metallic particles, we assume the probability of the mixture constituent p in contact with $\mathcal{S}$ is equal to its occupied volume fraction [77], i.e.,

$$\varsigma_p = \xi_p. \tag{D.2}$$

The physical basis for this assumption comes from reducing the size of particles with uniform geometry. This assumption is valid when mixtures contain granules

of the same size and dimension, thus, is invalid for mixtures containing particles with different geometry, e.g., both flake and spherical particles as shown in Figure (46). In this case, the cut-away shows that the cross section of a flake can take up a disproportionate part of the total surface area. Therefore, the mixture rule in equation (D.2) would be invalid for such a mixture.

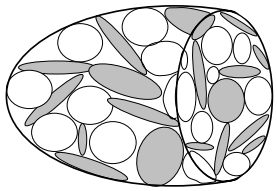

Figure 46: Schematic for mixtures containing flake and spherical particles.

Using the assumption in equation (D.2), the total mixture traction $\bar{\boldsymbol{t}}$ and Cauchy stress tensor $\bar{\boldsymbol{\sigma}}$ are given by [98],

$$\bar{\boldsymbol{t}} = \sum_{p} \boldsymbol{t}_p, \tag{D.3}$$

and

$$\bar{\boldsymbol{\sigma}} = \sum_{p} \boldsymbol{\sigma}_p, \tag{D.4}$$

so that

$$\bar{\boldsymbol{t}} = \bar{\boldsymbol{\sigma}}^T \mathbf{n}_{\mathcal{S}}. \tag{D.5}$$

The Cauchy stress tensor in equation (D.4) is decomposed into its hydrostatic P and deviatoric $\boldsymbol{\sigma}^{'}$ components,

$$\bar{\boldsymbol{\sigma}} = -\bar{P}\boldsymbol{I} + \bar{\boldsymbol{\sigma}}^{'} \tag{D.6}$$

where $\boldsymbol{I}$ is the second-order identity tensor and the assumption is that the mixture is isotropic.

Thermomechanical constitutive relationships include an equation of state in the form $P_p = f_p(\rho, e)$ and a strength relationship in the form $\boldsymbol{\sigma}_p^{'} = \boldsymbol{\sigma}_p^{'}\left(\boldsymbol{D}, \bar{T}, \boldsymbol{z}\right)$ for constituent p, where $\boldsymbol{D}$ is the symmetric part of the velocity gradient defined. $\bar{T}$

is the mixture temperature. $\boldsymbol{z}$ denotes internal state variables [77]. Note that the overbar denotes mixture averaged quantities. The velocity gradient is defined as

$$L = \nabla \boldsymbol{v} = \frac{\partial v}{\partial x} \tag{D.7}$$

Here, we have adopted the notation used by Rajagopal and Tao [98] to express ∇ as the gradient from an Eulerian point of view. Then we have the symmetric part of the velocity gradient defined as

$$D = 1/2 \left(L + L^T \right). \tag{D.8}$$

Thermodynamic equilibrium is assumed between mixture constituents only in the macro-scale model. According to the thermodynamic equilibrium assumption and using equation (D.2), the mixture average shear modulus is written as,

$$\bar{\mu}(\bar{T}) = \frac{1}{\alpha_o} \sum_p \xi_p \mu_p(\bar{T}). \tag{D.9}$$

$\mu_p(\bar{T})$ is assumed to depend linearly on temperature such that $\mu_p(\bar{T} = T_o) = \mu_o$ and $\mu_p(\bar{T} = T_{m,p}) = 0$. T_m is the melting temperature. $\bar{\mu}(\bar{T}) = 0$ when $T \geq T_{m,p}$ for any constituent p in the mixture. $\alpha_o = \rho/\rho_d$ is the porosity where ρ_d is the non-porous density and the subscript o denotes the initial or zero pressure state.

The material is assumed to yield when the equivalent stress exceeds the mixture yield stress, i.e., $\sigma_{eq} > \bar{Y}_{mix}$. Von Mises or maximum distortion energy criterion, is used and the radial return method is applied to the stress deviators. The equivalent stress is

$$\begin{aligned} \sigma_{eq} &= \sqrt{3J_2} \\ &= \sqrt{\frac{(\sigma_{11}-\sigma_{22})^2+(\sigma_{22}-\sigma_{33})^2+(\sigma_{33}-\sigma_{11})^2+6(\sigma_{12}^2+\sigma_{23}^2+\sigma_{31}^2)}{2}} \\ &= \sqrt{\tfrac{3}{2}\sigma_{ij}^{'}\sigma_{ij}^{'}} \end{aligned} \tag{D.10}$$

where J_2 is the second deviatoric stress invariant and $\sigma_{ij}^{'}$ are components of the stress deviator tensor. Subscripts ij represent the coordinates.

With 1D strain, equivalent stress is given by,

$$\sigma_{eq} = \sqrt{\frac{3}{2}\left(\left(\bar{\sigma}_{xx}^{\prime}\right)^2 + 2\left(\bar{\sigma}_{yy}^{\prime}\right)^2 \right)} \tag{D.11}$$

where the shock propagates along the x-axis. The stress deviators are given in rate form by,

$$\dot{\bar{\sigma}}'_{xx} = \frac{4}{3}\bar{\mu}\frac{\partial \bar{\mathrm{v}}_x}{\partial x} \quad , \quad \dot{\bar{\sigma}}'_{yy} = \dot{\bar{\sigma}}_{zz} = -\frac{2}{3}\bar{\mu}\frac{\partial \bar{\mathrm{v}}_x}{\partial x}. \tag{D.12}$$

Equation (D.12) is valid for small strains and is appropriate for mixtures containing binders such as epoxy since since these materials yield at small strains.

The porous mixture yield strength is given by,

$$\bar{Y}_{mix} = \frac{1}{\alpha}\bar{Y} \tag{D.13}$$

where the assumption in equation (D.2) gives,

$$\bar{Y} = \sum_p \xi_p Y_p. \tag{D.14}$$

Constituent yield strength Y_p generally depends on the effective mixture shear strain rate $\dot{\bar{\gamma}}$ and mass-fraction averaged temperature $\bar{T}$, i.e., $Y_p = Y_p(\dot{\bar{\gamma}}, \bar{T})$. Individual strength models are discussed in Appendix (D.3).

D.2 Constituent Equation of State

The relationship needed to link pressure to the density and internal energy of the material is called the equation of state (EOS). The two most commonly used models used for the high pressure regimes found in shock physics are the Grüneisen and the Murnaghan EOS. Much of the experimental EOS data that has been gathered for solids and liquids contains material parameters for these two models.

The Mie-Grüneisen EOS is extensively used in the determination of shock, residual temperatures, and for predicting the shock response of porous materials. The Grüneisen EOS can easily be derived from the Rankine-Hugoniot equations [85] and is written in terms of the specific energy e or temperature T and specific volume v as,

$$P(e,v) = \frac{C_o^2\,(v_o - v)}{\left[v_o - S_1\,(v_o - v)\right]^2} + \frac{\Gamma}{v}\left[e - \frac{1}{2}\left(\frac{C_o\,(v_o - v)}{v_o - S_1\,(v_o - v)}\right)^2\right] \tag{D.15}$$

where C_o is the acoustic wave speed, S_1 is the slope of the linear $U_s - U_p$ curve,U_p is the particle velocity, and Γ is the Grüneisen parameter. Equation (D.15) is not easily inverted, i.e., solved for v.

The Grüneisen parameter is defined as

$$\Gamma = V\left(\frac{\partial P}{\partial e}\right)_V = \frac{\Gamma_o \rho_o}{\rho} \,. \tag{D.16}$$

The Murnaghan EOS [86] is derived from the variation of the bulk modulus with respect to pressure and takes the form in terms of the reference temperature T_o as

$$P = \frac{\beta_{T_o}}{\beta'_{T_o}}\left[\left(\frac{\rho}{\rho_o}\right)^{\beta'_{T_o}} - 1\right] + C_v \Gamma_M \rho_o \left(T - T_o\right) \tag{D.17}$$

where $\beta_{T_o} = -V(\partial P/\partial V)|_{T_o}$ is the isothermal bulk modulus at the reference temperature, $\beta'_{T_o} = (\partial\beta/\partial P)|_{T_o}$ is the pressure derivative of the isothermal bulk modulus at the reference temperature, C_v is the specific heat capacity under constant volume, ρ_o is the reference density, and Γ_M is a material parameter similar to the Grüneisen parameter Γ. Equation (D.17) is easily inverted, i.e., solved for ρ.

EOS parameters are given in Table (15). For simplicity, the Grüneisen parameter is assumed to be constant and is estimated using the common approximation $\Gamma = 2S_1 - 1$ [85]. All other Grüneisen parameters were obtained from [80] where values for $Al_{(s)}$ were taken from the $Al - 1100$ data. Further details are given by R. A. Austin [4]. All of the Murnaghan parameters are obtained from Bennett, Horie, and Hwang [11] with the exception of the isothermal bulk modulus[20] β_{T_o} since these values are reported one order of magnitude too low.

D.3 Constituent Strength Models

Strength models are available for Ni and Al for a range of strain-rates and effective plastic strain. A brief description of the two models used in this thesis is provided here; the literature should be referenced for complete details and material parameters. Both models are not valid for strain rates $\dot{\epsilon} > 10^5 s^{-1}$.

D.3.1 Aluminum

A constitutive model for the stress-strain response of high-purity aluminium has been proposed by Klepaczko et al [69]. Here, thermally activated mechanisms are used to model the kinetics of dislocation glide and the rate-sensitive generation of dislocations is taken into account. Thus, the model is sensitive to variations in temperature and strain rate. The current state of the microstructure is tracked through the dislocation density, which serves as a single, physically based internal state variable. The evolution of the dislocation density is based on the competing processes of dislocation generation and annihilation.

It is assumed that the flow stress in shear may be decomposed as $\tau = \tau_u + \tau^*$, where τ_u is the internal (athermal) stress and τ^* is the effective (thermally activated) stress. The decomposition of the flow stress assumes the existence of different barriers that impede the motion of dislocations. The internal stress is associated with long-range obstacles that are athermal in character (e.g. grain walls, cell walls and cell dislocations). The internal stress is expressed as

$$\tau_u = \alpha_i \mu(T) b \sqrt{\hat{\rho}} \tag{D.18}$$

where α_i is the dislocation/obstacle interaction coefficient, μT is the temperature-dependent shear modulus in equation (D.19), b is the Burgers vector, and $\hat{\rho}$ is the dislocation density.

$$\mu(T) = \mu_o \left[1 - \frac{T}{T_m} \exp \left\{ \theta_* \left(1 - \frac{T_m}{T} \right) \right\} \right] \tag{D.19}$$

where T_m is the melting temperature and θ_* is a material constant.

The effective stress is associated with weaker obstacles (e.g. forest dislocations and Peierls barriers) that may be overcome by thermal activation. The effective stress is cast in a generalized Arrhenius form,

$$\tau^* = \tau_0^* \left(\hat{\rho} \right) \left[1 - \left\{ \frac{kT}{\Delta G_0} \ln \left(\frac{v_0 \left(\hat{\rho} \right)}{\dot{\bar{\gamma}}^p} \right) \right\}^{1/q} \right]^{1/p} \tag{D.20}$$

where $\dot{\bar{\gamma}}^p$ is the effective plastic shear strain rate, $\tau_0^*(\hat{\rho}) = \Delta G_0\sqrt{\hat{\rho}}/(ba)$ is the thermally activated part of the threshold stress (i.e. the stress barrier associated with short range obstacles at 0 K with activation distance a), $v_0(\hat{\rho}) = f\hat{\rho}v_D b^2$ is the attempt frequency factor at $0K$, k is Boltzmann's constant, ΔG_0 is the activation energy at $0K$, and p and q are constants that describe the shape of the energy barrier. Here, f is the fraction of mobile dislocations and v_D is the Debye frequency. The dislocation density is updated to account for the evolution of the microstructure during a general load history. The rate of change in the dislocation density with respect to the effective plastic shear strain is expressed as

$$\frac{\partial\hat{\rho}}{\partial\dot{\bar{\gamma}}^p} = M_{II}(\dot{\bar{\gamma}}^p) - k_a(\dot{\bar{\gamma}}^p, T)[\hat{\rho} - \hat{\rho}_0]. \tag{D.21}$$

Here, $M_{II}(\dot{\bar{\gamma}}^p)$ is the rate-dependent dislocation multiplication term, $\hat{\rho}_0$ is the initial dislocation density, and $k_a(\dot{\bar{\gamma}}^p, T)$ is the dislocation annihilation factor given by

$$k_a(\dot{\bar{\gamma}}^p, T) = k_o\left(\frac{\dot{\bar{\gamma}}^p}{\dot{\gamma}_0}\right)^{-2m_0 T} \tag{D.22}$$

where k_o is the anihilation factor at $0K$, m_0 is the strain-hardening rate-sensetivity const., and $\dot{\gamma}_0 = v_0(\hat{\rho})$ is the threshold strain rate.

D.3.2 Nickel

An internal state variable model for noncrystalline high-purity nickel ($Ni270$) is proposed by Follansbee et al [43]. State variables are defined for dislocations interacting with interstitial carbon atoms (55 ppm for $Ni270$) and for dislocations interacting with other dislocations. The following material parameter values are for $Ni270$.

Thermal activation is similar to the Klepaczko model in that the deformation kinetics at constant structure are described using an Arrhenius expression of the form

$$\dot{\epsilon} = \dot{\epsilon}_0 \exp\left[\frac{\Delta G(\sigma_t/\hat{\sigma}_t)}{kT}\right] \tag{D.23}$$

where $\hat{\sigma}_t$ is the mechanical threshold stress, ΔG is the free energy, $\dot{\epsilon}_0$ is a constant, and k is Boltzmann's constant.

The yield stress in equation (D.24) is decomposed into the athermal component $\sigma_a = 50MPa$ and the thermally activated component $s(\dot{\epsilon}, T)$. The subscript I denotes the contribution from dislocation interactions with carbon atoms and the subscript ϵ denotes the contribution from interactions with stored dislocations. The mechanical threshold stresses $\hat{\sigma}$ are the internal state variables in this model.

$$\sigma = \sigma_a + \left[\left(s_I \left(\dot{\epsilon}, T \right) \hat{\sigma}_I \right)^n + \left(s_\epsilon \left(\dot{\epsilon}, T \right) \hat{\sigma}_\epsilon \right)^n \right]^{1/n} \tag{D.24}$$

where $n = 1$ is the exponent in the power law superposition rule employed [43]. The phenomenological relation used for describing s is given by

$$s_i = \left(1 - \left[\frac{kT}{g_{oi}\mu(T)b^3} \ln \frac{\dot{\epsilon}_{0i}}{\dot{\epsilon}} \right]^{1/q_i} \right)^{1/p_i} \tag{D.25}$$

where Burgers vector is $b = 2.517\mathring{A}$ and g_{oi} is the normalized total activation free energy that characterizes obstacle i and $\dot{\epsilon}_{0i} = 10^7 s^{-1}$. $g_{oI} = 0.103$ corresponding to $\hat{\sigma} = 11MPa$ and $g_{o\epsilon} = 1$ (typical for long-range dislocation/dislocation interactions which are less thermally activated) [43]. The material parameters p_i and q_i have physical interpretations [71] similar to those used in the Klepaczko model. Here, $p_\epsilon = p_I = 2/3$ and $q_\epsilon = q_I = 1$ which correspond to box-like obstacles.

The mechanical threshold stress evolves according to

$$\frac{d}{d\epsilon}\hat{\sigma}_\epsilon = \theta_0 \left(\dot{\epsilon} \right) \left(1 - \frac{\tanh \left[\frac{2\hat{\sigma}_\epsilon}{\hat{\sigma}_{\epsilon_s}} \right]}{\tanh(2)} \right) \tag{D.26}$$

where $\hat{\sigma}_{\epsilon_s}$ is the steady state value of $\hat{\sigma}_\epsilon$ and θ_0 is the Stage II hardening rate. These parameters are fit to strain-rate data [43] and given by $\theta_0 = 5.04 + 0.103 \ln(\dot{\epsilon})\ GPa$ and $\hat{\sigma}_{\epsilon_s} = 870.8 + 12.8 \ln(\dot{\epsilon})\ MPa$.

The temperature dependent shear modulus is given by

$$\mu(T) = 84.52 - \frac{8.839}{\exp \frac{258}{T} - 1} \quad \{GPa\}. \tag{D.27}$$

The remaining constituent material properties are listed in Table (16).

D.4 Hollow Sphere Pore Collapse Results

As with the modified Carroll-Holt model, computation is performed with 4^{th} order Runge-Kutta and a time step of $0.5ns$. Figures (47-49) show the sensitivity to changes in the material parameters with respect to the pore closure, temperature, stress, and strain rate. These results show that the temperature near the center of the pore, $r = 0$, is much higher than in the modified Carroll-Holt model. Additionally, strain rates in the hollow sphere model are significantly higher.

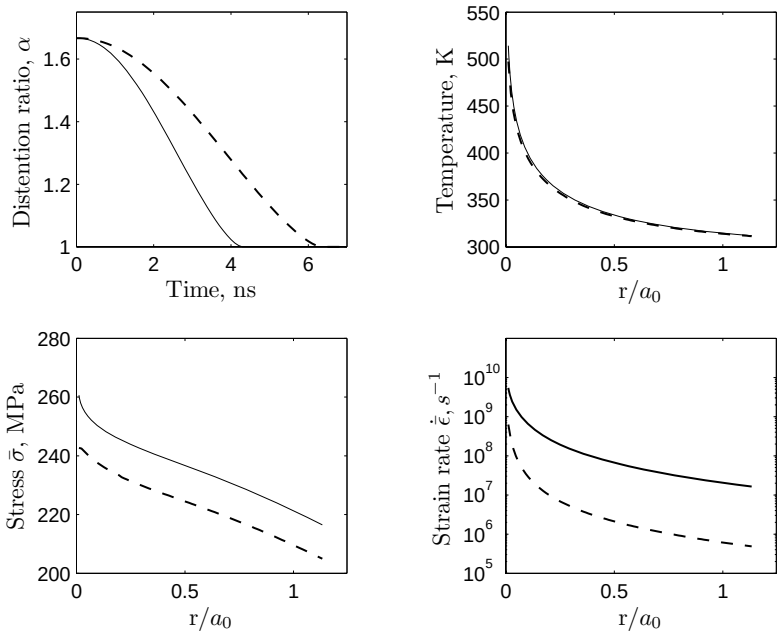

Figure 47: Pore collapse with $P = 5GPa$, $a_o^{'} = 10\mu m$, and $\mu_f = 1$ with $C_I = 0$ in the solid line and $C_I = 1$ in the dashed line. Temperature, stress, and strain rate are given at the point of pore closure.

D.5 Bisection Method Applied to the Mixture Equation of State

The equation of state for the mixture takes the form,

$$\bar{P} = f(\bar{\rho}\bar{T}) \tag{D.28}$$

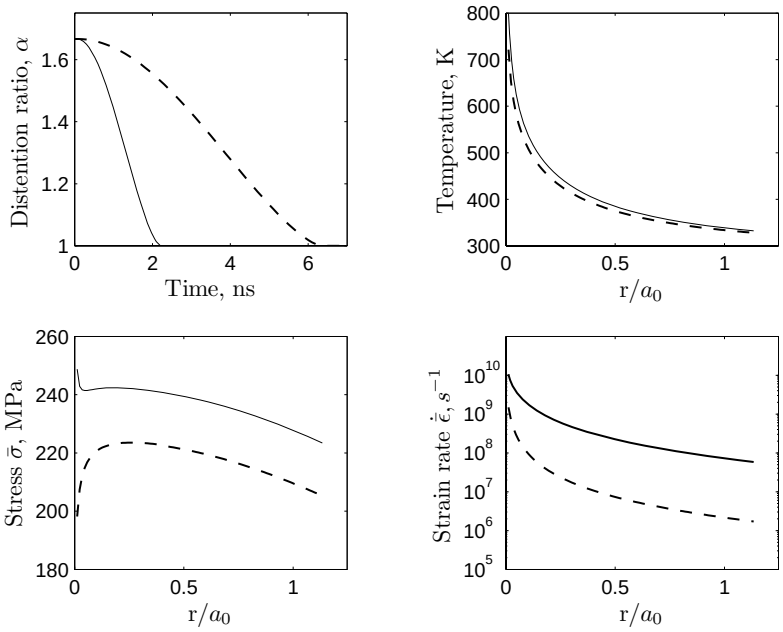

Figure 48: Pore collapse with $P = 5GPa$, $C_I = 1$, and $\mu_f = 1$ with $a_o^{'} = 10\mu m$ in the solid line and $a_o^{'} = 20\mu m$ in the dashed line. Temperature, stress, and strain rate are given at the point of pore closure.

where $\bar{P}$ is the mixture pressure, $\bar{\rho}$ is the mixture density, and $\bar{T}$ is the mixture temperature. As the density and temperature increase, the pressure increases monotonically. This is proved by the second law of thermodynamics, i.e.,

$$\delta W_u < -dU + T_R dS - P_R dV + \sum \mu_{iR} dN_i \tag{D.29}$$

where δw_u is the amount of useful work done by the sub-system, over and beyond the work $P_R dV$ done by the sub-system expanding against the surrounding external pressure. $\mu_i R$ is the chemical potential defined in equation (C.9) and N_i is the number of particles of each species i. Any increase in temperature or pressure results in usable work. In addition, energy contributions from chemical interactions generates useful work. $f(\bar{\rho}\bar{T})$ is monotonic and continuous since $d\bar{\rho}$ is proportional to dV.

The bisection method repeatedly divides an interval in half and then selects the subinterval in which a root exists. For the mixture equation of state, the root is located at $\bar{\rho}^*$ to give the pressure $\bar{P}^*$ where $\bar{\rho}^*$ is known. Given two points, $f(\bar{\rho}_1, \bar{T})$

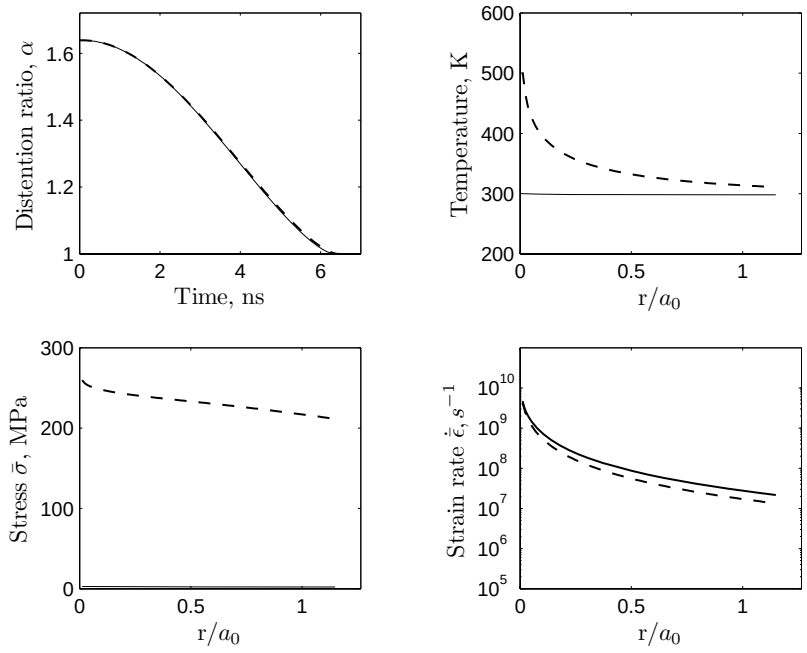

Figure 49: Pore collapse with $P = 5GPa$, $a_o^{'} = 10\mu m$, and $C_I = 1$ with $\mu_f = 0$ in the solid line and $\mu_f = 1$ in the dashed line. The lines nearly overlap in the upper left plot. Temperature, stress, and strain rate are given at the point of pore closure.

and $f(\bar{\rho}_2, \bar{T})$ such that $\bar{\rho}_1 < \bar{\rho}^* < \bar{\rho}_2$, we know by the intermediate value theorem that f must have at least one root in the interval $[f(\bar{\rho}_1), f(\bar{\rho}_2)]$ as long as f is continuous on this interval. The bisection method divides the interval in two by computing $f(\bar{\rho}_3, \bar{T}) = 1/2[f(\bar{\rho}_3, \bar{T}) + f(\bar{\rho}_3, \bar{T})]$. There are two possibilities, either $\bar{\rho}_3 < \bar{\rho}^*$ or $\bar{\rho}_3 > \bar{\rho}^*$. Since f is monotonic, if $\bar{\rho}_3 < \bar{\rho}^*$, then the root now lies within the interval $[f(\bar{\rho}_3), f(\bar{\rho}_2)]$. If $\bar{\rho}_3 > \bar{\rho}^*$, then the root lies within the interval $[f(\bar{\rho}_1), f(\bar{\rho}_3)]$.

Table 15: Equation of state and thermodynamic material parameters for the $Fe_2O_3 - Al$ system.

Parameter	$Al_{(s)}$	$Al_{(l)}$	$Fe_2O_{3(s)}$	$Al_2O_{3(l)}$	$Fe(l)$	$Epon828$	$Units$
ρ_o	2700	2380	5274	2960	6590	1200	$kg \cdot m^{-3}$
C_p	0.90	0.90[a]	0.607	0.714	0.450	2.10	$kJ \cdot kg^{-1} \cdot K^{-1}$
k_q	222	222[a]	5	35	76.2	0.2	$W \cdot m^{-1} \cdot K^{-1}$
C_o	5.38	–	6.30	–	–	2.60	$km \cdot s^{-1}$
S_1	1.34	–	1.176	–	–	1.59	–
Γ	1.68	–	2.00[c]	–	–	2.18	–
β_{S_o}	76.7/79.0[d]	52.3	202.7/207.0[d]	252.0	136.0	8.11[b]	GPa
β'_{S_o}	3.693	3.693[a]	4.35	5.00	3.97	5.36[b]	–
Γ_M	2.00	2.00[a]	1.99	1.32	2.10	2.18[c]	–

[a] Indicates that the solid properties were used.

[b] Grüneisen values are used with approximations from equation (3.2).

[c] Assume that $\Gamma = \Gamma_M$.

[d] Adjusted to fit the Grüneisen $T = 298K$ isotherm over the range $0 \leq P \leq 30GPa$).

Table 16: Material properties.

Parameter	$Al-1100$ [66]	Ni	$Units$
Shear modulus, μ	26.0	76	GPa
Melting temperature, T_m	926	1728.15	K
Latent heat of melting, ΔH_m	390	305.6	$kJ \cdot kg^{-1}$

Appendix E

SYNTHETIC ANNEALING

The MSR and DPS model discussed in this thesis employ the nearest-neighbour $NN1$ distribution to quantitatively measure a micro structure distribution. For the MSR model, contact site locations with correlated temperature distributions are determined by a synthetic annealing procedure. The DPS model requires algorithms that synthetically generate microstructure based on prescribed mixture parameters. Important $NN1$ distribution definitions are given here. The detailed annealing procedure is given by Austin [4].

For 2D representations, spatial locations of particles (x_k, y_k) are given randomly by a uniform distribution, i.e., $u_i \in [0, 1]$,

$$(x_k, y_k) = (u_i X, u_{i+1} Y) \tag{E.1}$$

where X and Y are scalar dimensions. This procedure is supplemented by the addition of certain conditions such as to prevent excessive overlaps between particles.

Experimental results suggest that the $NN1$ distribution follow the Gaussian or normal distribution, which is given approximately by,

$$P\left[d_k\right|\left(d_i - \delta d/2\right) < d_k \leq \left(d_i + \delta d/2\right)] = a_{NN} \cdot \exp\left\{-\frac{1}{2}\left(\frac{d_i - \mu}{\sigma}\right)^2\right\} \tag{E.2}$$

for $i = 1, ..N_d$, where N_d is the number of bins selected to discretize $NN1$, δd is the width of the bins, μ is the mean, σ is the standard deviation, d_i is the distance between the site and its nearest-neighbour, a_{NN} is the scaling parameter so that the sum of the probabilities of each value of d_i sum to unity, i.e., $a_{NN} \cdot \sum_{i=1}^{N_d} P(d_i) = 1$.

Let $P(d_i)|_{syn}$ denote the synthetic probability obtained from the annealed configuration and $P(d_i)|_{act}$ denote the actual or experimental distribution from equation

(E.2). The objective function to be minimized is

$$e_{NN} = \sqrt{\sum_{i=1}^{N_d} (P(d_i)|_{syn} - P(d_i)|_{act})^2}. \tag{E.3}$$

The coordinates (x_k, y_k) are randomly perturbed using an iterative simulated annealing technique [68] until $NN1$ distributions closely match the experimental observations, i.e., e_{NN} is sufficiently small.

Appendix F

NUMERICAL INTEGRATION

F.1 Hyperbolic Equations

The states on the left and right side of the discontinuity u_L and u_R (u is the density, velocity, or energy) are approximated by extrapolating the cell average by monotone upstream-centered schemes for conservation laws reconstruction, therefore, the flux at the interface F_I at time t^n is defined by,

$$F_I^{n,L} = f\left(u_L^n\right) - v^n u_L^n = f\left(u_R^n\right) - v^n u_R^n = F_I^{n,R} \tag{F.1}$$

where $f(u)$ is the hyperbolic equation and v is the material velocity.

We denote the numerical approximation of U_j^n and $F_{j+1/2}^{n+1/2}$ be $\mathcal{U}_j^n$ and $\mathcal{F}_{j+1/2}^{n+1/2}$ respectively. The monotone upstream-centered schemes for conservation laws reconstruction is used with Lax-Friedrich's Flux [107] given by,

$$\mathcal{F}_{j+1/2}^n = \frac{1}{2}\left[f\left(\mathcal{U}_{j+1/2}^{nL}\right) + f\left(\mathcal{U}_{j+1/2}^{nR}\right)\right] - \frac{\alpha^n}{2}\left(\mathcal{U}_{j+1/2}^{nR} - \mathcal{U}_{j+1/2}^{nL}\right) \tag{F.2}$$

where $\mathcal{U}_{j+1/2}^{nL}$ and $\mathcal{U}_{j+1/2}^{nR}$ are the left and right hand values (respectively) from the monotone upstream-centered schemes for conservation laws reconstruction at $x_{j+1/2}$ and α is the maximum eigenvalue of the characteristics. To calculate α we first calculate the acoustic sound speed C in equation (F.3).

$$C^2 = \left(\frac{\partial P}{\partial \rho}\right)_e + \frac{P}{\rho^2}\left(\frac{\partial P}{\partial e}\right)_\rho . \tag{F.3}$$

v is the material velocity. The maximum eigenvalue is approximated by,

$$\alpha_i = \max_i \left\{C_i - \mathrm{v}_i\ ,\ \ C_i\ ,\ \ C_i + \mathrm{v}_i\right\} \tag{F.4}$$

for all i nodes in the sample material (may be 1D, 2D or 3D with appropriate number scheme). For example, C_i is the acoustic sound speed for the i^{th} node. The maximum

value $\max_i \alpha_i$ is used to calculate the maximum allowable time step. In the case when the computation of the EOS is iterative, we numerically approximate the derivatives with centered differences in ρ and T.

F.2 Interface Tracking

The ghost fluid method [42] is employed with a minor difference. Instead of the entropy extrapolation used in [42], the density and specific internal energy are extrapolated to first order as shown in Figure (50). The interface velocity is the average of the velocity at nodes j and $j+1$.

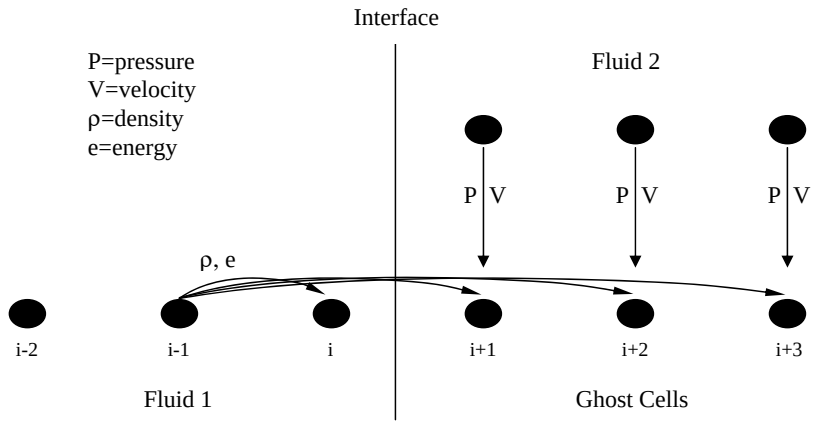

Figure 50: Ghost fluid method with density extrapolation.

F.3 Equation of State Algorithm Code

The following MATLAB function is used to compute the homobaric equation of state.

```
function [P,alpha,v] = ...
    homobaric(rho_bar,T,P_us,alphao,n,Pe,Ps,rhodo,phi,eos,eos_type, wflag)


global Tol_rho  % Homobaric EOS tollerance on density (nominal 0.0001)
global max_iter_ho % nominal -> max_iter = 15


% Written by: Derek Reding
```

```
% Last updated on: 01/17/07

% Homobaric Case - COMMENTS--------------------------------------
% INPUTS:
% rho_bar = input mixture density - remains constant (kg/m^3)
% T = temperature - remains constant (degrees K)
% P_us = pressure from uniform strain case for SAME rho_bar  (Pa)
% alphao = initial porosity at P=0
% n = polynomial for porosity pressure dependence (quadratic -> n=2)
% Pe = elastic limit (Pa)
% Ps = pore collapse strength (Pa)
% rhodo = initial constitutent density - (vector)
% phi = constituent mass fractions - (vector)
% v = input volume fractions (sum(v)~=1 if alpha>1) - (vector)
% eos = equation of state constants (4) for each material using
    %   either Gruneisen or Murnhaghan EOS models
% eos(k,1) = Beta_To (bulk modulus)  (Pa)
    % Murnaghan
    % eos(k,1) = Beta_To (bulk modulus)  (Pa)
    % eos(k,2) = n  (slope of bulk modulus)
    % eos(k,3) = Gamma (Gruniesen constant - Murnhagan)
    % eos(k,4) = Cv (specific heat capacity)  (J/Kg*K)
    % Gruneisen
    % eos(k,1) = C  (acoustic velocity)  (m/s)
    % eos(k,2) = Gamma (Gruniesen constant)
    % eos(k,3) = S  (slope of Up-Us)
    % eos(k,4) = Cv (specific heat capacity) (J/Kg*K)
% eos_type = 1 for Murnaghan EOS, 2 for Gruneisen
% wflag = when wflag==1, suppress homogeneous warnings with error<1%

% OUTPUTS:
% P = output mixture averaged pressure - uniform strain  (Pa)
% alpha = output porosity
```

```
% v = output volume fractions (sum(v)~=1 if alpha>1)  - (vector)

% CONSTANTS:
To = 298;  % deg K
%-------------------------------------------------------------------------
% initialize bounds on Pressure
 P_L = 0;   Note: using P_L = P_ho(k-1) may be faster, but not needed

for k = 1:length(rhodo)  % calculate thermal pressure for each constituent
    if eos_type(k) == 1  % then use Murnhaghan EOS
        P_min(k) = eos(k,3)*rhodo(k)*eos(k,4)*(T-To);
    else  % then use Gruneisen EOS
        P_min(k) = eos(k,2)*rhodo(k)*eos(k,4)*(T-To);
    end
end

P_L = max(P_min);  % limiting case
if P_L>=P_us  % then no iterations required!!!
%     disp('Temperature exceeding normal limiting case')
    P = P_L;
    alpha = p_alpha(P,alphao,Pe,Ps,n);
    % Calculate constituent densities
    for k = 1:length(rhodo)
        if eos_type(k) == 1  % then use Murnhaghan EOS
rd(k) = BM_EOSinv(rhodo(k),P,T,eos(k,1),eos(k,2),eos(k,3),eos(k,4));
        elseif eos_type(k) == 2 % then use Gruneisen EOS

rd(k) = MG_EOSinv(rhodo(k),P,T,eos(k,1),eos(k,2),eos(k,3),eos(k,4));
        end
    end
    % re-scale vol fracs
    v = rho_bar*phi./rd;  % calculate new v's (only for homobaric case)
    v_sum = sum(v);  % sum volume fractions, v_sum<=1
```

```
    v = v/(alpha*v_sum);  % porous volume fractions

else  % Iterate: normal case where temperature does not dominate mix EOS
    P_U = P_us;  % NORMAL limiting case (P from US for SAME rho_bar)

n_iter = 0;  % number of iterations (initialize)
breaker = 0;  % break
while(breaker==0)  % iterate to find P that satisfies Homo-mix rule
    P_bar = 1/2*(P_U + P_L);
    alpha_star = p_alpha(P_bar,alphao,Pe,Ps,n);
    % Calculate constituent densities
    for k = 1:length(rhodo)
        if eos_type(k) == 1  % then use Murnhaghan EOS
rd(k) = BM_EOSinv(rhodo(k),P_bar,T,eos(k,1),eos(k,2),eos(k,3),eos(k,4));
        elseif eos_type(k) == 2 % then use Gruneisen EOS
rd(k) = MG_EOSinv(rhodo(k),P_bar,T,eos(k,1),eos(k,2),eos(k,3),eos(k,4));
        end
    end
    % re-scale vol fracs
    v = rho_bar*phi./rd;  % calculate new v's (only for homobaric case)
    % note: (try using bulk modulus and/or shear modulus for
    %           proportional scaling instead of density)
    % re-scale vol fracs (overwrite old v's)
    v_sum = sum(v);  % sum volume fractions, v_sum<=1
    v = v/(alpha_star*v_sum);
    % apply mixture rule to get new average density (new guess)
    rho_star = rd*v';  % volume average - density (dot product)
    error = max(  abs((rho_star - rho_bar)/rho_bar) ); % error in density
    if error<=Tol_rho
        breaker =1;  % density is within tolerance
    elseif rho_star > rho_bar  % density too high, P_bar too high
        P_U = P_bar;
    else
```

```
        P_L = P_bar;
    end
    n_iter = n_iter+1;
    if n_iter ==max_iter_ho
        %         fprintf('Error: Homobaric solution does not converge\n')
        if (wflag~=0) & (error*100>wflag)
fprintf(['Homobaric solution solution does not converge, error = ',...
    num2str(error*100) ,' %%,  ']);
fprintf(['Pressure is = ',num2str(P_bar/(1e9)),' GPa \n']);
        end

        breaker =1;
    end
end  % end iteration on P - loop
P = P_bar;
alpha = alpha_star;

end  % end of NORMAL iteration case
```

The following Matlab function is used to compute the uniform strain equation of state.

```
function [P,alpha] = ...
    uniform_strain(rho_bar,T,alpha_min,alphao,n,Pe,Ps,...
    rhodo_bar,v,eos,eos_type)

global Tol_alpha % Uniform Strain EOS tollerance on alpha (nominal 0.0001)
global max_iter_us % nominal -> max_iter = 20
% Note: Nominal tollerance MUST BE LESS THAN 0.001

% Written by: Derek Reding
% Last updated on: 01/17/07
```

```
%     Uniform Strain Case - COMMENTS-------------------------------------
% INPUTS:
% rho_bar = input mixture density - remains constant (kg/m^3)
% T = temperature - remains constant (degrees K)
% alpha_min = minimum previous value of alpha (irreversible for P>Pe,
    %   otherwise alphaU=alphao)
% alphao = initial porosity at P=0
% n = polynomial for porosity pressure dependence (quadratic -> n=2)
% Pe = elastic limit (Pa)
% Ps = pore collapse strength (Pa)
% rhodo_bar = dense mixture average initial density (P=0)
% v = input volume fractions (sum(v)~=1 if alpha>1) - (vector)
% note: for uniform strain, v = vo, where vo is altered for phase changes
% eos = equation of state constants (4) for each material using
    %   either Gruneisen or Murnhaghan EOS models
% eos(k,1) = Beta_To (bulk modulus)  (Pa)
    % Murnaghan
    % eos(k,1) = Beta_To (bulk modulus)  (Pa)
    % eos(k,2) = n  (slope of bulk modulus)
    % eos(k,3) = Gamma (Gruniesen constant - Murnhagan)
    % eos(k,4) = Cv (specific heat capacity)  (J/Kg*K)
    % Gruneisen
    % eos(k,1) = C  (acoustic velocity)  (m/s)
    % eos(k,2) = Gamma (Gruniesen constant)
    % eos(k,3) = S  (slope of Up-Us)
    % eos(k,4) = Cv (specific heat capacity) (J/Kg*K)
% eos_type = 1 for Murnaghan EOS, 2 for Gruneisen

% OUTPUTS:
% P = output mixture averaged pressure - uniform strain  (Pa)
% alpha = output porosity
% v = output volume fractions (sum(v)~=1 if alpha>1)  - (vector) (not
```

```
% needed -discontinued)

% CONSTANTS:
% Tol_alpha = 0.0001; % tollerance, e.g. Tol_alpha = 0.001 = 0.1% error
% max_iter_us = 20;  % nominal -> max_iter_us = 15
%-------------------------------------------------------------------------
% initialize lower bound on alpha
% alpha_L = rhodo_bar/rho_bar; % not working so well...
alpha_L = 1;
if alpha_L<1  % ensure that lower bound is greater than 1
    alpha_L = 1;
end
% initialize upper bound on alpha
alpha_U = alphao;  % use if Pressure is not MONOTONIC
% alpha_U = alpha_old;  % use if we know that Pressure is MONOTONIC
% note: using alpha_old does not help much.  Also, as long as alpha is
% irreversible, this pressure monotinicity does not matter.

n_iter = 0;  % number of iterations (initialize)
breaker = 0;  % break
if (((rho_bar*alphao)/rhodo_bar == 1) && (alphao~=1))
    P = 0;
    alpha = alphao;
else
while(breaker==0)
    alpha_star = 1/2*(alpha_U + alpha_L);
    rho_in = rho_bar*alpha_star;  % updated rho_in
    % re-scale vol fracs (overwrite old v's)
    v_sum = sum(v);  % sum volume fractions, v_sum<=1
    v = v/v_sum;  % v = v/(alpha_star*v_sum);
    % Calculate constituent pressures
    for k = 1:length(v)
        if eos_type(k) == 1  % then use Murnhaghan EOS
```

```
    Pd(k) = BM_EOS(rhodo_bar,rho_in,T,eos(k,1),eos(k,2),eos(k,3),eos(k,4));
        elseif eos_type(k) == 2 % then use Gruneisen EOS
  Pd(k) = MG_EOS(rhodo_bar,rho_in,T,eos(k,1),eos(k,2),eos(k,3),eos(k,4));
        end
    if Pd(k)<0
       Pd(k) = 0;  % can not have negative pressures!
    end
    end
    % Calculate average pressure
    P_bar = Pd*v';  % volume average  (old: P_bar = alpha_star*Pd*v';)
    % calculate corresponding porosity from p-alpha model
    alpha_inv = p_alpha(P_bar,alphao,Pe,Ps,n);

    error = (alpha_star-alpha_inv)/alpha_star;  % true error
    if abs(error)<=Tol_alpha  % if difference is below tolerance, break
        breaker =1;
    elseif alpha_star >= alpha_inv
        alpha_U = alpha_star;
        n_iter = n_iter+1;
    else
        alpha_L = alpha_star;
        n_iter = n_iter+1;
    end
    if n_iter == max_iter_us
fprintf(['Uniform Strain solution does not converge, pct_error = ',...
            num2str(error*100) ,'\n'])
        breaker =1;
    end
end
% output quantities
P = P_bar;
alpha = alpha_star;
% ONLY after convergence has occured, check to see if alpha is higher than
```

```
% any previous value at this location in x (irreversibility)
if alpha>alpha_min
    alpha = alpha_min;
end
% numerical error can produce negative pressures -> fix
if (P<0) && (rho_bar>=rhodo_bar/alphao)
    P = 0;
end
end
```

Appendix G

GAS-GUN SIMULATION CODE

The following MATLAB functions are used to compute the 1D gas-gun simulation.

```
function [Us_obs,Up_bar ,P_bar ] = ...
    main_rxn_impact(Ao,phi_max,dt_rxn,T_rxn,Tmelt, n,Pe,Ps,alphao, ...
    dt_ro,n_r, a_o,C_I,mu_f, Cm, wflag,select_mat,pltflag, ...
    vo,Velocity,Tf,L1,L2,nx_b,CFL,  n_extra,nx,Pmax, select_mix, ...
    V_p,t_ramp,select_bc, select_pore, select_impact)
global crossing  % number of cells that the material interface has crossed
%
% Written by: Derek Reding
% last updated on: 10-01-07
% ghost fluid method, 2nd order RK (not on fluxes)
%
% Notes: 1) include strain rate sensetive Fe2O3 constitutive models, mu,yo
%        2) work on Ni+Al heat of rxn
%        3) for Ni+Al, make kq, mu, yo functions of Temperature!
%        4) create option to calculate P in BOTH steps
%        5) Find EOS parameters, kq, Cp, for feAl2O3 (Hercynite)
%        6) use liquid densities, rho when phi_L>0
%        7) update conductivity at the material interface
%--------------------------------------------------------------------------
%--------------------------------------------------------------------------
% INPUTS:
% Ao = % frequency factor  (nominal Ao = 100000)
% phi_max = .1;  % fraction of reaction completion (phi_max<=1)
% dt_rxn = maximum time step used in chemical reactions (sec)
% T_rxn = temperature at which reaction initiates (K)
```

```
% Tmelt = melting temperature of Al (K)(particle size dependent)
% n = P-alpha model polynomial order (n),  quadratic ->   n=2
% Pe = elastic pore strength (Pa)  (Pe = 250e6) Nominal
% Ps = pore collapse strength (Pa)   (Ps = 3e9) Nominal
% alphao = Initial Distension ratio (alphao>=1)
% dt_ro = pore collapse - pore collapse EOS time step (sec) (max allowable)
% n_r = pore collapse - number of 1D spatial grids in radial dir. (r-coord)
% a_o = pore collapse -initial pore radius (m)
% C_I = pore collapse - scaling factor to affect mix density (0<=mu_f<=1)
% mu_f = pore collapse -non-dimensional friction coefficient (0<=mu_f<=1)
% Cm = P-alpha model - fraction of Homobaric Pressure assumed
     % e.g. for pure Uniform Strain, Cm=0.  for Homobaric, Cm=1
% wflag = flag, when wflag==1, suppress homogeneous warnings with error<1%
% select_mat =  if select_mat = 1, choose Ni+Al
              % if select_mat = 2, choose Al+Fe2O3
% vo = volume fractions of dense mixture  [1,nc+1]
% Velocity = impact velocity (m/s)
% Tf = total run time (sec)
% L1 = length of impactor (m)
% L2 = length of target (m)
% nx_b = number of elements for inside of body
% CFL = fraction of maximum allowable time step
% n_extra =  extra nodes on either side of materials
% nx =  total number of cells plus a few on the end
% Pmax = max pressure,(Pa) must be known a-priori for Us_obs calc and Homo
% select_mix = choice of EOS mixture rule
    % select_mix = 1  -> Bennett-Horie mix rule  (simple)
    % select_mix = 2  -> Rigorous mixture rules (use Cm)
    % V_p = particle velocity (m/s)
% t_ramp = % if select_bc = 1, use particle velocity bc
           % if select_bc = 2, use impacting plate
% select_bc  =1 for velocity bc, =2 for impacting plate
% select_pore = choice of collapse model:
```

```
    % select_pore = 1 -> Holt-Carrol
    % select_pore = 2 -> P-alpha
%
% OUTPUTS:
% U_obs = observed shock velocity (m/s)
% Up_bar = observed particle velocity (m/s)
% P_bar = observed pressure in sample mixture (target) (Pa)
%-------------------------------------------------------------------------
%-------------------------------------------------------------------------
% INITIALIZATION
%-------------------------------------------------------------------------
%-------------------------------------------------------------------------
% Material Properties
%-------------------------------------------------------------------------
%-------------------------------------------------------------------------
% Define impactor material
if select_impact == 1  % DEFINE STEEL MATERIAL PROPERTIES
    rho_sto = 7.77e3;   % Density of steel
    kq_st = 31;  % thermal conductivity of steel = 31 (W/mK)
    Cv_st = 440;    % specific heat capacity constant volume (J/Kg*K)
    Cp_st = 150;    % specific heat capacity constant pressure (J/Kg*K)

    E_st = 200e9;  % Elastic Modulus (Pa)
    mu_st = 80e9;  % Shear Modulus (Pa)
    yield_st = 250e6;   % Elastic Yield Strength (Pa)

    % Gruneisen EOS
    Gammag_st = 2.170;
    C_st = 4570;    % Acoustic wave speed (m/s)
    S_st = 1.49;    % slope of Us - Up curve

    eos_st = [C_st,Gammag_st,S_st,Cv_st];
else  % DEFINE COPPER MATERIAL PROPERTIES
```

```
    rho_sto = 8.93e3;   % Density of steel   (COPPER - Huayun '2002)

    kq_st = 401;  % thermal conductivity of steel = 31 (W/mK)
    Cv_st = 385;  % specific heat capacity constant volume (J/Kg*K)
    Cp_st = 385;  % specific heat capacity constant P (J/Kg*K) - update

    E_st = 117e9;  % Elastic Modulus (Pa)
    mu_st = 46e9;  % Shear Modulus (Pa)
    yield_st = 33e6;   % Elastic Yield Strength (Pa)

    % Gruneisen EOS
    Gammag_st = 2.0;  %  approx of S = 2*S1 - 1
    C_st = 3933;    % Acoustic wave speed (m/s)  (COPPER - Michell '1981)
    % note C has uncertaity -> +/- 42  (m/s)
    S_st = 1.500;    % slope of Us - Up curve   (COPPER - Michell '1981)
    % note S has uncertaity -> +/- 0.025  (m/s)

    eos_st = [C_st,Gammag_st,S_st,Cv_st];
end
%-------------------------------------------------------------------------
% Sample Material properties for
% select_mat = 1,  Reaction:  3Al + Ni -> Al3Ni             + epoxy + pores
% select_mat = 2,  Reaction:  2Al + Fe2O3 -> Al2O3 + 2Fe    + epoxy + pores
%-------------------------------------------------------------------------
if select_bc == 1  % apply velocity bc to sample
    nx = nx_b + n_extra/2;
else % use impacting plate (L1)
    nx = nx_b + n_extra;
end
if select_mat == 1
    [rhod_m,vo_m,v_m,rhood,rho_react,phi_ep, ...
        rho_o,phi_m,yield_mix, eos,eos_type, ...
        plast_const,pore_hist,pore_hist_r,r0] = ...
```

```
        sample_material_NiAl(vo,alphao,a_o,nx,n_r);
elseif select_mat == 2
    [rhod_m,vo_m,v_m,rhood,rho_react,phi_ep, ...
        rho_o,phi_m,yield_mix, eos,eos_type, ...
        plast_const,pore_hist,pore_hist_r,r0] = ...
        sample_material_FeAl(vo,alphao,a_o,nx,n_r);
else
    error('Must enter a valid material selection, select_mat=1,2')
end

%-------------------------------------------------------------------------
% Constants
%-------------------------------------------------------------------------
R = 8.3145;   % universal gas constant  (J  K-1  mol-1 )
To = 298;  % reference temperature (K)
% R = 1.3806505*10e-23; % universal gas constant  (joule/kelvin )
%-------------------------------------------------------------------------
%-------------------------------------------------------------------------
%-------------------------------------------------------------------------
% INITIALIZE NUMERICAL MODEL
%-------------------------------------------------------------------------
%-------------------------------------------------------------------------
% emp=zeros(1,nx);  vx=emp;   rho=emp;   Cv=emp;   kq=emp;   mu=emp;

if select_bc == 1  % apply velocity bc to sample
    dx = L2/nx_b;  x = dx/2:dx:L2-dx/2+ n_extra/2*dx;
    x_start = dx/2;
    x_end = nx*dx - n_extra/2*dx - dx/2;
    % Initialize Interface locations
    jL = 1; % not used - passed as filler into const. function
    sigmaI = dx;                        jI = 1;
    sigmaR = x_end + dx/2;              jR = nx - n_extra/2;
    % RHS material only
```

```
vx = zeros(1,nx);
rho = rhood'/alphao;

% Calculate INITIAL DENSE mixture averaged quantities
% Mixture heat capacity, Cp_bar (J/mol-K)
% Mixture thermal conductivity, kq_bar (W/mK)
% Mixture shear modulus, mu_bar (Pa)
if select_mat==1 % Ni+Al
    [Cp_bar] = cp_AlNi(T,phi_m(1,:)); %  (J/kg-K) [1,1]
    Cp = Cp_bar*ones(1,nx);
    [kq_bar] = kq_ni_al(T,phi_m(1,:)); %  (W/mK) [1,1]
    kq = kq_bar*ones(1,nx);
    [mu_bar] = mu_ni_al(T,phi_m(1,:)); % Shear Modulus (Pa)
    mu = mu/3;  % Temperature problems when mu is too high
else  % Fe2O3+Al
    [Cp_bar] = cp_fe2o3_al(To,phi_m(1,:)); %  (J/kg-K) [1,1]
    Cp = Cp_bar*ones(1,nx);
    [kq_bar] = kq_fe2o3_al(To,phi_m(1,:)); %  (W/mK) [1,1]
    kq = kq_bar*ones(1,nx);
    [mu_bar] = mu_fe2o3_al(To,phi_m(1,:)); %  (Pa) [1,1]
    mu = mu_bar*ones(1,nx);
    mu = mu/3;  % Temperature problems when mu is too high
end
m = rho.*vx;  % momentum
P = zeros(1,nx);  % Pressure (Pa)
sigmax = zeros(1,nx);  % Stress in x-direction (Pa)
sigmax_dev = zeros(1,nx);  % Deviatoric Stress (Pa)
T = To*ones(1,nx);  % Temperature (K)
e = Cp.*T;  % specific internal energy of dense material (J/kg)
% specific total energy (J/m^3)
E = alphao*rho.*e + 1/2*alphao*rho.*vx.^2;
q = zeros(1,nx);  % Heat flux (W/m^2)
phi_L = zeros(1,nx);  % fraction of reactants in liquid state
```

```
    % assume: 0<=phi_L<=1-phi_ep, with porportional melting (non-physical)
    % this is consistent with the solid-liquid approach Meyers'94
    % generally, constituents with lower melting temp will melt first
else  % use impacting plate (L1)
    dx = (L1+L2)/(nx_b);   x=dx/2:dx:(L1+L2)-dx/2+ n_extra*dx;
    x_start = n_extra/2*dx + dx/2;
    x_end = nx*dx - n_extra/2*dx - dx/2;
    % Initialize Interface locations
    sigmaL = x_start - dx/2;            jL = n_extra/2 + 1;
    sigmaI = L1 + x_start - dx/2;       jI = round(n_extra/2 + L1/dx);
    sigmaR = x_end + dx/2;              jR = nx - n_extra/2;

    % LHS material
    vx(1:jI) = Velocity*ones(1,jI);  % Velocity (m/s)
    rho(1:jI) = rho_sto*ones(1,jI); % Density (kg/m^3)
    Cp(1:jI) = Cp_st*ones(1,jI);  % heat capacity
    kq(1:jI) = kq_st*ones(1,jI);  % conductivity
    mu(1:jI) = mu_st*ones(1,jI);  % shear strength

    % RHS material
    vx(jI+1:nx) = zeros(1,nx-jI);  % Velocity (m/s)
    rho(jI+1:nx) = rhood(jI+1:nx)/alphao; % Density (kg/m^3)
%     rhood(jI+1)
%     rho(jI+1)
    % Calculate INITIAL DENSE mixture averaged quantities
    % Mixture heat capacity, Cp_bar (J/mol-K)
    % Mixture thermal conductivity, kq_bar (W/mK)
    % Mixture shear modulus, mu_bar (Pa)
    if select_mat==1 % Ni+Al
%         Cp_bar =  710.0905
%         kq_bar =  166.8464
%         mu_bar =  4.6423e+010
        [Cp_bar] = cp_AlNi(To,phi_m(1,:)); %  (J/kg-K) [1,1]
```

```
        Cp(jI+1:nx) = Cp_bar*ones(1,nx-jI);
        [kq_bar] = kq_ni_al(To,phi_m(1,:)); %  (W/mK) [1,1]
        kq(jI+1:nx) = kq_bar*ones(1,nx-jI);
        [mu_bar] = mu_ni_al(To,phi_m(1,:)); % Shear Modulus (Pa)
        mu(jI+1:nx) = mu_bar*ones(1,nx-jI)/3;
        % note: Temperature problems when mu is too high, so /3
    else  % Fe2O3+Al
%         Cp_bar =  714.8628
%         kq_bar =   59.8052
%         mu_bar =  8.3936e+010
        [Cp_bar] = cp_fe2o3_al(To,phi_m(1,:)); %  (J/kg-K) [1,1]
        Cp(jI+1:nx) = Cp_bar*ones(1,nx-jI);
        [kq_bar] = kq_fe2o3_al(To,phi_m(1,:)); %  (W/mK) [1,1]
        kq(jI+1:nx) = kq_bar*ones(1,nx-jI);
        [mu_bar] = mu_fe2o3_al(To,phi_m(1,:)); %  (Pa) [1,1]
        mu(jI+1:nx) = mu_bar*ones(1,nx-jI)/3;
        % note: Temperature problems when mu is too high, so /3
    end
    m = rho.*vx;  % momentum
    P = zeros(1,nx);  % Pressure (Pa)
    sigmax = zeros(1,nx);  % Stress in x-direction (Pa)
    sigmax_dev = zeros(1,nx);  % Deviatoric Stress (Pa)
    T = 298*ones(1,nx);  % Temperature (K)
%     e(jL:jI) = Cp(jL:jI).*T(jL:jI);  % specific internal energy (J/kg)
%     e(jI+1:jR) = Cp(jI+1:jR).*T(jI+1:jR);
    e = Cp.*T;  % specific internal energy of dense material (J/kg)
    % E = specific total energy (J/m^3)
    E(jL:jI) = rho(jL:jI).*(e(jL:jI) + 1/2*vx(jL:jI).^2);
    E(jI+1:jR) = alphao*rho(jI+1:jR).*(e(jI+1:jR) + 1/2*vx(jI+1:jR).^2);
    q = zeros(1,nx);  % Heat flux (W/m^2)
    phi_L = zeros(1,nx);  % fraction of reactants in liquid state
    % assume: 0<=phi_L<=1-phi_ep, with porportional melting (non-physical)
    % this is consistent with the solid-liquid approach Meyers'94
```

```
    % generally, constituents with lower melting temp will melt first
end
jIo = jI;  % store to track how many cells have been crossed

% Calculate Initial time step ---------------
% find maximum eigenvalue in the steel material
[alpha_st] = alpha_steel(rho(jL),P(jL),e(jL),vx(jL), ...
    rho_sto,C_st,Gammag_st,S_st);
% find the maximum eigenvalue in the porous material
C = zeros(1,nx);
[Po,alphapo,C(jI+1)]=rsm_eos2(rho(jI+1),T(jI+1), ...
    alphao,alphao,alphao,n,Cm,Pe,Ps, Pmax, wflag, select_mix, ...
    rhod_m,rhood(jI+1),vo_m(jI+1,:),phi_m(jI+1,:),eos,eos_type, Cp(jI+1));
alpha_mix = max([C(jI+1)-vx(jI+1), C(jI+1), C(jI+1)+vx(jI+1)]);
% alpha_mix = 1.5524e+003 3Al+Ni
% alpha_mix = 1.4728e+003 2Al+Fe2O3

alpha_max = max([alpha_st,alpha_mix]);
dt = CFL*dx/alpha_max;
if select_bc == 1  % apply velocity bc to sample
    dt = 0.01e-9;  % initial guess for minimum time step (sec)
else  % use impacting plate (L1)
    for j=jL:jI   % define local values
        alpha(j) = alpha_st;
    end
end

% define local values
for j=jI+1:jR
    alpha(j) = alpha_mix;
end
Co = C(jI+1);  % initial acoustic velocity in mixture
C = ones(1,nx)*Co; %(approximated using P-alpha for first small time step)
```

```
%-------------------------------------------------------------------------
%-------------------------------------------------------------------------
% RUN MAIN CODE (ghost fluid method)
%-------------------------------------------------------------------------
%-------------------------------------------------------------------------
time(1) = 0; counter = 0; k = 1;
flag_tf = 1;  breaker = 0;
emp = zeros(1,nx);
rho1 = emp;   m1 = emp;  E1 = emp;  vx1=emp;  e1 = emp;  T1 = emp;
rho2 = emp;   m2 = emp;  E2 = emp;  vx2=emp;  e2 = emp;  T2 = emp;
alphap = alphao*ones(1,nx);

% fprintf(['Initial density is = ',num2str(rho(jI+1)),' kg/m^3 \n'])
% for kk=1:10
while(breaker == 0)
%     dt
    k_time=k;
% %     k_iter_junk = k
% % % % % % %     time_junk = time(k)
    if select_bc == 1  % apply velocity bc  (quadratic pg 99 Austin)
        if time(k)<t_ramp
            vx(jI+1) = (time(k)/t_ramp)^2*V_p;
        else  % use impacting plate (L1)
            vx(jI+1) = V_p;
        end
        jT = jI+1;  % starting counter
    else  % use impacting plate (L1)
        jT = jL;  % starting counter
    end
    %---------------------------------------------------------------------
    % Begin first step
    %---------------------------------------------------------------------
    % 1) CONSERVATION EQUATIONS at t(n+1)
```

```
    if select_bc == 1  % apply velocity bc
        [rho1,phi_m1,m1,E1,e1,vx1,T1,phi_L1]= ...
            muscl_rxn_reimann_vel(rho,phi_m,e,T,Cp,vx, alphap,sigmax,q,...
            phi_max,Ao,T_rxn,Tmelt,dt_rxn,rho_react,phi_ep, ...
            select_mat,phi_L,vo, alpha,dt,dx,x,nx, jI,jR);
    else  % use impacting plate (L1)
        [rho1,phi_m1,m1,E1,e1,vx1,T1,phi_L1] =  ...
            muscl_rxn_reimann(rho,phi_m,e,T,Cp,vx,  alphap,sigmax,q, ...
            phi_max,Ao,T_rxn,Tmelt,dt_rxn, rho_react,phi_ep,  ...
            select_mat,phi_L,vo, alpha,dt,dx,x,nx, jL,jI,jR);
    end
    % calculate vo_m, rhood using new mass fractions, phi_m1
    [vo_m,rhood] = avg_mix_rxn_new(phi_m1,rhod_m,jI,jR);
%     phi_junk = phi_m1(jI+1)
    for j=jT:jR
        if T1(j)<0
            error('Temperature is below zero! See First step in main funciton');
        end
    end

    % 2) CONSTITUTIVE at t(n+1)
% %     fprintf(['C before first step = ', num2str(C) ,' ,   \n'])
    step = 1;  % first step in 2-step time scheme  (for EOS)
    if select_bc == 1  % apply velocity bc  (quadratic pg 99 Austin)
        [sigmax1,sigmay1,sigmax_dev1,sigmay_dev1,P1,q1,alphap1,C1, ...
            pore_hist1,pore_hist_r1] = ...
            const_rxn_reimann_vel(rho1,phi_m1,vo_m,vo,T,T1,vx,sigmax_dev,q,kq, ...
            eos,eos_type,rhood,rhod_m,rho_o,alphao,alphap,Co,C,P, ...
            yield_st,yield_mix,mu,Cp, rho_sto, eos_st, Pmax, wflag, select_mix, ...
            plast_const,pore_hist,pore_hist_r, r0, dt_ro,n_r, a_o,C_I,mu_f, ...
            select_pore,  n,Cm,Pe,Ps, nx,dx,dt,  jI,jR, step,k_time);
    else  % use impacting plate (L1)
        %     junk_alpha = alphap(jI)
```

```
        [sigmax1,sigmay1,sigmax_dev1,sigmay_dev1,P1,q1,alphap1,C1, ...
            pore_hist1,pore_hist_r1] = ...
            const_rxn_reimann(rho1,phi_m1,vo_m,vo,T,T1,vx,sigmax_dev,q,kq, ...
            eos,eos_type,rhood,rhod_m,rho_o,alphao,alphap,Co,C,P, ...
            yield_st,yield_mix,mu,Cp, rho_sto, eos_st, Pmax, wflag, select_mix, ...
            plast_const,pore_hist,pore_hist_r, r0, dt_ro,n_r, a_o,C_I,mu_f, ...
            select_pore,  n,Cm,Pe,Ps, nx,dx,dt,  jL,jI,jR, step,k_time);
    end
% %     fprintf(['C after first step = ', num2str(C1) ,' ,   \n\n'])

    % 3) Update Cp, k_q and mu at t(n+1)
    % Note: v_m=vo_m only for US assumption
   for j=jI+1:jR
%        [Cp(j)] = cp_fe2o3_al(T1(j),phi_m(j,:)); %  (J/kg-K) [1,1]
        % Note: upadate k_m as a function of T here
%         kq(j) = (kq_m(j,:)*vo')/alphap1(j);
%         mu(j) = (mu_mix(j,:)*vo')/alphap1(j);
   end
    %---------------------------------------------------------------------
    % Begin second step
    %---------------------------------------------------------------------
    % 1) CONSERVATION EQUATIONS at t(n+2)
    if select_bc == 1  % apply velocity bc  (quadratic pg 99 Austin)
        [rho2,phi_m2,m2,E2,e2,vx2,T2,phi_L2]=...
            muscl_rxn_reimann_vel(rho1,phi_m1,e1,T1,Cp,vx1, alphap1,...
            sigmax1, q1,phi_max,Ao,T_rxn,Tmelt,dt_rxn,rho_react,phi_ep,...
            select_mat,phi_L1,vo, alpha,dt,dx,x,nx, jI,jR);
    else  % use impacting plate (L1)
        [rho2,phi_m2,m2,E2,e2,vx2,T2,phi_L2] = ...
            muscl_rxn_reimann(rho1,phi_m1,e1,T1,Cp,vx1, alphap1,...
            sigmax1,q1, phi_max,Ao,T_rxn,Tmelt,dt_rxn,rho_react,phi_ep,...
            select_mat,phi_L1,vo, alpha,dt,dx,x,nx, jL,jI,jR);
    end
```

```
    % calculate vo_m, rhood using new mass fractions
    [vo_m,rhood] = avg_mix_rxn_new(phi_m2,rhod_m,jI,jR);

    % 2) CONSTITUTIVE at t(n+2)
% % %     fprintf(['C before second step = ', num2str(C1) ,' ,   \n'])
    step = 2;  % second step in 2-step time scheme
    if select_bc == 1  % apply velocity bc  (quadratic pg 99 Austin)
        % Note: pore_hist2,pore_hist_r2 are not used after this
        % **********  IMPORTANT **************
        % Potential problem: if a(j) does not correspond with the old
        % alphap(j), then everything gets messed up
        [sigmax2,sigmay2,sigmax_dev2,sigmay_dev2,P2,q2,alphap2,C2, ...
            pore_hist2,pore_hist_r2] = ...
            const_rxn_reimann_vel(rho2,phi_m2,vo_m,vo,T1,T2,vx1,sigmax_dev1,q1,kq, ...
            eos,eos_type,rhood,rhod_m,rho_o,alphao,alphap1,Co,C1,P1, ...
            yield_st,yield_mix,mu,Cp, rho_sto, eos_st, Pmax, wflag, select_mix, ...
            plast_const,pore_hist1,pore_hist_r1, r0, dt_ro,n_r, a_o,C_I,mu_f, ...
            select_pore,  n,Cm,Pe,Ps, nx,dx,dt,  jI,jR, step,k_time);
    else  % use impacting plate (L1)
        [sigmax2,sigmay2,sigmax_dev2,sigmay_dev2,P2,q2,alphap2,C2, ...
            pore_hist2,pore_hist_r2] = ...
            const_rxn_reimann(rho2,phi_m2,vo_m,vo,T1,T2,vx1,sigmax_dev1,q1,kq, ...
            eos,eos_type,rhood,rhod_m,rho_o,alphao,alphap1,Co,C1,P1, ...
            yield_st,yield_mix,mu,Cp, rho_sto, eos_st, Pmax, wflag, select_mix, ...
            plast_const,pore_hist1,pore_hist_r1, r0, dt_ro,n_r, a_o,C_I,mu_f, ...
            select_pore,  n,Cm,Pe,Ps, nx,dx,dt,  jL,jI,jR, step,k_time);
    end

    %-----------------------------------------------------------------------
    % Calculate new values (2nd Order R-K scheme)
    %-----------------------------------------------------------------------
    % a) calculate new values at t(n+1)
    % Note: Update alphap only for calculating new Cp,kq,mu, thus this is
```

```
    % approximate i.e., see rho average above
    if select_pore==1    %---------  Holt-Carrol ------------------
        alphap = alphap1;
    else  %---------  P-alpha ------------------
        alphap = 1/2*(alphap1 + alphap2);
        %         alphap = alphap1;
    end
    rho(jT:jR) = 1/2*(rho(jT:jR) + rho2(jT:jR));
    % % %     rho(jT:jR) = rho1(jT:jR);
    m(jT:jR) = 1/2*(m(jT:jR) + m2(jT:jR));
    E(jT:jR) = 1/2*(E(jT:jR) + E2(jT:jR));
    vx(jT:jR) = m(jT:jR)./rho(jT:jR);
%     e(jT:jR) = E(jT:jR)./rho(jT:jR) -1/2*vx(jT:jR).^2;
    if select_bc == 1  % apply velocity bc  (quadratic pg 99 Austin)
        e(jT:jR) = E(jT:jR)./(rho(jT:jR).*alphap(jT:jR)) -1/2*vx(jT:jR).^2;
    else  % use impacting plate (L1)
        e(jT:jI) = E(jT:jI)./rho(jT:jI) -1/2*vx(jT:jI).^2;
        e(jI+1:jR) = E(jI+1:jR)./(rho(jI+1:jR).*alphap(jI+1:jR))...
            -1/2*vx(jI+1:jR).^2;
    end




    if select_bc == 2  % use impacting plate (L1)
        E(jI) = 1/2*(E(jI) + E(jI-1));  % help reduce overheat @ interface
        e(jI) = 1/2*(e(jI) + e(jI-1));  % these two lines are optional
    end
    T(jT:jI) = e(jT:jI)./Cp(jT:jI);
%     DT(jT:jR) = 1/2*(DT1(jT:jR) + DT2(jT:jR));
%     DT_tot(jT:jR) = DT_tot(jT:jR) + DT(jT:jR);

    phi_m = 1/2*(phi_m1 + phi_m2);
    phi_L = 1/2*(phi_L1 + phi_L2);
```

```
    %     v_m = 1/2*(v_m1 + v_m2);

    for j=jI+1:jR
        % Note: upadate Cp_m,kq_m,mu_mix as a function of T here
        if select_mat == 1    % Ni+Al
            [Cp_bar(j)] = cp_AlNi(T(j),phi_m(j,:)); %  (J/kg-K) [1,1]
        else  % Fe2O3+Al
            [Cp(j)] = cp_fe2o3_al(T(j),phi_m(j,:)); % (J/kg-K) [1,1]
        end

%         Cp(j) = (Cp_m(j,:)*phi_m(j,:)')/alphap(j);
%         kq(j) = (kq_m(j,:)*vo')/alphap(j);
%         mu(j) = (mu_mix(j,:)*vo')/alphap1(j);
    end
% %     T(jI+1:jR) = e(jI+1:jR)./(Cp(jI+1:jR)./alphap(jI+1:jR));
% Re-calculate temperature using new Cp(T) - for consistency purposes
T(jI+1:jR) = e(jI+1:jR)./Cp(jI+1:jR);
    % calculate vo_m, rhood using new mass fractions  (P = 0)
%     nc = 6;
%     [vo_m,rhood] = avg_mix_rxn(phi_m,  rhod_m,nc,nx_b,jI,jR,select_mat);
    [vo_m,rhood] = avg_mix_rxn_new(phi_m,rhod_m,jI,jR);

% %     C = 1/2*(C1+C2);  % local speed of sound
    C = C1;
    sigmax(jT:jR) = sigmax1(jT:jR);
    sigmax_dev(jT:jR) = sigmax_dev1(jT:jR);
    P(jT:jR) = P1(jT:jR);   %update to use EOS for new rho,T
    q(jT:jR) = 1/2*(q(jT:jR) + q2(jT:jR));


    % Update pore collapse history parameters to t(n+1) -------------------
    % note: consider to eliminate this step by letting pore_hist=pore_hist1
    % in the output of t(n+1) const function,  consider to average t(n),t(n+2)
```

```
    if select_pore==1    % ---------  Holt-Carrol ------------------
        % pore_hist = x(2,1) = [a,adot]
        pore_hist = pore_hist1;  % stay consistent with P,sigma above
        pore_hist_r = pore_hist_r1;  % stay consistent with P,sigma above
%     pore_hist = 1/2*(pore_hist+pore_hist2);
    end
    % end Update pore collapse history parameters to t(n+1) ---------------

    % b) Reconstruct new interfaces at t(n+1)
    if select_bc == 1  % apply velocity bc to sample
        sigma_in = ([sigmaI,sigmaR]);  j_int = ([jI,jR]);
        [sigma_out,j_int] = interface_reimann_vel(...
            sigma_in,   vx,   x,nx,dx,dt,  j_int);
        sigmaI=sigma_out(1);   sigmaR=sigma_out(2);
        jI1 = j_int(1);  jR1 = j_int(2);
    else  % use impacting plate (L1)
        sigma_in = ([sigmaL,sigmaI,sigmaR]);  j_int = ([jL,jI,jR]);
        [sigma_out,j_int] = interface_reimann(...
            sigma_in,   vx,   x,nx,dx,dt,  j_int);
        sigmaL=sigma_out(1);    sigmaI=sigma_out(2);   sigmaR=sigma_out(3);
        jL1 = j_int(1);    jI1 = j_int(2);  jR1 = j_int(3);
    end

    % c) advect values on free edges
    if jI1>jI  % Contact interface  (extrapolate from LHS)
        crossing=jI-jIo+1;
        fprintf('\n interface has crossed node %i \n ',crossing);
    end
    if select_bc == 2  % use impacting plate (L1)
        if jL1<jL  % LHS
            error_flag =1
        end
        % once material crosses cell edge, it becomes the impactor material
```

```
    if jI1>jI  % Contact interface  (extrapolate from LHS)
        vx(jI1) = vx(jI);
        rho(jI1) = 2*rho(jI) - rho(jI-1);
        E(jI1) = 1/2*(E(jI) + E(jI-1));  % to prevent over heating
        e(jI1) = 1/2*(e(jI) + e(jI-1));  % to prevent over heating
        T(jI1) = 1/2*(T(jI) + T(jI-1));  % to prevent over heating
        q(jI1) = 1/2*(q(jI) + q(jI-1));  %
        Cp(jI1) = Cp(jI); % material property for impactor
        kq(jI1) = kq(jI); % material property for impactor
        mu(jI1) = mu(jI); % material property for impactor
        % keep plastic flow within same material
        sigmax_dev(jI1) = sigmax_dev(jI);
        sigmax(jI1) = sigmax(jI);
        %         P(jI1) = P(jI);
    end
    jL = jL1;  % update left index
end
if jR1>jR  % RHS
    rho(jR+1) = rho(jR);
elseif jR1<jR
    error_flag = 2
end
jI = jI1;    jR = jR1;  % update remaining indicies
%--------------------------------------------------------------------------
% Calculate shock speed
%--------------------------------------------------------------------------
% Track shock front location (for calculating Shock Speed Us)
[x_Us(k)] = track_Us(P,Pmax,x,jL,jR);
%--------------------------------------------------------------------------
% Calculate new time step
%--------------------------------------------------------------------------
% - find the maximum eigenvalue in the porous material (alpha_max)
if select_bc == 1  % apply velocity bc to sample
```

```
    for j=jI+1:jR
        alpha(j) = max([C(j)-vx(j), C(j), C(j)+vx(j)]);
    end
    alpha_max = max(abs(alpha(jI+1:jR)));
else % use impacting plate (L1)
    % find maximum eigenvalue in the steel material
    for j=jL:jI
        [alpha(j)] = alpha_steel(rho(j),P(j),e(j),vx(j), ...
            rho_sto,C_st,Gammag_st,S_st);
    end
    for j=jI+1:jR
        alpha(j) = max([C(j)-vx(j), C(j), C(j)+vx(j)]);
    end
    alpha_max = max(abs(alpha(jL:jR)));
end

dt = CFL*dx/alpha_max;
if select_pore==1    % ---------  Holt-Carrol ------------------
    if k==1
        dt = .5e-9;
    end
    if k==2
        Co = C(jI+1);
        % C is approximated using P-alpha for first small time step
        C = ones(1,nx)*Co;
    end
end

time(k+1) = time(k) + dt*flag_tf;
if time(k+1)>=Tf
    if time(k+1) ==Tf
        breaker = 1;
    else
```

```
            dt = Tf - time(k); % Correct final time step
            time(k+1) = Tf;  % Ensure final time is correct
            flag_tf = 0;
            k = k+1;
        end
    else
        k = k+1;
        counter = counter +1;
        if counter == 10
%             fprintf('time = %6.2f \n',k); %nt = k
fprintf('time = %6.4g ns after %i time steps\n ',time(k)*1e9,k-1);
%             disp('time = %g, after %g time steps',[time(k),k]); %nt = k
%             time_out = time(k)
            counter = 0;
        end
    end
% Store pressure history at the interface (inside sample material)
    P_hist(k) = P(jI+1);
end
%--------------------------------------------------------------------------
%--------------------------------------------------------------------------
% POST PROCESSING
%--------------------------------------------------------------------------
%--------------------------------------------------------------------------
% % Shock Speed  (linear fit of the location of the shock front vs time)
nfig = 5;  % number for figure showing the interpolation data
[Us_obs] = plot_Us(x_Us,time,k,nfig);
% % Pressure and Up
g1 =  1;
P_choose(g1) = P(jI+3);  % start measuring within the bulk material
xPavg(g1) = x(jI+3);
g2 =  1;
Up_choose(g2) = vx(jI+3);  % start measuring within the bulk material
```

```
xUpavg(g2) = x(jI+3);
param_error = 0.02; % within param_error% of P,Up  (nominal = 0.05 = 5%)
for j=jI+4:jR
    if abs(P(j)-P_choose(1))/P_choose(1) < param_error
        g1 = g1 + 1;
        P_choose(g1) = P(j);
        xPavg(g1) = x(j);
    end
    if abs(vx(j)-Up_choose(1))/Up_choose(1) < param_error
        g2 = g2 + 1;
        Up_choose(g2) = vx(j);
        xUpavg(g2) = x(j);
    end
end
P_bar = mean(P_choose);  % calculate the average pressure
Up_bar = mean(Up_choose);  % calculate the average Up

fprintf('Us_obs = %6.3f m/s, P_bar= %6.3f GPa, Up_bar = %6.3f m/s\n', ...
    Us_obs,P_bar/1e9,Up_bar)



function [rho,phi,m,E,e,vx,T,phi_L] = ...
    muscl_rxn_reimann(rho,phi,e,T,Cp,vx,...
    alphap,sigmax,q, phi_max,Ao, T_rxn,Tmelt,dt_rxn,rho_react,phi_ep,...
    select_mat, phi_L,vo, alpha,dt,dx,x,nx, jL,jI,jR)
%
% Written by: Derek Reding
% Last modified: 10-01-07
% Solves the conservation equations using linear stensil (MUSCL algorithm)
% includes reaction
%-------------------------------------------------------------------------
% INPUTS:
% rho  = porous mixture density [1,nx]
```

```
% phi  = mass fractions  [nc,nx,nt]
% e = specific internal energy of dense material (J/kg)  [1,nx]
% T = temperature of dense material (K)  [1,nx]
% Cp = specific heat capacity constant pressure (J/Kg*K) [1,nx]
% vx = mix velocity parallel to the motion of the shock front (m/s) [1,nx]
% alphap = current distension ratio (alphao>=1) [1,nx]
% sigmax = un-returned deviatoric stress in x-dir (Pa)  [1,nx]
% q = heat flux (W/m^2) [1,nx]
% phi_max = fraction of reaction completion (phi_max<=1)  [1,1]
% Ao = frequency factor  (nominal Ao = 10e3)  [1,1]
% T_rxn = temperature at which reaction initiates (K) [1,1]
% Tmelt = melting temperature of Al (K)(particle size dependent) [1,1]
% dt_rxn = maximum time step used in chemical reactions (sec)  [1,1]
% rho_react = basis for internal energy definition (kg/m^3) [1,1]
% phi_ep = mass fraction of epoxy [1,1]
% select_mat = 2; if select_mat = 1, choose Ni+Al
                % if select_mat = 2, choose Al+Fe2O3
% phi_L = fraction of reactants in liquid state [1,nx]
% vo = volume fractions of dense mixture  [1,nc+1]
% alpha = maximum eigenvalue at each node [1,nx]
% dt = time step (sec) [1,1]
% dx = spatial step size (m) [1,1]
% x = spatial coordinates (uniform grid) (m) [1,nx]
% nx = total number of cells plus a few on the end  [1,1]
% jL = index of node within (impactor) material at the left boundary
% jI = index of node within (impactor) material at the interface boundary
% jR = index of node within (sample/mixture) material at the right boundary
%
% OUTPUTS:
% rho = updated porous mixture density from conservation laws [1,nx]
% phi = mass fractions for the mixture [nc,nx,nt]
% m = updated momentum (kg/m^2) [1,nx]
% E = updated specific total energy of dense material (J/m^3)  [1,nx]
```

```
% e = updated specific internal energy of dense material (J/kg)  [1,nx]
% vx = mix velocity parallel to the motion of the shock front (m/s) [1,nx]
% T = updated temperature of dense material (K)  [1,nx]
% phi_L = updated fraction of reactants in liquid state [1,nx]
%
%-------------------------------------------------------------------------
ns = length(phi(1,:));  % number of species in mixture
DE = zeros(1,nx);  % Change in energy due to reaction
sigmax_interface = 1/2*( sigmax(jI) + sigmax(jI+1) );  % 1st order interp
% sigmax_interface =  (sigmax(jI) + sigmax(jI+1))  - ...
%     1/2*(sigmax(jI-1) + sigmax(jI+2));   % 2nd order interpolation

% material 1
% left bc - free surface  (extrapolate values)
rho(jL-1) = 2*rho(jL)-rho(jL+1);
phi(jL-1) = phi(jL);
phi_L(jL-1) = phi_L(jL);
vx(jL-1) = vx(jL);
sigmax(jL-1) = 0;
e(jL-1) = e(jL);
q(jL-1) = 0;
% right bc - ghost cell at interface
% rho_int(1) = 2*rho(jI)-rho(jI-1);
rho_int(1) =1/2*(rho(jI)+rho(jI-1));
vx_int(1) = vx(jI+1);  % velocity of Pa = velocity of B
sigmax_int(1) = sigmax_interface;   % stress in x-dir is equal !!!
% % % sigmax_int(1) = sigmax(jI+1);   % stress in x-dir is equal !!!
e_int(1) = e(jI);  % to prevent over heating
q_int(1) = q(jI);  %

% material 2
%left bc - ghost cell at interface
% rho_int(2) = 2*rho(jI+1)-rho(jI+2);
```

```
rho_int(2) =1/2*(rho(jI+1)+rho(jI+2));
vx_int(2) = vx(jI);
sigmax_int(2) = sigmax_interface;   % stress in x-dir is equal !!!
% % % sigmax_int(2) = sigmax(jI);   % stress in x-dir is equal !!!
e_int(2) = e(jI+1);
q_int(2) = q(jI+1);
% right bc - free surface  (extrapolate values)
rho(jR+1) = 2*rho(jR)-rho(jR-1);
phi(jR+1) = phi(jR);
phi_L(jR+1) = phi_L(jR);
vx(jR+1) = vx(jR);
sigmax(jR+1) = 0;
e(jR+1) = e(jR);
q(jR+1) = 0;

% function values on regular cells and free surface ghost cells
m(jL-1:jR+1) = rho(jL-1:jR+1).*vx(jL-1:jR+1);
for j=jL-1:jR+1
    fphi(j,:) = m(j)*phi(j,:);
    fphi_L(j) = m(j)*phi_L(j);
end
phi(jI,:) = phi(jI+1,:);  fphi(jI,:) = fphi(jI+1,:);  % redundant statment
phi_L(jI) = phi_L(jI+1);  fphi_L(jI) = fphi_L(jI+1);
f_m(jL-1:jR+1) = m(jL-1:jR+1).*vx(jL-1:jR+1) - sigmax(jL-1:jR+1);
% E(jL-1:jR+1) = rho(jL-1:jR+1).*(e(jL-1:jR+1) + 1/2*vx(jL-1:jR+1).^2);
E(jL-1:jI) = rho(jL-1:jI).*(e(jL-1:jI) + 1/2*vx(jL-1:jI).^2);
E(jI+1:jR+1) = rho(jI+1:jR+1).*alphap(jI+1:jR+1).*(e(jI+1:jR+1) + ...
    1/2*vx(jI+1:jR+1).^2);

f1_E(jL-1:jR+1) = E(jL-1:jR+1).*vx(jL-1:jR+1);
f2_E(jL-1:jR+1) = - sigmax(jL-1:jR+1).*vx(jL-1:jR+1);
f3_E(jL-1:jR+1) = q(jL-1:jR+1);
% function values on intersecting ghost cells
```

```
m_int = rho_int.*vx_int;
% % % f_phi_int(1,:) = m_int(1)*phi_int(1,:);
% % % f_phi_int(2,:) = m_int(2)*phi_int(2,:);
f_m_int = m_int.*vx_int - sigmax_int;
% E_int = rho_int.*(e_int + 1/2*vx_int.^2);
E_int(1) = rho_int(1).*(e_int(1) + 1/2*vx_int(1).^2);
E_int(2) = alphap(jI+1)*rho_int(2).*(e_int(2) + 1/2*vx_int(2).^2);
f1_E_int = E_int.*vx_int;
f2_E_int = - sigmax_int.*vx_int;
f3_E_int = q_int;

for j = jL-1 : jR+1
    if j == jL-1
        slope_rho = (rho(j+1)-rho(j))/dx;  %cons mass
        slope_phi = zeros(1,ns);  % cons species
        slope_phif = zeros(1,ns);
        slope_phi_L = 0;  % mass fraction of liquid reactants
        slope_phif_L = 0;
        slope_m = (m(j+1)-m(j))/dx;  % cons mom
        slope_mf = (f_m(j+1)-f_m(j))/dx;
        slope_E = (E(j+1)-E(j))/dx;   % cons energy
        slope_Ef1 = (f1_E(j+1)-f1_E(j))/dx;
        slope_Ef2 = (f2_E(j+1)-f2_E(j))/dx;
        slope_Ef3 = (f3_E(j+1)-f3_E(j))/dx;
    elseif j == jI
        slope_rho = minmod((rho_int(1)-rho(j))/dx,(rho(j)-rho(j-1))/dx);
        slope_phi = zeros(1,ns);
        slope_phif = zeros(1,ns);
        slope_phi_L = 0;
        slope_phif_L = 0;
        slope_m =  minmod((m_int(1)-m(j))/dx,(m(j)-m(j-1))/dx);
        slope_mf = minmod((f_m_int(1)-f_m(j))/dx,(f_m(j)-f_m(j-1))/dx);
        slope_E = minmod((E_int(1)-E(j))/dx,(E(j)-E(j-1))/dx);
```

```
    slope_Ef1= minmod((f1_E_int(1)-f1_E(j))/dx,(f1_E(j)-f1_E(j-1))/dx);
    slope_Ef2= minmod((f2_E_int(1)-f2_E(j))/dx,(f2_E(j)-f2_E(j-1))/dx);
    slope_Ef3= minmod((f3_E_int(1)-f3_E(j))/dx,(f3_E(j)-f3_E(j-1))/dx);

    s_rho_i(2) = (rho(j+1)-rho_int(2))/dx;  % material 2 ghost cell
    s_m_i(2) =  (m(j+1)-m_int(2))/dx;
    s_mf_i(2) = (f_m(j+1)-f_m_int(2))/dx;
    s_E_i(2) = (E(j+1)-E_int(2))/dx;
    s_Ef1_i(2) = (f1_E(j+1)-f1_E_int(2))/dx;
    s_Ef2_i(2) = (f2_E(j+1)-f2_E_int(2))/dx;
    s_Ef3_i(2) = (f3_E(j+1)-f3_E_int(2))/dx;
    [rho_p_i(2),rho_m_i(2),m_p_i(2),m_m_i(2), f_m_p_i(2),f_m_m_i(2),...
        E_p_i(2),E_m_i(2),f1_E_p_i(2),f1_E_m_i(2), f2_E_p_i(2),...
        f2_E_m_i(2), f3_E_p_i(2),f3_E_m_i(2)] = ...
        muscl_reconstruction(rho_int(2),s_rho_i(2),m_int(2), ...
        s_m_i(2),f_m_int(2), s_mf_i(2),  E_int(2),s_E_i(2), ...
        f1_E_int(2),s_Ef1_i(2),f2_E_int(2),s_Ef2_i(2),f3_E_int(2), ...
        s_Ef3_i(2) ,dx);
    phi_p_i(2,:) = phi(jI+1,:);  phi_m_i(2,:) = phi(jI+1,:);
    fphi_p_i(2,:) = fphi(jI+1,:);  fphi_m_i(2,:) = fphi(jI+1,:);
    phi_L_p_i(2) = phi_L(jI+1);  phi_L_m_i(2) = phi_L(jI+1);
    fphi_L_p_i(2) = fphi_L(jI+1); fphi_L_m_i(2) = fphi_L(jI+1);

elseif j == jI+1
    slope_rho = minmod((rho(j+1)-rho(j))/dx,(rho(j)-rho_int(2))/dx);
    slope_phi = zeros(1,ns);
    slope_phif = zeros(1,ns);
    slope_phi_L = 0;
    slope_phif_L = 0;
    slope_m =  minmod((m(j+1)-m(j))/dx,(m(j)-m_int(2))/dx);
    slope_mf = minmod((f_m(j+1)-f_m(j))/dx,(f_m(j)-f_m_int(2))/dx);
    slope_E = minmod((E(j+1)-E(j))/dx,(E(j)-E_int(2))/dx);
    slope_Ef1= minmod((f1_E(j+1)-f1_E(j))/dx,(f1_E(j)-f1_E_int(2))/dx);
```

```
    slope_Ef2= minmod((f2_E(j+1)-f2_E(j))/dx,(f2_E(j)-f2_E_int(2))/dx);
    slope_Ef3= minmod((f3_E(j+1)-f3_E(j))/dx,(f3_E(j)-f3_E_int(2))/dx);

    s_rho_i(1) = (rho_int(1)-rho(j-1))/dx;  % material 1 ghost cell
    s_m_i(1) =  (m_int(1)-m(j-1))/dx;
    s_mf_i(1) = (f_m_int(1)-f_m(j-1))/dx;
    s_E_i(1) = (E_int(1)-E(j-1))/dx;
    s_Ef1_i(1) = (f1_E_int(1)-f1_E(j-1))/dx;
    s_Ef2_i(1) = (f2_E_int(1)-f2_E(j-1))/dx;
    s_Ef3_i(1) = (f3_E_int(1)-f3_E(j-1))/dx;
    [rho_p_i(1),rho_m_i(1),m_p_i(1),m_m_i(1), f_m_p_i(1),f_m_m_i(1),...
        E_p_i(1),E_m_i(1),f1_E_p_i(1),f1_E_m_i(1), f2_E_p_i(1), ...
        f2_E_m_i(1), f3_E_p_i(1),f3_E_m_i(1)] = ...
        muscl_reconstruction( rho_int(1),s_rho_i(1),m_int(1), ...
        s_m_i(1),f_m_int(1), s_mf_i(1),  E_int(1),s_E_i(1), ...
        f1_E_int(1),s_Ef1_i(1), f2_E_int(1),s_Ef2_i(1), ...
        f3_E_int(1), s_Ef3_i(1) ,dx);
    phi_p_i(1,:) = phi(j,:);  phi_m_i(1,:) = phi(j,:);
    fphi_p_i(1,:) = fphi(j,:);  fphi_m_i(1,:) = fphi(j,:);
    phi_L_p_i(1) = phi_L(j);  phi_L_m_i(1) = phi_L(j);
    fphi_L_p_i(1) = fphi_L(j);  fphi_L_m_i(1) = fphi_L(j);

elseif j == jR+1
    slope_rho = (rho(j)-rho(j-1))/dx;  %cons mass
    slope_phi = zeros(1,ns);  % cons species
    slope_phif = zeros(1,ns);
    slope_phi_L = 0;  % cons species
    slope_phif_L = 0;
    slope_m = (m(j)-m(j-1))/dx;  % cons mom
    slope_mf = (f_m(j)-f_m(j-1))/dx;
    slope_E = (E(j)-E(j-1))/dx;   % cons energy
    slope_Ef1 = (f1_E(j)-f1_E(j-1))/dx;
    slope_Ef2 = (f2_E(j)-f2_E(j-1))/dx;
```

```
    slope_Ef3 = (f3_E(j)-f3_E(j-1))/dx;
else  % main nodes
    slope_rho = minmod((rho(j+1)-rho(j))/dx,(rho(j)-rho(j-1))/dx);
    for k=1:ns
        slope_phi(1,k) = minmod((phi(j+1,k)-phi(j,k))/dx,...
            (phi(j,k)-phi(j-1,k))/dx);
        slope_phif(1,k) = minmod((fphi(j+1,k)-fphi(j,k))/dx,...
            (fphi(j,k)-fphi(j-1,k))/dx);
    end
    slope_phi_L(1) = minmod((phi_L(j+1)-phi_L(j))/dx,...
        (phi_L(j)-phi_L(j-1))/dx);
    slope_phif_L(1) = minmod((fphi_L(j+1)-fphi_L(j))/dx,...
        (fphi_L(j)-fphi_L(j-1))/dx);
    slope_m =  minmod((m(j+1)-m(j))/dx,(m(j)-m(j-1))/dx);
    slope_mf = minmod((f_m(j+1)-f_m(j))/dx,(f_m(j)-f_m(j-1))/dx);
    slope_E = minmod((E(j+1)-E(j))/dx,(E(j)-E(j-1))/dx);
    slope_Ef1= minmod((f1_E(j+1)-f1_E(j))/dx,(f1_E(j)-f1_E(j-1))/dx);
    slope_Ef2= minmod((f2_E(j+1)-f2_E(j))/dx,(f2_E(j)-f2_E(j-1))/dx);
    slope_Ef3= minmod((f3_E(j+1)-f3_E(j))/dx,(f3_E(j)-f3_E(j-1))/dx);
end
[rho_p(j),rho_m(j), m_p(j),m_m(j), f_m_p(j),f_m_m(j), E_p(j),E_m(j),...
    f1_E_p(j),f1_E_m(j), f2_E_p(j),f2_E_m(j), f3_E_p(j),f3_E_m(j)]=...
    muscl_reconstruction(rho(j),slope_rho,m(j),slope_m,f_m(j),...
    slope_mf,E(j),slope_E,f1_E(j),slope_Ef1, f2_E(j),slope_Ef2, ...
    f3_E(j),slope_Ef3,dx);
% cons mass species
phi_p(j,:) = phi(j,:) + slope_phi(1,:)*dx/2;
phi_m(j,:) = phi(j,:) - slope_phi*dx/2;
fphi_p(j,:) = fphi(j,:) + slope_phif*dx/2;
fphi_m(j,:) = phi(j,:) - slope_phif*dx/2;
% mass fraction of liquid reactants
phi_L_p(j) = phi_L(j) + slope_phi_L(1)*dx/2;
phi_L_m(j) = phi_L(j) - slope_phi_L*dx/2;
```

```
    fphi_L_p(j) = fphi_L(j) + slope_phif_L*dx/2;
    fphi_L_m(j) = phi_L(j) - slope_phif_L*dx/2;
end

% CALCULATE FLUXES at t^n  (for F(j) evaluated at x(j+1/2))
% Use Lax Friedrichs Flux, LFF
F_rho=zeros(1,nx);  F_m=zeros(1,nx);   F_E=zeros(1,nx);
F_phi=zeros(nx,ns);  F_phi_L=zeros(1,nx);
for j=jL-1:jR
    if j==jI
        % for material 1
        [F_rho_i(1),F_m_i(1),F_E_i(1)] = LF_flux(rho_p(j), ...
            rho_m_i(1), m_p(j),m_m_i(1), f_m_p(j),f_m_m_i(1), ...
            E_p(j),E_m_i(1),f1_E_p(j),f1_E_m_i(1), f2_E_p(j), ...
            f2_E_m_i(1), f3_E_p(j), f3_E_m_i(1), alpha(j));
        % for material 2
        [F_rho_i(2),F_m_i(2),F_E_i(2)] = LF_flux(rho_p_i(2), ...
            rho_m(j+1), m_p_i(2),m_m(j+1), f_m_p_i(2),f_m_m(j+1), ...
            E_p_i(2),E_m(j+1), f1_E_p_i(2),f1_E_m(j+1),f2_E_p_i(2), ...
            f2_E_m(j+1),f3_E_p_i(2), f3_E_m(j+1), alpha(j));

        for k=1:ns % cons mass species
            F_phi_i(1,k) = 1/2*( fphi_p(j,k) + fphi_m_i(1,k) ) - ...
                1/2*alpha(j)*( phi_m_i(1,k) - phi_p(j,k) );
            F_phi_i(2,k) = 1/2*( fphi_p_i(2,k) + fphi_m(j+1,k)  ) - ...
                1/2*alpha(j)*( phi_m(j+1,k) - phi_p_i(2,k)   );
        end
        % mass fraction of liquid reactants
        F_phi_L_i(1) = 1/2*( fphi_L_p(j) + fphi_L_m_i(1) ) - ...
            1/2*alpha(j)*( phi_L_m_i(1) - phi_L_p(j) );
        F_phi_L_i(2) = 1/2*( fphi_L_p_i(2) + fphi_L_m(j+1)  ) - ...
            1/2*alpha(j)*( phi_L_m(j+1) - phi_L_p_i(2)   );
```

```
    else  % for general cells and for free surfaces
         [F_rho(j),F_m(j),F_E(j)]=LF_flux(rho_p(j),rho_m(j+1),...
            m_p(j),m_m(j+1), f_m_p(j),f_m_m(j+1), E_p(j),E_m(j+1),...
            f1_E_p(j),f1_E_m(j+1), f2_E_p(j),f2_E_m(j+1), ...
            f3_E_p(j),f3_E_m(j+1), alpha(j));
        F_phi(j,:) = 1/2*( phi_p(j,:) + phi_m(j+1,:)  ) - ...
            1/2*alpha(j)*( phi_m(j+1,:) - phi_p(j,:)  );
        F_phi_L(j) = 1/2*( phi_L_p(j) + phi_L_m(j+1)  ) - ...
            1/2*alpha(j)*( phi_L_m(j+1) - phi_L_p(j)  );
    end
end

% Calculate U(n+1)
for j=jL:jR
    if j==jI
        rho(j) = rho(j) - (dt)*(1/dx)*( F_rho_i(1) - F_rho(j-1) );
        m(j) = m(j) - (dt)*(1/dx)*( F_m_i(1) - F_m(j-1) );
        E(j) = E(j) - (dt)*(1/dx)*( F_E_i(1) - F_E(j-1) );
    elseif j==jI+1
        rho(j) = rho(j) - (dt)*(1/dx)*( F_rho(j) - F_rho_i(2) );
        m(j) = m(j) - (dt)*(1/dx)*( F_m(j) - F_m_i(2) );
        E(j) = E(j) - (dt)*(1/dx)*( F_E(j) - F_E_i(2) );
    else
        rho(j) = rho(j) - (dt)*(1/dx)*( F_rho(j) - F_rho(j-1) );
        if j>jI+1
            dphi = - dt/dx*( F_phi(j,:) - F_phi(j-1,:) );
            phi(j,:) = phi(j,:) + dphi;
            dphi_L = - dt/dx*( F_phi_L(j) - F_phi_L(j-1) );
            phi_L(j) = phi_L(j) + dphi_L;
        end
        m(j) = m(j) - (dt)*(1/dx)*( F_m(j) - F_m(j-1) );
        E(j) = E(j) - (dt)*(1/dx)*( F_E(j) - F_E(j-1) );
    end
```

```
end
%-------------------------------------------------------------------------
% Add contributions due to chemical reaction and latent heat of melting
% Initialize
%-------------------------------------------------------------------------
% Tmelt = 660 + 273;  % melting temp of Al (K)(particle size dependent)
% Tmelt = 600;
if select_mat==1  % Ni + Al fprintf('Update muscl_rxn_reimann_vel.m \n')
    % 3Al(s) + Ni(s) --> 3Al(l) + Ni(s)  --> Al3Ni(l)
    nc = 3;
    % Molar masses (kg/mol)
    M_m = [0.0269815  0.0585934  0.13963802];
    G = [-3   -1   1 ];  % Stoich coefs   [Al Ni]
%     G = [-3   -1   3   1   1 ];  % Stoich coefs   [Al Ni]
    M_prod = M_m(nc)*G(nc)'/4; % (kg/1 mole of reactants)
    M_react = M_m(1:2)*abs(G(1:2))'/4;  % (kg/1 mole of reactants)
    rhod_m =  [2700   8909   3368  1200]; % density (kg/m^3)
    %--------------- Activation Energy due to Pressure --------------------
else % Al + Fe2O3
    % 2Al + Fe2O3 -> AlO + 2FeO + Al -> 1/3Al2O3 + 1/2FeAl2O4 + 1/3Al + 3/2Fe
    % Note: 1 mole reactants is  2/3Al + 1/3Fe2O3
    nc = 6;  % number of constituents that participate in the rxn
    % Reactant/Product Molar mass (kg/mol)
    M_m=([0.026981539  0.1596922  0.101961278  0.1738077  0.026981539 ...
        0.055847]);
    G = ([-2 -1  1/3  1/2  1/3  3/2]);  % Reactant Stoich coefs
    M_prod = M_m(3:nc)*G(3:nc)'/3; % (kg/1 mole of reactants)
    M_react = M_m(1:2)*abs(G(1:2))'/3;  % (kg/1 mole of reactants)
    rhod_m=([2380  5274  2960  3950  2380  5274  1200]); % density (kg/m^3)
    %--------------- Activation Energy due to Pressure --------------------
    % For Reaction Process:
    % consider reactants [Al Fe2O3] and transition state [AlO Fe2O Al]
    % combined = [Al Fe2O3  AlO Fe2O  Al ]  (reactant->transition state)
```

```
    % Molar mass (kg/m^3)
    M_tr = [0.026981539  0.1596922    0.0429815  0.12769  0.0269815];
    v_tr = [-2 -1  1  2  1];  % Stoich coeffs for 1 mole reactants
    rho_tr = [2380  5274  2960  5700  2380]; % density (kg/m^3)
    % Calculate molar volume (m^3/mol)
    V = M_tr.*v_tr./rho_tr;  % no implied volume constraints
    DV = V*ones(1,5)';  % sum of all molar volumes
    % Calculate energy contribution due to Pressure
% % %     dG_sigma_rxn = P(j)*DV;  % (J/mol)
    % Note: transition state values are mass fractions for lack of densities
end

% Chemical Reaction:
for j=jI+1:jR
    if T(j)>=T_rxn  % if temperature exceeds that of Aluminum rxn occurs
        phi_sum = sum( phi(j,1:2) );
        if phi_sum>0
            %         fprintf('Reacting!! \n')
            rhodd = rho(j)*alphap(j);
            [phi(j,:),DE]=reaction_bin(T(j),rhodd,phi(j,:),...
                Ao,G,M_m,M_react,rho_react,phi_max,phi_ep,nc, ...
                dt_rxn,dt,select_mat);
            % add heat contribution in dense mixture from reaction (J/m^3)
            E(j) = E(j) + DE;
        end
    end
end

% Heat of melting:
% strategy: use e, rho since these have not been updated
vx(jL:jR) = m(jL:jR)./rho(jL:jR);
e(jL:jI) = E(jL:jI)./rho(jL:jI) -1/2*vx(jL:jI).^2;
e(jI+1:jR) = E(jI+1:jR)./(rho(jI+1:jR).*alphap(jI+1:jR)) ...
```

```
    - 1/2*vx(jI+1:jR).^2;
T(jL:jR) = e(jL:jR)./Cp(jL:jR);

%  Tmelt = 10000;  uncomment to observe condition where melt doesn't occur
for j=jI+1:jR
    if T(j)>Tmelt  % if temperature exceeds melting may occur
        if phi_L(j)<1-phi_ep  % if some non-melted constituents remain
            % assume: epoxy is amorphous, thus, no melting heat needed
            %             fprintf('melting!\n')
            dG_heat = 390*1e3;  % latent heat for Al (J/kg)   (10.71 J/mol)
            % note:  Ni has dG_heat = 305 kJ/kg (Matweb)
            % 312 kJ/kg used for Ni3+Al reaction by Ben-Hor Ballotechnic 1994
            %
            phi_temp = zeros(1,nc+1);
            phi_temp(1:2) = phi_m(j,1:2)/sum(phi_m(j,1:2));
            if select_mat ==1  % Al + Ni
                rhod_noep = vo(1:2)*[2700  8909]'/sum( vo(1:2) ) ;
                [Cp_bar] = cp_AlNi(T(j),phi_temp); %  (J/kg-K) [1,1]
            else  % Al + Fe2O3
                rhod_noep = vo(1:2)*[2700  5274]'/sum( vo(1:2) ) ;
                [Cp_bar] = cp_fe2o3_al(T(j),phi_temp); %  (J/kg-K) [1,1]
            end

            % Calculate change in mass fractions to liquid
            DT_melt = (T(j)-Tmelt);
            rhodd = rho(j)*alphap(j);
            Dphi_L = DT_melt*rhodd*Cp_bar/(dG_heat*rhod_noep);
            phi_star = phi_L(j) + Dphi_L;  % new liquid mass fraction
%                 [DT_melt,phi_star,Cp_bar,rhodd,rhod_noep,dG_heat])
            % Calculate the heat contribution from melting (J/m^3)
            De = Cp(j)*DT_melt; % (J/m^3)
            % Subtract this energy contribution from the internal energy
            e(j) = e(j) - De;
```

```
            % Subtract this energy contribution from the total energy
            E(j) = E(j) - rho(j)*alphap(j)*De;

            % Adjust temperature and update liquid mass fraction:
            if phi_star<=1-phi_ep  % not all reactants are melted
                phi_L(j) = phi_star;
                T(j) = Tmelt;
            else  % melting is complete
                phi_L(j) = 1 - phi_ep;
                T(j) = Tmelt + dG_heat*rhod_noep*(phi_star-1+phi_ep)/...
                    (rho(j)*alphap(j)*Cp(j));
                De = Cp(j)*(T(j)-Tmelt); % (J/m^3)
                % add back energy
                e(j) = e(j) + De;
                E(j) = E(j) + rho(j)*alphap(j)*De;
            end
        end
    end
end

function [F_rho,F_m,F_E] = ...
    LF_flux(rho_L,rho_R, m_L,m_R, f_m_L,f_m_R, ...
    E_L,E_R,f1_E_L,f1_E_R, f2_E_L,f2_E_R, f3_E_L,f3_E_R, alpha)



% Note: Lax Friedrichs flux routine
%cons mass
F_rho = 1/2*( m_L + m_R ) - 1/2*alpha*( rho_R - rho_L );
% cons mom
F_m = 1/2*( f_m_L + f_m_R ) -  1/2*alpha*( m_R - m_L );
% cons energy
F_E = 1/2*( f1_E_L+f1_E_R + (f2_E_L+f2_E_R)  + (f3_E_L+f3_E_R)    )...
    - 1/2*alpha*(  E_R - E_L );
```

```
function  [rho_p,rho_m, m_p,m_m, f_m_p,f_m_m, ...
    E_p,E_m, f1_E_p,f1_E_m, f2_E_p,f2_E_m, f3_E_p,f3_E_m]=...
    muscl_reconstruction(rho,slope_rho,m,slope_m,f_m,slope_mf,...
    E,slope_E,f1_E,slope_Ef1,f2_E,slope_Ef2,f3_E,slope_Ef3 ,dx);
%-------------------------------------------------------------------------
%cons mass
rho_p = rho + slope_rho*dx/2;
rho_m = rho - slope_rho*dx/2;
% cons mom
m_p = m + slope_m*dx/2;
m_m = m - slope_m*dx/2;
f_m_p = f_m + slope_mf*dx/2;
f_m_m = f_m - slope_mf*dx/2;
% cons energy
E_p = E + slope_E*dx/2;
E_m = E - slope_E*dx/2;
f1_E_p = f1_E + slope_Ef1*dx/2;
f1_E_m = f1_E - slope_Ef1*dx/2;
f2_E_p = f2_E + slope_Ef2*dx/2;
f2_E_m = f2_E - slope_Ef2*dx/2;
f3_E_p = f3_E + slope_Ef3*dx/2;
f3_E_m = f3_E - slope_Ef3*dx/2;



function [phi,DE]=reaction_bin(T,rho,phi, ...
    Ao,G,M_m,M_react,rho_react,phi_max,phi_ep,nc, dt_rxn,dt,select_mat)
%
% By: Derek Reding
% Last modified on 09/27/07
% Note:  this function only calculates elementary reactions with two
% reactants, one of which must be aluminum with Tm
%
```

```
% Assume: adiabatic heating occurs during the time [t(n), t(n+1)]
% Reason: dt may be far too long for T(n) to be accurate, thus leading to
% extremly high values for Ao
%
% INPUTS:
% T = mixture temperature (K) at time t(n)
% Cp_bar = mixture heat capacity (dense mixture)
% rho = mix. density @ t(n) (non-porous - energy considerations) (kg/m^3)
% phi = mass fractions at time t(n)  (note: avoid confusion with phi_m)
% Ao = constant frequency factor
% G = stoichiometric coefficients
% M_m = molar mass for each constituent (kg/mol) [1,nc=6]
% rho_react =  basis for internal energy definition (kg/m^3) [1,1]
% phi_max = .1;  % fraction of reaction completion (phi_max<=1)
% phi_ep = mass fraction of inert material or binder such as epoxy
% nc = number of constituents in mixture (except binder)
% dt_rxn = maximum time step used in chemical reactions (sec)
% dt = time step in the continuum (sec)
%
% OUTPUTS:
% phi = new mass fractions @ t(n+1)  [1,nc]
% DE = total energy contribution from reaction in dense mix (J/m^3)  [1,1]
%
%--------------------------------------------------------------------------
%--------------------------------------------------------------------------
% Initialize time step and material parameters
%--------------------------------------------------------------------------
R = 8.3145;  % Universal Gas Constant (J/mol*K)
if dt_rxn>dt/2   % find correct reaction time step size, dt_r (sec)
    nt=2;
    dt_r = dt/2;
else
    nt = ceil(dt/dt_rxn);
```

```
    dt_r = dt/nt;
end


phi_in = phi;  % save initial mass fractions
if select_mat==1  % Ni + Al
    [Cp_bar] = cp_AlNi(T,phi); %  (J/kg-K) [1,1]
    if T>3000  % dG's are not valid for T>3000K
        T = 3000;
    end
    % dG_rxn = forward activation energy (J/1mol reactants)
    dG_rxn = -7.9*T + 7426.5;  % (R^2=0.9999)
    dG_rxn = -6.71377e+01*T + 1.17975e+05;   % (R^2=0.99899)
else  % Fe2O3 + Al
    if T>3000  % dG's are not valid for T>3000K
        T = 3000;
    end
    [Cp_bar] = cp_fe2o3_al(T,phi); %  (J/kg-K) [1,1]
    % dG_rxn = forward activation energy (J/1mol reactants)
    % source --> "Reaction_enthalpy_Fe2O3Al.xls"
    % in directory --> D:\Material Properties\Enthalpy_calculations\
    dG_rxn = -6.71377e+01*T + 1.17975e+05;   % (R^2=0.99899)
end % if select_mat


% Initialize the specific internal energy, E (J/m^3)
E = T*rho*Cp_bar;  % J/m^3
E_in =  E;  % save initial specific internal energy
%-------------------------------------------------------------------------
% Caclulate reaction rate
%-------------------------------------------------------------------------
% DPHI_tot = zeros(1,nt);
for k=1:nt
    if select_mat==1  % Ni + Al
        if T>3000  % dG's are not valid for T>3000K
```

```
        T = 3000;
    end
    [Cp_bar] = cp_AlNi(T,phi); %  (J/kg-K) [1,1]
    % dG_rxn = forward activation energy (J/1mol reactants)
    dG_rxn = -7.9*T + 7426.5;  % (R^2=0.9999)
else  % Fe2O3 + Al
    if T>3000  % dG's are not valid for T>3000K
        T = 3000;
    end
    [Cp_bar] = cp_fe2o3_al(T,phi); %  (J/kg-K) [1,1]
    % dG_rxn = forward activation energy (J/1mol reactants)
    % source --> "Reaction_enthalpy_Fe2O3Al.xls"
    % in directory --> D:\Material Properties\Enthalpy_calculations\
    dG_rxn = -6.71377e+01*T + 1.17975e+05;   % (R^2=0.99899)
end % if select_mat
% + dG_sigma_rxn;  % add in the sigma term later
kf = Ao*exp( -dG_rxn/(R*T) );  % Forward rxn rate constant
C = rho*phi(1:2)./M_m(1:2);  % Reactant Molarity (mol/m^3)
THETA = kf*C(1)^abs(G(1))*C(2)^abs(G(2));  % Fwd rxn rate
[phi,DPHI] = phi_cutoff(rho,phi, ...
    THETA,phi_max,phi_ep,  M_m,G,dt_rxn,nc);
if select_mat==1  % Ni + Al
    T_in = T;
    if T_in>4300;    T_in = 4300;    end
    dH_rxn = 4*(7.6305e-4*T_in^2 + 2.7527*T_in - 3.8825e4); % (R^2=0.9995)
else  % Fe2O3 + Al
    % dH_rxn is for 1 mol of reactants, i.e., 2/3Al+1/3Fe2O3
    % source --> "Reaction_enthalpy_Fe2O3Al.xls"
    % in directory--> D:\Material Properties\Enthalpy_calculations\
    % (J/1 mol reactants) (R^2=.984727)
    dH_rxn = 1.64536e+01*T - 2.41575e+05;
end
dH_rxn2 = dH_rxn/M_react;  % convert units to (J/kg reactants)
```

```
    dH_rxn3 = dH_rxn2*rho_react;  % convert units to (J/m^3 reactants)
    % note: DPHI approches ->   1-phi_ep
%     DPHI_tot(k) = DPHI_tot(k-1) + DPHI;
    dPHI_rxn = DPHI*dH_rxn3;  % *3/M_prod
    DE = dPHI_rxn;
    E = E + DE;
    % Calculate new temperature for reaction kinetics only
    T = E/(rho*Cp_bar); % assume Cp_bar is still valid (small dT)  (K)
end
DE = E - E_in;  % change in specific internal energy (J/m^3) [1,1]
dphi = phi_in - phi;  % change in mass fractions [1,nc]

function [Cp_bar] = cp_fe2o3_al(T,phi_m)
%
% By: Derek Reding
% Last modified on: 9/11/07
%
% Calculate the mass fraction average heat capacity  Cp (J/kg-K)
% Notes: 1) 1 mole of reactants = 2/3Al + 1/3Fe2O3
%        2) mixture constituents = [Al,Fe2O3,Al2O3,FeAl2O4,Al,Fe,epoxy]
%------------------------------------------------------------------------
% INPUTS:
% T = mixture temperature (K)  [1,1]
% phi_m = mixture mass fractions [1,nc+1=7]
% M_m = molar mass for each constituent (kg/mol) [1,nc=6]
% OUTPUTS:
% Cp_bar = mixture heat capacity (J/kg-K) [1,1]
%
%------------------------------------------------------------------------
% Reactant/Product Molar mass (kg/mol)
M_m=([0.026981539  0.1596922  0.101961278  0.1738077  0.026981539 ...
    0.055847]);
```

```
if T>3000
    T = 3000;  % Cp's are not valid for T>3000K
end
Cp = zeros(1,7);
Cp(1) = -9.2979*1e-13*T^4 + 8.0633*1e-09*T^3 - ...
    2.5213*1e-05*T^2 + 3.3461*1e-02*T + 1.5992*1e+01; % (R^2=.9777)
if T<=1000  % transition temperature (K)
    Cp(2) = -3.5429e-09*T^4 + 8.7446e-06*T^3 - 7.7377e-03*T^2 ...
        + 2.9905e+00*T - 3.0263e+02;  % (R^2=.98368)
else
    Cp(2) = 2.7499e-12*T^4 - 2.5802e-08*T^3 + 8.9653e-05*T^2 ...
        - 1.3678e-01*T + 2.1403e+02;  % (R^2=.99329)
end
Cp(3) = -1.9698*1e-11*T^4 + 1.2227*1e-07*T^3 - 2.7867*1e-04*T^2 + ...
    2.8563*1e-01*T + 1.6792*1e+01;  % (R^2=.9970)
Cp(4) = -1.1724*1e-11*T^4+9.1082*1e-08*T^3-2.5579*1e-04*T^2+ ...
    3.0990*1e-01*T + 5.6442*1e1; %  (R^2=.98717)
Cp(5) = Cp(1);
if T<=1184.81  % transition temperature (K)
    Cp(6) =  -4.4740e-10*T^4 + 1.1487e-06*T^3 - 1.0138e-03*T^2 + ...
        3.9130e-01*T - 2.8708e+01;  %  (R^2=.96505)
else
    Cp(6) = 1.4008e-11*T^4 - 1.1806e-07*T^3 + 3.5479e-04*T^2 - ...
        4.3974e-01*T + 2.2584e+02; %  (R^2=.97222)
end
Cp(7) = 2100;  % EPON828 (J/kg-K)
Cp(1:6) = Cp(1:6)./M_m;  %  convert units to (J/kg-K)
Cp_bar = Cp*phi_m';  % mixture heat capacity (J/kg-K)


function [sigmax,sigmay,sdev,sigmay_dev,P,q,alphap,C, pore_hist,pore_hist_r] = ...
    const_rxn_reimann(rho_new,phi_m,vo_m,vo,T,T_new,vx,sdev,q,kq, ...
    eos,eos_type,rhood,rhod_m,rho_o,alphao,alphap,Co,C,P, ...
```

```
    yield_st,yield_mix,mu,Cv, rho_sto, eos_st,  Pmax, wflag,select_mix, ...
    plast_const,pore_hist,pore_hist_r, r0, dt_ro,n_r, a_o,C_I,mu_f, ...
    select_pore,  n,Cm,Pe,Ps, nx,dx,dt,  jL,jI,jR, step,k_time);
global trigger_dense % density diff req. for pore-collapse EOS activation
global Tol_rho  % Homobaric EOS tollerance on % density (nominal 0.0001)
global eps1 % fraction of e,rho for numerical approx. of acoustic velocity
%
% Written by: Derek Reding
% Last modified on 08-14-07
% function to compute the CONSTITUTIVE LAWS
%-------------------------------------------------------------------------
% INPUTS:
% rho_new = updated porous mixture density from conservation laws
% phi_m = mass fractions for the mixture [nc,nx,nt]
% vo_m = initial (P=0) volume fractions for mixture
% vo = volume fractions of dense mixture  [1,nc+1]
% T = previous time step mixture temperature (K) [1,nx]
% T_new = updated mixture temperature (K) from conservation laws [1,nx]
% vx = mix velocity parallel to the motion of the shock front (m/s) [1,nx]
% sdev = previous time step (un-returned) deviatoric stress in x-dir (Pa)
% q = previous time step heat flux (W/m^2)
% kq = updated mixture averaged (volume fracs) thermal conductivity (W/mK)
% eos = set of eos material parameters for all mixture components (matrix)
% eos_type = specifies to use either Mei-Gruneisen or Murnaghan EOS model
% rhood = updated dense mixture initial density (kg/m^3)
% rhod_m = initial mixture constituent densities at P=0
% rho_o = initial porous mix density (without rxn => test values) (kg/m^3)
% alphao = Initial Distension ratio (alphao>=1)
% Co = Initial speed of sound in porous mixture material (m/s)
% C = speed of sound in porous mixture material (m/s)
% P = Pressure (Pa)
% yield_st = yield strength of steel or impactor (e.g. copper) (Pa)
% yield_mix = yield strength of mixture (Pa)
```

```
% mu = elastic shear strength (Pa)  (mixture and steel)
% Cv = heat capacity (J/Kg*K)       (mixture and steel)
% rho_sto = initial density of steel (P=0)  (kg/m^3)
% eos_st = set of eos material parameters for steel (vector)
% Pmax = max pressure,(Pa) must be known a-priori for Us_obs calc and Homo
% wflag = when wflag==1, suppress homogeneous warnings with error<1%
% select_mix = choice of EOS mixture rule
    % select_mix = 1  -> Bennett-Horie mix rule  (simple)
    % select_mix = 2  -> Rigorous mixture rules (use Cm)
% plast_const = [nc,:] = constitutive parameters for each constituent
% pore_hist = x(2,nx) = position and velocity of the inner surface (r=a)
% pore_hist_r(4,n_r,nx) = [T,gamma_p,rho_hat,sigma_e]
% r0 = initial lagrangean coordinates in pore collapse EOS a0<r<b0
% dt_ro = pore collapse - pore collapse EOS time step (sec) (max allowable)
% n_r = pore collapse - number of 1D spatial grids in radial dir. (r-coord)
% a_o = pore collapse -initial pore radius (m)
% C_I = pore collapse - scaling factor to affect mix density (0<=mu_f<=1)
% mu_f = pore collapse -non-dimensional friction coefficient (0<=mu_f<=1)
% select_pore = choice of collapse model:
    % select_pore = 1 -> Holt-Carrol
    % select_pore = 2 -> P-alpha
% n = P-alpha model polynomial order (n),  quadratic ->   n=2
% Cm =  fraction of Homobaric Pressure assumed
     %  e.g. for pure Uniform Strain, Cm=0.  for Homobaric, Cm=1
% Pe = elastic pore strength (Pa)  (Pe = 250e6) Nominal
% Ps = pore collapse strength (Pa)   (Ps = 3e9) Nominal
% nx = total number of cells plus a few on the end
% dx = spatial step size (m)
% dt = time step (sec)
% jL = index of node within (impactor) material at the left boundary
% jI = index of node within (impactor) material at the interface boundary
% jR = index of node within (sample/mixture) material at the right boundary
% step = step in 2-step time scheme (first or second)
```

```
% k_time = time step counter value
%
%-------------------------------------------------------------------------
% OUTPUTS:
% sigmax = stress in x-direction (Pa)
% sigmay = stress in y-direction (Pa)
% sdev = (un-returned) deviatoric stress in x-direction  (Pa)
% sigmay_dev = (un-returned) deviatoric stress in y-direction (Pa)
% P = Pressure (Pa)
% q = heat flux (W/m^2)
% alphap = Distension ratio (alphao>=1)
% C = speed of sound in porous mixture material (m/s)
% pore_hist = x(nc,nx) = position and velocity of the inner surface (r=a)
% pore_hist_r(4,n_r,nx) = [T,gamma_p,rho_hat,sigma_e]
%-------------------------------------------------------------------------
%-------------------------------------------------------------------------
% a) Pressure EOS  -> P(n+1)
C_st=eos_st(1);  Gammag_st=eos_st(2);  S_st=eos_st(3);  Cv_st=eos_st(4);
for j=jL:jI
    if rho_new(j) == rho_sto
        P(j) = 0;
    else
        [P(j)] = MG_EOS(rho_sto,rho_new(j),T_new(j), ...
            C_st,Gammag_st,S_st,Cv_st);
    end
    C(j) = C_st;
end
%-------------------------------------------------------------------------
% Solve the EOS for mixture
%-------------------------------------------------------------------------
% Calculate Pressure
v_m = vo_m;  % this is modfied only when homobaric assumption is used
for j=jI+1:jR
```

```
    rho_bar = rho_new(j);  % current porous mixture density
    if T_new(j)<298  % correct when oscillations occur in the temperature
        T_in = 298;  % prevent contribution for this case
    else
        T_in = T_new(j); % current temperature
    end
    alpha_min=alphao;  % no-irreversibility for now (function of x)

    if rho_bar<rho_o*(1+trigger_dense) % no density change->no calc. req.
        P(j) = 0;  alphap(j) = alphao;  C(j) = Co;
    else

    if select_pore==1    %---------  Holt-Carrol ------------------
        if step==1  % when step==2, then P,C remain unchanged
        % Note: alphap,rho_bar = constant (incompressibility assumption)
        rhod_s = rhod_m*vo';  % initial solid mixture density  (constant)
        alphap(j) = rhod_s/rho_bar;  % new porosity (assume incompressible)
        Tol_alpha_eos = 2*Tol_rho+2*eps1;

        if alphap(j)< (1 + Tol_alpha_eos);
            alphap(j)=1;
%             rho_bar;
        end
        alphap_hist = 1 + (alphao-1)*pore_hist(1,j).^3/a_o^3;

        % Enforce irreversible pore collapse condition
        if alphap(j)<alphap_hist % *(1-2*Tol_rho-2*eps1)
            [P_new,C(j), pore_hist(:,j),pore_hist_r(:,:,j)] = ...
                rsm_eos2_pore(rho_bar,T_in, alphao,alphap(j), n,Cm,Pe,Ps, ...
                wflag, dt_ro,n_r, a_o,C_I,mu_f, plast_const, ...
                pore_hist(:,j),pore_hist_r(:,:,j), r0, rhod_m,vo,phi_m(j,:), ...
                eos,eos_type, Cv(j), dt, select_mix, Co,k_time);
            if C(j)==0
```

```
                fprintf(['C_flag = ', num2str(C(j)) ,' ,   \n'])
            end
            % ensure monotonic pressure increase
            % - this may arrise from numerical instability
            if P_new>P(j)
                P(j) = P_new;
            end
        else  % Pore can not expand  (P,C = unchanged)
        end
        end  % end if step==1

    else  %---------  P-alpha ------------------
        [P(j),alphap(j),C(j)]=rsm_eos2(rho_bar,T_in, ...
            alpha_min,alphao,alphap(j), n,Cm,Pe,Ps, Pmax, wflag,select_mix,...
            rhod_m,rhood(j),vo_m(j,:),phi_m(j,:),eos,eos_type,Cv(j));
    end
        if P(j)<0
%             warning('Pressure is negative, %10.2f, at node %i',P(j),j);
            P(j) = 0;
        end
    end  % end (rho_bar==rho_o) conditional

end  % main loop on j

% Equilibrate pressure at the interface
P_avg = 1/2*(P(jI)+P(jI+1));  % 1st order interpolation
[alpha(jI+1)] = p_alpha(P_avg,alphao,Pe,Ps,n);
P(jI) = P_avg;
P(jI+1) = P_avg;

%-------------------------------------------------------------------------
% b)Apply Radial Return to previous time step deviators t(n)
for j=jL:jI % within impactor material
```

```
    s_eq = 3/2*sdev(j);  % J2 yield stress for 1-D strain
    if abs( s_eq ) > yield_st % yield criteria
        sdev(j) =  yield_st*sdev(j)/s_eq;  % deviatoric stress in x-dir
    end
end
for j=jI+1:jR  % within sample material
    s_eq = 3/2*sdev(j);  % J2 yield stress for 1-D strain
    if abs( s_eq ) > yield_mix % yield criteria
        sdev(j) =  yield_mix*sdev(j)/s_eq;  % deviatoric stress in x-dir
    end
end
%-------------------------------------------------------------------------
% c) Stress deviators and heat flux at t(n+1)

% material 1
% left bc - free surface  (extrapolate values)
vx(jL-1) = vx(jL);
sdev(jL-1) = 0;
T(jL-1) = 300;
q(jL-1) = 0;
% right bc - ghost cell at interface
vx_int(1) = vx(jI+1);  % velocity of Pa = velocity of B
sdev_int(1) = sdev(jI+1);   % stress in x-dir is equal
T_int(1) = T(jI); % to prevent over heating
q_int(1) = q(jI);  %

% material 2
%left bc - ghost cell at interface
vx_int(2) = vx(jI);
sdev_int(2) = sdev(jI);
T_int(2) = T(jI+1);
% T_int(2) = (2*T(jI+1)+T(jI+2))/3;
q_int(2) = q(jI+1);
```

```
% right bc - free surface  (extrapolate values)
vx(jR+1) = vx(jR);
sdev(jR+1) = 0;
T(jR+1) = 300;
q(jR+1) = 0;

for j=jL-1:jR+1
    if j == jL-1
        slope_sdev(j) = (sdev(j+1)-sdev(j))/dx;
        slope_vx(j) = (vx(j+1)-vx(j))/dx;
        slope_T(j) = (T(j+1)-T(j))/dx;
        slope_q(j) = (q(j+1)-q(j))/dx;
    elseif j == jI
        slope_sdev(j) = minmod((sdev_int(1)-sdev(j))/dx,...
            (sdev(j)-sdev(j-1))/dx);
        slope_vx(j) = minmod( (vx_int(1)-vx(j))/dx , (vx(j)-vx(j-1))/dx );
        slope_T(j) = minmod( (T_int(1)-T(j))/dx , (T(j)-T(j-1))/dx );
        slope_q(j) = minmod( (q_int(1)-q(j))/dx , (q(j)-q(j-1))/dx );

        s_sdev_i(2) = (sdev(j+1)-sdev_int(2))/dx;
        s_vx_i(2) = (vx(j+1)-vx_int(2))/dx;
        s_T_i(2) = (T(j+1)-T_int(2))/dx;
        s_q_i(2) = (q(j+1)-q_int(2))/dx;

        [sdev_p_i(2),sdev_m_i(2),vx_p_i(2),vx_m_i(2), T_p_i(2),T_m_i(2),...
            q_p_i(2),q_m_i(2)] = muscl_reconstruction2( ...
            sdev_int(2),s_sdev_i(2),vx_int(2),s_vx_i(2),T_int(2),...
            s_T_i(2),q_int(2),s_q_i(2),  dx);

    elseif j == jI+1
        slope_sdev(j) = minmod((sdev(j+1)-sdev(j))/dx,...
            (sdev(j)-sdev_int(2))/dx);
        slope_vx(j) = minmod( (vx(j+1)-vx(j))/dx , (vx(j)-vx_int(2))/dx );
```

```
        slope_T(j) = minmod( (T(j+1)-T(j))/dx , (T(j)-T_int(2))/dx );
        slope_q(j) = minmod( (q(j+1)-q(j))/dx , (q(j)-q_int(2))/dx );

        s_sdev_i(1) = (sdev_int(1)-sdev(j-1))/dx;
        s_vx_i(1) = (vx_int(1)-vx(j-1))/dx;
        s_T_i(1) = (T_int(1)-T(j-1))/dx;
        s_q_i(1) = (q_int(1)-q(j-1))/dx;

        [sdev_p_i(1),sdev_m_i(1),vx_p_i(1),vx_m_i(1), T_p_i(1),T_m_i(1),...
            q_p_i(1),q_m_i(1)] = muscl_reconstruction2( ...
            sdev_int(1),s_sdev_i(1),vx_int(1),s_vx_i(1),T_int(1),...
            s_T_i(1),q_int(1),s_q_i(1),  dx);

    else % main nodes
        slope_sdev(j) = minmod((sdev(j+1)-sdev(j))/dx,...
            (sdev(j)-sdev(j-1))/dx);
        slope_vx(j) = minmod( (vx(j+1)-vx(j))/dx , (vx(j)-vx(j-1))/dx );
        slope_T(j) = minmod( (T(j+1)-T(j))/dx , (T(j)-T(j-1))/dx );
        slope_q(j) = minmod( (q(j+1)-q(j))/dx , (q(j)-q(j-1))/dx );

    end
    [sdev_p(j),sdev_m(j),vx_p(j),vx_m(j), T_p(j),T_m(j),...
        q_p(j),q_m(j)] = muscl_reconstruction2( ...
        sdev(j),slope_sdev(j),vx(j),slope_vx(j),T(j),...
        slope_T(j),q(j),slope_q(j),  dx);
end

% Deviatoric stress and heat flux in x-direction at t(n+1)
for j=jL:jR
    if j == jI
        [sdev(j), q(j)] = upwind_flux( ...
            sdev_p(j-1),sdev_p(j),sdev_m(j), sdev_m_i(1), q_p(j-1), ...
            q_p(j),q_m(j),q_m_i(1), vx_m(j),vx_m_i(1), T_p(j),T_p(j-1), ...
```

```
            sdev(j),q(j), vx(j),  mu(j),kq(j),dx,dt);
    elseif j == jI+1
        [sdev(j), q(j)] = upwind_flux( ...
            sdev_p_i(2),sdev_p(j),sdev_m(j), sdev_m(j+1), q_p_i(2),...
            q_p(j),q_m(j),q_m(j+1), vx_m(j),vx_m(j+1), T_p(j),T_p_i(2),...
            sdev(j),q(j), vx(j),  mu(j),kq(j),dx,dt);

    else  % general cells
        [sdev(j), q(j)] = upwind_flux( ...
            sdev_p(j-1),sdev_p(j),sdev_m(j), sdev_m(j+1), q_p(j-1),...
            q_p(j),q_m(j),q_m(j+1), vx_m(j),vx_m(j+1), T_p(j),T_p(j-1),...
            sdev(j),q(j), vx(j),  mu(j),kq(j),dx,dt);
    end
end
sigmay_dev = -1/2*sdev;  % deviatoric stress in y-direction t(n+1)

%-------------------------------------------------------------------------
% d) Re-calculate stresses/deviators to include effects of new Pressure
% stress(n+1) = -P(n+1) + sdev(n+1)

sigmax(jL:jR) = - P(jL:jR) + sdev(jL:jR);
sigmay(jL:jR) = - P(jL:jR) + sigmay_dev(jL:jR);
% recalculate deviators to match new stresses
sdev(jL:jR) = 2/3*(sigmax(jL:jR)-sigmay(jL:jR));
sigmay_dev(jL:jR) = -1/2*sdev(jL:jR);

function [P,alphap,C] = rsm_eos2(rho,T,alpha_min,alphao,alphap, ...
    n,Cm,Pe,Ps,Pmax,wflag,select_mix, ...
    rhod_m,rhood,vo_m,phi_m,eos,eos_type,Cv)
global eps1 % fraction of e,rho for numerical approx. of acoustic velocity
%
% Written by: Derek Reding
% Last modified on 08-14-07
```

```
% function that performs the calculation of wave speed for mixture material
% UNIFORM STRAIN ASSUMPION    AND   HOMOBARIC ASSUMPTION
% ( Note: see rsm_eos1 for more detials on RSM)
%
% INPUTS:
% Pmax = max pressure,(Pa) must be known a-priori for Us_obs calc and Homo
% select_mix = choice of EOS mixture rule
    % select_mix = 1  -> Bennett-Horie mix rule  (simple)
    % select_mix = 2  -> Rigorous mixture rules (use Cm)
%-------------------------------------------------------------------------
e = Cv*T;  % internal energy
d_e = eps1*e;
eU = e + d_e;  % add differential amount
eL = e - d_e;  % subtract differential amount
TU = eU/Cv;  TL = eL/Cv;  % convert to temperatures

d_rho = eps1*rho;  % mixture density
rhoU = rho + d_rho;
rhoL = rho - d_rho;

if select_mix==1  % -> Bennett-Horie mix rule  (simple)
    if alphap>1  % then continue with iterative Homobaric solution
        [PU,alphap] = p_alpha_benhor94(rhoU,T,Pmax, ...
            alphao,n,Pe,Ps, rhod_m,phi_m,eos, wflag);
        [PL,alphap] = p_alpha_benhor94(rhoL,T,Pmax, ...
            alphao,n,Pe,Ps, rhod_m,phi_m,eos, wflag);
        DP_rho = (PU - PL)/(2*d_rho);

        [PU,alphap] = p_alpha_benhor94(rho,TU,Pmax, ...
            alphao,n,Pe,Ps, rhod_m,phi_m,eos, wflag);
        [PL,alphap] = p_alpha_benhor94(rho,TL,Pmax, ...
            alphao,n,Pe,Ps, rhod_m,phi_m,eos, wflag);
        DP_e = (PU - PL)/(eU-eL);
```

```
        [P,alphap] = p_alpha_benhor94(rho,T,Pmax, ...
            alphao,n,Pe,Ps, rhod_m,phi_m,eos, wflag);

        C = sqrt(DP_rho + P/rho^2*DP_e);
%         C = sqrt(DP_rho);
    else  % alphap=1, dense mixture (note: alphap must be zero)
        [P,C] = ben_hor94(rho,T,phi_m, eos,rhod_m);
    end  % alpha if statement
else  %  -> Rigorous mixture rules (use Cm)
    [PU,alphap,v_m] = homo_and_us(rhoU,T,alpha_min,alphao, ...
        n,Cm,Pe,Ps,wflag, rhod_m,rhood,vo_m,phi_m,eos,eos_type);
    [PL,alphap,v_m] = homo_and_us(rhoL,T,alpha_min,alphao, ...
        n,Cm,Pe,Ps,wflag, rhod_m,rhood,vo_m,phi_m,eos,eos_type);
    DP_rho = (PU - PL)/(2*d_rho);

    [PU,alphap,v_m] = homo_and_us(rho,TU,alpha_min,alphao, ...
        n,Cm,Pe,Ps,wflag, rhod_m,rhood,vo_m,phi_m,eos,eos_type);
    [PL,alphap,v_m] = homo_and_us(rho,TL,alpha_min,alphao, ...
        n,Cm,Pe,Ps,wflag, rhod_m,rhood,vo_m,phi_m,eos,eos_type);
    DP_e = (PU - PL)/(eU-eL);

    [P,alphap,v_m] = homo_and_us(rho,T,alpha_min,alphao, ...
        n,Cm,Pe,Ps,wflag, rhod_m,rhood,vo_m,phi_m,eos,eos_type);

    C = sqrt(DP_rho + P/rho^2*DP_e);
end

function [P,alpha] = p_alpha_benhor94(rho_bar,T,Pmax, ...
    alphao,n,Pe,Ps, rhod_m,phi_m, eos, wflag)

global Tol_rho  % Homobaric EOS tollerance on density (nominal 0.0001)
global max_iter_ho % nominal -> max_iter = 15
```

```
% Written by: Derek Reding
% Last updated on: 08/07/07
%
% Homobaric Case - COMMENTS---------------------------------------
% INPUTS:
% rho_bar = input mixture density - remains constant (kg/m^3)
% T = temperature - remains constant (degrees K)
% P_us = pressure from uniform strain case for SAME rho_bar  (Pa)
% alphao = initial porosity at P=0
% n = polynomial for porosity pressure dependence (quadratic -> n=2)
% Pe = elastic limit (Pa)
% Ps = pore collapse strength (Pa)
% rhod_m = initial mixture constituent densities at P=0
% phi_m = constituent mass fractions - (vector)
% v = input volume fractions (sum(v)~=1 if alpha>1) - (vector)
% eos = equation of state constants (4) for each material using
    %   either Gruneisen or Murnhaghan EOS models
% eos(k,1) = Beta_To (bulk modulus)  (Pa)
    % Murnaghan
    % eos(k,1) = Beta_To (bulk modulus)  (Pa)
    % eos(k,2) = n  (slope of bulk modulus)
    % eos(k,3) = Gamma (Gruniesen constant - Murnhagan)
    % eos(k,4) = Cv (specific heat capacity)  (J/Kg*K)
    % Gruneisen
    % eos(k,1) = C  (acoustic velocity)  (m/s)
    % eos(k,2) = Gamma (Gruniesen constant)
    % eos(k,3) = S  (slope of Up-Us)
    % eos(k,4) = Cv (specific heat capacity) (J/Kg*K)
% eos_type = 1 for Murnaghan EOS, 2 for Gruneisen
% wflag = when wflag==1, suppress homogeneous warnings with error<1%
%
% OUTPUTS:
```

```
% P = output mixture averaged pressure - uniform strain  (Pa)
% alpha = output porosity
% v = output volume fractions (sum(v)~=1 if alpha>1)  - (vector)
%
%--------------------------------------------------------------------------
%--------------------------------------------------------------------------
% CONSTANTS:
To = 298;  % deg K
% Tol_rho = 0.0001; % tollerance, e.g. Tol_alpha = 0.01 = 1% error
% max_iter = 35;  % nominal -> max_iter = 15
%--------------------------------------------------------------------------
% fully dense initial mixture density  {kg/m^3}
rho_bardo = 1/sum(phi_m./rhod_m);

% Initialize parameter vectors
Beta_M = eos(:,1)';
n_M = eos(:,2)';
Gamma_M = eos(:,3)';
Cv_M = eos(:,4)';
nc = length(Beta_M);  % number of constituents

% Apply mixture rules for Ben-Horie '94 (ballotechnic) ----------
% we apply Beta_So rule to Beta_To (since assume Beta_So = Beta_To approx.)
% Mixture averaged isothermal bulk modulus (Pa)
Beta_bh = 1/rho_bar*1/sum(phi_m./rhod_m./Beta_M);
n_bh = rho_bardo*Beta_bh^2*sum( phi_m./rhod_m.*(ones(1,nc) + n_M)./Beta_M.^2 ) -1;
CvGamma = Beta_bh*sum( phi_m.*Cv_M.*Gamma_M./Beta_M);
Gamma_bh = 2;  % arbitraty value
Cv_bh = CvGamma/Gamma_bh;
% % Beta_bh = 8.5862e+010;
% % n_bh = 4.0134;
% % CvGamma = 1.6166e+003;
% % Gamma_bh = 2;
```

```
% % Cv_bh = 808.3058;
%-------------------------------------------------------------------------
% initialize bounds on Pressure
% P_L = 0;  % Note: using P_L = P_ho(k-1) may be faster, but not needed
% P_L = 0  does not allow will have problems if themal contribution to
% pressure is higher than P_bar, thus we have the following:
% Pt = Gamma*rho_o*Cv*(T-To);  % pressure from Thermal contribution (Pa)
% P_min = Cv_Gamma*;
P_U = Pmax*2;
P_L = 0;
%-------------------------------------------------------------------------
%-------------------------------------------------------------------------
% Begin iterations
%-------------------------------------------------------------------------
%-------------------------------------------------------------------------
n_iter = 0;  % number of iterations (initialize)
breaker = 0;  % break
while(breaker==0)  % iterate to find P that satisfies Homo-mix rule
    P_bar = 1/2*(P_U + P_L);
    alpha_star = p_alpha(P_bar,alphao,Pe,Ps,n);
    % Calculate mixture density
    rd = BM_EOSinv(rho_bardo,P_bar,T,Beta_bh, n_bh, Gamma_bh, Cv_bh);
    rho_star = rd/alpha_star; % porous mixture density

    error = max(  abs((rho_star - rho_bar)/rho_bar) ); % error in density


    if error<=Tol_rho
        breaker =1;  % density is within tolerance
    elseif rho_star > rho_bar  % density too high, P_bar too high
        P_U = P_bar;
    else
        P_L = P_bar;
```

```
    end
    n_iter = n_iter+1;
    if n_iter ==max_iter_ho
        %         fprintf('Error: Homobaric solution does not converge\n')
        if (wflag~=0) & (error*100>wflag)
fprintf(['p_alpha_benhor94 does not converge, error = ',...
    num2str(error*100) ,' %%,  ']) 
fprintf(['Pressure is = ',num2str(P_bar/(1e9)),' GPa \n'])
        end

        breaker =1;
    end
end  % end iteration on P - loop
P = P_bar;
alpha = alpha_star;

% Assure that complete pore closure can occur ------------------------------
error_alpha = alpha-1;
if error_alpha<Tol_rho  % 0.01
    alpha = 1;
end

function  [rho] = BM_EOSinv(rho_o,P,T,beta,n,Gamma,Cv)
% Birch Murnhagan EOS Inverse
To = 298;  % deg K
rho = rho_o*(n/(beta)*(P - Gamma*rho_o*Cv*(T-To) ) + 1)^(1/n);
% P  = beta/n*((rho/rho_o)^n - 1) + Gamma*rho_o*Cv*(T-To);

function [vo_m,rhood] = avg_mix_rxn_new(phi,rho,jI,jR)
% Last updated on 09/27/07  By Derek Reding
% Calculates updated original volume fractions
% (vo_m changes after reaction occurs, thus rhood changes too)
%-------------------------------------------------------------------------
```

```
% INPUTS:
% phi = mass fractions of constituents
% rho = constituent densities at P=0, T=300K
% nc = number of constituents that take place in the reaction
% nx =  total number of cells plus a few on the end
% jI = index of node within (impactor) material at the interface boundary
% jR = index of node within (sample/mixture) material at the right boundary
% selection =  if selection = 1, choose Ni+Al
             % if selection = 2, choose Al+Fe2O3
% OUTPUTS:
% vo_m = Volume Fractions of solid mixture (dense, d)
% rhood = initial dense mixture avg density (changes time,x) (kg/m^3)
%-------------------------------------------------------------------------
for j=jI+1:jR
    rhood(j) = 1/sum(phi(j,:)./rho);
    vo_m(j,:) = phi(j,:).*rhood(j)./rho;
end

function [sigma1,jI1] = ...
    interface_steel_nial_reimann(sigma, vx, x,nx,dx,dt, jI )
% Last modified on: 10-30-06
% Calculates new interfaces and and updates the location of
% new interface nodes
% At the interface, jI, velocity is simply averaged (note: this should be
% updated to extrapolate the velocity instead

%-------------------------------------------------------------------------
% UPDATE LOCATION OF SURFACES
vxI(1) = vx(jI(1));  %velocity at the LHS free interface
vxI(2) = 1/2*(vx(jI(2))+vx(jI(2)+1));  %velocity at the contact interface
vxI(3) = vx(jI(3));  %velocity at the RHS free interface
for i=1:3
    dsigma = vxI(i)*dt;
```

```
    sigma1(i) = sigma(i) + dsigma;
end

%-------------------------------------------------------------------------
% UPDATE LOCATION OF NODES AT THE SURFACES
% LHS
if vxI(1)>=0
    if x(jI(1)) - sigma1(1) < 0 % interface crossed cell center jI
        jI1(1) = jI(1)+1;
    else
        jI1(1) = jI(1);
    end
else
    if x(jI(1)) - sigma1(1) > dx % interface crossed cell center jI-1
        jI1(1) = jI(1)-1;
    else
        jI1(1) = jI(1);
    end
end

% contact and RHS
for i=2:3
    if vxI(i)>=0
        if sigma1(i) - x(jI(i))  > dx % interface crossed cell center jI+1
            jI1(i) = jI(i)+1;
        else
            jI1(i) = jI(i);
        end
    else
        if sigma1(i) - x(jI(i))  < 0 % interface crossed cell center jI
            jI1(i) = jI(i)-1;
        else
            jI1(i) = jI(i);
```

```
        end
    end
end


function [phi_out,DPHI] = ...
    phi_cutoff(rho,phi_m,THETA,phi_max,phi_ep, M_m,G,dt_rxn,nc)
% function [phi_out,dphi_out,DTHETA_out,DPHI] = ...
%     phi_cutoff(rho,phi_m,THETA,phi_max,phi_ep, M_m,G,dt_rxn,nc)
%
% Written by: Derek Reding
% Last edited on: 09/11/07
% Note: - can only be used for binary reactions
%       - only forward reaction considered
%       - used by "reaction_bin_tester.m"
%-------------------------------------------------------------------------
% Inputs:
% rho = porous mixture density (kg/m^3)
% phi_m = mass fractions (before this reaction step)
% PHI_mass = rate of formation of mass fractions (NON-intert constituents)
% THETA = reaction rate
% phi_max = fraction of reaction completion (0<=phi_max<=1)
% phi_ep = mass fraction of epoxy or other inert material
% M_m = molar mass
% G = stoichiometric coefficient
% dt_rxn = time step for the reaction step (sec) (note: dt_rxn<=dt)
% ns = total number of species or constituents in the mixture
% nc = number of NON-intert constituents
% nr = number of reactant constituents = 2 for this function
%-------------------------------------------------------------------------
% Outputs:
% phi_new = new mass fractions for only
% dphi_out = updated change in mass fractions
% DTHETA_out = Actual change in concentration
```

```
%-------------------------------------------------------------------------
PHI_mass = THETA*M_m.*G/rho; % rate mass fraction source term [1,nc]
dphi = dt_rxn*PHI_mass;  % change in mass fractions
% sum_dphi = sum(dphi)
% trial mass fracs of reactants and products (after reaction)
phit = phi_m(1:nc) + dphi;   % [1,nc]
% sum_phit = sum(phit)
DTHETA_out = dt_rxn*THETA;  % initialize change in concentration, Dtheta

if phit(1)<=0  % if reactant 1 runs out
    %     disp('reactant 1 ran out');
    DTHETA = -1/G(1)*(-phit(1))/M_m(1)*rho;   % Correction to make phi(1)=0
    DTHETA_out = DTHETA_out - DTHETA;   % Actual change, Dtheta
    for j=1:nc
        phit(j) = phit(j) - DTHETA*M_m(j)*G(j)/rho;
    end
    if phit(1)<0; phit(1)=0; end  % prevent roundoff errors
end

if phit(2)<=0  % if reactant 2 runs out
    %     disp('reactant 2 ran out');
    DTHETA = -1/G(2)*(-phit(2))/M_m(2)*rho;  % Correction to make phi(1)=0
    DTHETA_out = DTHETA_out - DTHETA;  % Actual change, Dtheta

    for j=1:nc
        phit(j) = phit(j) - DTHETA*M_m(j)*G(j)/rho;
    end
    if phit(1)<0; phit(1)=0; end  % prevent roundoff errors
    if phit(2)<0; phit(2)=0; end  % prevent roundoff errors
end

% if maximum limit for product formation occurs
phi_prod = sum(phit(3:nc));  % sum up product mass fractions
```

```
phi_max2 = phi_max-phi_ep;
if phi_prod>phi_max2
%     disp('maximum reaction products have been formed');
    phi_ex = phi_prod - phi_max2; % excess mass fraction for product(s)
    % Correction -> phi(products)=0
    DTHETA = -phi_ex/(-G(3:nc)*M_m(3:nc)')*rho;
    DTHETA_out = DTHETA_out - DTHETA;  % Actual change, Dtheta
    for j=1:nc
        phit(j) = phit(j) - DTHETA*M_m(j)*G(j)/rho;
    end
end

%-------------------------------------------------------------------------
phi_out = phit/(sum(phit)+phi_ep) ;  % Enforce consistency
phi_out(nc+1) = phi_ep;
% phi_junk = phi_out
% sum_phi_junk = sum(phi_junk)

dphi_out = phi_out(1:nc) - phi_m(1:nc);
DPHI = sum(dphi_out(1:2));  % note: DPHI<=0
```

Appendix H

2-D SIMULATION CODE

```
% Program to calculate the axisymmetric (about the x-axis) problem from
% Wilkins "Computer Simulation of Dynamic Phenomena", 1999.

%%%%%%%%%%%%%%%%%%%%%%%%%%%%%%%%%%%%%%%%%%%%%%%%%%%%%%%%%%%%%%%%%%%%%%%%
%  COMPLETE VERSION
% - progress for the hour glass viscosity
% - assume acceleration is only in x-direction
%%%%%%%%%%%%%%%%%%%%%%%%%%%%%%%%%%%%%%%%%%%%%%%%%%%%%%%%%%%%%%%%%%%%%%%%

% Simulation of a rod impacting a rigid wall
close all;
clear all;
clc;
warning off MATLAB:divideByZero

% SPECIFY INITIAL CONDITIONS
t_run = 1e-4;     % specify the run time for the simulation (s)
vel = 300;    % velocity in x-direction at t=0  (m/s)
Vo = 1;    % Vo = rho_o/rho_i
S_init = 0;    % initial stress throughout rod is zero
omega_init = 0;   % initial angular velocity about the x-axis
thetao = 0;    % initial angle of the projectile about the x-axis
cfl = .25;    % cfl condition

% GEOMETRY OF CYLINDRICAL OBJECT
% Lo = .5;   % Lo = 0.1;     % length (m) along x-direction
% R = .1;   % R  = 0.01;    % radius (m) along y-direction
```

```
Lo =.05;   %  length (m) along x-direction
R = .01;   %  radius (m) along y-direction
nx = 50;   % nx = 103;     % number of nodes in the x-direction
ny = 8;   % ny = 13;    % number of nodes in the y-direction
% nx = 20;
% ny = 10;
dx = Lo/(nx-1);
dy = R/(ny-1);

% Material properties
rho_al = 2700;  % density of aluminum (kg/m^3)
E_al = 70e9;   % modulus of elasticity (Pa)
G_al = E_al/2.6;     % shear modulus (Pa)
K_al = 70e9/1.2;  % bulk modulus (Pa)
Yo_al = 290e6;
% Flow stress for 6070 Aluminum (Pa)->69e6 Pa  (2.9e-3 Mbars = 290e6 Pa)
Co = 2;    % quadratic q constant  (Co=2 for 1D strain)  p94
CL = 1;    % linear q constant  (CL=1 for 1D strain)
% Mie-Gruneisen EOS --------------------
C_al = 5380;  %  Sound speed (m/s)
S_al = 1.34;  %  Slope of Us-Up curve
Gammag_al = 2.0;  %  Gamma
Cv_al = 931;
To = 298;
Eo = Cv_al*To;

k = 1;  % initialize time step for t = to
for j=1:ny
    for i=1:nx
        % INITIAL COORDINATES
        x(i,j,k) = (i-1)*dx;
        y(i,j,k) = (j-1)*dy;
        Theta(i,j,k) = thetao;
```

```
        % INITIAL VELOCITY
        vxh(i,j,k) = vel;    % initial velocity in x-direction  at k=1/2
        if i==nx
            vxh(i,j,k) = 0; % fixed wall
        end
        vyh(i,j,k) = 0;      % initial velocity in y-direction  at k=1/2
        Omegah(i,j,k) = 0;    % initial angular velocity about x-axis at k=1/2
        omegah(i,j,k) = omega_init;   % initial velocity about x-axis at k=1/2
    end
end

% MASS ZONING for k==1 (pg 86)
xin(1:nx,1:ny) = x(1:nx,1:ny,k);   yin(1:nx,1:ny) = y(1:nx,1:ny,k);
[Aout,v0out,Mout,Vout] = masso_fun(xin,yin,nx,ny,Vo,rho_al);
A(1:nx-1,1:ny-1,k) = Aout;   v(1:nx-1,1:ny-1,k) = v0out;
  M(1:nx-1,1:ny-1) = Mout;   V(1:nx-1,1:ny-1,k) = Vout;
rho(1:nx-1,1:ny-1,k) = rho_al;   % initialize density as the reference density

for j=1:ny-1
    for i=1:nx-1
        % INITIAL STRESS
        Sxx(i,j,k) = 0;   Syy(i,j,k) = 0;   Stt(i,j,k) = 0;
        % stress is zero throughout the rod at k = 1
        Sxy(i,j,k) = 0;   Syt(i,j,k) = 0;   Stx(i,j,k) = 0;
        sxx(i,j,k) = 0;   syy(i,j,k) = 0;   stt(i,j,k) = 0;
        % stress deviators at k = 1
        % INITIAL STRAIN
        exxh(i,j,k) = 0;   eyyh(i,j,k) = 0;   etth(i,j,k) = 0;
        % Initial strains at k = 1/2 are zero
        exyh(i,j,k) = 0;   eyth(i,j,k) = 0;   etxh(i,j,k) = 0;
        edxxh(i,j,k) = 0;  edyyh(i,j,k) = 0;  edtth(i,j,k) = 0;
        % strain rates at k = 1/2
        edxyh(i,j,k) = 0;  edyth(i,j,k) = 0;  edxth(i,j,k) = 0;
```

```
        ep(i,j,k) = 0;   % plastic strain at k = 1/2
        % INITIAL ENERGY/PRESSURE         E(t=0)/P(t=0)     for  k=1
        E(i,j,k) = Eo;
        P(i,j,k) = 0;
        % INITIAL ARTIFICIAL VISCOSITY FOR CALCULATING SHOCKS
        qh(i,j,k) = 0;    % dsth = 0 initially, therefore there is
        no viscous damping at k=1/2
        % INITIAL Strain in the direction of the acceleration
        dsth(i,j,k) = 0;   % initially there is no strain rate at k=1/2
    end
end

% Calculate "initial time step" (initial guess)  k=1/2, k=1, k=3/2
xin(1:nx,1:ny) = x(1:nx,1:ny,k);   yin(1:nx,1:ny) = y(1:nx,1:ny,k);
Ain(1:nx-1,1:ny-1) = A(1:nx-1,1:ny-1,k);   dsthin(1:nx-1,1:ny-1) =
dsth(1:nx-1,1:ny-1,k);
[dthout] = timeo_fun(xin,yin,Ain,rho_al,K_al,Co,CL,dsthin,nx,ny,cfl);
dth(k) = dthout;      % initial time step k=1/2
dth(k+1) = dth(k);    % initially guess the time step for k=3/2
dt(k) = 1/2*(dth(k)+dth(k+1));   % initially this is the first
guess for dt for k=1
t(k) = 0;  % initialize run time
%-------------------------------------------------------------------------
% Main program (for t>0)
nt = 10;
for k=1:nt
    % while(1)
    % EQUATIONS OF MOTION   (get x,y for k+1)
    xin(1:nx,1:ny) = x(1:nx,1:ny,k);   yin(1:nx,1:ny) = y(1:nx,1:ny,k);
    Thetain = Theta(1:nx,1:ny,k);
    vxhin(1:nx,1:ny) = vxh(1:nx,1:ny,k);    vyhin(1:nx,1:ny) = ...
    vyh(1:nx,1:ny,k);
    omegahin(1:nx,1:ny) = omegah(1:nx,1:ny,k);  Omegahin(1:nx,1:ny) = ...
```

```
Omegah(1:nx,1:ny,k);
Sxxin(1:nx-1,1:ny-1) = Sxx(1:nx-1,1:ny-1,k);  Syyin(1:nx-1,1:ny-1) =
Syy(1:nx-1,1:ny-1,k);   Sttin(1:nx-1,1:ny-1) = Stt(1:nx-1,1:ny-1,k);
Sxyin(1:nx-1,1:ny-1) = Sxy(1:nx-1,1:ny-1,k);  Stxin(1:nx-1,1:ny-1) =
Stx(1:nx-1,1:ny-1,k);   Sytin(1:nx-1,1:ny-1) = Syt(1:nx-1,1:ny-1,k);
Ain(1:nx-1,1:ny-1) = A(1:nx-1,1:ny-1,k);   Vin(1:nx-1,1:ny-1) =
V(1:nx-1,1:ny-1,k);   rhoin(1:nx-1,1:ny-1) = rho(1:nx-1,1:ny-1,k);
dthin = dth(k+1);    dtin = dt(k);
[xout,yout,Thetaout,xhout,yhout,vxhout,vyhout,
omegahout,Omegahout] =velocity_fun10(xin,yin,Thetain,vxhin,...
vyhin,omegahin, Omegahin,Sxxin,Syyin,...
    Sttin,Sxyin,Stxin,Sytin,Ain,M,Vin,dtin,dthin,nx,ny,Vo,rhoin,k);


x(1:nx,1:ny,k+1) = xout;   y(1:nx,1:ny,k+1) = yout;
Theta(1:nx,1:ny,k+1) = Thetaout;
xh(1:nx,1:ny,k+1) = xhout;   yh(1:nx,1:ny,k+1) = yhout;
vxh(1:nx,1:ny,k+1) = vxhout;   vyh(1:nx,1:ny,k+1) = vyhout;
omegah(1:nx,1:ny,k+1) = omegahout;
Omegah(1:nx,1:ny,k+1) = Omegahout;
%     vyhout_junk = vyh(nx,1,k+1)
% %     vxhout_junk = vxh(2,1,k+1)
% %     x_junk = x(2,1,k+1)
%     y_junk = y(2,1,k+1)
if  k==5
    i=nx-1;  j=ny;
    vy_junk1 = vyh(i+1,j,k)
    vy_junk2 = vyh(i+1,j,k+1)
end

% MASS ZONING   (get A,V for k+1)
xin(1:nx,1:ny) = x(1:nx,1:ny,k+1);   yin(1:nx,1:ny) = ...
y(1:nx,1:ny,k+1);   Min=M;   % conservation of mass M=const
[Aout,vout,Vout,rho_out] = mass_fun(xin,yin,nx,ny,Vo,rho_al,Min);
```

```
A(1:nx-1,1:ny-1,k+1) = Aout;   v(1:nx-1,1:ny-1,k+1) = vout;
 V(1:nx-1,1:ny-1,k+1) = Vout;  rho(1:nx-1,1:ny-1,k+1) = rho_out;

for j=1:ny-1
    for i=1:nx-1
        % k = 1
        Ah(i,j,k+1) = 1/2*(A(i,j,k)+A(i,j,k+1));
        % area at k=3/2
        Vh(i,j,k+1) = 1/2*(V(i,j,k)+V(i,j,k+1));
        % volume at k=3/2
        DVh(i,j,k+1) = 1/2*(V(i,j,k+1)-V(i,j,k));
        % change in volume at k=3/2

        % CALCULATION OF INCREMENTAL STRAIN  (pg 89-90)
        calculate the strain at the k = 3/2 time step
        edxxh(i,j,k+1) = 1/(2*Ah(i,j,k+1))*((vxh(i+1,j,k+1)-
        vxh(i,j+1,k+1))*
        (yh(i+1,j+1,k+1)-yh(i,j,k+1)) ...
            - (yh(i+1,j,k+1)-yh(i,j+1,k+1))*(vxh(i+1,j+1,k+1)
            -vxh(i,j,k+1)) );
        edyyh(i,j,k+1) = - 1/(2*Ah(i,j,k+1))*( (vyh(i+1,j,k+1)-
        vyh(i,j+1,k+1))*(xh(i+1,j+1,k+1)-xh(i,j,k+1)) ...
            - (xh(i+1,j,k+1)-xh(i,j+1,k+1))*(vyh(i+1,j+1,k+1)-
            vyh(i,j,k+1)) );
        edtth(i,j,k+1) = DVh(i,j,k+1)/(Vh(i,j,k+1)*dth(k+1))  -
        (edxxh(i,j,k+1)+edyyh(i,j,k+1));

        edxyh(i,j,k+1) = 1/(2*Ah(i,j,k+1))*( (vyh(i+1,j,k+1)-
        vyh(i,j+1,k+1))
        *(yh(i+1,j+1,k+1)-yh(i,j,k+1)) ...
            - (yh(i+1,j,k+1)-yh(i,j+1,k+1))*(vyh(i+1,j+1,k+1)-
            vyh(i,j,k+1)) + ((vxh(i+1,j,k+1)-vxh(i,j+1,k+1))*
            (xh(i+1,j+1,k+1)-xh(i,j,k+1)) ...
```

```
    - (xh(i+1,j,k+1)-xh(i,j+1,k+1))*(vxh(i+1,j+1,k+1)
    - vxh(i,j,k+1)))  );

edyth(i,j,k+1) = - 1/(2*Ah(i,j,k+1))*(
(yh(i+1,j,k+1)*omegah(i+1,j,k+1)-yh(i,j+1,k+1)*
omegah(i,j+1,k+1))*(xh(i+1,j+1,k+1)-xh(i,j,k+1)) ...
    - (xh(i+1,j,k+1)-xh(i,j+1,k+1))*(omegah(i+1,j+1,k+1)*
    yh(i+1,j+1,k+1)-omegah(i,j,k+1)*yh(i,j,k+1))  ) ...
    - 1/4*(omegah(i,j,k+1)+omegah(i+1,j,k+1)+
    omegah(i+1,j+1,k+1)+omegah(i,j+1,k+1));
edtxh(i,j,k+1) = 1/(2*Ah(i,j,k+1))*(   (yh(i+1,j,k+1)*
omegah(i+1,j,k+1)-yh(i,j+1,k+1)*
omegah(i,j+1,k+1))*(yh(i+1,j+1,k+1)-yh(i,j,k+1)) ...
    - (yh(i+1,j,k+1)-yh(i,j+1,k+1))*(omegah(i+1,j+1,k+1)*
    yh(i+1,j+1,k+1)-omegah(i,j,k+1)*yh(i,j,k+1))  );
Dexxh(i,j,k+1) = edxxh(i,j,k+1)*dth(k+1);
% incremental strains at k+1/2
Deyyh(i,j,k+1) = edyyh(i,j,k+1)*dth(k+1);
Detth(i,j,k+1) = edtth(i,j,k+1)*dth(k+1);
Dexyh(i,j,k+1) = edxyh(i,j,k+1)*dth(k+1);
Deyth(i,j,k+1) = edyth(i,j,k+1)*dth(k+1);
Detxh(i,j,k+1) = edtxh(i,j,k+1)*dth(k+1);

% ARTIFICIAL VISCOSITY FOR CALCULATING SHOCKS
% Calculate the rate of strain in the direction of
the acceleration, dsth
vx_aveh_l = 1/4*(vxh(i,j,k) +  vxh(i+1,j,k) + vxh(i+1,j+1,k)
+ vxh(i,j+1,k));     % for k-1/2
vy_aveh_l = 1/4*(vyh(i,j,k) +  vyh(i+1,j,k) + vyh(i+1,j+1,k)
+ vyh(i,j+1,k));     % for k-1/2
vx_aveh_u = 1/4*(vxh(i,j,k+1) +  vxh(i+1,j,k+1) +
 vxh(i+1,j+1,k+1) + vxh(i,j+1,k+1));     % for k+1/2
vy_aveh_u = 1/4*(vyh(i,j,k+1) +  vyh(i+1,j,k+1) +
```

```
            vyh(i+1,j+1,k+1) + vyh(i,j+1,k+1));     % for k+1/2
            Ax = (vx_aveh_u - vx_aveh_l);   % for k
            Ay = (vy_aveh_u - vy_aveh_l);   % for k
            if (Ax^2+Ay^2)>0
                cosa = Ax/sqrt(Ax^2+Ay^2);
                sina = Ay/sqrt(Ax^2+Ay^2);
            else
                cosa = 1;
                sina = 0;
            end
            % calculate d/dx(vx) (vx_x) with x, y at k=3/2  x(1), y(1)
            vx_x(i,j,k) = edxxh(i,j,k+1);
            vy_y(i,j,k) = edyyh(i,j,k+1);
            vxy_xy(i,j,k) = edxyh(i,j,k+1);
            dsth(i,j,k+1) = vx_x(i,j,k)*cosa^2;  % k=3/2
            % Determine the characteristic length (assume that the
            shock moves along the x-axis for now)
            L_char(i,j,k+1) = 1/2*(x(i+1,j,k+1)+x(i+1,j+1,k+1)) -
            1/2*(x(i,j,k+1)+x(i,j+1,k+1));

            % real characteristic length ???
            if ((nt == 2) && (i==nx-2))
%                 fprintf('L_char = %f',L_char(i,j,k+1))
            end



            % Determine the local sound speed
            a(i,j,k) = sqrt(abs(P(i,j,k))/rho_al);

            if dsth(i,j,k+1) >= 0
                qh(i,j,k+1) = 0;    % k=3/2
            else
                qh(i,j,k+1) = Co^2*rho_al*L_char(i,j,k+1)^2*
```

```
    dsth(i,j,k+1)^2 + CL*rho_al*a(i,j,k)*
    abs(dsth(i,j,k+1));   % k=3/2
end

%  CALCULATION OF STRESSES (90-91)     (for k = 2)
% lower case s refers to deviators
sin_omegah(i,j,k+1) = 1/2*(   1/(2*Ah(i,j,k+1))*(
 (vyh(i+1,j,k+1)-vyh(i,j+1,k+1))*(yh(i+1,j+1,k+1)-
yh(i,j,k+1)) ...
    - (yh(i+1,j,k+1)-yh(i,j+1,k+1))*(vyh(i+1,j+1,k+1)
    -vyh(i,j,k+1)) ...
    - ((vxh(i+1,j,k+1)-vxh(i,j+1,k+1))*(xh(i+1,j+1,k+1)
    -xh(i,j,k+1)) ...
    - (xh(i+1,j,k+1)-xh(i,j+1,k+1))*(vxh(i+1,j+1,k+1)-
    vxh(i,j,k+1)))  )    )*dth(k+1);     %  k=1
omega_h(i,j,k+1) = asin(sin_omegah(i,j,k+1));
cos2omegah(i,j,k+1) = cos(2*omega_h(i,j,k+1));

dxx(i,j,k) = (sxx(i,j,k)-syy(i,j,k))/2*
(cos2omegah(i,j,k+1)-1) - Sxy(i,j,k)*2*sin_omegah(i,j,k+1);
dyy(i,j,k) = -dxx(i,j,k);
dxy(i,j,k) = Sxy(i,j,k)*(cos2omegah(i,j,k+1)-1) +
(sxx(i,j,k)-syy(i,j,k))/2*(2*sin_omegah(i,j,k+1));

% deviatoric stresses
sxx(i,j,k+1) = sxx(i,j,k) + 2*G_al*(Dexxh(i,j,k+1)-
1/3*DVh(i,j,k+1)/Vh(i,j,k+1)) + dxx(i,j,k); % + qxx(i,j,k);
syy(i,j,k+1) = syy(i,j,k) + 2*G_al*(Deyyh(i,j,k+1)-
1/3*DVh(i,j,k+1)/Vh(i,j,k+1)) + dyy(i,j,k); % + qyy(i,j,k);
stt(i,j,k+1) = stt(i,j,k) + 2*G_al*(Detth(i,j,k+1)-
1/3*DVh(i,j,k+1)/Vh(i,j,k+1));
Sxy(i,j,k+1) = Sxy(i,j,k) + G_al*Dexyh(i,j,k+1) +
dxy(i,j,k); % + qxy(i,j,k);    % Shear Stresses
```

```
Syt(i,j,k+1) = Syt(i,j,k) + G_al*Deyth(i,j,k+1);
Stx(i,j,k+1) = Stx(i,j,k) + G_al*Detxh(i,j,k+1);

% MATERIAL INTERNAL ENERGY (pg 96)  (needs dt(k=3/2))
sxxh(i,j,k+1) = 1/2*(sxx(i,j,k) + sxx(i,j,k+1));
% average stresses for k=3/2
syyh(i,j,k+1) = 1/2*(syy(i,j,k) + syy(i,j,k+1));
stth(i,j,k+1) = 1/2*(stt(i,j,k) + stt(i,j,k+1));
Sxyh(i,j,k+1) = 1/2*(Sxy(i,j,k) + Sxy(i,j,k+1));
Syth(i,j,k+1) = 1/2*(Syt(i,j,k) + Syt(i,j,k+1));
Stxh(i,j,k+1) = 1/2*(Stx(i,j,k) + Stx(i,j,k+1));
DZh(i,j,k+1) = Vh(i,j,k)*(sxxh(i,j,k+1)*edxxh(i,j,k+1)
+ syyh(i,j,k+1)*edyyh(i,j,k+1) ...
    + stt(i,j,k+1)*edtth(i,j,k+1) + Sxy(i,j,k+1)*
    edxyh(i,j,k+1) + Syt(i,j,k+1)*edyth(i,j,k+1) + ...
    Stx(i,j,k+1)*edtxh(i,j,k+1)  )*dth(k+1);

% EOS from pages 96 and pg 63
if V(i,j,k+1)>1; V(i,j,k+1)=1;  end
rho_in = rho_al/V(i,j,k+1);  rho_o = rho_al;
Cv=Cv_al;  T = E(i,j,k)/Cv;   % Approximate, should
include E(i,j,k+1) in P(E,V)
Gamma = Gammag_al;    S1 = S_al;   C = C_al;
P(i,j,k+1) = MG_EOS(rho_o,rho_in,T,C,Gamma,S1,Cv);
% pressure (Pa)
P(i,j,k+1) = P(i,j,k+1)/100;  % convert to units (mbar)
q_bar(i,j,k) = 1/2*(qh(i,j,k)+qh(i,j,k+1));
%  averaged artificial viscosity
E(i,j,k+1) = E(i,j,k) - ( P(i,j,k) + q_bar(i,j,k) )
*DVh(i,j,k+1) + DZh(i,j,k+1) ...
    - 1/2*(P(i,j,k+1) - P(i,j,k))*DVh(i,j,k+1);

% CALCULATION OF TOTAL STRESSES (90-91)     (for k = 2)
```

```
        Sxx(i,j,k+1) = sxx(i,j,k+1) - (P(i,j,k+1) + qh(i,j,k+1));
        Syy(i,j,k+1) = syy(i,j,k+1) - (P(i,j,k+1) + qh(i,j,k+1));
        Stt(i,j,k+1) = stt(i,j,k+1) - (P(i,j,k+1) + qh(i,j,k+1));

        % VON MISES YIELD CONDITION (pg 92)
        J(i,j,k+1) = (sxx(i,j,k+1)^2+syy(i,j,k+1)^2+
        stt(i,j,k+1)^2)/2 ...
            + Sxy(i,j,k+1)^2 + Syt(i,j,k+1)^2 + Stx(i,j,k+1)^2;
        m(i,j,k+1) = sqrt(2/3)*Yo_al/sqrt(2*J(i,j,k+1));
        if m(i,j,k+1)<1
            sxx(i,j,k+1) = sxx(i,j,k+1)*m(i,j,k+1);
            syy(i,j,k+1) = syy(i,j,k+1)*m(i,j,k+1);
            stt(i,j,k+1) = stt(i,j,k+1)*m(i,j,k+1);
            Sxy(i,j,k+1) = Sxy(i,j,k+1)*m(i,j,k+1);
            Syt(i,j,k+1) = Syt(i,j,k+1)*m(i,j,k+1);
            Stx(i,j,k+1) = Stx(i,j,k+1)*m(i,j,k+1);
        end

        % EQUIVALENT PLASTIC STRAIN (pg 92)
        for strain at (k=3/2)
        % Simply used for observation - both plastic and elastic
        strain are still included in the incremental strains above
        Dep(i,j,k+1) = (1/m(i,j,k+1)-1)*Yo_al/(3*G_al);
        if Dep(i,j,k+1) >= 0
            ep(i,j,k+1) = ep(i,j,k) + Dep(i,j,k+1);
        else
            ep(i,j,k+1) = 0;
        end
    end  % loop on nx
end   % loop on ny

% Calculate dt(k+3/2)
xin(1:nx,1:ny) = x(1:nx,1:ny,k+1);
```

```
     yin(1:nx,1:ny) = y(1:nx,1:ny,k+1);
    Ain(1:nx-1,1:ny-1) = A(1:nx-1,1:ny-1,k+1);
    rhoin(1:nx-1,1:ny-1) = rho(1:nx-1,1:ny-1,k+1);
    dsthin(1:nx-1,1:ny-1) = dsth(1:nx-1,1:ny-1,k+1);
    dthin = dth(k+1);   Pin(1:nx-1,1:ny-1) = P(1:nx-1,1:ny-1,k+1);

    [dthout] = time_fun10(xin,yin,Ain,rhoin,K_al,Co,CL,dsthin,
    nx,ny,cfl,dthin,Pin);
    dth(k+2) = dthout;   % dt(k+3/2)
    dt(k+1) = 1/2*(dth(k+1)+dth(k+2));   % dt(k+1)
    t(k+1) = t(k) + dt(k+1);  % update the total run time t(k+1)
end

% function to do the mass zoning
function [A,v,V,rho] = mass_fun(x,y,nx,ny,Vo,rho_al,M)
% MASS ZONING (pg 86)
% Calculation of the initial volume/mass of the zones  (k)
for j=1:ny-1
    for i=1:nx-1
        y1 = y(i,j);      y3 = y(i+1,j+1);
        y2 = y(i+1,j);    y4 = y(i,j+1);
        x1 = x(i,j);      x3 = x(i+1,j+1);
        x2 = x(i+1,j);    x4 = x(i,j+1);
        ybar_a(i,j) = 1/3*(y2+y3+y4);
        ybar_b(i,j) = 1/3*(y1+y2+y4);
        A_a(i,j) = 1/2*( x2*(y3-y4) + x3*(y4-y2) + x2*(y2-y3)  );
        A_b(i,j) = 1/2*( x2*(y4-y1) + x4*(y1-y2) + x1*(y2-y4)  );
        A(i,j) = A_a(i,j) + A_b(i,j);   % ??????  not sure about this
        v(i,j) = ybar_a(i,j)*A_a(i,j) + ybar_b(i,j)*A_b(i,j);
        % calculation of the volume of the zones for k
        V(i,j) = (rho_al/M(i,j))*v(i,j); % conservation of mass (pg 88)
        rho(i,j) = rho_al/V(i,j);     % calculation of density
    end
```

```
end

% function to calculate the velocity of the nodes at k+1/2 given the
% stresses at k
function [xout,yout,Thetaout,xhout,yhout,vxhout,vyhout,omegahout,
Omegahout] = ...
    velocity_fun10(x,y,Theta,vxh,vyh,omegah,Omegah,Sxx,Syy,Stt,
    Sxy,Stx,Syt, ...
    A,M,V,dt,dth,nx,ny,Vo,rho,k)

% EQUATIONS OF MOTION (pg 87-88)
for j=1:ny
    for i=1:nx
        % node values
        if j>1
            y1 = y(i,j-1);   x1 = x(i,j-1);
        end
        if i<nx
            y2 = y(i+1,j);   x2 = x(i+1,j);
        end
        if j<ny
            y3 = y(i,j+1);   x3 = x(i,j+1);
        end
        if i>1
            y4 = y(i-1,j);   x4 = x(i-1,j);
        end

        % zone values
        if ((i<nx) && (j<ny))
            A1 = A(i,j);   V1 = V(i,j); M1 = M(i,j); rho1 = rho(i,j);
            Sxx1 = Sxx(i,j);   Syy1 = Syy(i,j);   Stt1 = Stt(i,j);
              Sxy1 = Sxy(i,j);   Stx1 = Stx(i,j);   Syt1 = Syt(i,j);
        end
```

```
if ((i>1)  && (j<ny))
    A2 = A(i-1,j);   V2 = V(i-1,j);   M2 = M(i-1,j);
    rho2 = rho(i-1,j);
    Sxx2 = Sxx(i-1,j);   Syy2 = Syy(i-1,j);
    Stt2 = Stt(i-1,j);   Sxy2 = Sxy(i-1,j);
    Stx2 = Stx(i-1,j);   Syt2 = Syt(i-1,j);
end
if ((i>1) && (j>1))
    A3 = A(i-1,j-1);   V3 = V(i-1,j-1);   M3 = M(i-1,j-1);
     rho3 = rho(i-1,j-1);   Sxx3 = Sxx(i-1,j-1);
    Syy3 = Syy(i-1,j-1);   Stt3 = Stt(i-1,j-1);
    Sxy3 = Sxy(i-1,j-1);   Stx3 = Stx(i-1,j-1);
     Syt3 = Syt(i-1,j-1);
end
if ((i<nx) && (j>1))
    A4 = A(i,j-1);   V4 = V(i,j-1);   M4 = M(i,j-1);
      rho4 = rho(i,j-1); Sxx4 = Sxx(i,j-1); Syy4 = Syy(i,j-1);
    Stt4 = Stt(i,j-1);   Sxy4 = Sxy(i,j-1);
    Stx4 = Stx(i,j-1);   Syt4 = Syt(i,j-1);
end



% CALCULATE THE VELOCITY  (for k+1/2)
% Define velocities at the boundary zones
if j==1   % fixed bc along x-axis
    if i==nx  % lower right hand corner
        vxhout(i,j) = 0;   vyhout(i,j) = 0;
        Omegahout(i,j) = 0;
    elseif i==1   % lower left hand corner
        phi(i,j) = 1/4*(  rho1*A1/V1  );
        alpha(i,j) = (  Sxy1*A1/M1  );
        vxhout(i,j) = vxh(i,j) - dt/(2*phi(i,j))*(Sxx1*(y2-y3)
         - Sxy1*(x2-x3)  ) + dt*alpha(i,j);
```

```
        vyhout(i,j) = 0;
        Omegahout(i,j) = 0;
    else   % fixed bc along x-axis (general)
        phi(i,j) = 1/4*(  rho1*A1/V1 + rho2*A2/V2 );
        alpha(i,j) = 1/2*(  Sxy1*A1/M1 + Sxy2*A2/M2  );
        vxhout(i,j) = vxh(i,j) - dt/(2*phi(i,j))*
        (  Sxx1*(y2-y3) + ...
            Sxx2*(y3-y4) - Sxy1*(x2-x3) - Sxy2*(x3-x4)  )
            + dt*alpha(i,j);
        vyhout(i,j) = 0;
        Omegahout(i,j) = 0;
    end
elseif i==nx    % fixed bc in x-direction at the wall
interface (x=Bar_length)
    % (and the point is not along the x-axis, j=1)
    if j==ny   % upper right hand corner
        phi(i,j) = 1/4*(    rho3*A3/V3  );
        beta(i,j) = (   (Syy3-Stt3)*A3/M3  );
        Omegahout(i,j) = 0;
        vxhout(i,j) = 0;
        vyhout(i,j) = vyh(i,j) + dt/(2*phi(i,j))*(
         Syy3*(x4-x1) - Sxy3*(y4-y1)   )  + dt*beta(i,j);
    else    % along the fixed boundary on the right hand side
        phi(i,j) =  1/4*(   rho2*A2/V2 + rho3*A3/V3  );
        beta(i,j) = 1/2*(  (Syy2-Stt2)*A2/M2 + (Syy3-Stt3)*A3/M3  );
        Omegahout(i,j) = 0;
        vxhout(i,j) = 0;
        vyhout(i,j) = vyh(i,j) + dt/(2*phi(i,j))*(
        Syy2*(x3-x4) + Syy3*(x4-x1) - Sxy2*(y3-y4) ...
            - Sxy3*(y4-y1)   ) + dt*beta(i,j);
    end
elseif i==1     % free bc along the free back end of the rod
    % (and the point is not along the x-axis, j=2)
```

```
    if j==ny   % upper left hand corner
        phi(i,j) = 1/4*(  rho4*A4/V4  );
        alpha(i,j) = (  Sxy4*A4/M4  );
        beta(i,j) = (   (Syy4-Stt4)*A4/M4  );
        Gamma(i,j) = (    Syt4*A4/M4  );
        Omegahout(i,j) = Omegah(i,j) - (dt/(2*phi(i,j))*(
        Stx4*(y1-y2) - Syt4*(x1-x2)  ) -
        dt*2*Gamma(i,j)  )*y(i,j);
        vxhout(i,j) = vxh(i,j) - dt/(2*phi(i,j))*( Sxx4*(y1-y2)
        - Sxy4*(x1-x2)   ) + dt*alpha(i,j);
        vyhout(i,j) = vyh(i,j) + dt/(2*phi(i,j))*( Syy4*(x1-x2)
        - Sxy4*(y1-y2)   ) + dt*( beta(i,j)+
        (omegah(i,j))^2*y(i,j) );
    else  % free bc along the left hand side
        phi(i,j) = 1/4*(    rho1*A1/V1 + rho4*A4/V4   );
        alpha(i,j) = 1/2*(  Sxy1*A1/M1 + Sxy4*A4/M4   );
        beta(i,j) = 1/2*(  (Syy1-Stt1)*A1/M1 + (Syy4-Stt4)*A4/M4  );
        Gamma(i,j) = 1/2*(    Syt1*A1/M1 + Syt4*A4/M4  );
        Omegahout(i,j) = Omegah(i,j) - (   dt/(2*phi(i,j))*
        (  Stx1*(y2-y3) + Stx4*(y1-y2) - Syt1*(x2-x3) ...
            - Syt4*(x1-x2)    ) - dt*2*Gamma(i,j)  )*y(i,j);
        vxhout(i,j) = vxh(i,j) - dt/(2*phi(i,j))*
        ( Sxx1*(y2-y3) + Sxx4*(y1-y2) - Sxy1*(x2-x3) ...
            - Sxy4*(x1-x2)     ) + dt*alpha(i,j);
        vyhout(i,j) = vyh(i,j) + dt/(2*phi(i,j))*
        ( Syy1*(x2-x3) + Syy4*(x1-x2) ...
            - Sxy1*(y2-y3) - Sxy4*(y1-y2)   ) +
             dt*(beta(i,j)+(omegah(i,j))^2*y(i,j));
    end
elseif j==ny     % free bc along the outer surface of
the rod along the length
        phi(i,j) = 1/4*(    rho3*A3/V3 + rho4*A4/V4   );
        alpha(i,j) = 1/2*(  Sxy3*A3/M3 + Sxy4*A4/M4   );
```

```
            beta(i,j) = 1/2*(  (Syy3-Stt3)*A3/M3 +
             (Syy4-Stt4)*A4/M4  );
            Gamma(i,j) = 1/2*(  Syt3*A3/M3 + Syt4*A4/M4  );
            Omegahout(i,j) = Omegah(i,j) - (dt/(2*phi(i,j))*(
            Stx3*(y4-y1) + Stx4*(y1-y2) - Syt3*(x4-x1) ...
                - Syt4*(x1-x2)    ) - dt*2*Gamma(i,j)  )*y(i,j);
            vxhout(i,j) = vxh(i,j) - dt/(2*phi(i,j))*( Sxx3*(y4-y1)
            + Sxx4*(y1-y2) - Sxy3*(x4-x1) ...
                - Sxy4*(x1-x2)     ) + dt*alpha(i,j);
            vyhout(i,j) = vyh(i,j) + dt/(2*phi(i,j))*( Syy3*(x4-x1)
            + Syy4*(x1-x2) - Sxy3*(y4-y1) ...
                - Sxy4*(y1-y2)   ) + dt*(beta(i,j)+
                (omegah(i,j))^2*y(i,j));

            if  k==5 & i==nx-1
                vy_junk_inner = vyh(i,j)
            end
        else   % Define velocities at general zones
            phi(i,j) = 1/4*(   rho1*A1/V1 + rho2*A2/V2 + rho3*A3/V3
            + rho4*A4/V4 );
            alpha(i,j) = 1/4*( Sxy1*A1/M1 + Sxy2*A2/M2 + Sxy3*A3/M3
            + Sxy4*A4/M4 );
            Gamma(i,j) = 1/4*( Syt1*(A1/M1) + Syt2*(A2/M2) + Syt3*(A3/M3)
            + Syt4*(A4/M4) );
            beta(i,j) = 1/4*( (Syy1-Stt1)*A1/M1 + (Syy2-Stt2)*A2/M2
            +(Syy3-Stt3)*A3/M3 + (Syy4-Stt4)*A4/M4  );
            Omegahout(i,j) = Omegah(i,j) - (   dt/(2*phi(i,j))*
            (Stx1*(y2-y3) + Stx2*(y3-y4) + Stx3*(y4-y1) ...
                + Stx4*(y1-y2) - Syt1*(x2-x3) - Syt2*(x3-x4) -
                Syt3*(x4-x1) - Syt4*(x1-x2)   ) - dt*2*Gamma(i,j)  )*y(i,j);
%             vxhout(i,j) = vxh(i,j) - dt/(2*phi(i,j))*(Sxx1*(y2-y3)
            + Sxx2*(y3-y4) + Sxx3*(y4-y1) + Sxx4*(y1-y2) - Sxy1*(x2-x3) ...
%                 - Sxy2*(x3-x4) - Sxy3*(x4-x1) - Sxy4*(x1-x2)  )
```

```
            + dt*alpha(i,j);
            vxhout(i,j) = vxh(i,j) - dt/(2*phi(i,j))*(Sxx1*(y2-y3)
            + Sxx2*(y3-y4) + Sxx3*(y4-y1) + Sxx4*(y1-y2) - Sxy1*(x2-x3) ...
                - Sxy2*(x3-x4) - Sxy3*(x4-x1) - Sxy4*(x1-x2)  )
                + dt*alpha(i,j);
            vyhout(i,j) = vyh(i,j) + dt/(2*phi(i,j))*(Syy1*(x2-x3)
            + Syy2*(x3-x4) + Syy3*(x4-x1) + Syy4*(x1-x2) - Sxy1*(y2-y3) ...
                - Sxy2*(y3-y4) - Sxy3*(y4-y1) - Sxy4*(y1-y2)  ) + dt*(
                beta(i,j)+(omegah(i,j))^2*y(i,j) );
        end

        % calculate new (x, y) coordinates for k+1
        xout(i,j) = x(i,j) + vxhout(i,j)*dth;  % use dth(k+1)
        yout(i,j) = y(i,j) + vyhout(i,j)*dth;
        % calculate half steps (averaged values of x,y for k+1/2)
        xhout(i,j) = 1/2*(x(i,j)+xout(i,j));       % x at k+1/2
        yhout(i,j) = 1/2*(y(i,j)+yout(i,j));       % y at k+1/2
        % calculate the angular velocity at k+1/2
        if j==1
            omegahout(i,j) = 0;
        else
            omegahout(i,j) = Omegahout(i,j)/(yhout(i,j))^2;
        end
        Thetaout(i,j) = Theta(i,j) + omegahout(i,j)*dth;
    end
end

function  [P] = MG_EOS(rho_o,rho,T,C,Gamma,S1,Cv)
% Mie Gruneisen EOS
% C = C*1000;  % convert from km/s to m/s
To = 298;  % deg K
N = 1 - rho_o/rho;
Ph = rho_o*C^2*N/(1 - S1*N)^2;
```

```
P = Ph + Gamma*rho*Cv*(T-To);
% P  = rho_o*C^2*N*(1-(Gamma/2)*N/(1-N))/(1 - S1*N)^2 +
% Gamma*rho*Cv*(T-To);


function [dthout] = time_fun(x,y,A,rho,K_al,Co,CL,dsth,nx,ny,cfl,dthin,P)
% function to calculate the time step for k+3/2
% change rho from reference density to calculated value from EOS
for j=1:ny-1
    for i=1:nx-1
        d1 = sqrt((x(i+1,j+1)-x(i,j))^2 + (y(i+1,j+1)-y(i,j))^2);
        d2 = sqrt((x(i+1,j)-x(i,j+1))^2 + (y(i,j+1)-y(i+1,j))^2);
        d_max = max(d1,d2);    % largest diagonal dimension in each zone
        L_d(i,j) = A(i,j)/d_max;  % minimum zone thickness
        a = sqrt(P(i,j)/rho(i,j));   % local speed of sound
        b = 8*(Co^2+CL)*L_d(i,j)*dsth(i,j);
        dth_ij(i,j) = 0.67*L_d(i,j)/sqrt(a^2+b^2);
    end
end
dthout = min(min(dth_ij(2:nx-1,2:ny-1)))*cfl;  % initial time step is k=1/2
if dthout>1.1*dthin
    dthout = 1.1*dthin;
end
```

REFERENCES

[1] "Facility for the analysis of chemical thermodynamics (http://www.crct.polymtl.ca/fact/)." 2007.

[2] "Heterogeneous reaction." 2007.

[3] "Merriam webster's online dictionary." 2008.

[4] Austin, R. A., "Numerical simulation of the shock compression of microscale reactive particle systems," Master's thesis, Georgia Institute of Technology, 2005.

[5] Austin, R. A., McDowell, D. L., and Benson, D. J., "Numerical simulation of shock wave propagation in spatially-resolved particle systems," *Modeling Simul. Mater. Sci. Eng.*, vol. 14, pp. 537–561, 2006.

[6] Baer, M. R. and Nunziato, J. W., "Two-phase mixture theory for the deflagration-to-detonation transition (ddt) in reactive granular materials," *International Journal of Multiphase Flow*, vol. 12, no. 6, pp. 861–889, 1986.

[7] Batsanov, S. S., "Specific features of solid-phase reactions induced by shock waves," *Combustion, Explosion, and Shock Waves*, vol. 42, no. 2, pp. 237–241, 2006.

[8] Batsanov, S. S., Doronin, G. S., Kolchkov, S. V., Litvak, G. S., and Nigmatullina, V. M., "Synthesis reactions behind shock fronts," *Shock Waves*, vol. 22, no. 6, p. 765, 1986.

[9] Bdzil, J. B., Menikoff, R., Son, S. F., Kapila, A. K., and Stewart, D. S., "Two-phase modeling of deflagration-to-detonation transition in granular

materials: A critical examination of modeling issues," *Physics of Fluids*, vol. 11, no. 2, pp. 378–402, 1999.

[10] Bennett, L. S. and Horie, Y., "Shock-induced inorganic reactions and condensed phase detonations," *Shock Waves*, vol. 4, pp. 127–136, 1994.

[11] Bennett, L. S., Horie, Y., and Hwang, M. M., "Constitutive model of shock-induced chemical reactions in inorganic powder mixtures," *J. Appl. Phys.*, vol. 76, no. 6, pp. 3394–3402, 1994.

[12] Benson, D. J., "Computational methods in lagrangian and eulerian hydrocodes," *Computer Methods in Applied Mechanics and Engineering*, vol. 99, pp. 235–394, 1992.

[13] Benson, D. J., "An analysis by direct numerical simulation of the effects of particle morphology on the shock compaction of copper powder," *Modelling Simul. Mater. Sci. Eng.*, vol. 2, 1994.

[14] Benson, D. J., "A multi-material eulerian formulation for the efficient solution of impact and penetration problems," *Computational Mechanics*, vol. 15, pp. 558–571, 1995.

[15] Benson, D. J., Nesternko, V. F., Jonsdottir, F., and Meyers, M. A., "Quasistatic and dynamic regimes of granular material deformations under impulse loading," *J. Mech. Phys. Solids*, vol. 45, no. 11, pp. 1955–1999, 1997.

[16] Bevington, P. R. and Robinson, D. K., *Data Reduction and Error Analysis for the Physical Sciences*. Boston: McGraw-Hill, 1992.

[17] Bolkohovitinov, L. G. and Batsanov, S. S., "Theory of solid-state detonation," *Combustion, Explosion, and Shock Waves*, vol. 43, no. 2, pp. 219–221, 2007.

[18] Borg, J. P., Cogar, J. R., Lloyd, A., Ward, A., and Chapman, D., "Computational simulations of the dynamic compaction of porous media," *International Journal of Impact Engineering*, pp. 109–118, 2006.

[19] Boslough, M. B., "Shock-induced solid-state chemical reactivity studies using time-resolved ratdiation pyrometry," *International Journal of Impact Engineering*, vol. 5, no. 173, pp. 173–180, 1986.

[20] Boslough, M. B., "A thermochemical model for shock-induced reactions (heat detonations) in solids," *J. Chem. Phys.*, vol. 92, pp. 1839–1848, 1990.

[21] Boslough, M. B. and Graham, R. A., "Submicrosecond shock-induced chemical reactions in solids: first real-time observations," *Chemical Physics Letters*, vol. 121, no. 4–5, p. 446, 1985.

[22] Bowden, F. P. and Yoffe, A. D., *Initiation and growth of Explosives in Liquids and Solids*. Cambridge, Massachusetts: Cambridge University, 1952.

[23] Boyer, M. H., "Calculation of the characteristics of detonation waves in real materials," *Journal of Applied Physics*, vol. 40, no. 2, 1969.

[24] Carroll, M. M. and Holt, A. C., "Static and dynamic pore-collapse relations for ductile porous materials," *J. Appl. Phys.*, vol. 43, no. 4, 1972.

[25] Carroll, M. M., Kim, K. T., and Nesterenko, V. F., "The effect of temperature on viscoplastic pore collapse," *J. Appl. Phys.*, vol. 59, no. 6, 1986.

[26] Carter, R. E. *Journal of Chemimcal Physics*, vol. 35, pp. 2010–2015, 1961.

[27] Carter, R. E. *Journal of Chemimcal Physics*, vol. 35, pp. 1137–1138, 1961.

[28] Chen, H. C., Lasalvia, J. C., Nesterenko, V. F., and Meyers, M. A., "Shear localization and chemical reaction in high-strain, high-strain rate deformation of ti-si powder mixtures," *Acta mater.*, vol. 46, no. 9, pp. 3033–3046, 1998.

[29] Choi, H. J., Austin, R. A., Allen, J. K., McDowell, D. L., Mistree, F. M., and Benson, D. J., "An approach for robust design of reactive powder metal mixtures based on non-deterministic micro-scale shock simulation," *Journal of Computer-Aided Materials Design*, vol. 12, pp. 57–85, 2005.

[30] da Silvia, M. G. and Ramesh, K. T., "The rate-dependent deformations of porous pure iron," *International Journal of Plasticity*, vol. 13, no. 6–7, pp. 587–610, 1997.

[31] Danielewski, M. and Filipek, R., "Interdiffusion in oxide solid solutions, simulation of the process and calculation of intrinsic diffusivities," *Molecular Crystals and Liquid Crystals Science and Technology, Section A: Molecular Crystals and Liquid Crystals*, vol. 341, pp. 277–282, 2000.

[32] Dienes, J. K., Zuo, Q. H., and Kershner, J. D., "Impact initiation of explosives and propellants via statistical crack mechanics," *Journal of the Mechanics and Physics of Solids*, vol. 54, no. 6, pp. 1237–1275, 2006.

[33] Do, I. P. H. and Benson, D. J., "Modeling of shock-induced chemical reactions," *International Journal of Computational Engineering Science*, vol. 1, no. 1, pp. 61–79, 2000.

[34] Do, I. P. H. and Benson, D. J., "Micromechanical modeling of shock-induced chemical reactions in heterogeneous multi-material powder mixtures," *International Journal of Plasticity*, vol. 17, pp. 641–668, 2001.

[35] Dremin, A. N. and Breusov, O. N. *Russ. Chem. Rev.*, vol. 37, p. 392, 1968.

[36] Dunin, S. Z. and Surkov, V. V., "Effects of energy dissipation and melting on shock compresion of porous bodies," *Journal of Applied Mechanics and Technical Physics*, vol. 23, no. 1, pp. 123–134, 1982.

[37] Eakins, D. and Thadhani, N. N., "Discrete particle simulation of shock wave propagation in a binary ni+al powder mixture," *J. Appl. Phys.*, vol. 101, p. 043508, 2007.

[38] Eakins, D. E., *Role of Heterogeneity in the Chemical and Mechanical Shock-Response of Nickel and Aluminum Powder Mixtures*. PhD thesis, Georgia Institute of Technology, School of Materials Science and Engineering, 2007.

[39] Eakins, D. E. and Thadhani, N. N., "Role of constituent configuration on shock-induced reactions in a ni+al powder mixture," in *2005 Materials Research Society Fall Meeting*, 2006.

[40] Eyring, H., Powel, R. E., Duffrey, G. H., and Darlin, R. B., "The stability of detonation," *Chemical Rev.*, vol. 45, no. 69, 1949.

[41] Fan, R. H., Lu, H. L., Sun, K. N., Wang, W. X., and Yi, X. B., "Kinetics of thermite reaction in al-fe$_2$o3 system," *Thermochimica Acta*, vol. 440, no. 2, pp. 129–131, 2006.

[42] Fedkiw, R. P., Aslam, T., Merriman, B., and Osher, S., "A non-oscillatory eulerian approach to interfaces in multimaterial flows (the ghost fluid method)," *J. Comp. Phys.*, vol. 152, pp. 457–492, 1999.

[43] Follansbee, P. S., Huang, J. C., and Gray, G. T., "Low-temperature and high-strain-rate deformation of nickel and nickel-carbon alloys and analysis of the constitutive behavior according to an internal state variable model," *Acta metall. mater.*, vol. 38, no. 7, pp. 1241–1254, 1990.

[44] Geng, H., Tan, H., and Wu, Q., "A new equation of state for porous materials with ultra-low densities," *Journal of Physics: Condensed Matter*, vol. 14, pp. 10855–10859, 2002.

[45] Geng, H., Wu, Q., Tan, H., Cai, L., and Jing, F., "Extension of the wujing equation of state for highly porous materials: Calculations to validate and compare the thermoelectron model," *Journal of Applied Physics*, vol. 92, no. 10, pp. 5917–5923, 2002.

[46] Geng, H., Wu, Q., Tan, H., Cai, L., and Jing, F., "Extension of the wujing equation of state for highly porous materials: Thermoelectron based theoretical model," *Journal of Applied Physics*, vol. 92, no. 10, pp. 5924–5929, 2002.

[47] German, R. M., *Sintering Theory and Practice*. New York: Wiley, 1996.

[48] Glimm, J., Li, X., Liu, Y., Xu, Z., and Zhao, N., "Conservative front tracking and level set algorithms," *Proc. Natl. Acad. Sci.*, vol. 98, no. 25, pp. 14198–14201, 2001.

[49] Gordopolov, A. and Viljoen, H. J., "A study in mechano-chemistry: pressure induced reactions and non-equilibrium phenomenon," in *American Institute of Chemical Engineers Annual Conference Proceedings*, 2004.

[50] Grady, D. E. and Winfree, N. A., *Fundamental issues and applications of shock-wave and high-strain rate phenomena*. Amsterdam: Elservier-Science, 2001.

[51] Grady, D. E., Winfree, N. A., Kerley, G. I., Wilson, L. T., and Kuhns, L. D., "Computational modeling and wave propagation in media with inelastic deforming microstructure," *J. Phys. IV*, pp. 15–20, 2000.

[52] Graham, R. A., "High pressure eplosive processing of ceramics," tech. rep., 1987.

[53] Gur'ev, D. L., Gordopolov, Y. A., and Batsanov, S. S., "Solid-state synthesis of znte in shock waves," *Combustion, Explosion, and Shock Waves*, vol. 42, no. 1, pp. 116–123, 2006.

[54] Gur'ev, D. L., Gordopolov, Y. A., Batsanov, S. S., Merzhanov, A. G., and Fortov, V. E., "Solid-state detonation in the zinc-sulfur system," *Combustion, Explosion, and Shock Waves*, vol. 42, no. 1, pp. 116–123, 2006.

[55] Halloran, J. W. and Bowen, H. K., "Iron diffusion in iron-aluminate spinels," *J. Am. Ceram. Soc.*, vol. 63, no. 1-2, pp. 58–65, 1980.

[56] Hanagud, S. and Ross, B., "Larege deformation, deep penetration theory for a compressible strain- hardening target material," *AIAA Journal*, vol. 9, no. 5, 1971.

[57] Hanson, K. M., "Uncertainty quantification of simulation codes based on experimental data," in *41st Aerospace Sciences Meeting and Exhibit*, pp. 179–188, 2003.

[58] Helander, T. and Agren, J., "A phenomenological treatmtent of diffusion in al-fe and al-ni alloys having b2-b.c.c. ordered structure," *Acta mater.*, vol. 47, no. 4, 1999.

[59] Hemez, F. M., Brock, J. S., and Kamm, J. R., "Non-linear error ansatz models in space and time for solution verification," in *47th AIAA/ASME/ASCE/AHS/ASC Structures, Structural Dynamics, and Materials Conference*, no. AIAA-2006-1995, 2006.

[60] Herrmann, W., "Constitutive equation for the dynamic compaction of ductile porous materials," *J. Appl. Phys.*, vol. 40, no. 6, 1968.

[61] Horie, Y., Hamate, Y., and Greening, D., "Mechanistic reactive burn modeling of solid explosives," Tech. Rep. LA-14008, Los Alamos National Laboratories, Los Alamos, NM, 2003.

[62] Horie, Y. and Kipp, M. E., "Modeling of chemical reactions in the mixture of al-ni powders under shock-wave compression," *Shock Waves in Condensed Matter*, pp. 387–390, 1988.

[63] Jeffrey, A., *Advanced Engineering Mathematics*. New York: Harcourt/Academic Press, 2002.

[64] Jordan, J. L., Dick, R., Ferranti, L., Thadhani, N. N., Austin, R. A., McDowell, D. L., and Benson, D. J., "Equation of state of aluminum-iron oxide(fe_2o_3)-epoxy composite: modeling and experiment," in *14th American Physical Society Topical Conference on Shock Compression of Condensed Matter*, vol. 15, 2005.

[65] Kamenetskii, D. A., *Diffusion and Heat Transfer in Chemical Kinetics*. New York-London: Plenum Press, 1969.

[66] Kaufman, G. J., *Aluminum Alloy Database*. New York, NY: Knovel, 2004.

[67] Kee, R. J., Rupley, F. M., Meeks, E., and Miller, J. A., "Chemkin-iii: A fortran chemical kinetics package for the analysis of gas-phase chemical and plasma kinetics," Tech. Rep. Technical Report SAND96-8216, Sandia National Laboratories, Albuquerque, NM, 1996.

[68] Kirkpatrick, S., "Optimization by simulated annealing: quantitative studies," *J. Stat. Phys.*, vol. 34, pp. 975–86, 1984.

[69] Klepaczko, J. R., Sasaki, T., and Kurokawa, T., "On rate sensetivity of polycrystalline aluminum at high strain rates," *Trans. Japan Soc. Aeror. Space Sci.*, vol. 36, pp. 170–187, 1993.

[70] Knupp, P. M. and Salari, K., *Verification of computer codes in computational science and engineering*. Boca Raton, London, New York, Washington, D.C.: Chapmann & Hall/CRC, 2003.

[71] Kocks, U. F. and Ashby, A. S., *Progress in Material Science*. New York: Pergamon Press, 1975.

[72] Lee, E. L. and Tarver, C. M., "Phenomenological model of shock initiation in heterogeneous explosives," *Phys. Fluids*, pp. 2362–2372, 1980.

[73] Leer, V., "Towards the ultimate conservative difference scheme," *J. Comp. Phys.*, vol. 32, pp. 101–136, 1979.

[74] Lin, S. J., Barson, S. L., and Sindir, M. M., "Development of evaluation criteria and a proceedure for assessing predictive capability and code performance," in *Advanced Earth-to-Orbit Propulsion Technology Conf.*, 1992.

[75] Linan, A. and Williams, F. A., "Theory of ignition of a reactive solid by constant energy flux," *Combustion Sci. Technol.*, vol. 3, pp. 91–98, 1971.

[76] Logan, R. W. and Nitta, C. K., "Comparing 10 methods for solution verification, and linking to model validation," *Journal of Aerospace Computing, Information, and Communication*, vol. 3, pp. 354–373, 2006.

[77] Lu, X., *Non-Equilibrium Thermodynamic Models for the Dynamic Behavior of Polycrystalline Solids*. PhD thesis, Georgia Institute of Technology, School of Aerospace Engineering, 2002.

[78] Lu, X., Narayanan, V. N., and Hanagud, S., "Shock compression of materials," in *14th American Physical Society Topical Conference on Shock Compression of Condensed Matter*, vol. 15.

[79] L.Youngs, D., *Numerical Methods for Fluid Dynamics*, ch. Time dependent multi-material flow with large fluid distortion, pp. 273–285. London; New York: Academic Press, 1982.

[80] Marsh, S. P., *LASL Shock Hugoniot Data*. Berkeley, Los Angeles, London: University of California Press, 1980.

[81] McClintock, F. A., Kaplan, S. M., and Berg, C. A., "Ductile fracture by hold growth in shear bands," *International Journal of Fracture Mechanics*, vol. 2, no. 4, pp. 614–627, 1966.

[82] McClintock, F. A., Kaplan, S. M., and Berg, C. A., "A criterion for ductile fracture by the growth of holes," *Journal of Applied Mechanics*, pp. 363–371, 1968.

[83] McGlaun, J. M., "Improvements in csqii: a transmitting boundary condition," Tech. Rep. Technical Report SAND82-1248, Sandia National Laboratories, Albuquerque, NM, 1982.

[84] McQueen, G., Marsh, S. P., Taylor, J. W., Fritz, J., and Carter, W. J., *High Velocity Impact Phenomena*, ch. The Equation of State of Solids from Shock Wave Studies, p. 230. New York: Academic, 1970.

[85] Meyers, M. A., *Dynamic Behavior of Materials*. New York: John Wiley and Sons, Inc., 1994.

[86] Murnaghan, F. D., "Finite deformations of an elastic solid," *American Journal of Mathematics*, vol. 49, pp. 235–260, 1937.

[87] Namjoshi, S. A. and Thadhani, N. N., "Modeling the reaction synthesis of shock-densified titanium-silicon powder mixture compacts," *Metallurgical and Materials Transactions B*, vol. 31B, pp. 307–316, 2000.

[88] Narayanan, V. N., *Non-Equilibrium Thermodynamics of Multifunctional Energetic Structural Materials*. PhD thesis, Georgia Institute of Technology, School of Aerospace Engineering, 2005.

[89] Nelder, J. A. and Mead, R., "A simplex method for function minimization," *Computer Journal*, vol. 7, 1965.

[90] Nesterenko, V. F., "Micromechanics of powders under strong impulse loading," in *Proceedings of X All-Union Conference*, pp. 212–220.

[91] Nesterenko, V. F., *High-Rate Deformation of Heterogeneous Materials*. Novosibirsk: Nauka, 1992. (in Russian).

[92] Nesterenko, V. F., *Dynamics of Heterogeneous Materials*. New York: Springer-Verlag, 2001.

[93] Neumann, J. V. and Richtmyer, R. D., "A method for the numerical calculation of hydrodynamic shocks," *J. Appl. Phys.*, vol. 21, pp. 232–257, 1950.

[94] of Aeronautics, A. I. and Staf, A., *AIAA Guide for the Verification and Validation of Computational Fluid Dynamics Simulations*. American Institute of Aeronautics & Astronautics, 1998.

[95] Oh, K. H. and Persson, P. A., "Equation of state for extrapolation of high-pressure shock hugoniot data," *Journal of Applied Physics*, vol. 65, no. 10, pp. 3852–3856, 1989.

[96] Ott, J. B. and Boerio-Goates, J., *Chemical Thermodynamics: principles and applications*. London: Academic Press, 2000.

[97] R. A. Austin, title=Personal written correpondence, i. y.

[98] Rajagopal, K. R. and Tao, L., *Mechanics of Mixtures*. Singapore: World Scientific, 1995.

[99] Reding, D. J. and Hanagud, S., "Uncertainty quantification for multi-functional energetic structural material simulations," in *48th AIAA/ASME/ASCE/AHS/ASC Structures, Structural Dynamics, and Materials Conference*, no. AIAA-2007-1936, 2007.

[100] Reding, D. J. and Hanagud, S., "Chemical reactions in reactive powder metal mixtures during shock compression," *Journal of Applied Physics*, vol. 105, no. 1, 2008.

[101] Reding, D. J., Lu, X., Narayanan, V. N., and Hanagud, S., "Constitutive modeling of multi-functional structural energetic materials: plasticity effects," in *47th AIAA/ASME/ASCE/AHS/ASC Structures, Structural Dynamics, and Materials Conference*, no. AIAA-2006-1950, 2006.

[102] Roache, P. J., *Verification and Validation in Computational Science and Engineering*. Albuquerque, NM: Hermosa Publishers, 1998.

[103] Roache, P. J., "Conservatism of the grid convergence index in finite volume computations on steady-state fluid flow and heat transfer," *Journal of Fluids Engineering*, vol. 125, pp. 731–733, 2003.

[104] S. Hanagud, X. L. and Zaharieva, R., "Equation of state & failure criterion of dual functional structural energetic materials," 2007.

[105] Schmalzried, H., *Chemical Kinetics of Solids*. New York: VCH Publishers, 1995.

[106] Shaffer, P. T. B., *Properties of High-Temperature Materials*, vol. 1. New York: Plenum: Plenum Press Handbooks of High-Temperature Materials, 1964.

[107] Shu, C. W., "Essentially non-oscillatory and weighted essentially non-oscillatory schemes for hyperbolic conservation laws," *ICASE*, no. Report No. 97-65, pp. 1–78, 1997.

[108] Slack, G. A., "$FeAl_2O_4 - MgAl_2O_4$: Growth and some thermal, optical, and magnetic properties of mixed sincle crystals," *Physical Review*, vol. 134, no. 1964, pp. A1268–A1280, 1964.

[109] Smith, D. P. and Chaudhri, M. M., "Kinetic analysis of solid-state reactions: an improved analysis method," in *1995 Materials Research Society Symposium Proceedings*, vol. 418, pp. 105–110, 1995.

[110] Song, I. and Thadhani, N. N., "Shock-inducded chemical reactions and synthesis of nickel aluminides," *Metallurgical Transactions A*, vol. 23, pp. 41–48, 1992.

[111] Tang, Z. P., Liu, W., and Horie, Y., "Numerical investigation of pore collapse under dynamic compression," pp. 309–212, 2000.

[112] Thadhani, N. N., "Shock-induced and shock-assisted solid-state chemical reactions in powder mixtures," *J. Appl. Phys.*, vol. 76, no. 4, pp. 2129–2138, 1994.

[113] Thadhani, N. N., Graham, R. A., Royal, T., Dunbar, E., Anderson, M. U., and Holman, G. T., "Shock-induced chemical reactions in titanium-silicon powder mixtures of different morphologies: Time-resolved pressure mesurements and materials analysis," *J. Appl. Phys.*, vol. 82, no. 3, pp. 1113–1128, 1997.

[114] Torunov, S. I. and Trofimov, V. S., "Detonation hugoniots of powdered ti-c, ti-b, fe_2o_3-al mixtures with gasifying additives," *Chem. Phys. Reports*, vol. 17, no. 11, pp. 2167–2177, 1999.

[115] Wagner, C. *Z. anorg. allg. Chem.*, vol. 236, no. 236, p. 320, 1938.

[116] Wang, J., Li, X., and Yan, H., "Research of energy deposition caused by pore collapse," *Combustion, Explosion, and Shock Waves*, vol. 41, no. 3), year=2005, pages=357–362,.

[117] Washburn, E. W., *International Critical Tables of Numerical Data, Physics, Chemistry and Technology (1st Electronic Edition)*. Knovel, (1926–1930; 2003).

[118] Wilkins, M. L., *Computer Simulation of Dynamic Phenomena*. New York: Springer-Verlag, 1999.

[119] Wu, Q. and F. Jing, title=Thermodynamic equation of state and application to Hugoniot predictions for porous materials, j. v. n. p. y.

[120] Xu, X. and Thadhani, N. N., "Investigation of shock-induced reaction behavior of as-blended and ball-milled $ni+ti$ powder mixtures using time-resolved stress measurements," *J. Appl. Phys.*, vol. 96, no. 4, pp. 2000–2009, 2004.

[121] Yoshida, M., "Program mixture," tech. rep., CETR Report, New Mexico Institute of Mining and Technology, 1986.

[122] Yurek, G. J., Rapp, R. A., and Hirth, J. P., "Kinetics of the displacement reaction between iron and cu//2o," *Metallurgical Transactions*, no. 5, pp. 1293–1300, 1973.